Effect of internal stress and microstructure on the hydriding of Pd thin films

Renaud Delmelle

Composition of the jury:

Prof. Joris Proost (advisor)	Université catholique de Louvain
Prof. Thomas Pardoen	Université catholique de Louvain
Prof. Laurent Francis	Université catholique de Louvain
Prof. Yaroslav Filinchuk	Université catholique de Louvain
Prof. Dominique Schryvers	Universiteit Antwerpen
Dr. Andreas Borgschulte	EMPA Materials Science and Technology
Prof. Grégoire Winckelmans (president)	Université catholique de Louvain

Louvain-la-Neuve, December 17, 2012

Abstract

Hydrogen is gaining more and more importance as an energy carrier for mobile and stationary applications as a consequence of both environmental and economical realities. Thin film metal hydrides occupy an important place in this context, providing technological answers to crucial detection and permeation issues, but also turning out to be an excellent research solution for storage issues, enabling for cheap and efficient large scale compositional studies for a wide range of alloys. In these fields of applications, internal stress and microstructural effects are of fundamental importance, as they affect both hydride kinetic and thermodynamic behaviours, which are key technological parameters that determine, for instance, the autonomy of hydrogen vehicles, the filling time of hydrogen tanks, the response time of hydrogen sensors, the energetic efficiency of fuel cells or the resistance to embrittlement of hydrogen pipeline steels. However, these effects still suffer from a lack of understanding, especially as regards their respective kinetic implications. More specifically, the separation of the internal stress contribution from the microstructural contribution - which would bring fundamental information to the debate - is experimentally difficult to perform.

In the present thesis work, a high resolution in-situ experimental approach has been considered. It allows to accurately measure the internal stress evolution in a cantilevered thin film specimen during its deposition, hydrogen cycling and annealing. Together with the construction of a self-consistent kinetic model for thin film hydriding, and using Pd as a model system, that technique enabled to propose, for the first time, a quantitative interpretation of the effect of internal stress on the hydriding properties independently of the microstructure, and inversely, to quantitatively address the effect of microstructure independently of internal stress. Our results show that both contributions are kinetically and thermodynamically substantial, and may lead to interesting materials engineering applications.

Scientific output

International peer-reviewed papers

1. **R. Delmelle**, S. Michotte, M. Sinnaeve and J. Proost, *"Effect of internal stress on the hydriding kinetics of nanocrystalline Pd thin films"*, Acta Materialia, submitted (2012).

2. **R. Delmelle** and J. Proost, *"An in situ study of the hydriding kinetics of Pd thin films"*, Physical Chemistry Chemical Physics 13 (2011) 11412-11421.

3. **R. Delmelle**, G. Bamba and J. Proost, *"In situ monitoring of hydride formation in Pd thin film systems"*, International Journal of Hydrogen Energy 35 (2010) 9888-9892.

International patents

1. J. Proost, **R. Delmelle** and S. Michotte, *"Device, method and system for improved storage, uptake and release of hydrogen"*, world patent PCT/EP2011/058164, filed 19^{th} May 2011.

International conference contributions

1. **R. Delmelle**, O. De Liedekerke, S. Michotte and J. Proost, *"Effect of internal stress on the hydriding kinetics of Pd thin film systems"*, 7^{th} International Conference on Diffusion in Solids and Liquids, Vilamoura (2011).

2. **R. Delmelle**, S. Michotte and J. Proost, *"In-situ study of the effect of internal stress on the hydriding kinetics of Pd-based thin film systems"*,

12^{th} International Conference on Modern Materials and Technologies, Montecatini Terme (2010).

3. **R. Delmelle** and J. Proost, *"In-situ study of hydriding kinetics in Pd-based thin film system"*, 18^{th} World Hydrogen Energy Conference, Essen (2010).

4. **R. Delmelle** and J. Proost, *"In-situ monitoring of hydriding kinetics using high resolution curvature measurements"*, Materials Research Society Fall Meeting, Boston (2009).

5. M.-S. Colla, **R. Delmelle**, A. Boe, M. Coulombier, J.-P. Raskin, J. Proost and T. Pardoen, *"Impact of hydriding cycles on mechanical properties of palladium thin films"*, 4^{th} Innovations in Thin Film Processing and Characterization, Nancy (2009).

6. **R. Delmelle**, M.-S. Colla, T. Pardoen and J. Proost, *"In-situ study of the kinetics and durability of Pd-hydride formation for integrated hydrogen sensor applications"*, Materials Research Society Spring Meeting, San Francisco (2009).

7. **R. Delmelle**, G. Bamba, M. Sinnaeve and J. Proost, *"In-situ monitoring of hydrogen storage in Pd thin film systems"*, 8^{th} International Symposium on Hydrogen Power - Theoretical and Engineering Solutions, Lisbon (2009).

Contents

Introduction

In today's industrialised society, hydrogen is gaining more and more importance as an energy carrier for mobile and stationary applications. This energy transition requires many challenging technological advances, as the hydrogen molecule is highly volatile and carries an important amount of energy. One can cite hydrogen storage, hydrogen detection and hydrogen permeation as critical fields of applications. Metal hydrides provide effective solutions in this context because they can bring hydrogen to a solid-state form at room temperature, and because they can react rapidly, selectively, and efficiently with gaseous hydrogen. Their study is also fundamental in the context of hydrogen embrittlement in steels, which is a critical field of research regarding applications like hydrogen pipelines or high pressure vessels. Metal hydrides are known for more than one century, but their understanding is still in progress. The metal-hydrogen bond is complex and sensitive to any modification in the material structure and composition, or in the environment. Moreover, the possibilities are infinite in terms of alloy design, continuously giving rise to new metal hydrides and new hydriding properties.

In these domains, metal hydrides are particularly useful in thin film form. At a scientific level, the use of thin film technologies enables to take advantage of specific surface properties and to perform advanced nanostructuring, but also to study a wide range of metals and alloys efficiently and at reduced cost. At a more technological level, thin films are suitable materials for the design of miniaturised, cheap and low-consumption hydrogen sensor and permeation systems.

A crucial parameter in the use of solid-state hydrides - as well as in the use of thin film materials - is the internal stress state of the thin film system. The deposition process itself introduces stress components in the thin film, and the interaction of thin metal films with hydrogen gas also produces large amounts of stress. On the one hand, the effect of internal stress on the hydriding properties of metals is promising in terms of applications and still needs scientific investigation, especially at the kinetic level. One the other hand, the control

of internal stress is crucial for the durability of such applications. The huge amounts of stress undergone by thin metal films subjected to hydrogen cycling frequently leads to film delamination and plasticity phenomenons.

The microstructural parameters of thin film metal hydrides are also of primary importance regarding their hydriding behaviour. Crystalline defects each interact with hydrogen in a specific way, which can substantially change the material hydriding properties. The understanding of the kinetic and thermodynamic impacts of defects in the hydriding mechanism - especially in thin film form, where fine defect engineering techniques exist - is important for the effectiveness of metal hydride applications.

In particular, stress-related and microstructural contributions are difficult to separate from each other. Many efforts are needed in this context, and the present thesis work aims at the completion of this task, notably by means of advanced control of thin film deposition conditions and by using Pd-H as a model system. The objectives of this thesis work were then defined as:

- Developing a high resolution in-situ stress measurement technique compatible with thin film deposition, hydriding and annealing experiments.
- Determining the role of internal stress on the Pd thin films hydriding properties.
- Determining the role of microstructure on the Pd thin films hydriding properties.

A high resolution in-situ approach, based on the use of the multi-beam optical sensor, has been combined, respectively, to a magnetron sputtering setup and to a high vacuum chamber dedicated to hydrogen cycling. These combinations are commonly used in vacuum environments. This is not the case of the annealing setup, which is an original combination of annealing and hydrogen cycling experiments with in-situ stress and temperature measurements. That setup has been designed, installed and tested in the course of this thesis work.

The hydriding kinetics of the Pd thin films has been studied thanks to the building of an original kinetic model. The effect of internal stress on the hydriding kinetics has been studied by properly adjusting the deposition conditions in order to obtain different internal stress states without significantly changing the specimen microstructure. The effect of microstructure has been investigated by performing annealing experiments on batches with a given internal stress state, thereby changing the microstructure and the internal stress in the Pd thin films, the latter being adjusted so that it becomes close to the internal stress state of a given as-deposited batch.

With respect to the objectives of this thesis work, the following contributions have been achieved:

- The development of an original high resolution in-situ stress measurement technique compatible with both thin film annealing and hydrogen cycling experiments.
- The achievement of an original, self-consistent interpretation of the Pd thin films hydriding kinetics.
- The proposal, for the first time, of a quantitative interpretation of the effect of internal stress on the hydriding kinetics of Pd thin films, independently of the microstructure.
- Inversely, the use of a similar approach to isolate and quantitatively study the effect of microstructure on Pd thin films hydriding properties.

The structure of this text is organised as follows: the state-of-the-art on thin film metal hydrides is firstly covered in Chapter 1, from their general role in the so-called hydrogen society to the existing knowledge on their thermodynamic and kinetic behaviour, and on possible internal stress and microstructural effects. Chapter 2 is dedicated to the description of the in-situ stress measurement approach and its combination with thin film deposition, hydriding and annealing. The characterisation techniques used on the specimens are described as well. In Chapter 3, the construction of the kinetic model for Pd thin film hydriding is described in detail. Equilibrium and reversibility issues are addressed as well. Chapters 4 and 5 present the results on the respective effects of internal stress and microstructure on the hydriding properties of the Pd thin films. Several remarks on the definition and implications of the hydrogen society are finally proposed as an appendix. It is important to realise that the present work is a small brick in the huge wall of the construction of a cleaner global energy production system. This vision is too often seen as prophetic when presented to the society, the main reason being because it is too often erroneously presented.

Chapter 1

State-of-the-art on thin film metal hydrides

This first chapter is dedicated to the presentation of the current existing knowledge on the hydriding of thin metallic films, and to the positioning of the present thesis in this field of research and technology.

The different types of applications of thin film metal hydrides will be presented first. The main technological challenges that still have to be faced in this context will be identified. It will also be explained how the current thesis work can bring answers to these challenges.

The thermodynamics and kinetics of thin film metal hydride formation will then be addressed, with an emphasis on the Pd hydride, explaining why it has been chosen as a model system in this thesis. The chemical and mechanical behaviours of the Pd hydride in thin film form will be presented.

We will then focus on the current issues on the role of internal stress on the hydriding mechanism of thin metallic films. Although internal stress is a key issue in the engineering of thin film metallic hydrides, a lack of extensive studies still exists in this specific field of literature.

Finally, the existing knowledge on the impact of microstructure on the hydriding behaviour of thin metallic films will be explained. This issue is of primary importance in applications requiring solid-sate hydrides.

1.1 Thin film metal hydrides: applications

Thin films are the object of more and more attention in today's society. The most widely spread applications of thin films are electronic semiconductor devices and optical coatings. High-reflectivity mirror coatings deposited on insulating substrates are used since the 1930s [1], while thin film electronics arose in the 1970s with the birth of the Silicon Valley [2]. More and more applications arose since the first commercial uses of thin films. One can cite protection against corrosion [3], solar cells [4] or sensing devices [5] as representative examples.

The definition of thin films is not completely rigid. The thickness of such films is practically between several monolayers - down to a few nanometers - and several micrometers. If the thickness of the film is above 1 μm, one will use the term 'thick film' instead of 'thin film'. The substrate onto which the film is deposited is typically several hundred micrometers thick, but it can sometimes be much thicker. In this type of multilayered structure, the surfaces have a substantial influence on the materials physical properties. The relationships between the thin film and its substrate - notably through their respective lattice structures and thermal expansion behaviours - plays also a critical role on the film properties.

A hydride comes from the bonding of one or more hydrogen atom(s) with another element [6]. The bond can be covalent or ionic. In the case of crystalline solids, hydrogen can occupy interstitial sites of the host lattice. In the case of metal hydrides, these three cases are possible as well [7]. Alkali metals form ionic hydrides (LiH, NaH), in which the hydrogen atoms have a negative charge. Alkaline earth metals form iono-covalent bondings (MgH_2, BeH_2). Transition metals form interstitial hydrides, where the hydrogen atoms occupy part of the interstitial sites available in the host metallic lattice (PdH_x, FeH_x). Base metals usually from iono-covalent hydrides, such as AlH_3. The enthalpy of formation of metallic hydrides can be positive of negative, which means that all the hydrides are not necessarily thermodynamically stable. In the specific case of transition metals, the sign and amplitude of the enthalpy of formation both depend on the position of the metal in the periodic table of the elements [7].

In this section, the two main fields of applications of metal hydrides in thin film form are presented. It will be explained how the specific properties of this films allow adapting hydrogen-sensitive materials to specific applications, by improving their hydriding properties, by reducing their size or their cost. We will also discuss the role of the present thesis work in these applications fields.

1.1.1 Hydrogen detection

The transition to a hydrogen economy cannot be carried out without effective, cheap and low-consumption hydrogen sensors. In air, the LEL (Lower Explosive Limit[1]) of hydrogen is only 4% [8]. The potential hazards are manageable in stationary and transport applications involving the use of gaseous hydrogen [9], but they have to be carefully managed. The explosion of hydrogen is indeed extremely fast and devastating. Hydrogen sensing is also useful in medical applications, for the detection of certain diseases and to detect environmental pollution [10].

Thin film materials are used for the detection of various types of gases such as carbon monoxide [11] and dioxide [12], nitrogen dioxide [13], water [14], oxygen [15], methane [16], methanol [17], ethanol [18], ammonia [19], and as will be discussed here, hydrogen [20]. The choice of the material depends on the gas that must be detected, as well as on the other gases that can be present. There exist many types of thin film gas sensors, based on different physico-chemical phenomenons. The choice of the type of sensor used often depends on the application considered. The choice of the substrate can be critical as well.

The different types of thin film hydrogen sensors can be classified as a function of their respective detection principles:

- Catalytic thin film hydrogen sensors are based on the heat released by the chemical reaction between hydrogen and oxygen adsorbed on the sensor surface. The sensor response is important because of the large amount of heat released by the combustion of hydrogen [21]. The sensing element surface is activated with a catalyst such as Pd or Pt. There exist two types of catalytic thin film hydrogen sensors: pellistor-type sensors [22], where the electric signal is generated by a change in the resistivity if the sensing element when the latter is heated by the combustion of hydrogen, and thermoelectric-type sensors [23], where the Seebeck effect is used to generate the signal. Both types of sensors require thin film micromachining techniques. These sensors are highly accurate, but they suffer from a lack of selectiveness.
- Thermal conductivity thin film hydrogen sensors are based on the heat losses from the sensing element to the surrounding gas [24]. If hydrogen is present, the sensing element will loose more heat because of the high thermal conductivity of hydrogen. This technique offers a wide detection range, but is not very accurate [20].

[1] The Lower Explosive Limit of a flammable gas or vapor is its minimum concentration required to support its combustion in air, in presence of an ignition source. Combustion is possible between the LEL and the UEL (Upper Explosive Limit) of a flammable gas or vapor.

- Electrochemical thin film hydrogen sensors can detect changes in charge transport or electrical properties due to electrochemical reactions occurring at a sensing electrode. The electrolyte present between the sensing electrode and the counter electrode can be a solid, thereby allowing for miniaturisation. These type of sensors can work in amperometric [25] or potentiometric [26] mode, but the amperometric sensors are often preferred for their better sensitivity.

- Resistance-based thin film hydrogen sensors can be of two types: firstly, metal-oxide sensors [27] rely on a change in the sensing layer resistance when hydrogen reacts with oxygen previously adsorbed on a metal-oxide surface (e.g. SnO_2). Secondly, metal resistors [28] are based on the fact that the resistivity of metals decreases when absorbing hydrogen. These types of resistor have fast response times and a good selectivity. Palladium is often the preferred metal because of its fast, reversible interaction with hydrogen at room temperature.

- Work function semiconductor thin film hydrogen sensors are based on the MOS (Metal-Oxide-Semiconductor) structure. They consist of a semiconductor layer onto which an insulator layer and a catalytic thin metal film (palladium is often preferred) are successively deposited. The hydrogen atoms assimilated by the top metallic layer adsorb at the interface between the oxide and metal layers, creating a dipole layer which shifts the energy levels at the metal-oxide interface [20]. This dipole layer corresponds to a measurable voltage change added to the applied voltage ΔV. Three types of detection principles can be considered, i.e. Shottky diodes [29], transistors [30] and capacitors [31]. As can be seen in Fig. 1.1, the voltage change ΔV is visible in the current-voltage or capacitance-voltage relationship. The MOS capacitors are the most commonly used, but the MOSFET models - which are still in development - are very promising [20].

- Mechanical thin film hydrogen sensors are typically composed of a Pd thin film deposited on one side of a cantilever [32]. These type of sensors can exhibit very high sensing properties, but still need research effort before being commercialised [20]. One of the most frequently encountered problems is delamination of the Pd film at high hydrogen concentrations. This sensing technique is very close to the in-situ approach considered to monitor the hydriding kinetics of out Pd thin films in this thesis work, as will be seen in next chapter. More sophisticated micromachined mechanical sensors also exist as prototype models [33].

- Optical thin film hydrogen sensors can also be designed using catalyst metals such as Pd and Pt, or with chemochromic materials such as WO_3 [20]. The optical properties of certain materials indeed change when

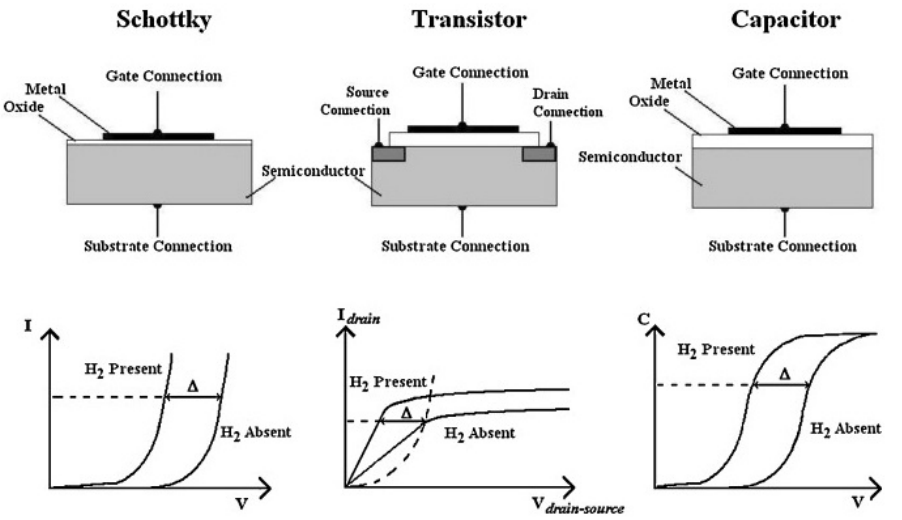

Figure 1.1: Cross sectional view of a basic MOS-Schottky diode, MOS-transistor and MOS-capacitor hydrogen sensor. Reproduced from Ref. [20].

interacting with hydrogen. Different types of optical sensors exist, i.e. reflectivity-based sensors [34], interferometric sensors [35], surface plasmon resonance (SPR) sensors [36], evanescent field based sensors [37], fibre Bragg grating (FBGs) sensors [38] and optical time domain reflectometry (OTDR) sensors [39]. Optical sensors still suffer from serious drawbacks such as surface poisoning or interference with ambient light. But they have very specific advantages, e.g. they are less sensitive to electromagnetic noise than the other types of sensors.

- Acoustic thin film hydrogen sensors are based on the change in the properties of acoustic waves due to hydrogen adsorption/absorption by a sensing material. As the mechanical sensors, they don't require the presence of oxygen to function. But they are sensitive to humidity and temperature. These sensors can be based on quartz crystal microbalances [40], surface acoustic wave devices [41] or sound velocity measurements [42].

An intelligent choice of the sensor technology as a function of the application can only be made through a systematic testing procedure. Some technologies are cheaper and more advanced than others, but some of them are at more early stages and will still improve significantly. A combination of different types of sensors is often the good choice for an optimal hydrogen sensing.

1.1.2 Hydrogen permeation

Biomass dedicated to hydrogen production firstly undergoes pyrolysis and tar decomposition, producing a mixture of gases containing H_2, CO, CO_2 and CH_4 [43]. At high temperature (800°C), the endothermic decomposition of methane is possible by providing water to the system:

$$CH_4 + H_2O = CO + 3H_2. \tag{1.1}$$

The same reaction occurs in the steam reforming of natural gas [44]. The carbon monoxide is converted into carbon dioxide by an exothermic reaction, well-known as the water-gas shift reaction:

$$CO + H_2O = CO_2 + H_2. \tag{1.2}$$

Hydrogen produced by natural gas steam reforming or by biomass gasification must thereby be extracted from a gas mixture potentially containing CO_2, remaining CO and CH_4, and also O_2 and N_2. Fig. 1.2 schematically shows the principle of gas-phase membrane separation.

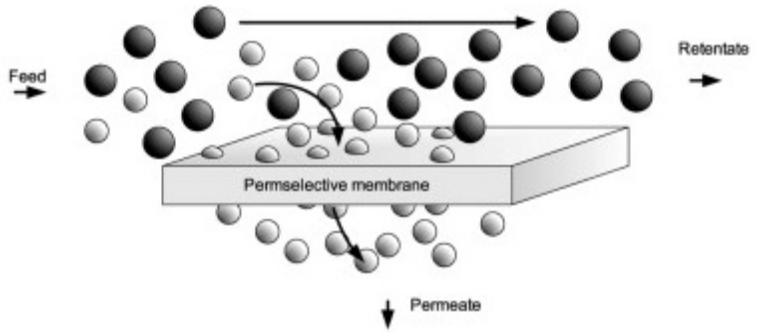

Figure 1.2: Simplified concept schematic of membrane separation. Reproduced from Ref. [44].

Hydrogen separation from other gases can be carried out by two different types of membranes:

Organic membranes can be biological or polymeric. They are used for many years for hydrogen purification in industry [44]. They have the advantages of being cheap and easy to process. They show an excellent selectivity to hydrogen because of its high diffusion coefficient compared to all other gases

except helium. Even if the intrinsic solubility of such membranes is weak, diffusion dominates and determines the overall selectivity. But if these membranes are suitable for industrial applications, this is not the case for reactors dedicated to hydrogen production, which requires a good resistance to high temperatures and harsh environments. This is not the case or organic membranes, which are structurally weak and prone to contamination [44].

Inorganic hydrogen separation membranes are much more resistant to high temperatures and contamination effects, but their price is higher than that of organic membranes [44]. Inorganic membranes can be metallic (dense) and ceramic (dense or porous). Dense metallic membranes are generally made of palladium, alone or with another element (Pd-Ag membranes are the most widely used [44]) and in the form of thin film, deposited by electroless plating [45], chemical vapor deposition or (CVD) [46] or magnetron sputtering [47]. They show excellent permeation kinetics and selectivity, but the metallic films can undergo phase transformations during the permeation process, leading to pinholes and microcracks which shorten the membrane life [48]. This underlines the importance of a well controlled alloy design adapted to the membrane working conditions. Micro- or nanoporous ceramic membranes - prepared by colloidal suspension [49] or by the sol-gel method [50] - achieve moderate to high selectivity and an excellent resistance to high temperatures. Their major drawback is a low hydrothermal stability.

Hydrogen permeation membranes are not only used for hydrogen purification from natural gas and biomass. Similar thin film structures can also be applied in solid oxide fuel cell (SOFC) and polymer electrolyte membrane fuel cell (PEMFC) technologies. Conventional SOFCs must be operated at 1000°C or more in order to achieve good power densities. Using thin film technologies enable to minimize the resistive losses across the solid electrolyte and to achieve reasonable power densities at lower operating temperatures [51]. Moreover, Pd and Pt catalysts for SOFCs and PEMFCs have an important impact on the fuel cell price. But these materials just need to be present at the surfaces of the fuel cell. Using less catalysts materials and keeping acceptable performances is possible by using thin film catalysts [52].

As an example of thin film fuel cell, Fig. 1.3 shows plane-view and cross-sectional SEM micrographs of different parts of a SOFC with a Ni/yttria-stabilized zircona (YSZ) anode, a YSZ solid electrolyte and a double-layer $La_{1-x}Sr_xMnO_3$ (LSM)-YSZ cathode [53]. That fuel cell exhibits good performances at 800°C, which enables to reduce the cost of materials and increase the durability of system components.

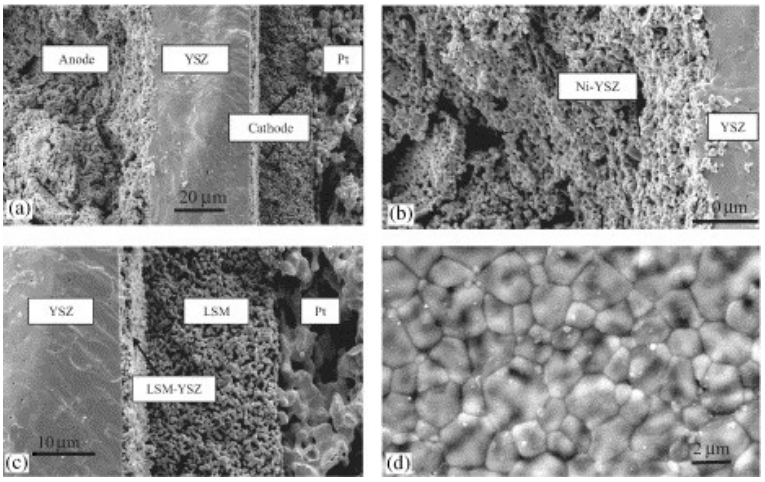

Figure 1.3: SEM micrographs of a thin film SOFC, showing: (a) fractured cell (cross section); (b) part of anode (cross section); (c) double-layer cathode (cross section) and (d) YSZ electrolyte film (plane-view). Reproduced from Ref. [53].

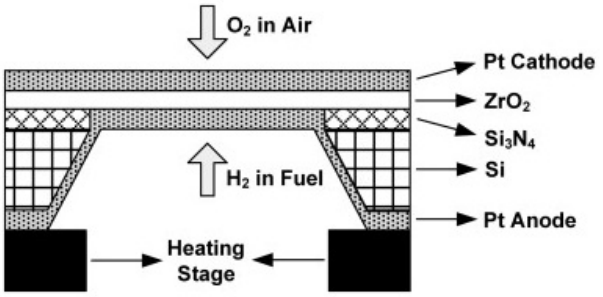

Figure 1.4: Cross-sectional view of a thin film micro-solid oxide fuel cell with a ZrO_2 solid electrolyte. A Pt anode covering the whole bottom is electrically connected to the heating stage. Reproduced from Ref. [54].

The design of such thin film SOFCs can even go further, by taking advantage of the small size of the system in order to integrate it into portable electronic devices such as laptops, personal digital assistants and scanners [54, 55]. The miniaturization of SOFCs gives rise to micro-SOFCs. An example of micro-SOFCs is shown in Fig. 1.4. This new type of SOFCs exhibit interesting energetic performances, and are the subject of ongoing researches.

1.2 Thin film metal hydrides: kinetics and thermodynamics

In this section, the thermodynamic and kinetic aspects of thin metallic films hydriding will be discussed. The derivation of Sievert's law, as well as the construction of pressure-composition (p-c) isotherms for metal hydrides will firstly be presented. A particular emphasis will be put on the palladium hydride. The differences in thermodynamic behaviour between bulky systems and thin films will then be addressed. It will be shown how specific features proper to thin films strongly modify the hydrogen equilibrium behaviour. The existing knowledge on the kinetics of formation of metal hydrides will then be presented, and the possible rate-limiting steps for hydride formation will be discussed. It will be shown that the specific structure of thin films can have important effects on the hydriding kinetics.

1.2.1 Hydriding thermodynamics

The thermodynamical aspects of the hydriding of metals will be presented here, with an emphasis on the palladium hydride. The differences in equilibrium hydriding behaviour between bulk and thin film specimens will be presented.

Sieverts' law

The well-known Sieverts' law has been formally presented by Adolf Sieverts in 1929 [56], who aimed to predict the solubility of gases interstitially dissolved in transition metals. It says, in substance, that the solubility of a diatomic gas is proportional to the square root of its partial pressure at equilibrium.

Let us formally derive Sieverts' law in the case of hydrogen interstitially dissolved in a metal. For this purpose, the chemical potentials of hydrogen in the gas phase and in the host lattice need to be expressed. In chemical thermodynamics, the chemical potential (μ) of a species is commonly expressed as a function of the activity of the species (a) in the following way:

$$\mu = \mu^0 + RT \ln a, \tag{1.3}$$

where μ^0 is the chemical potential of that species under standard conditions (at a pressure $p^0 = 1$ atm and a temperature $T^0 = 298.15$ K), T is the absolute temperature and R is the ideal gas constant. In the 1940s, Wagner expressed the activity of the hydrogen atom dissolved in a Pd lattice as follows [57]:

$$a_H = \gamma_H \frac{n_{eq}}{1 - n_{eq}} \tag{1.4}$$

where γ_H is the activity coefficient of the dissolved hydrogen atom and n_{eq} is the bulk H/Pd atomic ratio at equilibrium. The configurational term $n_{eq}/(1-n_{eq})$ accounts for an ideal statistical distribution of the hydrogen atoms in the host lattice in terms of Fermi-Dirac statistics. Consequently, if μ_H^0 is the hydrogen standard chemical potential, and if $\Delta\mu_H = RT \ln \gamma_H$ is the deviation from the ideal solution behaviour - called the excess chemical potential - then one can express the chemical potential of the hydrogen atom dissolved in the host lattice (μ_H) by combining Eq. (1.3) with Eq. (1.4):

$$\mu_H = \mu_H^0 + RT \ln\left(\frac{n_{eq}}{1 - n_{eq}}\right) + \Delta\mu_H. \tag{1.5}$$

The deviation from the ideal solution can be expressed as follows [57]:

$$\Delta\mu_H = \Delta\mu_{H^+} + \Delta\mu_{e^-}, \tag{1.6}$$

where $\Delta\mu_{H^+}$ and $\Delta\mu_{e^-}$ respectively account for the protonic and electronic term of the deviation from the ideal solution. This does not mean that the dissolved hydrogen atom is dissociated into a proton and an electron. As a matter of fact, the electronic states of the hydrogen atoms are located in the surrounding metal atoms of the host lattice. In the case of palladium, like with many other transition metals, the delocalised electrons occupy the electronic states of the 5s band. At the Fermi level, these electrons interact with the 4d band, which is characterised by a high density of states (see Fig. 1.5). The hydrogen atoms in the interstitial sites of palladium can then be seen as electronically screened protons [57].

The chemical potential of the hydrogen gas is expressed as follows [57]:

$$\mu_{H_2} = \mu_{H_2}^0 + RT \ln\left(\frac{p_{H_2}}{p^0}\right), \tag{1.7}$$

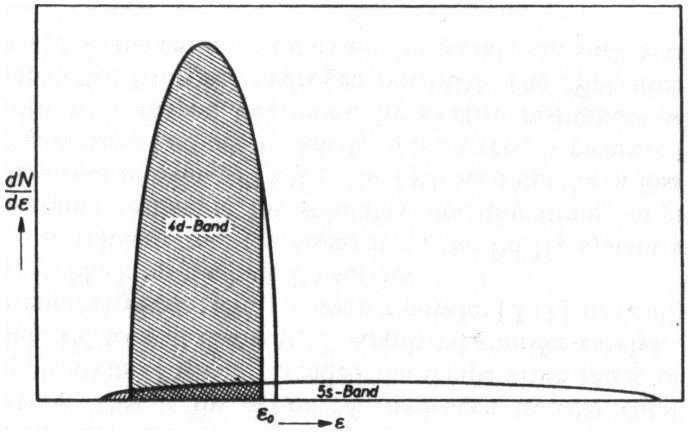

Figure 1.5: Schematic representation of the 4d and 5s bands in palladium. Reproduced from Ref. [57].

where $\mu^0_{H_2}$ is the standard chemical potential of the hydrogen gas and p_{H_2} is the partial pressure of the hydrogen gas. The hydrogen fugacity is set to 1 as the gas is at room temperature and at pressures well below the atmosphere. When the hydrogen atoms in the octahedral sites of the metal matrix are at equilibrium with the gaseous hydrogen outside the metal, their respective chemical potential are equal to each other:

$$\mu_H = \frac{1}{2}\mu_{H_2}. \tag{1.8}$$

Taking into account that the difference between the standard values of the chemical potential of the hydrogen atom in the gas phase and in the metal ($\mu^0_H - 1/2\mu^0_{H_2}$) is equal to the standard Gibbs free energy for the dissolution of one hydrogen atom (ΔG^0_H) [58], then one can define Sieverts' constant as the equilibrium constant for hydrogen dissolution:

$$K_s = \exp\left(\Delta G^0_H / RT\right) \cdot \sqrt{p_0} = \exp\left[\left(\mu^0_H - \frac{1}{2}\mu^0_{H_2}\right)/RT\right] \cdot \sqrt{p_0}, \tag{1.9}$$

Combining Eqs. (1.5), (1.7), (1.8) and (1.9) then results in

$$\ln\sqrt{p_{H_2}} = \ln\left(K_s \cdot \frac{n_{eq}}{1 - n_{eq}}\right) + \frac{1}{RT}\left(\Delta\mu_{H^+} + \Delta\mu_{e^-}\right). \tag{1.10}$$

In Eq. (1.6), the contribution $\Delta\mu_{H^+}$ to the chemical potential is purely mechanical [57]. It comes from the lattice expansion caused by the oscillations of protons in adjacent octahedrons. This contribution is often neglected. Smirnov and Pronchenko indeed found out that this contribution does not significantly contribute to the bond energy in the Pd-H system [59]. As regards the electronic contribution $\Delta\mu_{e^-}$, it is highly influenced by the hydrogen concentration in the host lattice. The H-H interaction energy is negative at small hydrogen concentrations, while it becomes positive at high concentrations. The electronic effects at large concentrations result in a repulsion of hydrogen atoms from each other, then increasing the effective bond energy with the metal matrix. The subsequent evolution of the chemical potential as a function of the H/Pd atomic ratio is shown in Fig. 1.6.

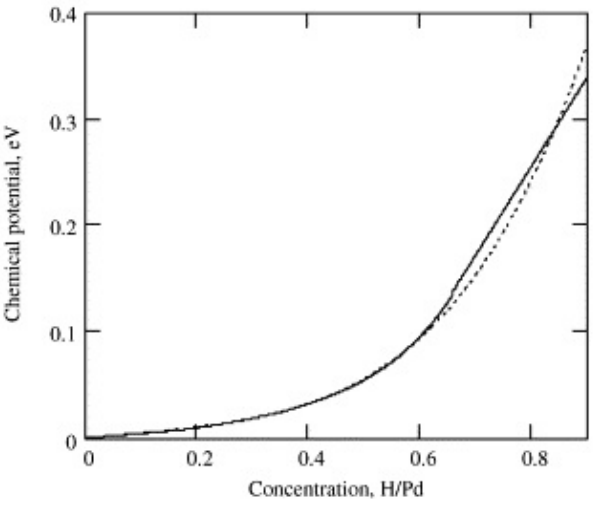

Figure 1.6: Concentration dependence of electron contribution to chemical potential (theoretical: dot-line, experimental: solid line). Reproduced from Ref. [59].

Eq. (1.6) can be nullified if $n_{eq} << 1$, as in the α-phase region of the Pd-H system. Moreover, this also results in $n_{eq}/(1 - n_{eq}) \cong n_{eq}$ and Eq. (1.10) then becomes:

$$K_s n_{eq} = \sqrt{p_{H_2}}. \tag{1.11}$$

Eq. (1.11) is the common form of Sieverts' law. The value of Sieverts' constant is typically 10-14 $atm^{1/2}$ at room temperature and low defectiveness

of the Pd host lattice [60]. The theoretical value of 20 $atm^{1/2}$ for a perfect Pd crystal has never been reached experimentally [61]. Bucur experimentally established the relationship between the defect concentration and Sieverts' constant, as shown in Fig. 1.7. Eq. (1.11) will be used in the course of this thesis work in order to calculate K_s in the α-phase region of our Pd thin films.

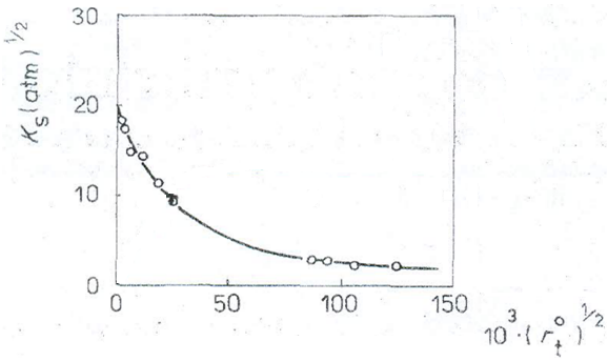

Figure 1.7: Evolution of Sieverts' constant as a function of the defect concentration ($r^0{}_t$ is the atomic ratio between the additional sites generated by the presence of defects and the palladium atoms in the sample). Adapted from Ref. [62].

Phase diagram of metal hydrides

The formation of a metal hydride can be described by the following reaction [63]:

$$\frac{y}{x}Me + H_2 = \frac{1}{x}Me_yH_{2x}. \tag{1.12}$$

The standard Gibbs free energy for metal hydride formation, ΔG^0, can thus be expressed in the following way [7],

$$\Delta G^0 = -RT \ln \frac{1}{p_{H_2}} = RT \ln p_{H_2}, \tag{1.13}$$

or, alternatively, as a function of the standard enthalpy change for hydride formation ΔH^0 and the standard entropy change for hydride formation ΔS^0 [7]:

$$\Delta G^0 = \Delta H^0 - T\Delta S^0. \tag{1.14}$$

Combining Eqs. (1.13) and (1.14) then provides:

$$\ln p_{H_2} = \frac{\Delta H^0}{RT} - \frac{\Delta S^0}{R}. \tag{1.15}$$

The phase diagrams of metal hydrides are usually constructed through the recording of pressure-composition (p-c) isotherms. An example of p-c isotherms is shown in Fig. 1.8.

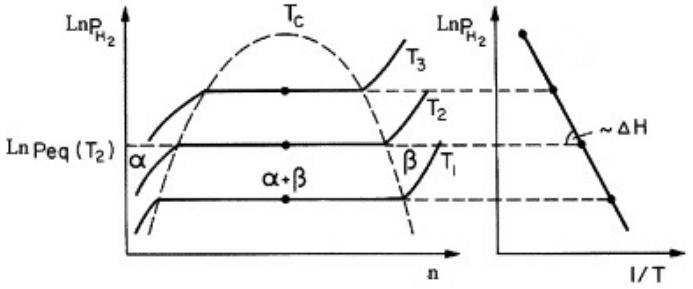

Figure 1.8: Phase diagram of a metal hydride, constructed from the recording of p-c isotherms. The construction of a Van't Hoff plot is also shown. Reproduced from Ref. [64].

When a relatively small amount of gaseous hydrogen is brought into contact with a metal, a solid solution is formed by the dissolution of hydrogen atoms in the host lattice, according to Sieverts' law (α phase in Fig. 1.8). In the $\alpha + \beta$ phase region, the solid solution is in equilibrium with its hydride and, according to the phase rule - $f = c - p + 2$, where f is the number of degrees of freedom of the system, c is the number of components and p is the number of phases - the system has one degree of freedom. In other words, the equilibrium hydrogen pressure is constant for a given temperature. When the conversion to the hydride phase is complete, the system recovers two degrees of freedom and the equilibrium pressure increases again with increasing hydrogen content until the hydride stoichiometry is reached. Let us finally indicate that the phase diagram shown in Fig. 1.8 describes an ideal behaviour such that adsorption and desorption isotherms would be the same. In practice, the addition of hydrogen into the host lattice generates lattice stress which, in turn, create a thermodynamic barrier that shifts the absorption and desorption isotherms. This behaviour is called intrinsic hysteresis [65].

One can also plot the equilibrium hydrogen pressure as a function of the reciprocal of the absolute temperature - according to Eq. (1.15) - in order to obtain a so-called Van't Hoff plot (see Fig. 1.8). ΔH^0 and ΔS^0 can be extracted from the slope and intercept, respectively.

The standard entropy change associated to metal hydride formation ΔS^0 is not interesting from an engineering point of view, because it does not vary much from one metal hydride to another [7]. The small standard entropy change between a metal and its hydride is typically on the order of 10^{-2} kJ/(molK). Therefore, ΔS^0 is mainly driven by the loss of standard entropy of hydrogen gas (0.130858 kJ/(molK) [7]). ΔS^0 is then always on the order of 0.1 kJ/(molK) for metal hydride formation. Kapischke and Hapke indeed confirmed this assumption for various metals and metallic alloys [63].

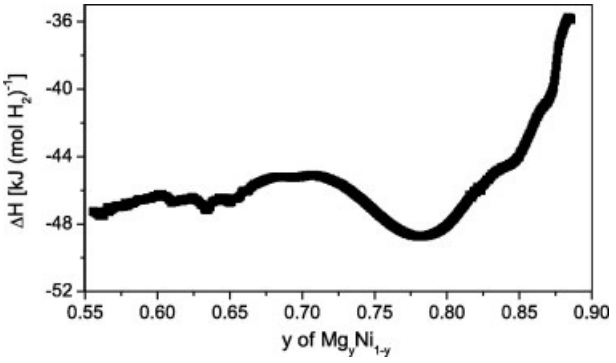

Figure 1.9: Evolution of the enthalpy of hydride formation as a function of alloy composition for the Mg-Ni system, measured optically by hydrogenography on Pd-capped Mg_yNi_{1-y} thin films. Reproduced from Ref. [66].

Concerning ΔH^0, metal hydrides are usually highly stable (for example, ΔH^0 = -75 kJ/mol for MgH_2 [67]), which is a problem regarding applications such as hydrogen storage. Ideal candidates for hydrogen storage applications would indeed exhibit a high reversible hydrogen storage capacity, but also plateau pressures reasonably close to the atmosphere at temperatures reasonably close to the ambiance regarding both hydrogen absorption and desorption. Such demanding properties oriented the research towards alloys instead of pure elements, which cannot meet these requirements by themselves [7]. An infinity of combinations exists between the different available elements, and the best way to study these combinations in an effective and cheap way is to use advanced thin film deposition techniques. A recently developed technique - called hydrogenography - enables to study a wide range of alloy compositions based on the combinatorial exploitation of the changes of metal hydrides optical properties upon hydrogen absorption and advanced thin film deposition techniques with chemical composition gradients [66, 68–70]. An example of the power of hydrogenography is shown in Fig. 1.9. The implementation of this technique to the Mg-Ni binary alloy enabled to determine the evolution of ΔH^0 over the whole alloy compositional range in a cheap and effective way [66]. This ap-

proach will enable to tune the hydriding thermodynamics of a wide range of materials.

Differences between thin film and bulk systems

The hydriding thermodynamic properties of thin metallic films can vary significantly from these of bulky systems [71], depending on some important characteristics of the thin films. The films thickness obviously is one of them. According to Salomons et al. [72], who measured gravimetric p-c isotherms on Pd thin films with different thickness. Isotherms measured for 50-nm-thick Pd layers showed significant differences from isotherms recorded for 300-nm-thick Pd layers. The limits of the miscibility gap measured on the thinner films, $n = \alpha_{max}$ and $n = \beta_{min}$, were respectively higher and lower than these of the thicker films, resulting in a narrowing of the miscibility gap. The pressure plateaus were also slightly sloped for the thinner films.

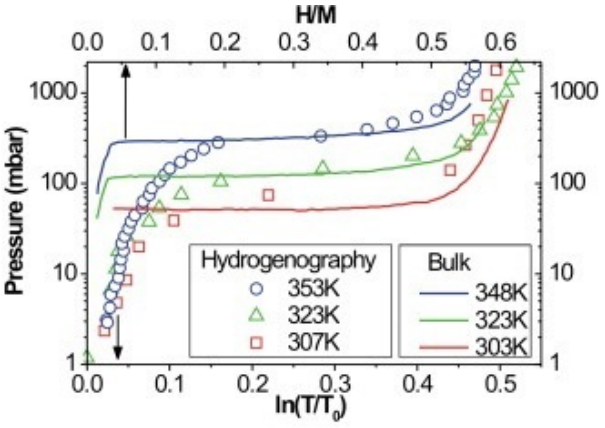

Figure 1.10: Hydrogenography p-t isotherms of a 38 nm thick $Pd_{95}Cu_5$ thin film. The results of Sakamoto et al. on bulk specimens are shown for comparison [73]. The upper horizontal axis indicates the ratio of the number of hydrogen atoms to the total number of metal atoms (n) and the lower horizontal axis shows the hydrogen concentration as $\ln(T/T_0)$, where T is the optical transmission. Reproduced from Ref. [74].

These effects have been explained by Salomons et al. in the following way [72]: they firstly took into account two microstructural contributions, i.e. a surface and a grain boundary contribution. On the one hand, the thinner films have a larger relative number of surface and subsurface site densities, which can result in a larger contribution from misfit dislocations if the film

thickness is on the same order or smaller than the critical thickness for misfit dislocation formation. And on the other hand, their films exhibited different grain sizes, and had therefore different fractions of grain boundaries. Dislocations and grain boundaries are indeed hydrogen trapping sites [71] which change the energetics of hydriding, as will be explained in section 1.5. But even when taking into account these microstructural contributions, Salomons et al. could not quantitatively explain the deviations observed with respect to bulk specimens. They concluded that stresses also have a non-negligible impact on the thermodynamic behaviour of thin films. That stress contribution will be presented in section 1.4.

Here, these differences between bulk and thin film metal hydrides are illustrated by the results of Westerwaal et al. [74], who recorded pressure-optical transmission (p-t) isotherms - which are qualitatively analogous to classical p-c isotherms - using the hydrogenography technique. They used $Pd_{95}Cu_5$ thin film specimens and compared their results with these of Sakamoto et al. [73] for bulk specimens, as shown in Fig. 1.10. One can indeed see the important narrowing of the miscibility gaps and the sloped pressure plateaus. Westerwaal et al. attribute the latter effect to strain development in the thin films during hydrogenation.

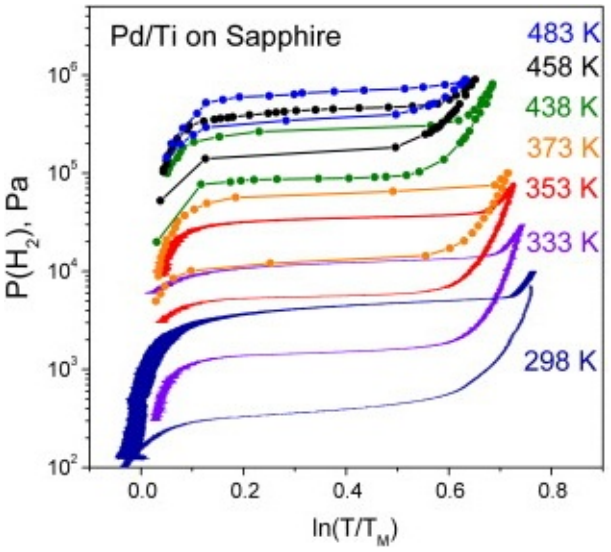

Figure 1.11: Hydrogenography p-t isotherms recorded in the temperature range 298-483 K on Pd/Ti thin films deposited on sapphire substrates by DC magnetron sputtering. Reproduced from Ref. [75].

Pivak et al. also used hydrogenography on Pd thin films [75], deposited by DC magnetron sputtering on a Ti adhesion layer (just like our Pd thin films, as will be seen in next chapter). As can be seen in Fig. 1.11, the intrinsic hysteresis of these thin films is important between hydrogen absorption and desorption isotherms. They indeed measured an enthalpy change of -31.9 kJ/mol for hydrogen absorption and -42.4 kJ/mol for hydrogen desorption, confirming the existence of a thermodynamic barrier for hydrogen absorption.

1.2.2 Hydriding kinetics

The hydriding mechanism of metals and metallic alloys involves solid-gas reactions, which differ from classic homogeneous reactions in some points [7]. The diatomic, gaseous hydrogen molecules firstly interact with the metal surface, onto which they are molecularly adsorbed and then dissociated. The adsorbed H atoms then diffuse into the bulk and form the hydride. The synthesis technique, activation procedure and past history of the chosen material critically influences the kinetic behaviour regarding these mechanisms because they determine the grain size, the defect concentration as well as the size and nature of the precipitates [7], which all influence the hydriding kinetics as will be explained in Chapter 5. In a way depending on the application considered, the engineering of hydrides should always carefully focus on the control these parameters. Hence, the use of nanostructured materials such as thin films [76] and powders [77] gives rise to specific kinetic behaviours. In this thesis, the strong links between our Pd thin films microstructure and hydriding kinetics will be explained.

Ball-milled powder materials such as Mg compounds [77], Ti-Mn-based Laves phase alloys [78, 79] and complex hydrides [80] are commonly used as hydrogen storage materials. Hydrides obtained by reactive ball milling (RBM) in presence of hydrogen exhibit a high active surface, a high defect concentration and facilitate the dispersion of catalysts. Fig. 1.12 shows the kinetic profile of hydrogen absorption and desorption from ball-milled Mg-Fe powders [77]. As already discussed above, Mg and its compounds are very promising hydrogen storage materials because of their high gravimetric hydrogen storage capacity. This is the case for the powders shown in Fig. 1.12, which absorb hydrogen up to 5 % by mass. The destabilisation of the Mg-H system is carried out thanks to the addition of Fe and the microstructural refinement subsequent to the ball-milling process, but the desorption temperatures are still too high as can be seen in Fig. 1.12. The kinetics of hydrogen uptake has also been significantly improved compared to pure Mg [77], which usually exhibits a poor hydrogen dissociation kinetics.

The kinetics of hydride formation and hydrogen desorption in powder materials is a wide field of research, which gave rise to many different kinetic models. So-called 1D, 2D and 3D diffusion models [77], contracting surface and volume models [81] and Johnson-Mehl-Avrami (JMA) nucleation and growth models [82] are widely used in this context. The ball-milling parameters (temperature, particle size, additive, etc.) critically determine the rate-limiting steps of the hydriding mechanism. As a result, the kinetic model chosen to interpret the experimental data can be very different from one study to another.

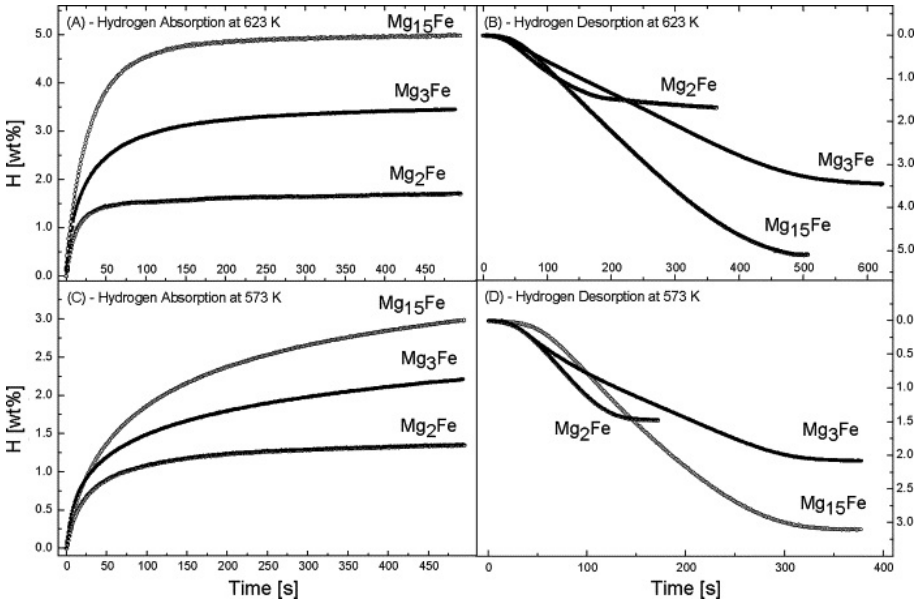

Figure 1.12: Hydrogen absorption/desorption rate of ball-milled powders for different Mg-Fe compositions: (A) absorption kinetics and (B) desorption kinetics at 623 K; (C) absorption kinetics and (D) desorption kinetics at 573 K. Reproduced from Ref. [77].

The situation is basically the same regarding thin metallic films, which are nanostructured materials as ball-milled powders. Here again, the deposition parameters and the past history of thin metallic films critically influence their hydriding kinetics. Similarly to what is usually done on the promising Mg element in powder form, Mg thin films can be alloyed [83] or finely nanostructured [84] in order to improve their hydriding kinetics. Pd catalysts are also typically used in order to improve the dissociation of hydrogen on the thin film surface [83–85]. Here, the latter are not dispersed in the host material as in powders. One can deposit a very thin Pd layer - typically less than 20 nm -

on top of the hydrogen-absorbing material for a maximum catalyst efficiency. These capping layers significantly improve the hydriding kinetics although requiring little amounts of catalyst materials.

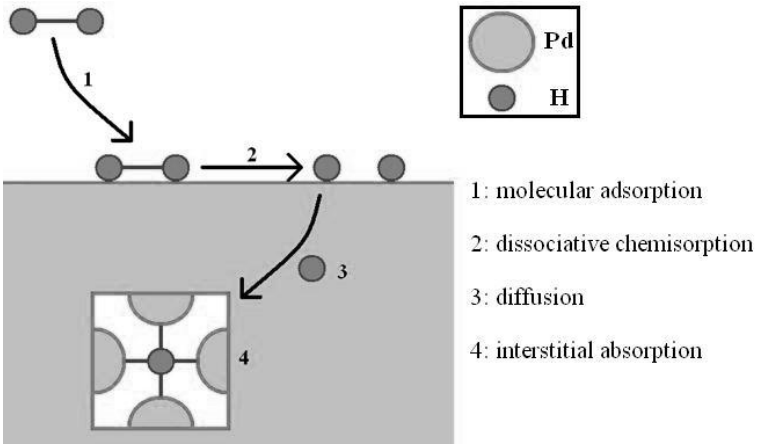

Figure 1.13: Schematic representation of the principal kinetic steps involved in Pd hydriding.

However, Despite the model status of the Pd-H system, and its extensive use as a catalyst in thin film form, the exact kinetic details and the corresponding rate-limiting step(s) of room temperature Pd hydriding are still a matter of debate [76,86]. As illustrated schematically in Figure 1.13, the Pd hydriding mechanism can be divided into four steps [57]. Firstly, gaseous H_2 molecules need to be adsorbed onto the metallic Pd surface. These adsorbed H_2 molecules then dissociate and the resulting H-atoms slip along a minimum energy path towards atomic well positions, from which they can diffuse into the Pd bulk. A Pd hydride is finally formed, with H-atoms mainly occupying the octahedral interstitial sites of the fcc Pd lattice. As explained in previous section, the configuration of those sites is equivalent to the positions occupied by strongly chemisorbed H-atoms on a (111) Pd surface [87][2].

Determining which of those four kinetic steps is rate-limiting is typically based on measuring, preferably in-situ, the time-evolution of a H-sensitive parameter with respect to the hydrogen partial pressure p_{H_2}. Such studies have already been reported, based for instance on measurements of Pd cantilever bending [86], optical reflection [76,88] or transmission [89], dilatometry [90] and

[2]As explained above, palladium is a very good catalyst for chemisorption because the hydrogen atoms are adsorbed in very deep potential wells. The adsorption enthalpy is indeed on the order of -100 kJ/mol. The surface sites are even more stable than the bulk sites, whose adsorption enthalpy is aroud -40 kJ/mol.

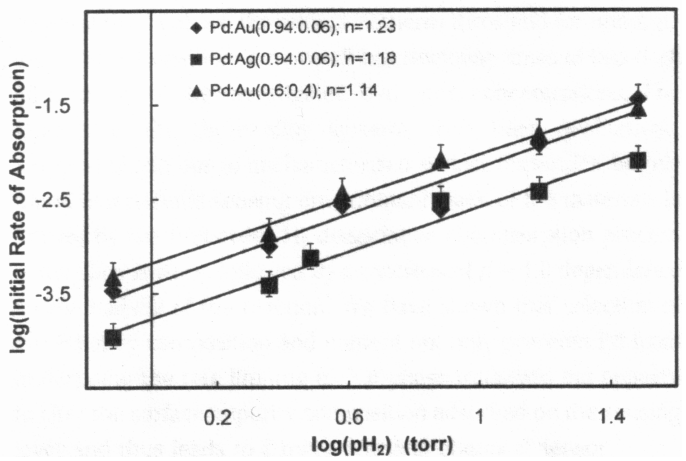

Figure 1.14: Hydriding rate of Pd-Au (Ag) thin films as a function of p_{H_2}. Reproduced from Ref. [76].

resistivity [91]. However, no consensus on an appropriate kinetic model seems to be available yet, neither qualitatively nor quantitatively. For instance, Zhao et al. [76] observed a linear dependence of the hydriding rate with p_{H_2} and therefore concluded that the Pd hydriding mechanism was rather controlled by surface interactions (see Fig. 1.14). On the other hand, Hu et al. [86] observed a bending rate of their Pd thin film specimens depending on $p_{H_2}^{1/2}$, in agreement with Sieverts' law (see Fig. 1.15).

With respect to the schematics of Fig. 1.13, no hydrogen diffusion step will be taken into account in the kinetic model that will be used throughout this thesis work, simply because of the Pd thin film geometry considered here. Indeed, one gets a first-order diffusion time on the order of milliseconds when dividing the square our Pd thin film thickness by the diffusion coefficient of H atoms in α-PdH ($D_\alpha = 10^{-7}$ cm^2/s [76]). This is five orders of magnitude below the time scale of the hydriding kinetics experimentally observed for our Pd thin films, as will be seen in this thesis work. As can indeed be seen in Fig. 1.16, the diffusion of H atoms in Pd is fast compared to most other compounds. In that figure, the diffusion coefficients of hydrogen in different metallic/complex hydrides are shown, and compared with these of species involved in other energy storage systems, i.e. H and Li in batteries [92]. As regards complex hydrides, subunits like Li and BH_4 are also diffusing species, and must therefore also be taken into account. The yellow zone represents water in pasta, i.e. 1 mm in 5 mn (for the sake of comparison). The pink zone represents Li in $LiBH_4$. The blue and red zones represent, respectively, H in NiMH batteries ($\cong$ 10 μm/min)

and Li in Li-ion batteries ($\cong$ 1 μm/min). Purple represents H in complex hydrides, i.e. several micrometers in days. Cyan represents H in ionic/covalent hydrides, the slowest of all compounds.

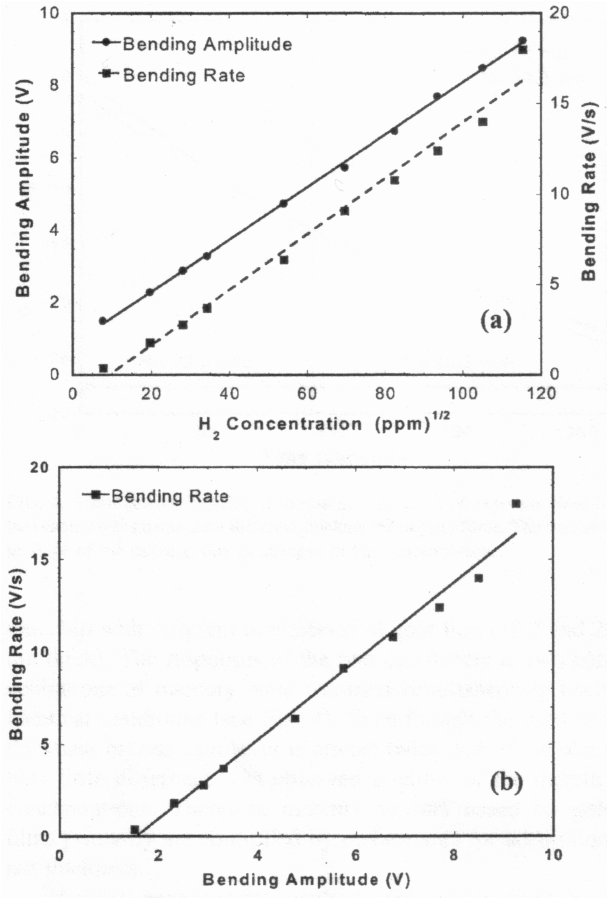

Figure 1.15: Bending amplitude and bending rate of Pd thin films in a cantilevered form submitted to hydrogen cycling. (a): Bending amplitude and bending rate as a function of $(p_{H_2})^{1/2}$. (b): Bending rate as a function of bending amplitude. Reproduced from Ref. [86].

As a result, the kinetic analysis that will be carried out on our Pd thin film specimens in this thesis work will be performed independently from the diffusion effect, thereby providing a direct access to the analysis of fundamental mechanisms of hydrogen adsorption and absorption.

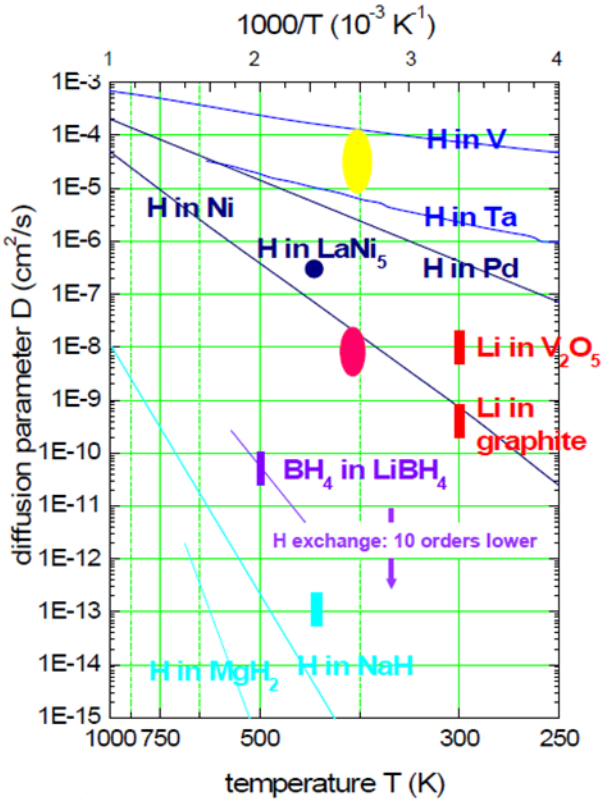

Figure 1.16: Diffusion coefficient of H, Li and BH_4 atoms in different compounds. Reproduced from Ref. [92].

1.3 The Pd-H system: a model system

As the aim of this thesis is to study the effect of microstructure and internal stress on the hydriding properties of thin films and not to focus on alloy optimisation, the choice of the metal has been directed towards model systems. Among the metals of which the interaction with hydrogen has since long been a topic of scientific and technological interest, the palladium-hydrogen system has particularly attracted intensive research efforts as a model system [57, 93]. Its high sensitivity and selectivity to H_2 gas and its ability to easily release hydrogen at room temperature made the Pd-H system very attractive for various experimental investigations for more than one century. A huge amount of experimental data is therefore available for this system, as well as results from atomic-scale numerical simulations. In this respect - and despite the rarity of

Pd - the Pd-H system is considered as a model system. For hydrogen storage materials, other inorganic compounds are nowadays considered to be more promising [94–96]. However, Pd is currently still being considered to be a good candidate for applications like hydrogen sensors [76] and gas purification membranes [97], especially in thin film form as a catalytic coating [87] (as already discussed in previous section).

The crystalline structure of the palladium hydride is an isotropically extended form of the face-centered cubic lattice of pure Pd in which the hydrogen atoms occupy part of the available octahedral sites [57]. The phase diagram of the Pd-H system for bulk Pd, recorded with p-c isotherms, is shown in Fig. 1.17. One may also record temperature-composition (T-c) isobars in order to build the PdH phase diagram in the T-c plane, as shown in Fig. 1.18.

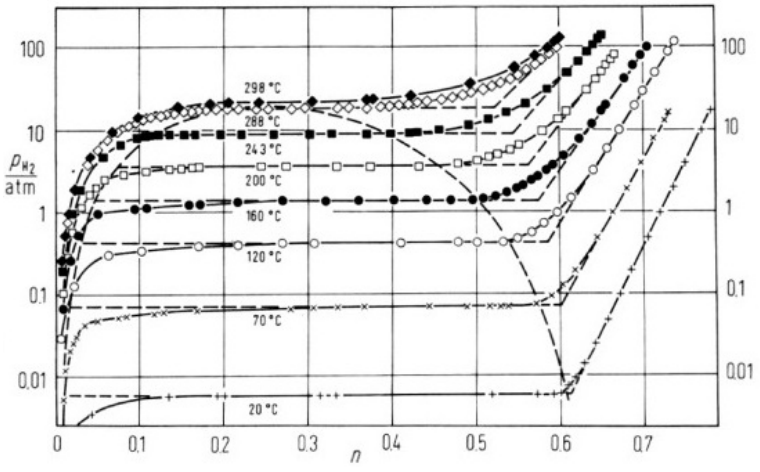

Figure 1.17: p-c desorption isotherms recorded on bulk Pd specimens at different temperatures, showing the construction of the Pd-H phase diagram. Reproduced from Ref. [98].

Below approximately 300°C, the homogeneous solid solution is split into two phases: the α phase, which has a low hydrogen content, and the β, hydrogen-rich phase. At room temperature, the limits of the miscibility gap are $n = \alpha_{max} = 0.008$ and $n = \beta_{min} = 0.607$ [57]. The lattice parameters of pure Pd and of the Pd-H system at the limits of the miscibility gap are [57]:

$$\begin{cases} a(0) = 0.3890nm. \\ a(\alpha_{min}) = 0.3894nm. \\ a(\beta_{min}) = 0.4025nm. \end{cases} \tag{1.16}$$

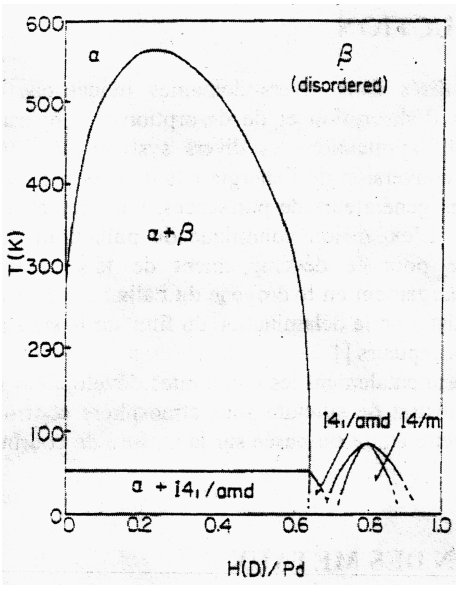

Figure 1.18: Pd-H temperature-composition phase diagram. Reproduced from Ref. [57].

The volume expansion subsequent to hydrogen absorption ΔV is equal to 1.57 cm^3 per gram of hydrogen in the $\alpha + \beta$ phase region, and goes down to 1.3 cm^3 per gram of hydrogen in the β phase region [57]. As the H atoms occupy the octahedral sites of the FCC Pd lattice, the composition of the hydride is PdH when all these sites are occupied, as suggested by Fig. 1.19. This stoichiometric composition has never been reached experimentally. [87].

As opposed to other metal hydrides (except for chromium hydride), the α and β phases of the PdH hydride exhibit the same crystalline structures. For all other metal hydrides, the tetrahedral sites are occupied before the octahedral sites [87]. In the β phase, the lattice expands as more and more octahedral sites are occupied, which results in a decrease of the standard enthalpy change for hydride formation. Levine and Weale found out this enthalpy to increase from -46.1 kJ/mol for $n = 0.225$ to -11.7 kJ/mol for $n = 0.65$ [99].

The hydrogen atoms adsorbed on the Pd surface can occupy different types of sites [87, 100]. The nature of the sites, as well as the preferred site for hydrogen adsorption, both depend on the texture of the surface. The configurations of these surface sites is shown in Fig. 1.20 for the (111), (100) and (110) surfaces.

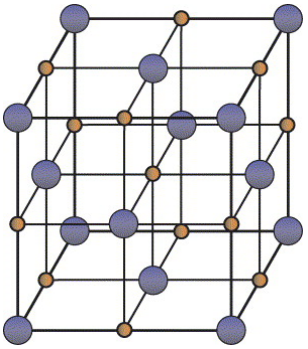

Figure 1.19: Unit cell of palladium metal (blue circles) showing octahedral sites that would be occupied by hydrogen (orange circles) in β-palladium hydride, for the limiting H/Pd ratio of 1. Reproduced from Ref. [87].

The (111) plane - the most compact one - shows four possible adsorption sites: the so-called 'top', 'hcp', 'bridge' and 'fcc' sites. Experimental and computational studies showed that the fcc site is the most stable, followed by the hcp and bridge sites [87]. The fcc sites are equivalent to the bulk octahedral sites for hydrogen absorption. Consequently, the surface coverage θ (equivalent to the surface H/Pd atomic ratio) is equal to 1 when all the fcc sites are occupied. The (111) surface configuration will be the only configuration considered in this thesis since our evaporated and sputtered Pd thin films tend to form this particular texture, as will be shown in Chapters 3, 4 and 5.

Regarding the (100) surface, there are three possible adsorption sites: the so-called 'hollow', 'bridge' and 'top' sites. The hollow site is the most stable [87]. Finally, the (110) surface - the less compact one - exhibits five possible adsorption sites: the so-called 'long bridge', 'short bridge', 'hollow', 'top' and 'pseudo-three-fold' sites. The pseudo-three-fold site is the most stable [87].

The standard enthalpy change relative to hydrogen adsorption starts from about -100 kJ/mol for a virgin surface, and then increases in the positive direction with increasing surface coverage [101] (Fig. 1.21). When the surface sites are saturated, the interaction between hydrogen atoms becomes highly repulsive and the standard enthalpy of adsorption becomes positive.

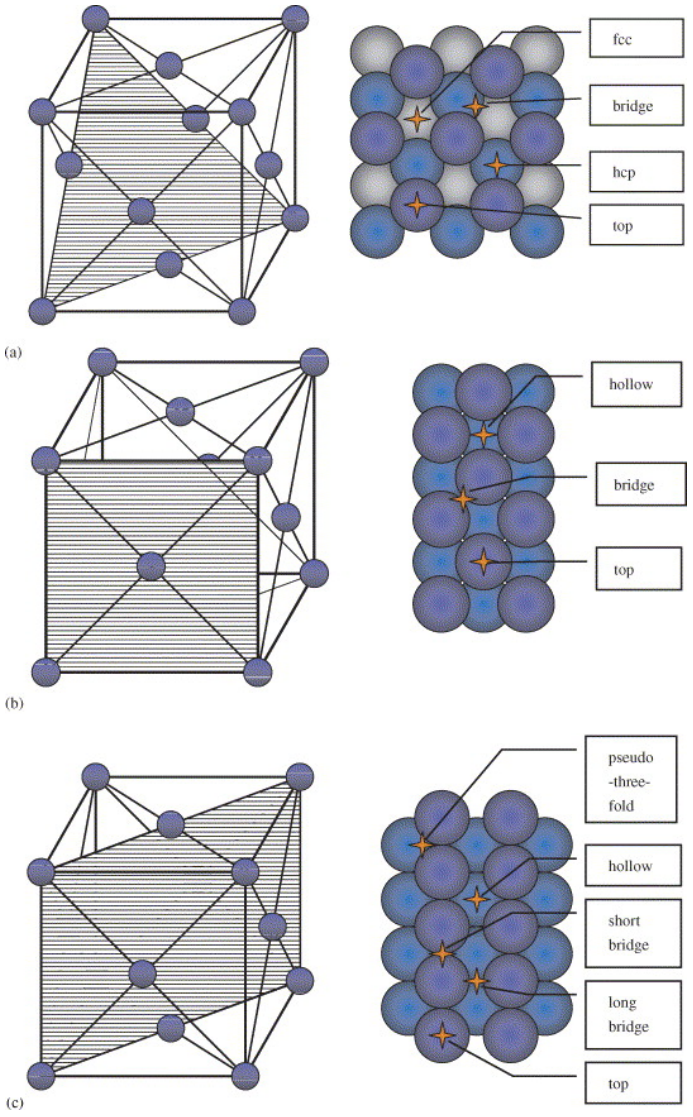

Figure 1.20: (a) Palladium unit cell showing (1 1 1) plane; schematic representation of fcc, bridge, hcp and top adsorption sites for palladium (1 1 1) plane. (b) Palladium unit cell showing (1 0 0) plane; schematic representation of hollow, bridge and top adsorption sites for palldium (1 0 0) plane. (c) Palladium unit cell showing (1 1 0) plane; schematic representation of pseudo-three-fold, hollow, short bridge, long bridge and top adsorption sites for palladium (1 1 0) plane. Reproduced from Ref. [87].

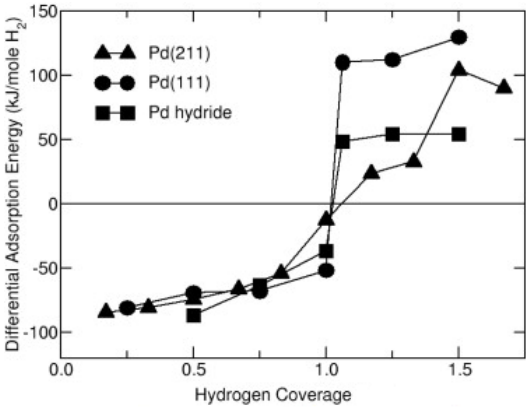

Figure 1.21: Differential adsorption energy for H as a function of the surface H coverage on Pd(1 1 1), Pd(2 1 1) and Pd hydride slabs. Reproduced from Ref. [101].

Like many other cubic crystalline solids, Pd is an anisotropic material and its linear elastic behaviour can be described with 3 elastic constants [102, 103]. These constants are, respectively, the C_{11}, C_{12} and C_{44} components of the Pd stiffness matrix. Rayne obtained C_{11} = 227.1 GPa, C_{12} = 176.1 GPa and C_{44} = 71.7 GPa at room temperature [102]. Therefore, the Pd anisotropy factor - defined as $A = C_{44}/C'$, where $C' = (C_{11} - C_{12})/2$ - is equal to 2.81. This anisotropy evolves with temperature [102], but also with the hydrogen content in the Pd lattice [104,105]. Schwarz et al. [104] showed that C_{44} decreases with increasing hydrogen content as a result of the expansion of the Pd lattice. They also showed that C' has a concave parabolic dependence with the hydrogen content in the miscibility gap of the Pd-H system, while it decreases with the hydrogen content in the β-phase. They attributed the latter effect to the fact that C' is softened by an anelastic relaxation resulting from changes in the shape of coherent precipitates.

As a consequence of this anisotropy, the elastic behaviour of Pd is dependent on the crystallographic orientation [103]. In a bulk sample with randomly oriented grains, one will obtain a Young's modulus of 121 GPa, a shear modulus of 44 GPa and a Poisson ratio of 0.39 [106].

In thin film form, the Young's modulus of Pd is usually reported as slightly smaller than the bulk value, whether invoking porosity [107] and/or texture [108] as possible origins of this effect. Colla et al. measured a Young's modulus of 120 GPa by nanoindentation on thin films with similar thickness (between 80 and 310 nm) and grain size (~ 30 nm in-plane) than the ones used in the present thesis [109,110]. The same authors also investigated the plasticity behaviour of

these films by means of on-chip tensile testing, finding a high strain hardening capacity, and partly attributing the latter to the presence of growth twins. A semi-analytical grain aggregate model has been proposed [109], taking into account the impact of twins, grain size and the presence of a thin surface layer. As can be seen in Fig. 1.22, this model is able to reproduce the strain hardening behaviour of the films (except for the thinnest one, which is underestimated) and the thickness effect on the limits of the elasto-plastic transition. As regards the latter effect, one can see that both the elasticity limit and the end of the elasto-plastic transition are shifted towards higher stress levels when the film thickness is decreased.

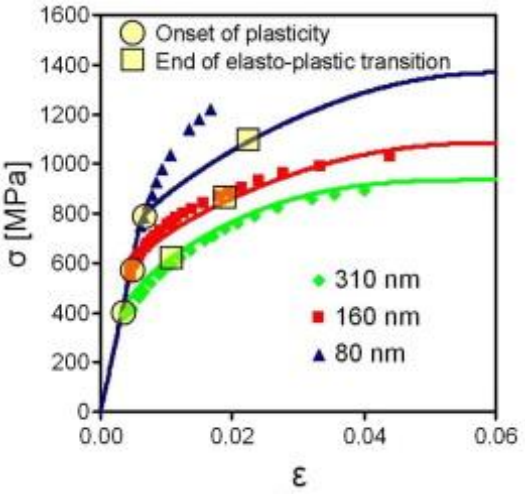

Figure 1.22: Comparison between measured and predicted stress-strain curves for Pd films with different thicknesses. Reproduced from Ref. [109].

The effect of hydrogen on the Young's modulus of Pd can be explained by considering lattice expansion, electronic contribution and, in the $\alpha + \beta$ region, the mechanical coexistence of the two phases. Fabre et al. measured the Young's modulus along the whole compositional range of the Pd-H system - taking into account these three effects - and found out a decrease of the Young's modulus with the hydrogen content [111], this decrease being much more pronounced in the $\alpha + \beta$ region. The elasto-plastic transition of Pd is also affected by the presence of hydrogen. Smith and Otterson showed that the Pd yield stress increases with increasing hydrogen content [112], invoking a classical solution strengthening behaviour[3]. However, in this thesis work, very

[3]The hydrogen present in the octahedral sites of the Pd lattice impedes the motion of dislocations, thereby increasing the stress needed to propagate them.

small hydrogen contents will be considered, so that the mechanical properties of pure, nanocrystalline Pd will be mostly used in the discussions.

1.4 The role of internal stress in the hydriding mechanism

Internal stresses play a key role in all the applications that involve the use of thin films. The physico-chemical links between the thin film and its substrate are notably of fundamental importance. More specifically, in the context of this thesis work, the internal stress that acts on the crystalline lattice of a thin metallic film - whether locally or globally - can change the energetic configuration of the hydrogen adsorption/absorption sites and/or the magnitude of the energy barriers that are crossed by the hydrogen atoms penetrating into the metal. The present section provides a review of the existing knowledge on the effect of these local and global stresses on the hydriding behaviour of thin films.

Let us firstly address the case of local stress (microscopic and nanoscopic). Although the interaction between hydrogen and metals has been widely studied for applications, like gas purification membranes and hydrogen storage or sensor systems, it is also often considered as an undesirable source of embrittlement in metallic alloys. In the field of hydrogen embrittlement in metals, local stresses are obviously highly important because their study can enable to predict the fracture conditions of hydrogen-containing structures like high pressure vessels [113] or hydrogen pipelines [114].

The existing fracture models involve accumulation of hydrogen atoms in the local tensile strain field around dislocations and crack tips, either invoking hydrogen-enhanced local plasticity (HELP mechanism) [115, 116], hydrogen-enhanced decohesion (HEDE mechanism) [117, 118] or hydride formation and cleavage [118, 119]. In these mechanisms, distortion of the host metal matrix caused by a local tensile strain field favours hydrogen accumulation in the available lattice sites as well as the formation of hydrogen trapping sites. In the HEDE mechanism, the accumulation of hydrogen around the crack tip lowers the surface energy of atomic planes and grain boundaries, then also lowering the Griffith criterion for brittle fracture and encouraging cleavage-like fracture modes. In the case of HELP, H forms Cottrell atmospheres around dislocation cores, facilitating dislocation motion or decreasing dislocation-dislocation interactions. This results in an enhancement of the material plastic strain capacity. Moreover, dislocation pile-ups generate cracks which can easily propagate. Finally, in the case of hydride formation and cleavage, brittle hydrides grow around dislocations, possibly leading to the formation of micro-cracks even at dilute bulk H-concentrations.

Recently, Song and Curtin developed a new model for hydrogen embrittlement in metals. Their model is a nanoscale analogy of hydride formation and cleavage, and has elements of the HEDE model. It consists of the formation of a so-called 'nanohydride' material, which blocks dislocation emission and absorption around the crack tip. The blunting of cracks is not possible anymore, which promotes brittle fracture and inhibits ductile fracture. This concept is illustrated in Fig. 1.23. However, several models are still competing in the field of hydrogen embrittlement, and these models point out the strong interaction existing between micro or nano stress fields generated by crystalline defects such as microcracks and dislocations. These studies are thus highly relevant regarding the present thesis work, whose aim is notably to understand the link between internal stress and the hydriding kinetics of highly defected metals.

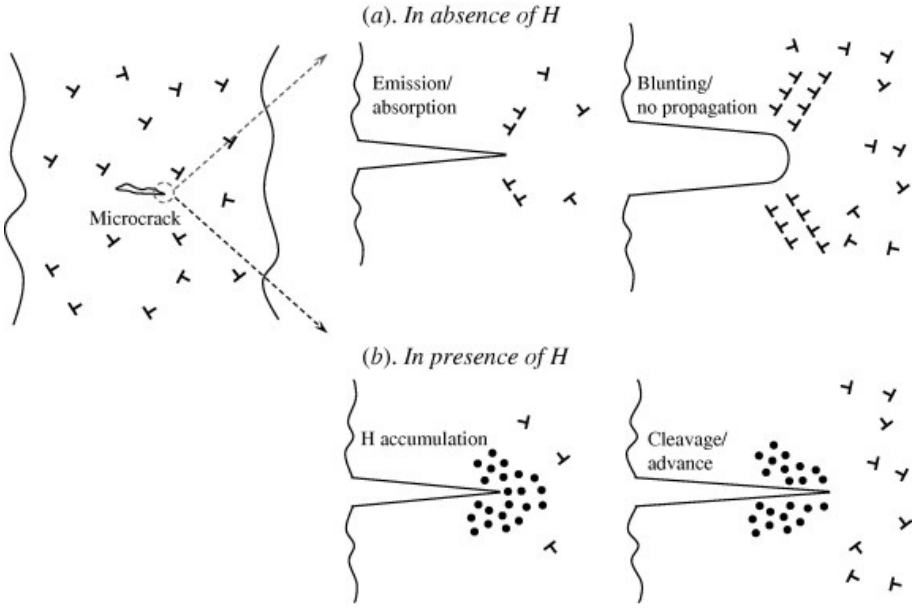

Figure 1.23: Schematic representation of the evolution of a pre-existing microcrack during mechanical loading: (a) in the absence of H, where the crack is blunted by emission and absorption of dislocations, and (b) in the presence of H, where accumulation of H near the crack tip inhibits emission and absorption, leading to cleavage fracture. Reproduced from Ref. [118].

Similar relationships between the mechanism of hydrogen uptake and the stress/strain state of the host metallic lattice are also of primary importance in hydrogen sensors, membranes or storage applications. In this kind of systems, an effect of internal stress on the hydriding thermodynamics has been reported

for both thin films [68, 120–122] and powders [123–125]. In thin films, internal stress can be generated in different ways, like clamping metallic layers and using different types of substrates [120], using layers partially or totally detached from their substrates [121], and through elastic constraints using sandwiched metallic layers [122]. In powders, the sensitive parameter is usually the milling time, for which an optimum exists, claimed to correspond to a state of the maximum internal stress [124, 125]. In these kind of studies, on will talk about global (macroscopic) stress rather than local stress, as the substrate-film relationship or the effects of the ball-milling process are applied homogeneously to the material.

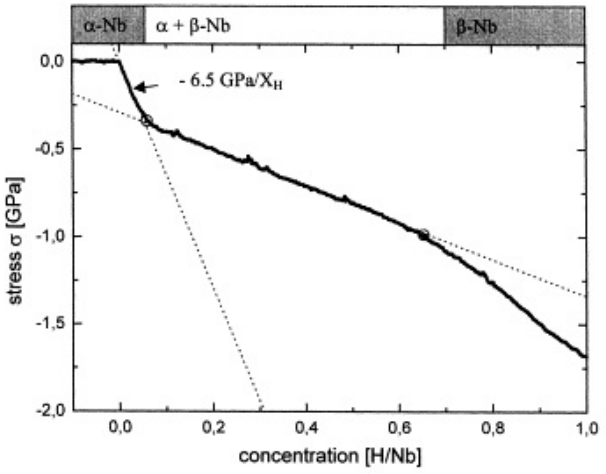

Figure 1.24: Stress-concentration curve of a 189 nm thick Nb film. The slope in the α-phase range almost follows the calculated stress. The changes of the slope can be assigned to the phase boundaries, which were determined by X-ray measurements. Reproduced from Ref. [126].

The global compressive stress developing in thin metallic films subjected to hydrogen cycling can be very important, on the order of the GPa [71]. This reality can be illustrated by the work carried out by Laudahn et al. [126], who used a two-beam optical sensor (close to the setup used in this thesis work) to derive the stress in their thin Nb films electrochemically charged with hydrogen. In fig. 1.24, one can indeed see the liner elastic relationship between stress and hydrogen concentration in the solid solution region. When the miscibility gap is reached, the apparition of a second phase enables the production of misfit dislocations, themselves being responsible of stress relaxation processes. As one may expect, plastic processes are still present in the pure hydride phase, but the latter seem to be less strong than in the two-phase region. This behaviour

is typical of thin metallic films attached to a substrate [71].

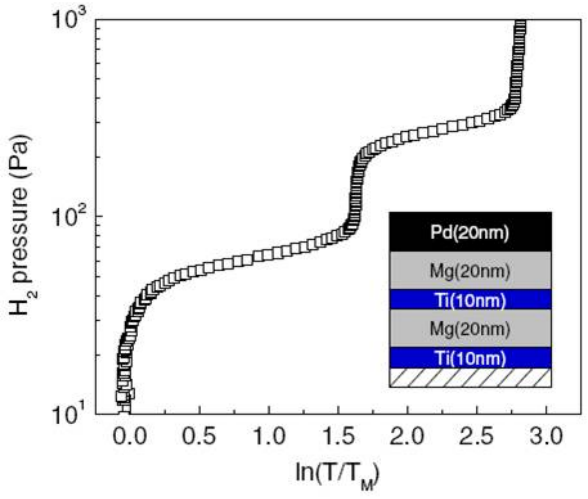

Figure 1.25: p-t isotherm of two Mg thin films in different internal stress states. Reproduced from Ref. [122].

If the stress change subsequent to the hydriding of thin metallic films is compressive, then tensile stress should act as a kind of driving force, thereby modifying the thermodynamic behaviour of the films. This idea has notably been addressed by Baldi et al. [122], who recorded p-t isotherms of Mg thin films sandwiched, respectively between an upper Pd and a lower Ti layers, and by two Ti layers. They found out that the plateau pressure of the isotherm is shifted towards higher values for the upper Mg thin film, which is in a more compressive state than the other one (see Fig. 1.25). In the present thesis work, a similar approach has been used, based on thin film growth stress control.

If the adhesion is not sufficiently good to support the high compressive stress undergone by the hydriding of a thin metallic film, buckling of the hydrogen-absorbing film can easily occur. This phenomenon enables the thin film to relax a large amount of stress, which will result in a modified thermodynamic behaviour. Wagner and Pundt showed this effect for $Pd_{0.98}Fe_{0.02}$ thin films deposited on silicon substrates (see Fig. 1.26). Part of their thin films remained attached to their substrates, while part of them were partially or totally buckled. This resulted in an important shift of the plateau pressure, in agreement with the results of Baldi et al. [122]. Delamination of thin Pd films can be avoided by using a Ti adhesion layer between the Pd thin film and its substrate [75], as can be seen in Fig. 1.27. Pivak et al. showed that the presence of a Ti adhesion layer enables the upper Pd thin film to release the

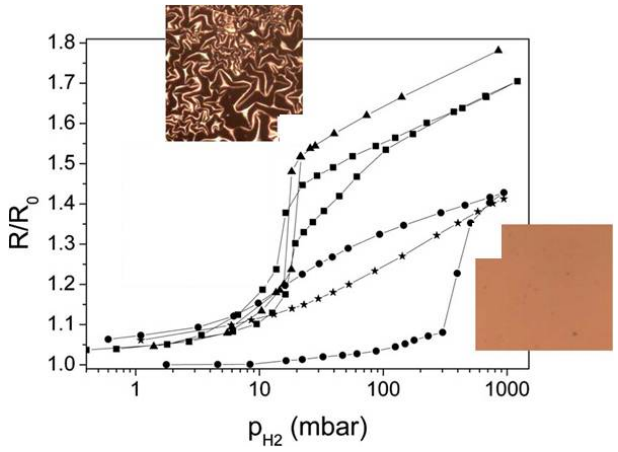

Figure 1.26: Pressure-electrical resistance isotherms of $Pd_{0.98}Fe_{0.02}$ thin films buckled (triangles, second loading), partially buckled (squares, second loading) and attached to their substrates (first loading: circles. Second loading: stars). Reproduced from Ref. [121].

compressive hydriding-induced stress by means of rearrangement and pile-up of the Pd atoms, while Pd thin films directly deposited on the substrate tend to release stress by buckling [75]. Although the adhesion energy has been accurately characterised, and the stress relaxation mechanisms with and without adhesion layer are known for different types of substrates such as silicon [127], sapphire [75], quartz [75] and polymers [128], no information seems available about the exact origin of these good adhesive properties. In this thesis work, Ti adhesion layers have systematically been used in our specimens. No delamination has been observed, even after several hydriding cycles.

The above studies provide clear evidence that both global and local internal stresses can have a non-negligible effect on the equilibrium hydriding behavior of metallic compounds, affecting thermodynamic parameters like equilibrium H-uptake and miscibility gaps [121,122]. On the other hand, a possible effect of internal stress on the kinetics of hydriding has to the best of our knowledge not been extensively considered so far. This is one of the main objectives of this thesis work.

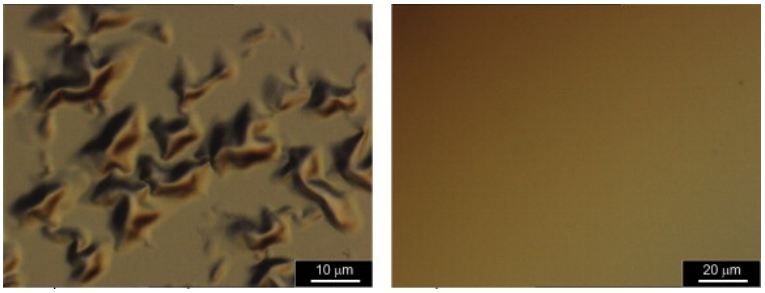

Figure 1.27: Optical microscopy micrographs of the Pd (left) and Pd/Ti (right) thin films after 17 and 18 hydrogenation cycles, respectively. Reproduced from Ref. [75].

1.5 The role of microstructure in the hydriding mechanism

Microstructure plays a key role in the mechano-chemical properties of materials, including their hydriding properties. In this section, we will address the existing knowledge on the role of microstructure on metal hydride formation. More precisely, we will only address here the microstructural effects which are relevant in the context of this thesis work.

The microstructure of a metal can offer several types of hydrogen trapping sites [71], in the bulk as well as in the surface and subsurface layers. In the case of nanostructured thin films as in this thesis work, crystalline grains are very small compared to bulk specimens, and the density of grain boundaries is very high. Grain boundaries offer low-energy sites for the absorbed hydrogen atoms, then acting as trapping sites for hydrogen [129]. Dislocations also play an important role, as hydrogen feels the local stress fields that they produce in the material [130]. Vacancies, which are other potential hydrogen trapping sites [131], can also be expected in high concentrations in our room temperature deposited Pd thin films, as will be seen in next section. Precipitates can also act as hydrogen trapping sites [132], but they won't be considered here, because we only have used pure palladium in this thesis work. The particular case of hydrogen interaction with twins will also briefly be addressed.

1.5.1 Grain boundaries

The effect of grain boundaries on the hydriding properties of metals has been the object of intensive studies, especially by using nanocrystalline palladium

(n-Pd) as a model system. Mütschele and Kirchheim used n-Pd specimens with a mean grain size of 10 nm obtained by gas-phase synthesis. [133, 134]. They found out an increase of the lower limit of the miscibility gap and a decrease of its upper limit, respectively. As explained above, this narrowing of the miscibility gap is commonly observed in nanocrystalline palladium, such as in thin film specimens. Mütschele and Kirchheim explained this behaviour by conceptually dividing their Pd specimens in two regions with different local solubility: the interior region, which has a similar behaviour to bulk Pd-H, and the grain boundaries, which exhibit sites of different energies than the bulk octahedral sites. These new sites exhibit a distribution of energies which has successfully been described by Mütschele and Kirchheim, by assuming a Gaussian distribution of energy with a width of 15 kJ/mol [133]. Their interpretation of the narrowing of the miscibility gap is based in this particular energy distribution [133, 134]: at low hydrogen concentrations, the low-energy sites existing at grain boundaries are filled with hydrogen, thereby increasing the mean hydrogen concentration. But at high hydrogen concentrations, only the interior regions can be additionally filled with hydrogen. The hydride total volume is less than that of a bulk material, and the mean hydrogen concentration is lowered. The narrowing of the miscibility gap can be described by the following equation:

$$\Delta n = (1 - f_{GB})\, \Delta n_{bulk} \tag{1.17}$$

where Δn, Δn_{bulk} and f_{GB} are, respectively, the width of the miscibility gap in the nanocrystalline Pd specimen (expressed in terms of the mean H/Pd atomic ratio n in the hydride phase), the width of the miscibility gap in a single-crystal bulk specimen and the relative fraction of available sites in grain boundaries. The massive concentration of hydrogen in the grain boundaries generates large stress fields inside the grains, and the grain-boundary energy can significantly change [133]. In some metals and alloys, this effect can lead to an amorphisation of the material [135, 136].

Lemier and Weissmüller obtained a good correlation with experimental data by assuming two different types of sites in the grain boundaries of nanocrystalline palladium specimens [90]. The first type of sites have a highly negative enthalpy of solution and are reversibly saturated at low hydrogen partial pressures. The other sites have a less negative value, but still more negative than the regular bulk sites. Moreover, the latter sites are not saturated, similarly to the regular bulk sites. Consequently, at very low hydrogen concentrations, the grain boundary diffusion of hydrogen is virtually stopped [138] by the deepest potential wells. At high hydrogen concentrations, the opposed tendency is observed, and the diffusion in the nanocrystalline material is faster than in Pd bulk [139]. This tendency can be illustrated with the results of

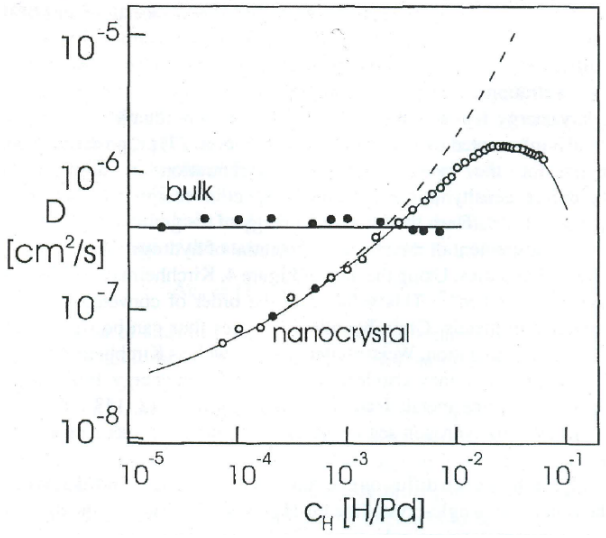

Figure 1.28: Diffusion coefficent of hydrogen in bulk (filled circles) and nanocrystalline (open circles) Pd-H as a function of the hydrogen concentration. Reproduced from Ref. [137].

Kirchheim [137], who compared the diffusion coefficient of hydrogen in bulk and nanocrystalline Pd specimens (see Fig. 1.28).

1.5.2 Dislocations

Dislocations in thin films are generated by the deposition process. They can also be created by both hydrogen absorption and desorption [71], where the dislocations accomodate the lattice mismatch present when the hydride phase nucleates and grows in the solid solution.

In particular, edge dislocations interact strongly with hydrogen atoms. The binding energy of hydrogen to the dislocation core in Pd is approximately 60 kJ/mol [130], higher than hydrogen in regular lattice sites. This value is believed to include a contribution from H-H interactions of 20 kJ/mol and a contribution from dislocation-H interactions of 40 kJ/mol. This strong link is due to a good interaction between the tensile strain field of the dislocation and the hydrostatic stress component of the hydrogen atoms [71]. The hydrogen enrichment region at the core of an edge dislocation is seen as cylindrical surface of constant hydrostatic stress located below the dislocation glide plane [140]. This cylinder is schematically shown in Fig. 1.29. The diameter of this cylinder

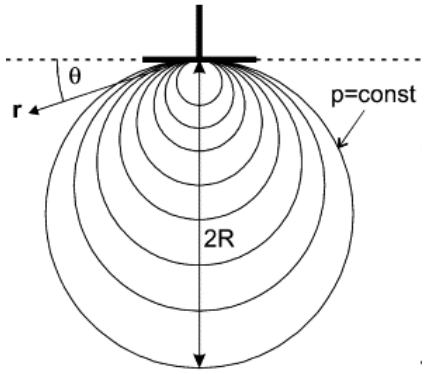

Figure 1.29: Cylindrical coordinates with the origin at the dislocation core, glide plane (dashed line) and circle (cylinder in 3 dimensions) of constant hydrostatic stress. Reproduced from Ref. [140].

was found to increase with the mean hydrogen concentration in the specimen [141], as can be seen in Fig. 1.30. If G is the palladium shear modulus, ν its Poisson ratio and b the Burgers vector of the dislocation, then one can express the pressure p on the cylindrical surface as:

$$p = \frac{Gb\,(1+\nu)}{3\pi\,(1-\nu)}\,\frac{1}{2R} \tag{1.18}$$

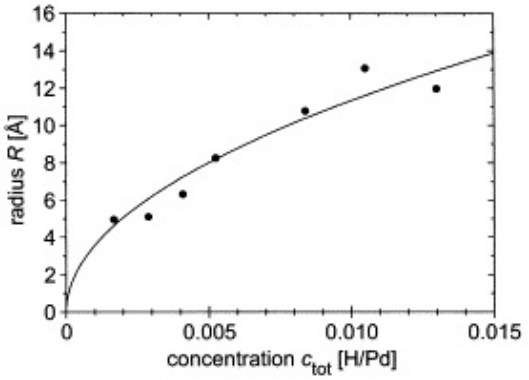

Figure 1.30: Measured (closed circles) and calculated (solid line) cylinder radii of segregated hydrogen at edge dislocations as a function of the hydrogen concentration. Reproduced from Ref. [141].

Edge dislocations thereby act as traps for hydrogen in palladium. Chemical potential-concentration isotherms measured on thin Pd films with different concentrations of dislocations revealed a strongly enhanced hydrogen solubility in the low hydrogen concentration range [142]. As opposed to edge dislocations, screw dislocations interact weakly with the hydrogen atoms [71]. The reason for this behaviour is that the shear stress components generated by the screw dislocations interacts poorly with the hydrostatic stress component of the interstitial hydrogen atoms.

It is also well-known that dislocations act as preferential pathways for hydrogen transport [143, 144], thereby also affecting the hydriding kinetics. In this thesis work, this effect will be analysed by changing the dislocation concentration in our Pd thin film specimens by means of high-vacuum annealing with in-situ curvature measurement.

1.5.3 Vacancies

Vacancies can be regarded as open volume defects forming an internal surface in the material [71]. As we showed above, the hydrogen adsorption sites are more stable than the absorption sites. Therefore, hydrogen in a vacancy will be more stable as well than regular bulk sites. Vacancies then also act as hydrogen traps.

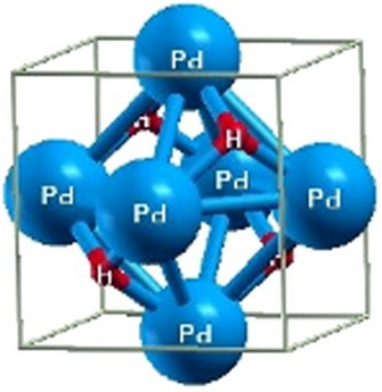

Figure 1.31: Atomic structure of the defect phase Pd_3VacH_4. Hydrogen atoms occupy tetrahedral interstitial positions. Reproduced from Ref. [145].

When hydrogen is present in a metal, the equilibrium vacancy concentration can be drastically modified. Fukai studied this phenomenon intensively, notably in the case of the palladium hydride [146]. He found out a lattice pa-

rameter decrease at high temperature and hydrogen pressure. He attributed this decrease of the lattice parameter to the presence of an extraordinary high vacancy concentration. These hydriding-induced vacancies are called superabundant vacancies (SAVs). They have been shown to remain in the material even when returning to normal temperature and pressure conditions. Fukai confirmed the presence of SAVs in many metals [131]. In Fe, six hydrogen atoms per vacancy have been reported [147], forming the so-called $VacH_6$ complex. But in Nb, $VacH_4$ complexes are rather formed [148]. The stability of complexes and their exact chemical composition as a function of the crystalline lattice is still under debate [71].

In the case of palladium, Fukai and Okuma suggested an ordered arrangement of the vacancy-hydrogen complexes in the form of Pd_3VacH_4 [146]. Isaeva et al. recently performed *ab initio* calculations on this defect phase [145], and surprisingly found out that in this particular configuration, the hydrogen atoms are more stable when they occupy tetrahedral interstitial sites, as shown in Fig. 1.31. But there are other possibilities, as in the case of other metals. For example, He et al. recently suggested that $VacH_2$ complexes are thermodynamically stable in palladium [149], as shown in Fig. 1.32. The hydrogen molecule itself could thereby be reformed in Pd vacancies.

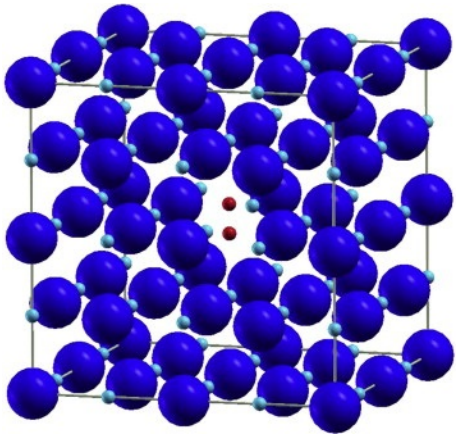

Figure 1.32: Atomic configuration of the hydrogen molecule in a vacancy of the palladium hydride. Large and small balls represent palladium and hydrogen atoms respectively. All octahedral sites are occupied by hydrogen atoms, which correspond to PdH. Red small balls represent the hydrogen molecule. Reproduced from Ref. [149].

The hydriding kinetics of metals is usually reported to be enhanced by the presence of vacancies [150–152]. This effect is seen as a critical issue in

steel embrittlement, while it constitutes a positive effect for hydrogen storage applications.

1.5.4 Twins

The exact role of twins on the hydrogen absorption by metals remains unclear. Several authors claim that twins can act as hydrogen traps [153, 154], but all studies do not confirm these observations. The latter works were carried out on steels, while Danaie et al. concluded that twins do not modify the thermodynamic behaviour of hydrogen in magnesium [155]. One can thereby expect that twins can act as traps only if the enthalpy of hydriding in lattice sites is low enough, which is not the case for all metals. However, Danaie et al. also observed a significant enhancement in the hydriding kinetics of their Mg powders. Twins can then also be considered a preferential pathways for hydriding.

1.6 Summary

In this chapter, the state-of-the-art of thin film metal hydrides has been covered and situated in the context of metal hydride materials, as well as in the context of a future society substantially relying on hydrogen as an energy vector. The objectives of this thesis work have been located in the field of thin film metal hydrides. The study of the thermodynamic behaviour of our Pd thin films will be compared to the large amount of data already present in the literature, while the study of their hydriding kinetics is expected to give insight into the understanding of the basic hydriding mechanisms thanks to the use of our high resolution in-situ approach. The effect of internal stress and microstructure on the hydriding behaviour of metals still need extensive quantitative studies, which is also one of our objectives. More precisely, on the experimental level, these effects are difficult to separate from each other. This can be possible here through the use of thin film technologies, as will be seen in the next chapters.

Chapter 2

Materials and methods[1]

The main experimental methods and procedures used in this thesis are presented in the present chapter. It includes the experimental approach used to monitor the deposition, the hydriding kinetics and thermodynamics, as well as the annealing of a thin metallic film in-situ, and the main characterisation methods used to study the films ex-situ. Firstly, the relationship between the specimen curvature and the internal stress in the thin metallic film - namely Stoney's equation - is presented and analysed, and its validity and limitations are discussed in the case of measurements in air and in vacuum. The measurement principle of the specimen curvature - adapted from previous works carried out in liquid environments by Vanhumbeeck [157] and Van Overmeere [158] - is then explained and discussed in details. Its application to thin film deposition (previously performed by Michotte and Proost [159]) is presented, as well as its applications to thin film hydriding and annealing (performed in the context of this thesis). The characterisation work carried out on the specimens considered in this thesis is finally summarised.

2.1 Using Stoney's equation

In this section, Stoney's equation is explained and its validity limits are discussed in terms of the experimental conditions specific to the present thesis work. Its particular derivations for application to the three experimental setups considered here - i.e. for thin film deposition, hydriding and annealing - is then presented.

[1] Most of the elements presented in this chapter have been published in an international peer-reviewed paper [156].

2.1.1 Validity and limitations of the stress derivation

In 1909, G. G. Stoney published the first scientific work aiming at the understanding of the relationship between stress and curvature in metallic coatings [160]. This early work was motivated by the fact that metallic coatings electrolytically deposited turned out to peel off in many cases - that is to say, for many different types of coatings and substrates - spontaneously and without assignable cause. Since then, many corrections and modifications have been brought out to the initial form of this relationship, called Stoney's equation. Indeed, the initial work of Stoney was partly erroneous, in particular because he considered uniaxial stress in the film instead of biaxial stress [161]. Some more recent works related to Stoney's equation aimed at the study of its accuracy [162, 163], while others managed to derive expressions for specific cases, like with a non-uniform temperature distribution [164] or with a position dependent stress distribution [165].

Nowadays, Stoney's equation is usually written in the following form [161]:

$$\langle \sigma_f \rangle t_f = \frac{Y_s t_s^2}{6} \kappa, \tag{2.1}$$

where $\langle \sigma_f \rangle$ and t_f are, respectively, the mean internal stress in the film and the thickness of the film. t_s is the thickness of the substrate onto which the film is deposited, and $Y_s = E_s/(1-\nu_s)$ is its biaxial modulus. κ is the measured curvature of the specimen, considered as initially flat before the film deposition in this version of Stoney's equation.

This contemporary form of Stoney's equation is therefore the result of several assumptions, partly built by Stoney himself and partly added or refined by more recent works. These assumptions are summarised below and their validity is discussed in the case of our experimental setup:

- Both substrate and film thicknesses are small compared with the lateral dimensions of the system [166]. In other words, Stoney's equation applies to thin film geometries, i.e. with one of the dimensions being several orders of magnitude smaller than the two others. This is obviously the case in this work, where the total thickness of the specimen does not exceed 425 μm, while the lateral dimensions of our cantilevers are typically 3 x 0.5 cm^2.
- The film must be thin compared to the substrate, i.e. the ratio t_f/t_s must be small. Respecting the condition $t_f/t_s < 0.01$ ensures an accurate use of Stoney's equation by keeping the error below 5% [167]. With the specimens used in this thesis, this ratio is equal to 10^{-3} in the worst case. This hypothesis is then valid here.

- The substrate is assumed to be homogeneous, isotropic and linear elastic [168]. The Si (100) substrates used here satisfy the homogeneity and isotropic conditions. The highest film stress observed in this thesis was -1GPa, with a film to substrate thickness ratio of $t_f/t_s = 4 \cdot 10^{-4}$. As the maximum substrate stress - at the interface between the film and substrate - is equal to $-4t_f/t_s\langle\sigma_f\rangle$ [169], this corresponds to a substrate stress of 1.6 MPa, far beyond the Si single crystal elasticity limit [170]. The film deposited onto the substrate is also assumed to be isotropic, which is the case with the nanocrystalline Pd thin films deposited in this thesis work (see the characterisation section for more details).

- A too large specimen curvature may lead to significant errors, as nonlinear effects arise when the specimen deformation is too important. Mézin defined a criterion based on the geometry of the specimen to evaluate the error that is made when measuring high curvatures, i.e. the error does not exceed 5% if the condition $\kappa < 2.2t_s/b^2$ is respected [171][2], where b is the specimen width. In this thesis, the worst case is obtained with a specimen width of 5mm and a substrate thickness of 180 μm. The maximum measured curvature in that case is 165km^{-1}, a much smaller value than the 15840km^{-1} predicted by this criterion.

- Edge effects near the periphery of the specimen are negligible, and all physical quantities are invariant under a change in position parallel to the interface [166]. This assumption is correct if the measurement is carried out far enough from the edges of the specimen (including the clamp). The region in which edge effects (like shear stress) are considered to take place is equal to five times the specimen thickness [172][3]. This assumption is respected here, as the maximum specimen thickness is 425 μm and the measurement is carried out 2.5mm from the edges of the specimen.

[2] Stoney's equation is only valid in the linear domain of small strains (material assumption) and small displacements (geometrical assumption stating that the deformed shape of the specimen remains spherical). The small strain assumption is connected to the previous assumption of linear elastic deformation of the substrate. But this is not enough to ensure the specimen curvature to be identical in all directions. Above a certain level of stress, the deformed shape can become cylindrical or ellipsoidal. In the case of a rectangular sample, Mézin showed that the factor $\kappa b^2/t_s$ determines the increase in stiffness along the sample width owing to the curvature along the sample length, and is then indicative for geometrical nonlinearity.

[3] The shear stress acting along the edge of the substrate is equal to zero at the very edge of the film (because the surface is stress free), increases up to a maximum value, and then progressively vanishes at a certain distance from the edge. This shear stress distribution is a function of the respective rigidities of the film and substrate. For a substrate with infinite rigidity, the maximum shear stress occurs about a half-film thickness from the edge of the film. For a substrate with finite elastic modulus (but more rigid than the film), the shear stress distribution is more extended, and typically vanishes at a distance of five times the specimen thickness.

- All stress components in the thickness direction vanish throughout the material [173]. This condition is respected if the former one is, i.e. far enough from the edges of the specimen.
- If using a clamped cantilevered specimen, its length should be much larger than its width. A ratio of 3 ensures the associated error to stay below 0.1% [174]. This assumption is verified here, as the lateral dimensions of our cantilevers are typically 3 x 0.5 cm^2.

If all the above conditions are satisfied, Stoney's equation is applicable and the stress distribution in the thin film and substrate can be schematically represented as in Fig. 2.1. Before discussing the stress distribution and its implications, it has to be noted here that the stress in the thin film has been arbitrarily set negative in Fig. 2.1 because in this thesis, the stress due to the hydriding of thin metallic films deposited onto a substrate is compressive. In general, the stress could be positive in the film, which does not change anything to this reasoning.

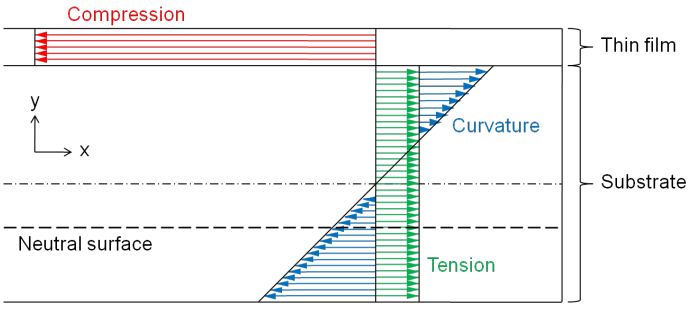

Figure 2.1: Stress distribution along the film (red) and substrate (green + blue) thickness. Both stress contributions arising from the requirements of equilibrium of forces (green) and moments (blue) in the substrate are represented.

If the film were not attached to the substrate, it would expand freely when absorbing hydrogen, and it would become longer than the substrate. To fit the film and substrate back together, one needs to apply a compressive force on the film (which results in the red biaxial compressive stress shown in Fig. 2.1) and an equal and opposite tension force on the edge of the substrate (which results in both the green biaxial tensile stress and the blue biaxial bending stress shown in Fig. 2.1). The total stress in the substrate then comes from 2 origins: the requirement of the equilibrium of forces in the specimen (green tension stress in Fig. 2.1) and the requirement of the equilibrium of moments in the specimen (blue curvature stress in Fig. 2.1). There exists a surface along the y-axis, called the neutral surface, where the stress is zero. This surface is

characterised by the fact that the components of the displacement of a point in the xz plane can be considered as equal to zero. The neutral surface is thereby neither expanded nor contracted. Janssen *et al.* recently found out that this surface is located at a distance of $2/3t_s$ from the interface between the film and the substrate [161]. The stress in the thickness direction (y-axis in Fig. 2.1) is equal to zero along the entire thickness of the specimen. The stress in the x and z directions are equal to each other, i.e. the stress is biaxial and rotationally symmetric in the plane of the film if the film mechanical properties are transversally isotropic [175]. As explained above, the stress in the film is much more important than the stress in the substrate (in this thesis, the compressive stress in the film can be on the order of the GPa, and the tensile stress in the substrate is on the order of the MPa). Consequently, the film can deform plastically.

The very small stress levels reached in the substrate of a thin film system is a very important asset in the use of Stoney's equation. Indeed, Eq. (2.1) only contains material properties of the substrate, which are often well known. Moreover, the requirement of elastic deformation of the substrate is easily met.

Using Stoney's equation is not the only way to measure thin film stress. Other techniques, based on X-ray or electron diffraction [176,177], are also being used for a long time. But these techniques cannot be applied in-situ with a lot of different systems as it is the case regarding curvature-based stress measurement techniques. The derivation of the thin film stress components using these techniques is also not as straightforward as with the Stoney relationship. In a detailed kinetic study like in this thesis work, these advantages are of primary importance.

2.1.2 Stress derivation for thin film deposition, hydriding and annealing

Stoney's equation, expressed in the form of Eq. (2.1), provides the stress evolution in a thin film specimen if one has a good knowledge of the substrate elastic properties. But the film thickness is an important parameter as well, as it may be constant throughout the whole measurement (like in hydriding and annealing experiments in this thesis), it may increase (like in deposition by magnetron sputtering in this thesis) or even decrease (for example, in the case of thin metallic film anodising, the metal film is consumed while the oxide film is growing, and both stress contributions need to be considered [157, 158]).

In the case of thin film deposition, the stress in the deposit cannot be directly deduced from Eq. (2.1) because the film thickness is not constant. Instead, the curvature data is deduced from the stress*thickness product by

introducing a differential notation in the left-hand side of Eq. (2.1):

$$\langle \sigma_f \rangle \, \Delta t_f = \frac{Y_s t_s^2}{6} \Delta \kappa, \tag{2.2}$$

where the local stress σ_f is defined as follows:

$$\int_0^t \sigma_f(y) \, dy = \langle \sigma_f \rangle t, \tag{2.3}$$

and assumed as homogeneous over the entire thickness t. Eq. (2.2) is then used in this work to extract the evolution of the mean film stress during deposition, more precisely by calculating the slope of the stress*thickness versus thickness curve. As will be explained in next section, the film stress can also be reasonably assumed as constant over the film thickness. The curvature evolution can therefore be seen as the image of the film thickness evolution.

In the case of thin film hydriding and annealing, one can have direct access to the film stress by deducing it from Eq. (2.1):

$$\Delta \sigma_f = \frac{Y_s t_s^2}{6 t_f} \Delta \kappa, \tag{2.4}$$

where the film stress is also assumed as homogeneous over the film thickness. In this case, the curvature evolution is the image of the film stress evolution due, respectively, to the interaction between hydrogen and the Pd thin film and to additional thermal/intrinsic stress generation during annealing.

2.2 In-situ curvature measurement

In the previous section, it has been shown that the direct link between the thin film stress and the specimen curvature is reliable and accurate in the context of the present thesis work. Let us now focus on the measurement of the specimen curvature. Many different techniques exist for the measurement of a wafer curvature. Here, we will discuss the main ones, i.e. differential capacitance, piezoresistivity, interferometry and laser beam deflection techniques.

The differential capacitance method is a transduction technique based on the capacitance measurement between two plates, one being a thin film cantilever undergoing a stress-induced curvature and the other, called the bottom electrode, being fixed to the substrate [178]. In practice, this system is generally

used to design temperature sensors [179], pressure sensors [180] or accelerometers [181]. It is effective for in-situ measurements, but difficult to design and implement as it requires complex micromachining techniques. Its is thereby inappropriate for the purpose of this present thesis, which requires the rapid testing of numerous, full-plate deposited thin film specimens.

Another kind of MEMS system can also be designed on the basis of a piezoresistive measurement [182]. This system leads to the same range of applications as the differential capacitance method [183], and then has the same drawbacks as the latter.

Interferometry is based on the measurement of the variations of the optical path of a laser beam on a single point of the specimen surface [184, 185]. This technique can reach very high levels of precision and can be used efficiently in-situ, but requires very complicated positioning methods.

The use of laser beams can also be made in a different way in order to measure thin film curvature. Laser beam deflection techniques enable the measurement of the specimen curvature by recording the position of one laser beam reflected off the specimen surface with a position sensitive detector [186]. This technique is the most commonly used because its is easy to implement, accurate, sensitive, non-invasive, and it can be performed in real time [187–189].

Nevertheless, the major drawback concerning interferometry and laser beam deflection techniques is the instability of the measurement regarding vibrations of the specimen, laser source and detector, inevitable when performing single laser beam measurements. As will be seen in the next section, the use of multiple beams allows to solve this problem.

2.2.1 The multi-beam optical sensor

Since the early developments, laser beam deflection techniques have undergone two major modifications, which improved their intrinsic accuracy and stability. The first important modifications were brought out in the eighties by Kobeda and Irene [190, 191], who decided to use two parallel incident beams instead of one. The curvature in then deduced from the differential spacing between the two reflected beams and the position sensitive detector is replaced by a CCD camera, thereby increasing the time resolution. But the most important improvement brought out by these modifications concerns the stability of the curvature measurement. Indeed, measuring a spacing instead of the position of a single beam allows to virtually reduce the noise due to the vibrations of the system because in principle, the latter affect every laser beam in the same manner.

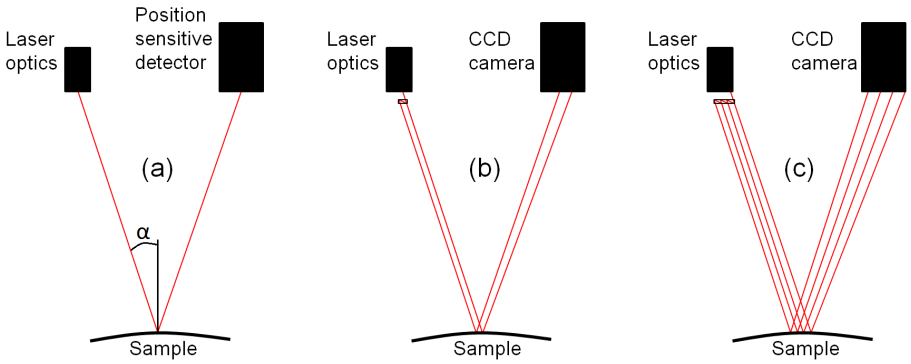

Figure 2.2: Evolutions of laser beam deflection techniques, from single-beam (a) to two-beam (b) and multi-beam (c) optical sensor.

In the nineties, Floro *et al.* further improved the technique [192] by using an array of laser beams instead of just two beams. The curvature of the specimen is then calculated through the mean differential spacing (MDS), which is simply the mean of all the differential spacings produced by the array of beams reflected off the specimen surface. The robustness of the technique has then been significantly increased, as the concurrent use of multiple beam spacings allows to statistically reduce the noise due to the vibrations of the system. This technique has been widely used in gaseous or vacuum environments [193–196], but also in liquids [197–199].

These major evolutions of laser beam deflection techniques are schematically represented in Fig. 2.2. To summarize, the multi-beam optical sensor is versatile, easy to implement for high resolution in-situ measurements, accurate and stable. This is why it has been chosen to monitor the curvature of our specimens during deposition and hydrogen cycling.

2.2.2 Validity and limitations of the curvature measurement

When measuring curvature with the multi-beam optical sensor, the relationship between the specimen curvature and the beam spacings originally derived by Floro *et al.* [192] is still the most commonly used in the literature:

$$\Delta\kappa = \frac{\cos\alpha}{2L}\frac{\Delta D}{D_0}, \tag{2.5}$$

where $\Delta\kappa = \kappa - \kappa_0$ is the specimen curvature (the subscript "0" refers to the specimen reference state before the start of the film deposition, hydriding or annealing), $\Delta D/D_0$ is the mean differential spacing between the reflected laser spots in the CCD camera[4], α is the angle of incidence of the laser beams on the specimen (shown in Fig. 2.2) and L is the distance between the specimen and the CCD camera.

This formula can be derived by assuming that the angles of incidence and reflection of the laser beams are small. More precisely, Van Overmeere showed that the error associated with this small-angle approximation can be kept below 1% for incident angles as large as 25° [158]. This condition is clearly respected here, as our curvature measurement setups have been designed to have $\alpha \approx 0°$. Another source of error when using large incident angles is the astigmatism of the laser beams [200]. This is not an issue here as well.

Eq. (2.5) also makes the implicit assumption that the substrate is flat in the reference state [157]. This assumption is true when monitoring thin film deposition on a silicon wafer, but this is not necessarily the case, for example when observing hydriding or annealing on a thin film with important internal growth stress. If the substrate is not flat in the reference state, Vanhumbeeck showed that the resulting error can be expressed as [157]:

$$\frac{\cos\alpha/2L}{\kappa_0 + \cos\alpha/2L}. \tag{2.6}$$

In the context of this thesis work, the maximum value of κ_0 is 18 km^{-1}, leading to a 2.3% error when using our calibration factors for thin film hydriding and annealing (see next sections). Experimental tests performed by comparing the curvature after Pd thin film deposition with measurements on flat mirrors confirmed that the maximum error is indeed on the order of 2%.

Important errors may arise when the specimen is in a different medium than the ambient air in the laboratory, such as liquids [201]. In this case, Eq. (2.5) becomes:

$$\Delta\kappa = \frac{\cos\alpha}{2Ln_{liq}}\frac{\Delta D}{D_0}, \tag{2.7}$$

where n_{liq} is the refractive index of the liquid. For example, using water would give a 33% error if erroneously using Eq. (2.5) instead of Eq. (2.7). In the present thesis work, the specimens are in air, in vacuum or in a mixture of

[4] i.e. the mean between the beam differential spacings, which can be written as $\sum_{i=1}^{n}\frac{\Delta d_i}{d_{i0}}$, where d_i is i^{th} beam spacing and n is the number of beam spacings.

argon and hydrogen. These media have very close refractive indexes [202, 203] and this source of error is negligible.

In some specific cases - i.e. when using extreme geometries or when measuring curvature in a liquid - other sources of errors need to be considered, such as the distance between the clamp and the incident beams, the spacing between the incident beams and the specimen to detector distance, as previously addressed by Van Overmeere [201]. In the context of this thesis work, these are all far below 1% and do not need to be considered.

2.2.3 Resolution of the curvature measurement in vacuum and gases

Fig. 2.3 shows a typical temporal evolution of the specimen curvature when performing a baseline measurement, showing a standard deviation of 0.1 km^{-1}, and therefore a resolution of 0.2 km^{-1}. This resolution depends on the theoretical resolution, i.e. on the factors described in previous section, that predict a maximal relative error of 2.5% when using Eq. (2.5) (considering two independent sources of errors, i.e. 1% due to small-angle approximation and 2.3% due to initial substrate curvature). But it is also affected by some experimental artifacts that will be described here, as well as solutions to avoid them or limit their influence.

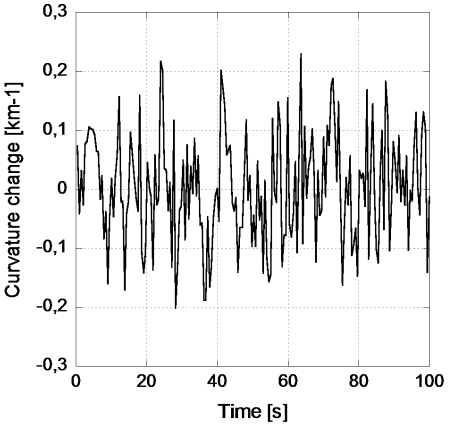

Figure 2.3: Typical baseline measurement recorded with our in-situ curvature measurement setup. The associated standard deviation is 0.1 km^{-1}.

The first resolution-limiting factor that may occur when measuring curvature in the context of this thesis work comes from convection effects taking place

in the gaseous mixtures inside or even outside the vacuum chamber. Indeed, the refractive index of gases is influenced by convection effects [204], which results in a change of the MDS - curvature proportionality, as explained in the previous section. Some convection effects are illustrated in Fig. 2.4 by blowing air and speaking next to the trajectory of the laser beams. On one hand, the air volume of the experimental room crossed by the laser beams should be protected from any air movement, either coming from thermal gradients or any type of ventilation. On the other hand, the same remark is valid concerning any gas mixture present in the vacuum chamber. As will be discovered in the next sections, these experimental artifacts are not an issue in our deposition and hydriding experimental setups. The particular case of the annealing setup will be the object of a detailed discussion later in this chapter.

As shown in Fig. 2.4, exposing the MOS optical elements to ambient light also results in an increase of the noise. Part of the ambient light spectrum may indeed not be filtered out by the CCD filter, therefore perturbing the optical measurement. Here, the resolution degrades by a factor 4 when removing the MOS protective shield. In general, this shield protects the MOS optical elements during the in-situ curvature measurement. But it has to be noted that it is sometimes necessary to remove this shield during a short period of time, for instance in order to manually translate the laser spots when spot is lost because of an obstacle on the beam trajectory or because the spot has left the CCD screen. Anyway, multiplying the resolution by 4 is still acceptable taken into account that the curvature changes measured in this thesis work are, in the worst case, on the order of 10 km^{-1} (except when using our deposition setup, but in that case, control of the mirror position is automatic).

A third possible source of resolution loss is the scattering of one or several beams due to an obstacle on the beams trajectory. In the context of this thesis work, where only vacuum and gases are crossed by the laser beams, two types of obstacles are possible. Firstly, obstacles may exist on the optical elements, i.e. dirts or scratches on optical windows, on calibration mirrors or on the CCD screen and filter. None of these elements are perfectly homogeneous and clean, and this is why the user must carefully check before the experiment if no such obstacles are present next to the beams location on the CCD screen. Secondly, the Pd thin film surface may also have some dirty areas, which should also be avoided by the user by storing the samples in a clean environment, and, if necessary, by using compressed dry air to clean the samples before the experiment. The effects of beam scattering on these kind of obstacles can be very different from each other, and often turn out to be dramatic for the curvature measurement. As an illustrative, basic example, Fig. 2.5 shows the effect of displacing a 1D array of laser spots towards a dirt that modifies the aspect of one of the spots on the CCD screen. Before translating the spots, the differential spacings are coherent with each other, as expected. When translating

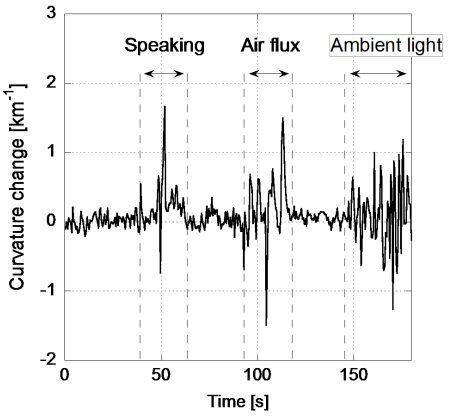

Figure 2.4: Influence of convection and light exposure effects on baseline measurement recording. These effects are produced by speaking, imposing an air flux or exposing the MOS optical elements (source, mirror and CCD camera) to ambient light.

the spots, the real-time differential spacings are obviously perturbed, showing that translating the spots during the experiment should be avoided unless this is absolutely necessary (and although this is mostly not detectable on the MDS signal). Finally, when the six spots end up at a new position, three out of the five recorded differential spacings go back to their initial value, while the two other differential spacings end up at a wrong value. Indeed, the presence of a dirt on one of the spots perturbs two spacings at a time (unless the spot is at one of the extremities of the array, which is not the case here).

If the signal to noise ratio is too high when measuring stress in a thin film system - because one of the resolution limiting factors is inevitable or simply because the observed phenomenon generates a too weak curvature signal - the resolution can still be improved by properly modifying the specimens. Indeed, by decreasing the biaxial modulus of the substrate or by increasing the t_f/t_s ratio, one can improve the effective resolution by increasing the proportionality constant between stress and curvature (see Eq. (2.1)).

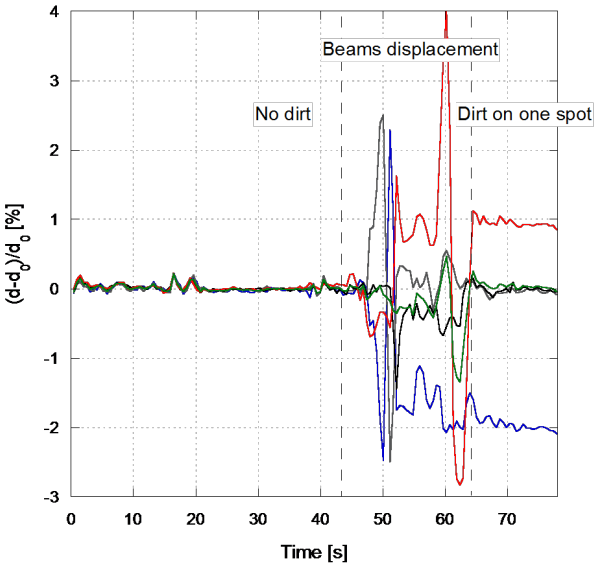

Figure 2.5: Baseline differential spacing measurement with six laser beams, followed by manual translation of the spots, and second (erroneous) baseline measurement with one of the spots on a dirt.

2.2.4 Application to thin film deposition

In the present thesis, the cantilevered thin film specimens have been prepared in the following way:

- Starting from double polished, 180 to 425 μm thick, monocrystalline Si (100) wafers, the substrates were generated by growing a 400 to 600 nm thick thermal oxide layer on both sides of the wafers by a wet oxidation process. The substrates obtained were then symmetrical, curvature-free and flat.
- Two different types of metallisation processes were then used to deposit the thin metallic films on one side of the substrate, namely a 5 to 10 nm Ti adhesion layer and a 30 to 400 nm Pd layer. The films which will be addressed in chapter 3 have been generated by e-gun evaporation without in-situ curvature measurement. The growth stress of the metallic deposit has then been measured ex-situ (see next section).
- The analysis of the hydriding response of the films addressed in chapter 4 require a fine in-situ control of the growth stresses in order to study the

effect of the latter on their hydriding kinetics and thermodynamics. The films addressed chapter 5 present the same requirement, as the aim of this section is to study the effect of microstructure on their hydriding kinetics and thermodynamics at constant internal stress level. Another type of metallisation process was then selected to enable an accurate control of the growth stress, i.e. DC magnetron sputtering, combined with our high resolution curvature measurement setup. A photograph of this setup is provided in Fig. 2.6. This setup is located in a ISO class 5 cleanroom.

- The specimens in their final form were cut out of the wafers in order to obtain 3 x 0.5 cm^2 cantilevers. As explained in previous section, this geometry is adapted to optimise the accuracy of the stress derivation with Stoney's equation.

Figure 2.6: Photograph of the sputtering setup. Upper left part: vacuum chambers. Lower left part: multi-beam optical sensor. Right part: control panels.

The adaptation of the multi-beam optical sensor to the magnetron sputtering technique - previously preformed by Michotte and Proost [159] - is schematically represented in Fig. 2.7. The curvature measurement system is a kSA Multi-beam Optical Sensor (kSA MOS) from k-Space Associates. The laser wavelength is 658 nm, and its power ranges from 0 to 18 mW (in practice, only powers up to 5 mW are used here because the silicon oxide layer and the metallic layers are highly reflective). Here, the array of beams is not a 1D array as suggested by Fig. 2.2, but a 2D array as the wafer off which the beams are reflected offers enough surface to measure the curvature in both directions in

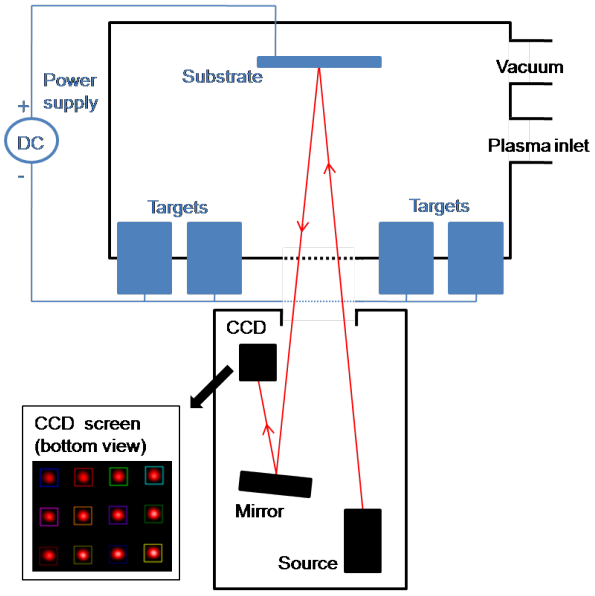

Figure 2.7: Schematic representation of the combination of the multi-beam optical sensor with the magnetron sputtering technique (not to scale). The red lines represent the trajectory of the laser beams. A bottom view of the CCD screen is also provided, showing the reflected laser spots.

the plane of the film. This 3 x 4 array contains 12 spots, so that the wafer curvature is measured with a total of 17 beam spacings (8 in one direction of the plane of the wafer and 9 in the other). The laser beams enter and leave the vacuum chamber through an optical port, and then are reflected by a mirror towards the CCD camera. The mirror position can be finely controlled by a spring system in order to adjust the position of the laser spots on the CCD detector. The calibration factor $2L/\cos\alpha$ necessary to derive the specimen curvature (see Eq. (2.5)) has been determined by performing measurements on a set of mirrors with a known radius of curvature. Its value is 1.376 m in the vertical direction, i.e. perpendicular to the plane of Fig. 2.7, and 1.366 m in the horizontal direction, i.e. parallel to the plane of Fig. 2.7 and in the plane of the wafer.

The magnetron sputtering system is from AJA International, Inc. The substrate is firstly introduced into a small, transition chamber - whose aim is to protect the main chamber from contamination, and which can be seen in Fig. 2.6 - before being introduced in the deposition chamber. The base pressure in the main chamber is on the order of 10^{-8} mbar, while it is on the order of 10^{-7}

mbar in the transition chamber. Once the base pressure is reached into the main chamber, the Ti adhesion layer and the Pd layer are successively deposited. An automatic control of the targets enables to instantaneously switch from Ti to Pd deposition. The Pd and Ti films have been deposited in DC mode at a 200 W power for Ti and a 120 W power for Pd, which resulted in a deposition rate of 3 Å/s throughout the whole deposition process.

The key issue in the design of this particular setup is that the substrate is rotating at a frequency of 40 rpm in order to obtain a homogeneous thickness of the deposit. The acquisition of the curvature measurement has then be set to the same frequency - by triggering the CCD at each rotation with a proximity sensor - in order to always measure at the same position of the wafer. As will be explained below, the homogeneity of the Pd thin film thickness has been checked by performing cross-sectional SEM measurements, and their roughness has been checked by performing AFM measurements.

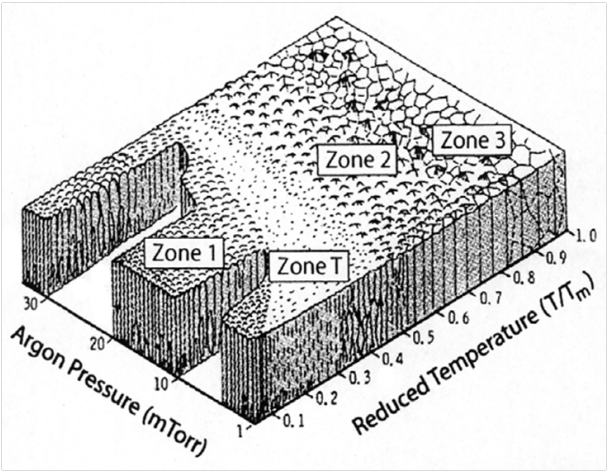

Figure 2.8: Thornton diagram showing the nanostructure of thin films deposited by sputtering as a function of the argon sputtering pressure and the deposition temperature (taken from Ref. [205]). Zone 1: porous columnar grains. Zone T: densely packed fibrous grains. Zone 2: well-defined, dense columnar grains. Zone 3: recrystallised structure consisting of equiaxed grains.

As the sputtered Pd films have all been deposited at room temperature in this work (T/T_m = 0.16, where T_m is the Pd melting point [206]), and according to the well-known Thornton diagram [205], shown here in Fig. 2.8, the low surface mobility of the atoms at such a deposition temperature does not allow for grain boundary migration and recrystallisation and therefore can be expected to result in the formation of nanocrystalline films with columnar grains. The

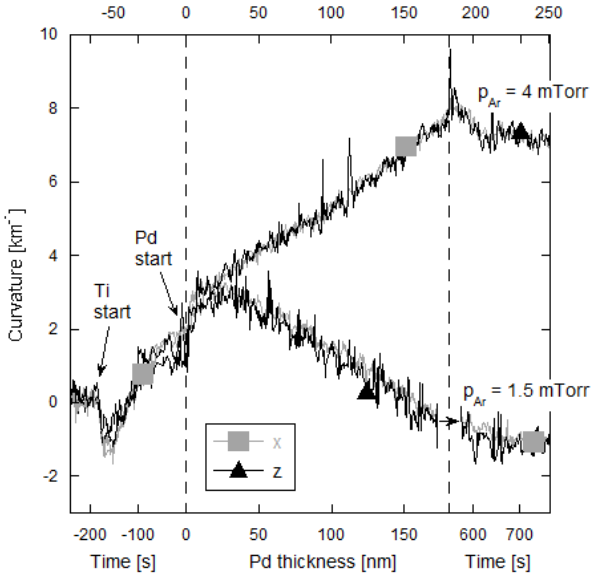

Figure 2.9: Evolution of the wafer curvature in the x and z directions as a function of time (before and during Ti layer deposition, as well as after Pd deposition) and Pd thickness (during Pd deposition) using 2 different argon sputtering pressures. A positive (convex) curvature is indicative for compressive stress, and for an increase of the distance between the laser spots on the CCD (see curvature stress in Fig. 2.5).

growth-induced stress in the deposit was varied by changing the argon sputtering pressure (p_{Ar}). It can indeed be expected that the lower the sputtering pressure, the higher the mean free path and therefore also the impact energy of sputtered atoms arriving at the surface of the deposit. This will in turn result in an increased compressive component of the growth stress in the film [207], and thereby in a convex wafer curvature. This is confirmed in Fig. 2.9, which shows the wafer curvature in the x and z directions as a function of time (before and during Ti layer deposition, as well as after Pd deposition) and Pd thickness (during Pd deposition). An initial baseline curvature measurement was first carried out before the Ti layer deposition at p_{Ar} = 3 mTorr for all specimens. The stress in the Ti film is slightly tensile during the first stages of deposition, and then becomes compressive after the deposit has turned from isolated aggregates to a continuous layer [208]. The growth-induced stress in the Pd layer is slightly compressive in the first tens of nanometers, and then reaches a constant value given by the constant slope of the stress*thickness vs. thickness curves (see Eq. (2.2)). Both the sign and magnitude of the latter is

indeed observed to strongly depend on the value of p_{Ar} used during Pd deposition. A fine control of p_{Ar} then enables to adjust accurately the internal stress in the Pd deposit, as shown in Fig. 2.10. The maximum error associated with the calculation of the internal stress is 10 MPa. Fig. 2.9 also shows that the internal stress in the deposit is biaxial, as expected.

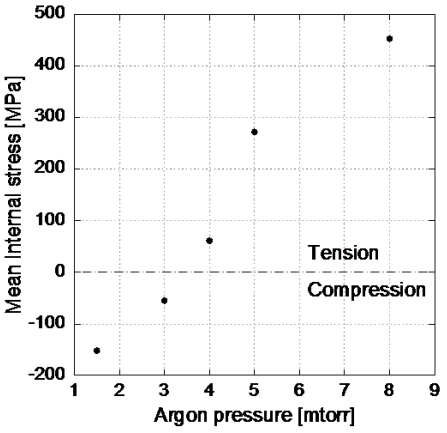

Figure 2.10: Evolution of the mean internal stress in the Pd deposit as a function of the argon sputtering pressure.

2.2.5 Application to thin film hydriding

The original experimental setup developed and used in this thesis work to study the hydriding kinetics of the Pd films from chapters 3 and 4 is shown in Figs. 2.11 and 2.12. The curvature measurement system is the same as the one described in previous section, except that since the specimen offers a much smaller surface than a whole wafer, a 1D array of laser beams is used. However, this choice is not an issue as the stress in the film is biaxial as long as the assumptions of Stoney's equation are valid. 5 laser beams beams are used, and the MDS is calculated with 4 beam spacings. The calibration factor $2L/\cos\alpha$ has then been calculated in the vertical direction, i. e. perpendicular to the plane of Fig. 2.12. Its value is 1.336 m for this hydriding setup.

The vacuum chamber is connected to a pumping system - involving a primary, rotary pump (type Balzers DUO 2.5, pumping speed: 2500 l/h for N_2 at 1 atm) and a diffusion pump (type Balzers DIFF 900, pumping speed: 450 l/s for N_2 at 10^{-4} Torr) - that enables base pressures on the order of 10^{-6} mbar. After pumping down, ultra-pure Ar/H_2 gas mixtures (Alphagaz grade

Figure 2.11: Photograph of the hydriding setup. Upper part: multi-beam optical sensor and vacuum/gas inlet control panel. Lower part: Vacuum chamber.

from Air Liquide) are introduced into the chamber to instantaneously impose a desired total pressure (50 - 760 Torr). The latter is continuously measured by two electronic gauges and one back-up manometer (Alcatel ACC 2009, ASD 2001 and BD 121, total measurement pressure range: $5 \cdot 10^{-9}$ - 1100 mbar). The composition of the gas mixtures used in this thesis work is Ar/H_2 (10%, 1% and 100ppm H_2), which allows to further adjust the accessible range of hydrogen partial pressures (p_{H_2}) in the chamber. The experiments performed with this setup can only be carried out at room temperature. Let us note here that this limitation has been solved in the course of this thesis by adapting the annealing setup to hydriding experiments, as will be explained in next section.

Our cantilevers - prepared as explained in previous section - were clamped in the vacuum chamber as illustrated in Fig. 2.13, with a steel clamping system controlled by two steel screws. The array of laser beams was reflected off the cantilevered specimens far enough from the clamp, i.e. at a distance from the clamp equal to at least the cantilever width, according to Saint-Venant's principle [209].

Fig. 2.14 shows a typical result for the evolution of the curvature change as a function of time, as obtained with our in-situ high resolution curvature

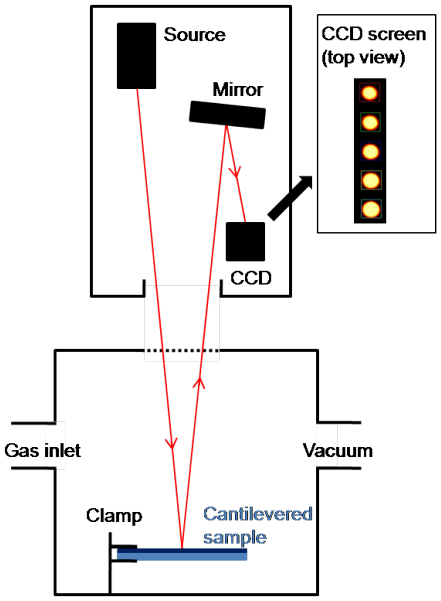

Figure 2.12: Schematic representation of the hydriding setup (not to scale). The red lines represent the trajectory of the laser beams. A top view of the CCD screen is also provided, showing the reflected laser spots.

measurement set-up during a complete hydriding/dehydriding cycle at p_{H_2} = 10.2 mbar. After an initial baseline curvature measurement in high vacuum during the first 164 sec, a Ar/(H_2 1%) gas mixture was introduced in the chamber to instantaneously generate the desired p_{H_2}. The resulting interaction of H with the Pd layer leads to a constrained volume expansion of the thin film system, which in turn induces changes in the specimen curvature as a result of compressive internal stresses developing in the Pd film. The curvature signal thus starts to increase rapidly and gradually reaches a constant value. The stress distribution in the specimen is as schematically illustrated in Fig. 2.1 - thereby giving rise to a convex wafer curvature - which means that the distance between each pairs of laser spots on the CCD screen increases, as suggested by the specimen illustrations in Fig. 2.2. When this constant value is reached, one can consider that chemical equilibrium is established between the gaseous H_2 available in the chamber and the atomic hydrogen stored inside the Pd film. After 1743 sec, the gas mixture was then pumped out of the chamber, resulting in a gradual decrease in the curvature signal as a result of room temperature dehydriding. The starting objective of this thesis work was the understanding of the kinetics and thermodynamics of such a hydriding cycle. This analysis will be explained and discussed in the next chapters.

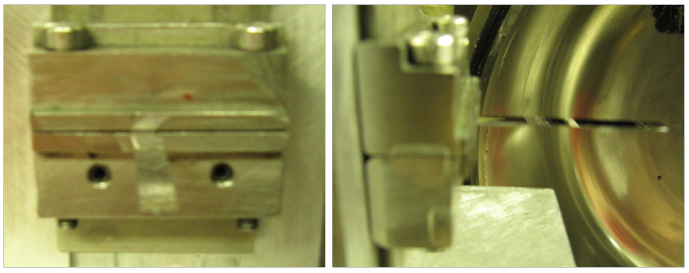

Figure 2.13: Front and side views of the clamping of our cantilevered specimens in the hydriding setup.

Reference experiments have also been performed on the same supporting substrate, but without Pd and Ti films. An example of such a blank experiment is also included in Fig. 2.14 for the same hydriding conditions (p_{H_2} = 10.2 mbar) as for the Pd thin film specimen. Those tests revealed, especially at near-atmospheric total chamber pressure, a small instantaneous curvature change when introducing the gas mixture. This curvature fully disappeared when the gas mixture was pumped out of the chamber again. A similar instantaneous curvature step is also visible on the Pd-coated specimen in Fig. 2.14 upon introducing the gas mixture. Its origin was firstly believed to reside in a slight change in the refractive properties of the chamber volume once filled with gas (especially at near-atmospheric conditions), thereby slightly changing the optical path length L (cfr. Eq. (2.7)). But this effect should be two orders of magnitude smaller than what is observed in Fig. 2.14, taken into account the fact that the refractive indexes of argon and hydrogen [202] are very close to the refractive index of air [203]. It is rather believed that, beside the very small change in the optical path length, the laser spots are instantaneously translated on the specimen, on the optical window of the vacuum chamber, on the mirror and on the CCD screen. The surfaces of these components are not perfectly homogeneous, especially the Pd surface which may have some rough of dirty zones. This type of imperfections may lead to a small translation of the CCD signal, as explained above. This explanation fits better with the fact that this effect is not always observed, and may lead to a positive or negative shift of the MDS data. As this curvature change is instantaneous and reversible, it can be easily corrected by systematically subtracting the curvature data from this artificial curvature step during a hydriding cycle (baseline correction). Moreover, as the effect is constant during the entire hydriding cycle, it does not affect our results. It can also be noted that this change is on the same order of magnitude as the curvature noise typically recorded on the equilibrium compressive stress plateau (cfr. Fig. 2.14).

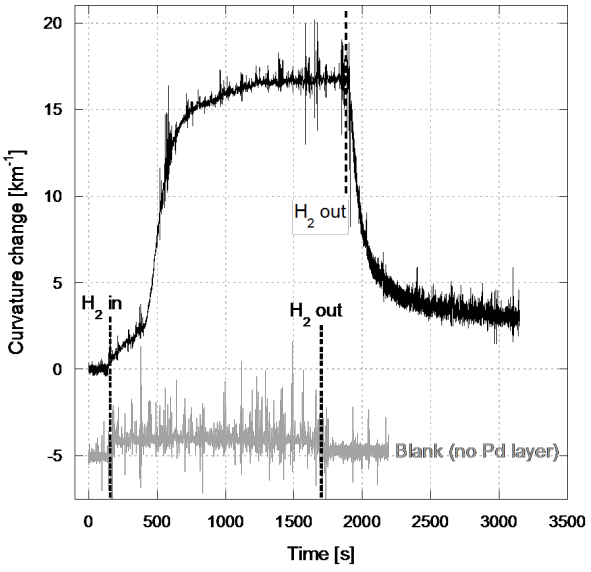

Figure 2.14: Typical evolution of the curvature change as a function of time during a hydriding/dehydriding cycle on a cantilevered Pd thin film specimen (p_{H_2} = 10.2 mbar). Also included are results from a blank experiment, carried out on a cantilever without Pd-film exposed to the same hydrogen partial pressure (results for the latter have been arbitrarily shifted down for clarity).

2.2.6 Application to thin film annealing

As the objective of chapter 5 is to study the effect of our Pd thin films microstructure on the hydriding kinetics and thermodynamics at constant internal stress level, a specific annealing experimental setup has been designed, installed and tested during the second half of the thesis, relying on the knowledge and expertise gained earlier. A photograph of this setup is provided in Fig. 2.15. The Pd thin films which have been used in this context have been deposited by DC magnetron sputtering at room temperature, and can therefore be expected contain a high concentration of crystalline defects[5] (cfr. Fig. 2.8). The annealing setup has then been created in order to be able to remove part of these defects while measuring the subsequent internal stress change in real time. The hydriding kinetics and thermodynamics of such an annealed specimen can therefore be compared with these of an as-deposited specimen with the same internal stress level.

[5]This expectation will be confirmed in next chapter.

Figure 2.15: Photograph of the annealing setup. Center: Vacuum chamber and furnace. Upper part: multi-beam optical sensor. Left part: furnace control panel. Right and lower right parts: vacuum pumps and gas inlets.

A schematic representation of the annealing setup is shown in Fig. 2.16. As one can conclude from Fig. 2.12, the geometrical configuration of the in-situ curvature measurement is the same as for the hydriding setup described in previous section. Moreover, the optical distance of the laser beams - as well as their angles of incidence and reflection - have also been kept the same, which led to the same value of the calibration factor ($2L/\cos\alpha = 1.336$ m).

Here, the vacuum chamber is a T-shaped quartz tube connected to a pumping system from Vacotec SA, consisting of a primary, rotary pump and a turbo molecular pump. Base pressures on the order of 10^{-6} mbar can be reached in the tube in about 20 minutes. The pressure in the chamber is measured with two electronic gauges (Alcatel ACC 2009 and ASD 2001, total measurement pressure range: $5 \cdot 10^{-9}$ - 1100 mbar). The furnace is from H & C SPRL. As the quartz tube and the pumping system, it has been specifically designed for this annealing setup. It has the shape of an octogonal right prism, and its eight resistances are circularly displayed around the center of its bases, where two circular holes allow to introduce the quartz tube. A third circular hole allow the third extremity of the tube to be inserted in the upper part of the ceramic shield of the furnace, so that the laser beams only travel through vacuum and

room temperature air. An insulating foam is used to prevent the heat from escaping from the space left by these 3 holes.

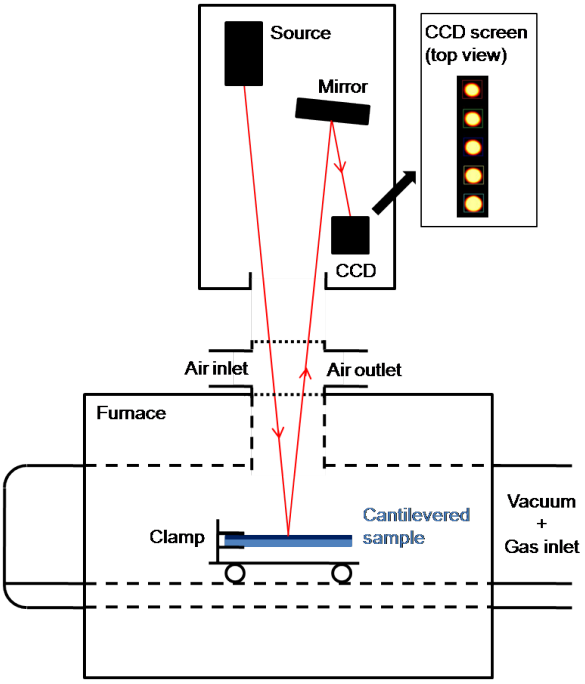

Figure 2.16: Schematic representation of the annealing setup (not to scale). The red lines represent the trajectory of the laser beams. A top view of the CCD screen is also provided, showing the reflected laser spots.

Due to this specific furnace geometry, the heat is homogeneous in the middle of the tube - below the kSA MOS system - where the specimen is located during the experiments. Heating is possible up to 1000°C, and specific temperature profiles can be programmed by the user. A thermocouple has been installed in the middle of the tube in order to be able to measure the specimen curvature in real time. Beside its main function, which is to perform curvature measurements while heating under vacuum, this setup has also been adapted to room temperature hydriding experiments just as described in previous section, simply by adding gas entries to the vacuum system. The fact that these two types of experiments can be performed in the same setup is a real benefit regarding the experiments which will be presented in chapter 5. Indeed, part of the latter involves the successive heating and hydrogen cycling of a Pd thin film specimen, which can be performed in the present setup without having to switch the specimen from one setup to another, and with one single clamping.

The clamping of the cantilevers has been adapted to the high temperature conditions to which it can be exposed by only using quartz elements, as shown in Fig. 2.17. A quartz rail has been installed in the tube, and a quartz wagon can be moved along the tube with a quartz hook. The clamping is performed in a rectangular hole in the wagon with a small triangular piece of quartz. The user stretches on the triangle, whose basis is slightly wider than the rectangular hole height. This results in a stable clamping of the specimen, very similar in its principle to the one used with the hydriding setup, but also resistant to high temperatures and to fast temperature changes.

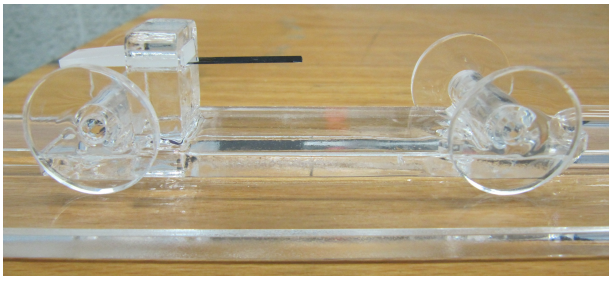

Figure 2.17: Side view of the clamping of our cantilevered specimens in the annealing setup, including the quartz wagon, the quartz rail and the quartz hook.

The major issue encountered during the first tests of this annealing setup was the high sensitivity of the curvature measurement regarding convection phenomenons. At the very first stages of the development of this setup, the tube was a simple cylinder and the laser beams travelled through vacuum, heated air and room temperature air. In this configuration, important convection phenomenons took place in the furnace air as soon as the heating started. When the temperature is not homogeneous on the trajectory of a laser beam travelling in air, the laser beam trajectory changes because the refractive index of air is influenced by the temperature [204]. At the onset of heating, the laser beams then started to oscillate independently with an important amplitude, and the subsequent noise was so important that no curvature measurement was possible. A T-shaped tube has then been designed in order to prevent the laser beams from travelling through the furnace air. But as the whole tube is heated during a thermal cycle, its optical window is also heated, as well as the air next to it. As can be seen in Fig. 2.18, the resulting convection effects are different than those that occurred with the initial cylindrical tube. These do not make the measurement impossible right from the beginning of the annealing experiment, but become more and more important in its course, and finally also render the measurement impossible. This delay of the convection phenomenon is due to the very high thermal inertia of the quartz tube (indeed, as one can

conclude from Fig. 2.19, the temperature is still slightly increasing inside the tube after the heating phase). A complete interpretation of the typical stress evolution observed in Fig. 2.18 will be provided in chapter 5.

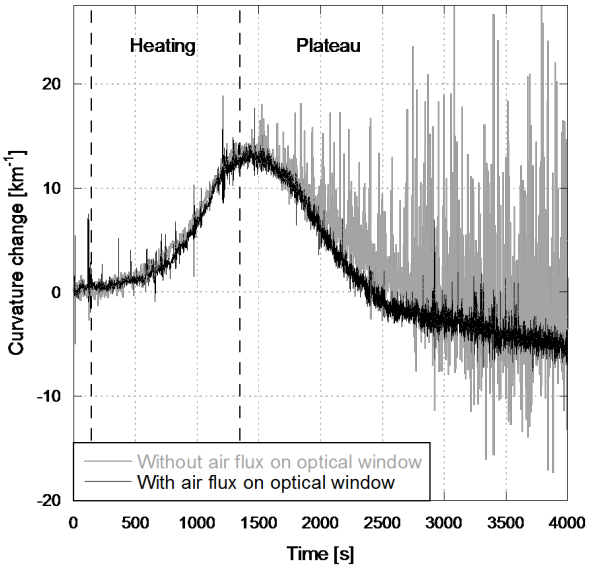

Figure 2.18: Evolution of the internal compressive stress change as a function of time during heating and high temperature maintaining of a cantilevered Pd thin film specimen at two different stages of our annealing setup development. The temperature profiles in the quartz tube are shown in Fig. 2.19.

This issue has finally been solved thanks to a last modification of the setup, which consisted in fixing a small steel tube on top of the furnace, above the quartz tube optical window. This tube is itself closed by an additional optical window. A continuous room temperature air flow is now imposed in this small air volume during the whole annealing cycle, so that the air above the quartz tube optical window is continuously renewed. As can be seen in Fig. 2.18, this totally eliminates the convection effect, but this also introduces a small, constant source of noise, as already suggested in Fig. 2.4. But this additional perturbation only multiplies the noise by a factor 2. To summarise, the noise is slightly smaller without air flow at the beginning of the experiment, but it is not critical for the optical measurement and it does not further dramatically increase.

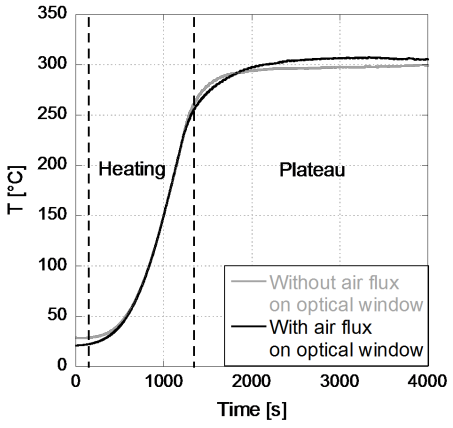

Figure 2.19: Evolution of the temperature inside the quartz tube during the experiments shown in Fig. 2.18.

2.2.7 Comparison with existing laser beam deflection techniques

The multi-beam optical sensor is not the only laser beam deflection technique used to measure stresses in thin films in-situ. Other very close techniques are used by several research groups, notably in order to study hydrogen-induced stress in thin films. Here, two other currently used laser beam deflection techniques are briefly presented and compared to our in-situ approach.

Pundt et al. developed a two-beam deflection technique [210] and applied it to the study of hydrogen-induced stress in Pd [210], Nb [126] and Y [211] thin films. As can be seen in Fig. 2.20, a first beamsplitter is used to generate two parallel laser beams, which are then reflected off the thin film sample in a vacuum chamber, and finally oriented towards two position sensitive detectors by a second beamsplitter. The authors demonstrated the good adaptability of their setup by performing both thin film deposition and hydrogen cycling experiments [210]. Conceptually, this approach is very similar to the one used in the present thesis work. The authors indeed claimed a spatial resolution on the order of 0.1 km^{-1}, very close (but slightly better) than the one obtained here. The most important difference between this setup and the one considered in this thesis is the fact that the position sensitive detectors used by Pundt et al. have a one-dimensional detection area with a sensitive length of 3 mm [210]. This does not allow to measure the sample curvature in the two directions of the plane of the deposit, and this gives less freedom of movement for the laser spots than when using a CCD detector with a sensitive area of 1 x 1 cm^2 as

the one used in this thesis. As already discussed above, one can also expect a lower robustness of the measurement when using only two beam spacings.

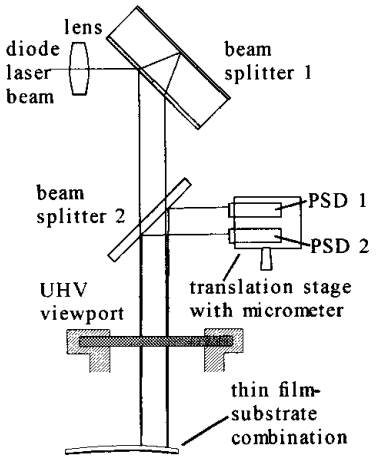

Figure 2.20: Schematic illustration of the two-beam experimental approach used by Pundt et al. to study the hydriding of thin metallic films. Reproduced from Ref. [210].

Ludwig et al. considered a very different approach [127], focused on the simultaneous testing of multiple samples rather than on an optimal resolution of the measurement. As shown in Fig. 2.21, in this case the samples are micromachined arrays of up to 16 cantilevers, fabricated by photolithography, thin film deposition and etching. The hydriding setup consists of a laser diode producing a set of parallel laser lines, which are successively reflected off the cantilevers in the vacuum chamber - each cantilever reflects at least two laser lines - projected on a semitransparent screen and detected by a CCD camera. In this case, the detection principle is closer to our case than the previous one, except that the laser spots are replaced by laser lines crossing the cantilevers along their widths. Consequently, curvature measurements are only possible in one direction (along the cantilever length). Nevertheless, this technique is very powerful as it allows to test multiple samples during one experiment (Ludwig et al. simultaneously tested Fe/Pd, Fe/Mg/Pd and Fe/Ti/Pd multilayers [127], and also performed a compositional study on Mg-Ni thin films [212]).

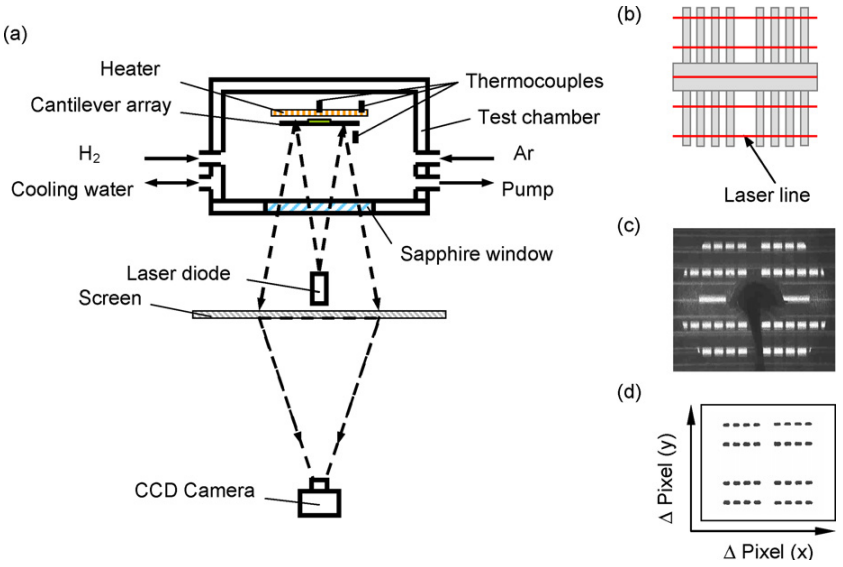

Figure 2.21: Schematic illustration of the experimental approach used by Ludwig et al. to study the hydriding of thin metallic films. (a) schematic of the gas phase apparatus, (b) schematic of laser lines projected on the array of cantilevers, (c) CCD camera picture of laser reflections from the cantilevers and (d) software-processed picture for pixel position determination. Reproduced from Ref. [127].

2.3 Characterisation techniques

In this section, the characterisation techniques used in this thesis work are presented, and their main experimental aspects are discussed. The motivations for the choice of each technique are also specified.

2.3.1 Scanning electron microscopy (SEM)

SEM microscopy was used in two ways: plane-view observations were performed in order to observe our Pd thin film surfaces (in particular to calculate the in-plane grain size), and cross-sectional observations were carried out to calculate the Pd thin films thicknesses. Two SEM microscopes were used in the course of this thesis, a Leo 982 FEG-SEM and a Jeol Ultra 55. Energies of the electron beam from 1 to 15 keV were used, depending on the magnitude of possible charging/contamination effects.

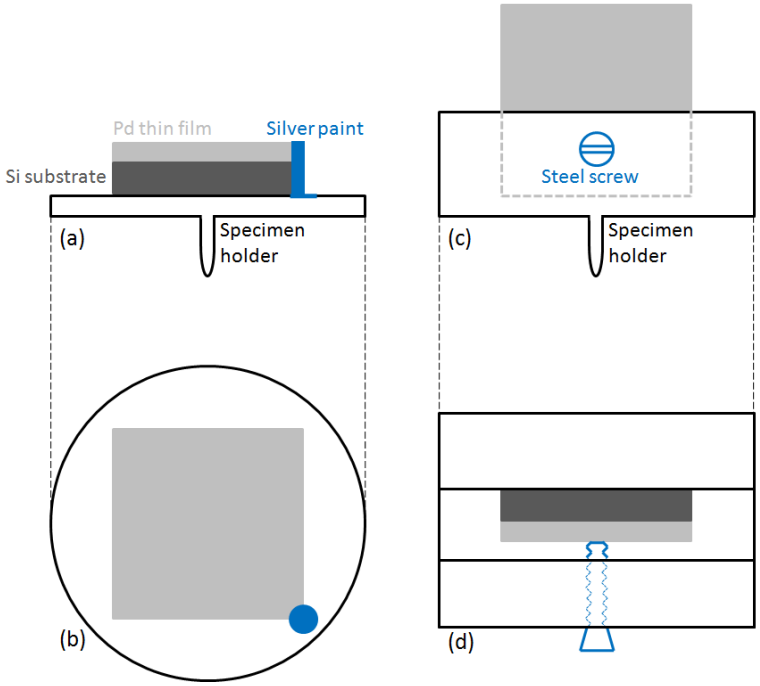

Figure 2.22: Schematic of the sample preparation for plane-view - (a) side view and (b) top view - and cross-sectional - (c) side view and (d) top view - SEM observations. In both cases, the samples are typically 1 x 1 cm^2 squares cut out of the wafers. Charging effects are avoided by using contacting elements, represented in blue.

Specimens for cross-sectional observations were prepared by propagating cracks through the monocrystalline silicon substrate with a diamond tip, leading to smooth fracture surfaces, suitable for accurate observations. The specimen holder was slightly rotated in order to mainly expose the Pd film to the electron beam and limit the charging effects on the back silicon oxide layer (the rotation was typically 0.5 - 1°). A correction factor has been applied to every thickness measured in the SEM. This factor has been defined in the following way: after having been oxidized on both sides and before metallisation, the silicon wafers used in this thesis work have been analysed with an ellipsometer. The thermal oxide thicknesses have been determined with an accuracy of 0.1% and the correction factor has been calculated for each wafer on basis of that measurement. A bridge of conductive silver paint has been applied to the specimens dedicated to plane-view observations in order to avoid any possible charging effect. Similarly, samples dedicated to cross-sectional observations are

inserted into a slit in the specimen holder, and the electrical contact is ensured by a steel screw. The specimen preparations for plane-view and cross-sectional observations are schematically shown in Fig. 2.22.

2.3.2 Inductively coupled plasma - optical emission spectrometry (ICP - OES)

ICP - OES measurements have been carried out on Pd thin films dissolved in a HCL(37%)/HNO_3(68%)/CH_3COOH(100%) acid mixture with relative proportions of 1/10/10. The ICP spectrometer is a commercial Varian 720-ES model, in which a SeaSpray nebulizer is coupled to a Twister cyclonic spray chamber to obtain a narrow distribution of the aerosol size (10 μm). The aerosol is injected in an Ar plasma formed in a standard axial torch. Quantification of emitted radiations from the plasma is performed in an optical block, made up of a grating coupled to a CaF_2 prism. A CCD camera was used for detection, measuring wavelength intensities from 167 to 785 nm. Although the signal from the 340.4 nm emission wavelength gave the most sensitive signal, the 360.9 nm (2 times less sensitive) and 229.6 nm (10 times less sensitive) emission wavelengths were also used and the three resulting signals were averaged. This approach is justified because the Pd concentration in the solution is high enough (several thousands of ppb in the worst cases). The time acquisition of this measurement is less than 1 sec. The choice of this technique was motivated by three reasons: determining the purity of the deposits, confirming the thin films thicknesses measured in the SEM and calculating the thin films densities.

Our dissolved Pd thin films - either coming from e-gun evaporated and magnetron sputtered deposits - were determined as highly pure (as expected), with no contaminant detected in concentrations exceeding 10 ppb (corresponding, in the worst case, to 0.3% of the palladium concentration).

As regards the Pd thin films thicknesses, their derivation comes from the following reasoning: if C_f is the concentration of the dissolved palladium film measured by the ICP device, V_{sol} is the volume of the solution, S_f is the film surface and ρ_{Pd} is the palladium mass density (12 g/cm^3 [206]), the Pd thin film thickness can then trivially be expressed as:

$$t_f = \frac{C_f V_{sol}}{S_f \rho_{Pd}}. \tag{2.8}$$

In order to obtain an accurate value of the thin film surface, the following relationship was considered:

$$S_f = \frac{M_s}{t_s \rho_{Si}}, \tag{2.9}$$

where M_s and ρ_{Si} are, respectively, the mass and the mass density of the substrate after the Pd thin film dissolution. The latter is assumed to be entirely composed of silicon, which is a reasonable assumption if on takes into account that the silicon oxide layers only represent 0.5% of the substrate thickness in the worst case, and that the mass densities of Si and SiO_2 are close to each other (2.33 g/cm^3 for Si and 2.18 g/cm^3 for SiO_2 [213]). The specimen mass is measured with a high precision balance and an accurate value of its thickness is obtained from the SEM observations.

One can also use Eqs. (2.8) and (2.9) in a different way, by using the Pd thin films thicknesses measured in the SEM in order to calculate the density of our nanocrystalline Pd thin films. The obtained values can be expected as slightly smaller than the bulk value because the mass density decreases with increasing fraction of crystalline defects such as grain boundaries [214]. Density measurements can therefore be an indication of the concentration of defects in our Pd thin films.

2.3.3 Rutherford backscattering spectrometry (RBS)

Compositional depths profiles have been performed on our thin film specimens by RBS. This allowed to simultaneously determine the thickness and composition of all the layers in our Pd thin film specimens, as RBS enables to extract the depth of one element as a function of the with and position shift of the peaks in the energy spectrum of the backscattered ions. These experiments have been performed in the linear accelerator TANDETRON at the LARN laboratory of Namur.

2 MeV α particles were used to bombard the films, with an incident angle of 0°. The backscattering angle was 165°, and the detector is a PIPS junction allowing for a resolution of 17 keV. The software RUMP was used to analyse the RBS spectra. Fig. 2.23 shows an example of the fitted spectrum of a Pd film specimen deposited by e-gun evaporation. As can be seen on this figure, the compositional depth profile established through the thin film system goes up to the underlying silicon substrate. Other RBS spectra revealed the presence of oxygen in the Pd layer, which enabled for a good interpretation of part of our results on the analysis of the Pd thin films hydriding kinetics, as will be explained in next chapter.

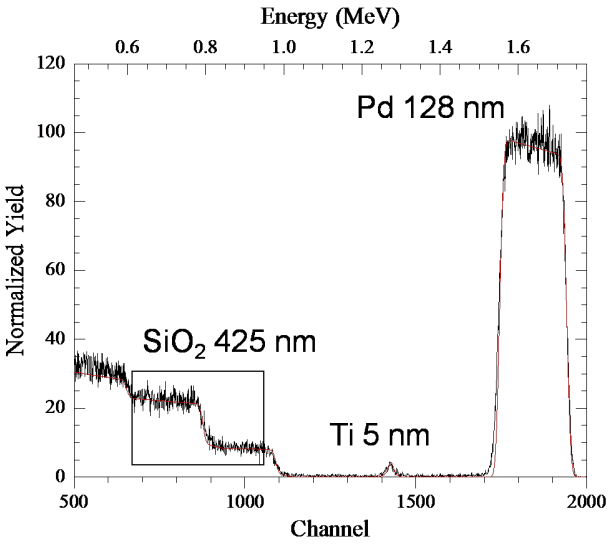

Figure 2.23: RBS spectrum of a 128 nm Pd thin film deposited by e-gun evaporation on a Si/SiO_2 substrate with a 10 nm Ti adhesion layer on top of it. A RUMP fit of the experimental is also provided (red solid line).

2.3.4 4-point probe resistivity measurements

The resistivity our Pd thin films has been measured as a function of temperature, and their temperature coefficient of resistance (TCR) has also been extracted from these measurements. These experiments have been of primary importance in the course of this thesis work, as some of our Pd thin films have been annealed in the context of the study of the effect of microstructure on the hydriding kinetics (see chapter 5). Indeed, the changes of microstructure subsequent to the heating of Pd can be interpreted by measuring its resistivity as a function of temperature [215]. Let us note here that this is also true regarding any other source of micrustructural change, such as electrical current [216].

These measurements have been carried out with a Linkam LTS 350 heating and freezing stage connected to an Autolab PGSTAT302N operating in constant-current mode (chronopotentiometry). Currents between 1 and 100 mA have been indifferently imposed, without any difference observed in the voltage evolution as a function of temperature. The voltage resolution is equal to 0.3 μV. Temperature was monitored with a TMS 94 temperature controller, and recorded with the Linksys 32 software. The distance between each contact point on the specimen was set equal to the specimen width, therefore avoiding the use of any correction factor taken into account the rectangular geometry

of the specimen and the fact that the ratio between its length and its width is ≥ 4 [217].

2.3.5 Ex-situ internal stress measurements

As the Pd thin films deposited by e-gun evaporation have not been subjected to in-situ curvature measurements like the films deposited by magnetron sputtering, a ex-situ technique has been used to determine their internal stress. As the ICP - OES measurements, this technique is highly destructive because it involves dissolution of the Pd thin film.

The cantilevers have been clamped in Epofix resin cast in a Teflon mold, and their curvature before dissolution of the Pd film has been measured with a muli-beam optical sensor. This setup, usually dedicated to thin film anodizing, is described in detail elsewhere [158]. It is adapted to such ex-situ curvature measurements because it allows to temporarily remove the specimen and its clamping from the electrochemical cell in order to dissolve the Pd film - using the same solution as for the ICP - OES measurements - and fix it back into the cell in order to measure its curvature after Pd dissolution. The internal stress in the Pd deposit is then deduced from the difference between the curvature measurements before and after Pd dissolution. Such measurement cannot be performed in-situ in the solution because of bubbling around the specimen during dissolution.

2.3.6 X-ray diffraction (XRD)

XRD diffractograms have been recorded on our Pd thin film specimens with a Bruker AXS D8 ADVANCE diffractometer, using Cu Kα radiation and recorded with an angle step of 0.02°. Although a detailed texture study of our Pd thin films is out of the scope of the this thesis work, these analyses have been relevant to some degree. The underlying motivation was firstly to perform basic texture analyses to confirm the pronounced (111) texture usually observed regarding vacuum deposited fcc thin metallic films [218–220]. Secondly, when the switch was operated from e-gun evaporated Pd thin films towards magnetron sputtered Pd thin films, questioning arose whether their texture was still the same or not. Finally, when thin Pd films with different internal stresses have been generated by magnetron sputtering for chapters 4 and 5, we also recorded diffractograms in order to check if there were significant texture differences between these deposits.

2.3.7 Atomic force microscopy (AFM)

Together with the cross-sectional SEM observations described above, several AFM measurements have been performed in order to check the roughness of the Pd thin films, using a Bruker Multimode Nanoscope 8 working in medium tapping mode. The aim of these measurement was firstly to check the homogeneity of the thickness of our specimens, and secondly to ensure that their roughness remains stable from one deposition condition to another in order to avoid any effect of the roughness on the films hydriding behaviour.

Fig. 2.24 shows an example of such measurements, performed on a Pd film deposited by sputtering with $p_{Ar} = 3.5$ mTorr. The homogeneity of the film thickness is confirmed, and the film root mean square (RMS) roughness is 1.9 nm, i.e. only 1.2% of the film thickness. Our magnetron sputtering technique indeed produces flat films with a low roughness. Moreover, Fig. 2.24 also shows another AFM measurement, performed on a Pd film deposited at $p_{Ar} = 7$ mTorr, revealing a RMS roughness of 2 nm (1.3% of the film thickness), showing that there is no roughness change as a function of p_{Ar}, as expected.

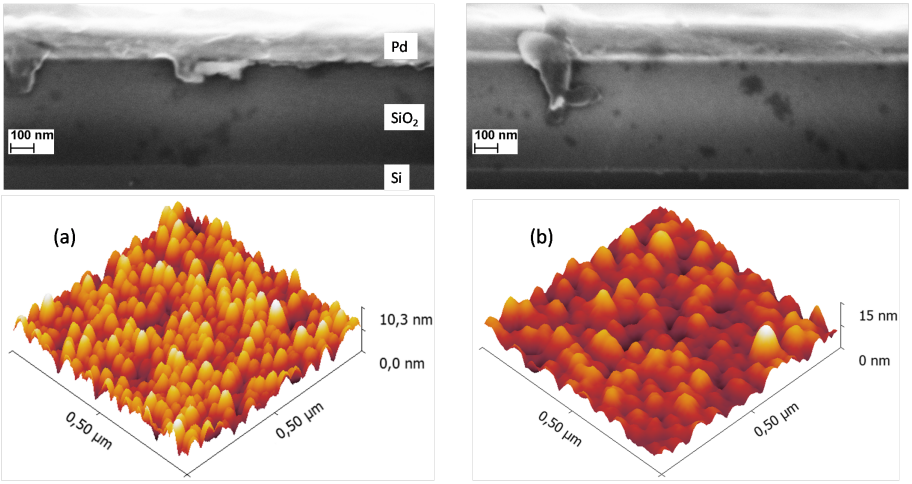

Figure 2.24: Cross-sectional SEM (up) and tapping mode AFM (down) images of Pd thin films deposited at (a) 3.5 mTorr and (b) 7 mTorr.

2.4 Conclusions

This chapter has been firstly dedicated to the presentation of the relationship between the Pd films internal stress and curvature, a key relationship for the

study of these films kinetic/thermodynamic behaviour upon hydrogen exposure. It has been shown that the hypotheses of Stoney's equation are respected in the context of this thesis work, and consequently that the stress derivation with this equation is reliable and accurate. The new in-situ high resolution curvature measurement setup has secondly been presented, as well as its application to Pd thin films deposition, hydriding and annealing. In these three cases, it has been shown that the hypotheses behind the curvature derivation from the reflected beams MDS are valid, and that the possible resolution-limiting factors are sufficiently small allow for a stable and accurate curvature measurement. In the particular case of Pd thin films annealing, it has been explained how an original experimental setup has been designed, installed and tested in the course of this thesis, and how the issues linked to the high temperature conditions of the curvature measurement - namely, the convection and clamping issues - have been successively understood and solved. Finally, the ex-situ characterisation techniques used in this work have been presented, and their use has been justified.

Chapter 3

Modelling the hydriding mechanism[1]

In this chapter, we will focus on the kinetic/thermodynamic analysis and interpretation of the data produced by the high resolution in-situ curvature measurement setup when exposing Pd films on Si cantilevers to gaseous hydrogen. We will first present the Pd films, and the characterisation results obtained on the as-deposited specimens. The hydriding cycles will then be described and basically interpreted. These first observations will third be the basis of an analysis of the equilibrium data, including the internal stress level when the equilibrium is reached between solid atomic hydrogen inside the Pd thin film and molecular gaseous hydrogen inside the vacuum chamber, i.e. thermodynamic data at room temperature, and the internal stress levels before introducing hydrogen inside the chamber and after pumping it down after one or several hydriding cycles, i.e. data relative to the reversibility of the Pd hydriding mechanism. The kinetic behaviour of the Pd thin film specimens - the core of the thesis - will then be presented and commented step by step. Finally, the batch-to-batch reproducibility of our hydriding cycles will be discussed in terms of the time between specimen deposition and hydriding.

[1] Most of the elements presented in this chapter have been published in an international peer-reviewed paper [221].

3.1 Experimental details

The Pd films addressed in this chapter come from two different batches. Both have been deposited by e-gun evaporation (keeping the same deposition parameters), but one has been stored in a dessicator during 12 months before being subjected to hydrogen cycling, and the other has been stored during 2 months only. The starting substrates were double polished, 425 μm thick monocrystalline Si (100) wafers. The latter have been oxidised by a wet oxidation process, which generated 425 nm thick SiO_2 thermal oxide layers on both sides of the wafers (measured by ellipsometry after oxidation). The Ti adhesion and the Pd layer have then been deposited on one side of the substrate.

Table 3.1: Thickness, density, grain size, (111) texture factor, average growth-induced stress and dry air exposure time of the Pd thin films studied in this chapter.

	Batch 1	Batch 2
Pd thickness [nm]	128	112
Density [g/cm^3]	11.1	11.3
Grain size [nm]	18	20
(111) texture factor [-]	38	37
Growth stress [MPa]	435	409
Dry air exposure [months]	12	2

Table 3.1 gathers, among others, the film thickness calculated from the ICP results, and further confirmed by SEM (cross-sectional) and RBS analyses. These values are close to each other, as expected[2]. The error on these values is below 1%. The densities are also close to each other, and slightly smaller than the Pd bulk density [206], as expected from a nanocrystalline metal with a high concentration of defects. One can also see that the grain sizes - measured in the SEM (plane-view) - are very close to each other as well, so that they can be considered as equal when taking into account the measurement accuracy, on the order of 1 nm. The same observation can be made as regards the (111) texture factors measured, which have been calculated from XRD diffractograms according to the following formula:

$$f_{311} = \left(\frac{I_{111}}{I_{311}}\right)_{film} \left(\frac{I_{311}}{I_{111}}\right)_{stand}, \tag{3.1}$$

[2]It will be shown further in this chapter that the difference between these two thickness values is small enough to exclude any effect on their hydriding kinetics.

where the left term is the ratio between the (111) and (311) peak intensities measured on the Pd films by XRD and the right term refers to standard intensity ratios, taken from Ref. [222]. The (111) texture factor has been defined this way because no secondary (200) peak was detected in the diffractograms. We have thus chosen the third peak in terms of standard intensity. The growth-induced stresses - obtained by ex-situ curvature measurements before and after Pd dissolution, with an associated resolution of less than 1% - are also close to each other[3]. The only parameter which has been intentionally set as different from one batch to the other is the dry air exposure time, in order to further study the batch-to-batch reproducibility.

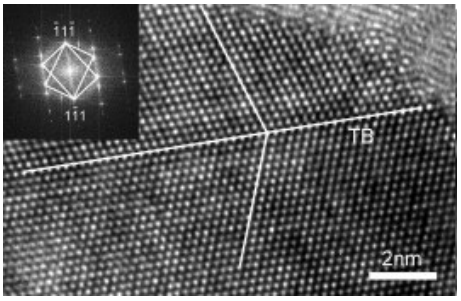

Figure 3.1: High-resolution TEM image of one twin boundary in a Pd thin film deposited by electron beam evaporation. Note the perfect coherency of the twin/matrix interface. Reproduced from Ref. [223].

Regarding the defects present in these Pd films, Wang et al. performed a high-resolution TEM analysis of specimens from the present set of batches [223], and confirmed the high concentrations of grain boundaries. Nanoscale growth twins have also been observed, as can be seen in Fig. 3.1.

All the experiments presented in this chapter have been performed at room temperature. Although hydriding experiments are reported here for p_{H_2} values up to 100 mbar, the quantitative kinetic analysis performed in this chapter is limited to the low p_{H_2}-range [2 - 10 mbar]. The results produced at higher hydrogen partial pressures have been analysed to extract equilibrium data only. As will be explained below, this confirmed that the α to β hydride phase transition - which would have unnecessarily complicated the kinetic analysis - is avoided by staying in this interval. The curvature data, obtained with Eq. (2.5) from the produced MDS data, has been converted to mean internal stress data with Eq. (2.4) (see previous chapter).

[3]Similarly, the analysis performed in Chapter 5 will show that no difference can be detected in the hydriding kinetics when comparing such close growth stress values.

3.2 Hydriding cycle

As already shown in Fig. 2.14, performing a complete hydriding/dehydriding cycle at room temperature consists in successively clamping the cantilever inside the vacuum chamber, reaching high vacuum conditions (on the order of 10^{-6} mbar), performing a baseline curvature measurement, introducing gaseous hydrogen inside the chamber, waiting for equilibrium (plateau in the curvature/stress data), pumping the gas out and waiting for equilibrium again. Fig. 3.2 shows such a hydriding cycle (performed at $p_{H_2} = 6$ mbar), in which the curvature data has been converted to the absolute internal stress inside the Pd thin film.

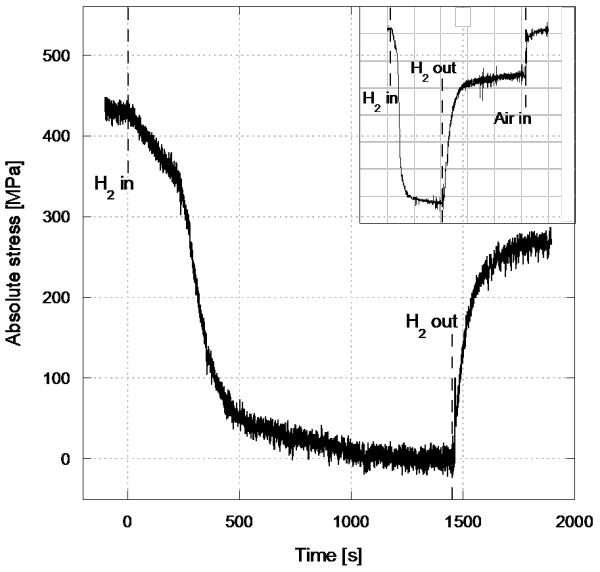

Figure 3.2: Evolution of the absolute internal stress as a function of time during a hydriding cycle recorded at $p_{H_2} = 6$ mbar. Inset: hydriding cycle recorded at $p_{H_2} = 5.5$ mbar, including venting with air after dehydriding in vacuum.

The absolute internal stress is obtained by converting the curvature data to compressive stress change data with Eq. (2.4). Indeed, as already discussed in previous chapter, a positive curvature signal corresponds to an increase of the distance between the laser spots on the CCD screen and therefore to a compressive stress in the Pd film, from which the laser beams are reflected. Secondly, the sign of the curvature data is changed in order to respect the usual

convention in continuum mechanics stating that a tensile stress is positive and a compressive stress is negative. Finally, the growth-induced stress existing in the Pd film before the hydriding cycle - which has been previously obtained by ex-situ curvature measurements on a specimen cut out from the same wafer - is added to the internal stress data in order to obtain the absolute internal stress in the film. The latter is obviously the most relevant for interpretation. Mathematically, if σ_0 is the Pd thin film growth stress (and then $\Delta\sigma_f = \sigma_f - \sigma_0$), the absolute internal stress can be derived from the following alternative form of Eq. (2.4):

$$\sigma_f = \sigma_0 - \frac{Y_s t_s^2}{6 t_f} \Delta\kappa. \tag{3.2}$$

The stress evolution shown in Fig. 3.2 is now discussed in detail. After an initial baseline curvature measurement in high vacuum, the Ar/H_2 gas mixture was instantaneously introduced in the chamber. As a result of the constrained volume expansion during Pd-H interaction, the internal stress in the Pd thin film increases rapidly in the compressive direction and gradually reaches a constant value. The gas mixture was then pumped out of the chamber, resulting in a gradual decrease of the internal stress as a result of room temperature dehydriding.

As to the latter, it appears that the internal stress does not go back to its initial value when the gas mixture is pumped out of the vacuum chamber. In other words, a residual[4] compressive hydriding-induced stress is systematically observed when leaving the specimen under vacuum after hydriding. The origin of this irreversible part of hydriding under vacuum can be interpreted by performing an additional operation at the end of the hydriding cycle, i.e. by venting the vacuum chamber with ambient air. This operation is shown in the inset of Fig. 3.2, with an additional hydriding cycle recorded at $p_{H_2} = 5.5$ mbar. It is clearly seen that the residual stress is fully released when the specimen is brought into contact with ambient air. This observation indicates that the residual stress observed after dehydriding in vacuum can be attributed to a small residual H-concentration in the Pd lattice, the removal of which can be achieved by venting with air so that a fully reversible hydriding cycle is finally obtained. This interpretation is of primary importance regarding the kinetic analysis that will be performed in the course of this chapter. Another interpretation would have been a plastic interpretation of the film due to the H-induced deformation. In next section, additional evidence will show that this second interpretation is not realistic.

[4] In this thesis work, the residual stress is defined as the difference between the absolute stress after dehydriding in vacuum and the absolute stress before bringing the specimen into contact with hydrogen, i.e. the growth-induced stress.

From Fig. 3.2, two distinct kinetic regimes can be distinguished from the two apparently linear regions of the stress-time curve at the beginning of the hydriding cycle. We anticipate that these two slopes reveal the presence of two rate-limiting steps in the course of a single hydriding cycle. A third regime is resolved in Fig. 3.2 as well, characterised by a gradual decrease of the hydriding rate with time until a constant equilibrium stress level is reached. The latter can be associated with chemical equilibrium between atomic H inside the Pd film specimen and gaseous H_2 available in the chamber. Such a characteristic hydriding behaviour with three kinetic regimes has been observed over the entire p_{H_2} interval considered for our kinetic analysis, and will be analysed in detail in this chapter.

3.3 Hydriding thermodynamics

This section is firstly dedicated to the study of the equilibrium relationship between molecular hydrogen in the vacuum chamber and atomic hydrogen inside a Pd film. The analysis of this relationship will enable, among others, to identify the α to β phase transition of the Pd hydride at room temperature. This transition will further be avoided in the context of our kinetic analysis. The hydriding reversibility will then be analysed and discussed. It will allow the identification of the hydriding-induced plasticity phenomenons taking place at high hydrogen partial pressures, and exclude the latter as well from our kinetic analysis. Generally speaking, this issue is very important regarding applications involving metallic hydrides.

3.3.1 Hydriding equilibrium

Figure 3.3 shows the absolute stress levels corresponding to the equilibrium plateau during hydriding experiments up to $p_{H_2} = 92$ mbar. From these results, the $\alpha \rightarrow \beta$ phase transition of Pd-hydride can be identified to start at room temperature between 10 and 20 mbar, in agreement with earlier equilibrium hydriding studies on Pd thin films [89]. As a result, the equilibrium stress levels reached in the p_{H_2}-range that will be considered in the kinetic study in next section (2-10 mbar) correspond to hydrogen concentrations located in the α phase region of the Pd-H system.

For a quantitative kinetic analysis, a link between the bulk H/Pd atomic ratio n and the measured internal compressive stress change $\Delta\sigma$ in the Pd films needs to be established. This can be done by linking $\Delta\sigma$ to the relative volume change $\Delta V/V$ during hydriding [224]:

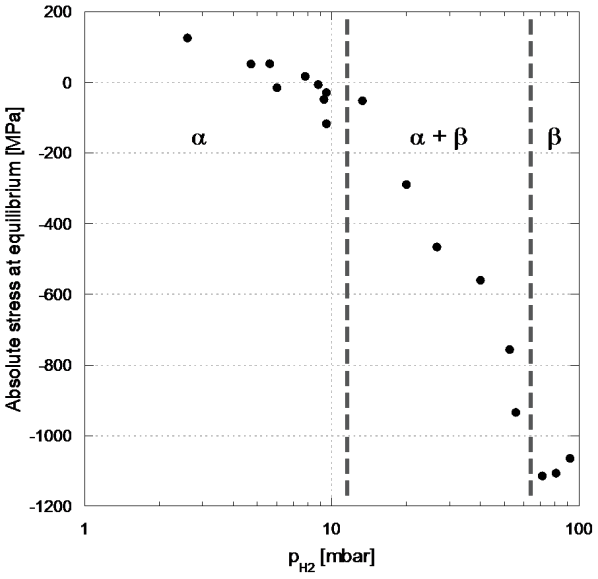

Figure 3.3: Equilibrium absolute stress as a function of p_{H_2}. The average initial tensile growth stress in the as-deposited films was 409 ± 2 MPa

$$\Delta\sigma = \frac{E_f}{3(1-\nu_f)}\left(\frac{\Delta V}{V}\right) = \frac{E_f}{3(1-\nu_f)}\left(\frac{\Delta v}{\Omega_{Pd}}\right) n \equiv Qn, \tag{3.3}$$

where E_f and ν_f are, respectively, Young's modulus and Poisson ratio of the Pd film. The ratio between $\Delta V/V$ and n is equal to $\Delta v/\Omega_{Pd}$, where Δv is the characteristic volume change per hydrogen atom, and Ω_{Pd} is the mean atomic volume of a Pd atom. This ratio, describing the lattice expansion due to hydrogen uptake, has been the object of many studies in the past, from which a value of 0.19 ± 0.01 can be derived [225]. Eq. (3.3) then links the measured hydriding-induced internal stress changes $\Delta\sigma$ to the bulk H/Pd atomic ratio n via some mechano-physical constants, which for convenience are grouped together into a single proportionality factor Q.

It should be noted that a possible complicating factor in Eq. (3.3) is the occurrence of the α to β phase transformation during Pd hydriding, each phase having its own characteristic lattice expansion behaviour so that the measured stress change will depend on the exact proportions of the α and β phases. Although the value of 0.19 has been suggested by Peisl [225] for the entire compositional range in the Pd-H system, the collected data are too scarce to state that there is no effect of the α to β phase transformation on the lattice

expansion. However, as already indicated in Fig. 3.3, this complicating factor does not need to be dealt with in our kinetic study because the α to β phase transformation is avoided by limiting the p_{H_2}-range below 10 mbar.

Eq. (3.3) also makes the explicit assumption that the deformation resulting from the hydriding-induced internal stress is elastic [128]. Thanks to the relatively high initial tensile growth stress of our as-deposited Pd films in this chapter, and the fact that the kinetic studies are limited to the α phase region, this condition is verified as well. In Fig. 3.2 for instance, it is seen that the equilibrium compressive stress change of the hydriding cycle is about 435 MPa. Taking into account the initial tensile growth stress level of 435 MPa in the as-deposited Pd film, this leads to an almost zero equilibrium stress value. Similarly, Fig. 3.3 shows that, over the entire α phase region, the maximum absolute value of the equilibrium stress level is smaller than 200 MPa, therefore well below the Pd yield stress measured in previous studies on nanocrystalline specimens, in tension [107] or in compression [226]. One can also take into account the effect of the small hydrogen content in the films, which would further increase the yield stress [112]. Plastic deformation of the Pd films during hydriding in the α phase region can therefore be reasonably excluded. As a result, the time derivative of the hydriding curves obtained experimentally can be considered as directly proportional to the hydriding velocity dn/dt. These observations also confirm our earlier finding that the residual stress observed in 3.2 after dehydriding in vacuum can be attributed to a small residual H-concentration in the Pd lattice.

Based on the above considerations, we can already use Eq. (3.3) to determine Sieverts' constant K_s from the experimental equilibrium stress data in the α phase region of Fig. 3.3. Indeed, when linearising these data as a function of ${p_{H_2}}^{1/2}$, according to Sieverts' law in α-PdH [57]:

$$(\Delta\sigma)_{eq} = Qn_{eq} = Q\frac{\sqrt{p_{H_2}}}{K_s}, \tag{3.4}$$

with n_{eq} the equilibrium atomic hydrogen concentration in the bulk. The slope of the linear fit shown in Figure 3.4 yields a K_s value equal to 3.3 ± 0.7 $\text{atm}^{1/2}$ (using E_{Pd} = 121 GPa and ν_{Pd} = 0.39 [106]]). Room temperature K_s values for Pd hydriding have been reported in a study by Bucur [62] to be in the range 2-20 $\text{atm}^{1/2}$, the higher value corresponding to a perfect crystal structure (i.e. well-annealed bulk palladium specimens) and the lower one corresponding to a relatively large concentration of structural defects, typical for as-evaporated thin Pd films [62]. Our own value is therefore in excellent agreement with the data from Bucur, recognising that our evaporated Pd thin films probably contain a large amount of defects resulting from the deposition process (mainly

grain boundaries and twins according to our characterisation work and to the work of Wang et al. [223]).

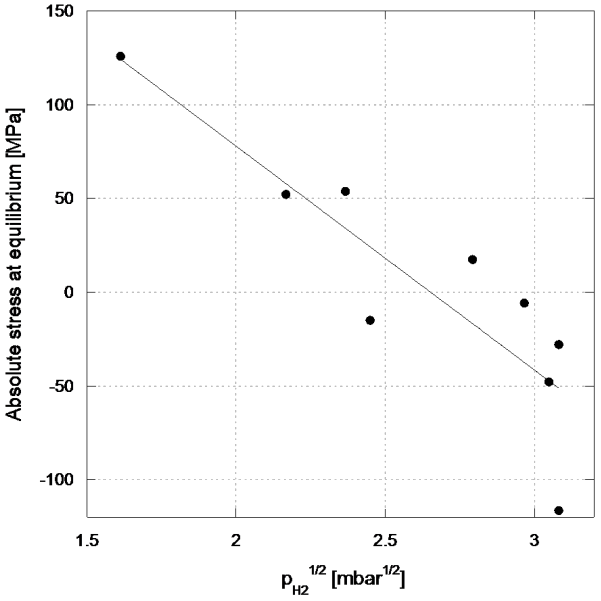

Figure 3.4: Equilibrium absolute stress as a function of ${p_{H_2}}^{1/2}$ in the α phase region.

3.3.2 Hydriding reversibility

As already discussed in the previous section, the internal stress in the Pd films does not go back to the initial value after dehydriding under vacuum. This initial value can be recovered by venting the chamber with ambient air (see Fig. 3.2), which shows that the origin of this residual compressive hydriding-induced stress is a small residual H-concentration remaining under vacuum in the Pd thin films. This interpretation can be correlated to the high level of defects observed in the present Pd films through the calculation of Sieverts' constant. Indeed, the thermodynamics of hydrogen trapping by crystalline defects such as voids, cracks and dislocations is very different from the thermodynamics of hydrogen in regular lattice sites [227].

The previous identification of the α to β phase transformation in the Pd films excludes any effects related to this transformation in the kinetic study. The magnitude of the internal stress observed when performing hydriding ex-

periments in the α phase also enable to reasonably exclude plasticity effects. However, this assumption can be confirmed by studying the residual hydriding-induced stress level in more details.

A first, insightful type of experiment can be performed by subjecting a Pd covered cantilever to multiple hydriding/dehydriding cycles. Such an experiment is shown in Fig. 3.5, where five successive hydriding cycles have been performed while decreasing the hydrogen partial pressure from cycle to cycle. In that figure, it appears that the residual stress level remains constant from cycle to cycle, despite the decreasing hydrogen partial pressure. This indicates that the irreversible part of the hydriding mechanism occurs only during the first cycle. This observation is in agreement with our interpretation of the irreversible part of hydriding, in that the residual atomic hydrogen that cannot be released by pumping down the gas mixture after the first cycle is still not released after the four other cycles, and also stays constant from cycle to cycle. Furthermore, regarding the possibility of plasticity mechanisms taking place in the Pd film, we can exclude it for two reasons. Firstly, the equilibrium absolute stress is below the Pd theoretical yield stress in each cycle [226], according to Fig. 3.3. And secondly, if plastic deformation had taken place during each cycle, the residual stress level would not have remained the same from cycle to cycle.

The Pd films - as long as one stays in the α phase - can thus sustain multiple hydrogen cycling without degradation. Therefore, such in-situ observations made during multiple cycling experiments provide a unique insight in the reversibility and long-term stability of applications involving metallic hydrides.

A second type of approach can be used to exclude plasticity effects in our kinetic analysis, i.e. observing hydriding cycles performed at higher hydrogen partial pressures in order to identify these plasticity effects. Without having been the object of any in-depth kinetic analysis, such experiments have therefore been performed, firstly in order to identify the α to β phase transformation in our Pd films. But the analysis of the residual stress level after pumping down also provides insightful information.

Indeed, the stress evolution shown in Fig. 3.6 can be compared to Fig. 3.2 in some points. The cycle has been performed at $p_{H_2} = 55.6$ mbar, well into the $\alpha + \beta$ phase region according to Fig. 3.3. As the absolute stress level at equilibrium is -935 ± 1 MPa, one can expect plasticity phenomenons to take place, as the nanocrystalline Pd compressive yield stress has been previously measured to be on the order of 1 GPa [226]. After pumping down, the dehydriding kinetic profile is similar to what is observed when performing such experiments in the α phase, but as opposed to the latter, the residual internal stress level after dehydriding in vacuum is tensile and different than

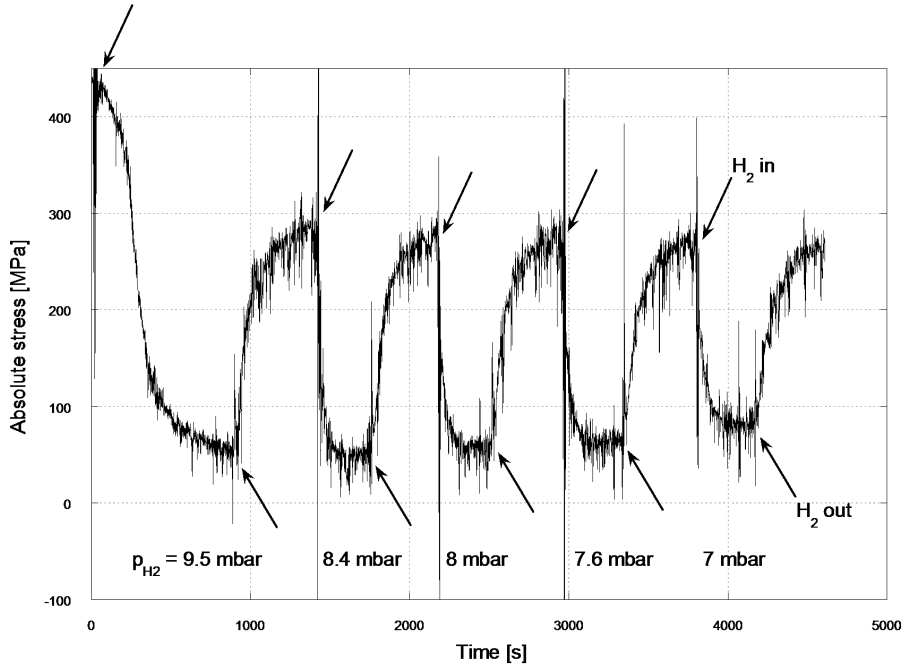

Figure 3.5: Evolution of the absolute stress during five hydriding/dehydriding cycles with decreasing hydrogen partial pressure.

the initial level. This residual stress cannot be only attributed to the presence of residual hydrogen in the Pd thin film, which would lead to a residual compressive stress. We attribute this behaviour to plasticity effects. This tensile residual stress has systematically been observed when performing experiments in the pressure range corresponding to the $\alpha + \beta$ and β regions of the Pd hydride (see Fig. 3.3). These hydriding-induced plasticity effects do not exclude the presence of residual hydrogen remaining in the Pd film under vacuum, as suggested by the stress evolution observed after venting in Fig. 3.6.

The hydriding and dehydriding kinetics observed in Fig. 3.6 also suggest different kinetic behaviours as the ones typically observed when performing hydriding/dehydriding cycles in the α phase region of Pd-H. More specifically, two "overshoots" in the curvature signal are observed, one before reaching the equilibrium plateau after introducing the gas mixture into the chamber, and a second one before reaching the residual stress plateau. We believe that these phenomenons are related to the large stress/strain undergone by the Pd lattice at such high hydrogen partial pressures. More specifically, looking at the de-

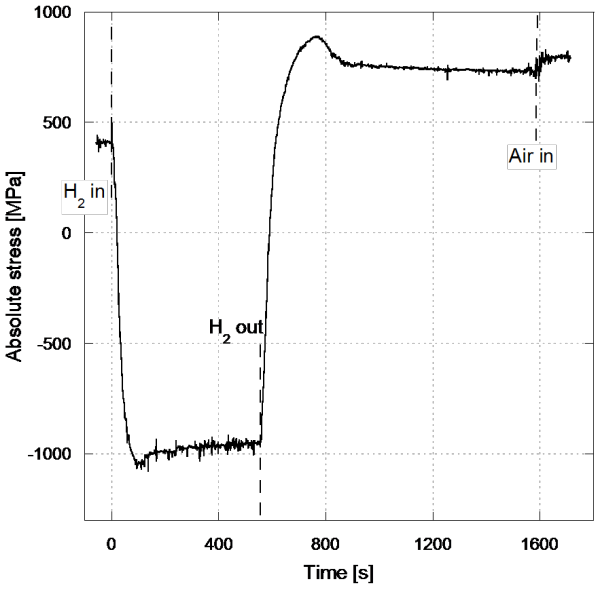

Figure 3.6: Evolution of the absolute internal stress as a function of time during a hydriding cycle recorded at $p_{H_2} = 55.6$ mbar.

hydriding behaviour from a purely mechanical point of view shows that the Pd thin film is undergoing a significant back stress - illustrated by the "overshoot" observed before the residual stress plateau under vacuum - which could be attributed to the so-called Bauschinger effect. This well-known effect, commonly observed in thin films [228], can be described as follows: after a material has been deformed plastically in a given direction, a reduction in the yield stress in the reverse direction is observed, with an associated plastic strain recovery. Rajagopalan et al. studied this strain recovery mechanism in thin metallic films, and attributed it to microstructural variations such as the size and orientation of individual grains, which exhibiting different yield stresses [229]. When the grains exhibit such mechanical heterogeneities, the stress distribution becomes inhomogeneous when the material deforms plastically. This results in local residual stresses upon loading in the reverse direction, which in turn favour plastic flow in the reverse direction, and hence strain recovery. In our Pd thin films, which are strongly (111) textured and where the grain size is relatively homogeneous, other sources of mechanical heterogeneity can be responsible for the strain recovery. Colla et al. recently investigated the strain hardening behaviour of Pd thin films [109], and suggested that a possible source could be the number of growth twins present in each grain (i.e. the more twins in a grain,

the higher its yield stress because twins favour dislocation pile-ups). However, although the back stress observed in Fig. 3.6 deserves attention, a deep study of this effect is out of the scope of the current thesis work.

3.4 Hydriding kinetics

The aim of this section is to use the high-resolution data obtained when performing hydriding cycles with our in-situ curvature measurement setup in order to analyse our Pd thin films hydriding kinetics, both qualitatively and quantitatively.

This analysis will be performed in two phases. The derivation of constitutive equations for the hydrogen adsorption and absorption velocities will first set the stage to the construction of a kinetic model for hydrogen adsorption and absorption into the Pd films. This kinetic model will then be used to analyse the experimental data. The rate-limiting steps of the hydriding mechanism will be determined next, as well as a quantitative data analysis, and thereby the derivation of relevant kinetic and thermodynamic parameters.

3.4.1 Constitutive equations

As can be seen in Fig. 1.13, the Pd hydriding mechanism involves four steps, i.e. molecular adsorption, dissociative chemisorption, diffusion and interstitial absorption. And as already discussed in the state-of-the-art, determining which one(s) is (are) rate-limiting is still a matter of debate, and many contradictory models have been proposed so far. When Pd is in thin film form, surface [76] and bulk [86] steps have recently been claimed to be rate-limiting. Ward and Dao proposed a more complete kinetic model, taking into account for all kinetics steps [230], using rate parameters estimated from surface science and membrane literature. Their calculations perfectly illustrate the complexity of the problem, showing that parameters such as specimen preparation, surface contamination and film thickness critically determine the kinetic behaviour of Pd hydriding. In this thesis, it will be reminded that diffusion cannot be rate-limiting when using Pd thin films - Ward and Dao indeed showed that diffusion is likely to be rate-limiting when the film thickness is at least on the order of the micrometer [230] - and the possible rate-limiting steps will be grouped into one surface step (adsorption) and one bulk step (absorption), according to Wagner's model [57]. As opposed to many authors, which usually consider one rate-limiting step throughout the whole hydriding mechanism, switches will be considered here between these two possible rate-limiting steps.

Following our previously reported basic analysis of a typical hydriding cycle at fixed p_{H_2} (see section 3.2), we will thus consider the possibility of two mechanistic steps to be rate-limiting during Pd thin film hydriding. One of these steps includes H_2 adsorption and its dissociative chemisorption on the Pd thin film surface, and will conveniently be called adsorption. The other one, denoted as absorption, is seen as an equilibrium reaction between atomic hydrogen at, respectively, the surface sites and the interstitial sites of the Pd hydride. In his classical hydriding model, Wagner wrote down the following reactions to describe each of these steps [57]:

$$H_2 + 2\,s = 2\,H\text{-}s, \tag{3.5}$$

$$H\text{-}s + i = H\text{-}i + s, \tag{3.6}$$

where s and i are a free surface adsorption site and an interstitial bulk absorption site, respectively, while H-s and H-i represent, respectively, a surface and bulk site occupied by atomic H.

Earlier studies claimed the existence of two possible adsorption sites on the Pd (111) surface [57]: the so-called strong and weak adsorption sites, which correspond to, respectively, very deep and rather flat potential wells. The strong adsorption sites are octahedral sites, also called fcc sites [87]. Despite the existence of three other highly exothermic surface sites (called bridge, top and hcp sites), it has been claimed that only the fcc sites need to be taken into account for strong chemisorption on (111) planes of Pd. As indeed suggested by Bucur in a thin film hydriding model [231], the strong adsorption sites are filled well before and much faster than the weak ones.

More recently, Johansson et al. obtained accurate quantitative data for the heat of adsorption on Pd (111) surfaces [101]. The heat of adsorption starts from about -100 kJ/mol H_2 at zero surface coverage θ, θ being the number of adsorbed hydrogen atoms divided by the number of adsorbed hydrogen atoms in a filled monolayer. It then gradually becomes less negative as θ increases, and rather abruptly takes on positive values somewhere in the range $0.75 < \theta < 1$. This result clearly suggests a more complex adsorption behavior that the one previously proposed by Bucur. Hong and Rahman arrived at a similar conclusion in their first-principles electronic structure calculations [232], showing that it is only after a substantial amount of hydrogen is adsorbed on the Pd (111) surface that hydrogen is able to further absorb into the bulk. Similarly, the potential energy surface for hydrogen adsorption/absorption [230] also indicates that a surface that is already substantially covered with hydrogen helps

the hydrogen atoms to further overcome the energy barrier to move into the bulk[5].

With respect to the schematics of Fig. 1.13, no hydrogen diffusion step will be taken into account in the present kinetic model neither, simply because of the Pd thin film geometry considered in our work. Indeed, one gets a first-order diffusion time on the order of milliseconds when dividing the square of the Pd film thickness by the diffusion coefficient of H-atoms in α-PdH ($D_\alpha \cong 10^{-7}$ cm^2/s [76]). This is five orders of magnitude below the time scale of the hydriding kinetics experimentally observed in Fig. 3.2 for our Pd thin films.

As to the adsorption step, described by reaction (3.5), an adsorption equilibrium constant K_{ad} can then be defined as follows:

$$K_{ad} \equiv \frac{k'_{ad}}{k''_{ad}} = \frac{[\text{H-s}]^2_{eq}}{p_{H_2}[\text{s}]^2_{eq}} = \frac{\theta^2_{eq}}{(1-\theta_{eq})^2}\frac{1}{p_{H_2}}, \tag{3.7}$$

where θ_{eq} is the equilibrium surface coverage. From reaction (3.5), the adsorption velocity r_{ad} then takes on the following form [233]:

$$\begin{aligned} r_{ad} &= k'_{ad}(1-\theta)^2 p_{H_2} - k''_{ad}\theta^2 \\ &= k'_{ad}\left[(1-\theta)^2 p_{H_2} - \frac{\theta^2}{K_{ad}}\right]. \end{aligned} \tag{3.8}$$

In a similar way, the absorption equilibrium constant can be deduced from reaction (3.6):

$$K_{ab} \equiv \frac{k'_{ab}}{k''_{ab}} = \frac{[\text{H-i}]_{eq}[\text{s}]_{eq}}{[\text{H-s}]_{eq}[\text{i}]_{eq}} = \frac{1-\theta_{eq}}{\theta_{eq}}\frac{n_{eq}}{1-n_{eq}}. \tag{3.9}$$

Note that the equilibrium constants K_{ad} and K_{ab} can be linked together with Sieverts' constant by grouping Eqs. (3.4), (3.7) and (3.9), and by assuming that $n_{eq} \ll 1$ in α-PdH:

$$K_{ad}K^2_{ab} = \frac{1}{K^2_s}. \tag{3.10}$$

[5]The original version of our kinetic model was based on the earlier vision of the hydriding mechanism accounting for weakly and strongly chemisorbed hydrogen. When we firstly submitted the paper dedicated to its description and application, the reviewer recommended us to deeply modify our model, although he recognised the intrinsic quality of the results. After an intense and fruitful interaction with the reviewer, the model turned out to be qualitatively and quantitatively improved, providing estimations of relevant kinetic and thermodynamic parameters for Pd thin film hydriding [221]

From reaction (3.6), the absorption velocity r_{ab} can then be written as

$$\begin{aligned} r_{ab} &= k'_{ab}(1-n)\theta - k''_{ab} n(1-\theta) \\ &= k'_{ab}\left[(1-n)\theta - \frac{n(1-\theta)}{K_{ab}}\right]. \end{aligned} \tag{3.11}$$

Finally, the evolution of the surface coverage θ and bulk H/Pd atomic ratio n can be deduced by combining the expressions (3.8) and (3.11) for the ad- and absorption velocities :

$$\frac{d\theta}{dt} = 2r_{ad} - r_{ab}, \tag{3.12}$$

$$\frac{dn}{dt} = r_{ab}. \tag{3.13}$$

When dealing with complex second order reactions as it is the case here, the derivation of such general rate expressions taking into account each of the two reaction steps is exceedingly tedious or even impossible to derive. The common alternative method in chemical kinetics consists in assuming a specific rate-controlling step right from the beginning, and considering the other reaction step to be in a pseudo steady-state [234]. In our case, if we assume that the two constant slopes observed in Fig. 3.2 during the first and second "linear" kinetic regimes reveal the presence of two different rate-limiting steps in the course of a single hydriding cycle, we can then derive simplified expressions for the adsorption and absorption velocities by assuming that, respectively, the absorption or adsorption step is in pseudo steady-state.

Let us first assume that adsorption is the rate-limiting step. In that case, we can consider $k'_{ab} \to \infty$, and as r_{ab} must remain finite according to Eq. (3.11) [234], this leads to

$$(1-n)\theta - \frac{n(1-\theta)}{K_{ab}} \to 0. \tag{3.14}$$

Rearranging Eq. (3.14) gives

$$\theta = \frac{1}{1 + K_{ab}\dfrac{1-n}{n}} \cong \frac{n}{n + K_{ab}}. \tag{3.15}$$

This equation then enables the elimination of the unobservable variable θ, since in the experimental approach based on in-situ curvature measurements,

we are only able to access the bulk H/Pd atomic ratio n and not the surface coverage θ (cfr. Eq. (3.3)). Inserting Eq. (3.15) into Eq. (3.8) finally gives:

$$r_{ad} = k'_{ad}\left[p_{H_2}\left(\frac{K_{ab}}{K_{ab}+n}\right)^2 - \frac{1}{K_{ad}}\left(\frac{n}{K_{ab}+n}\right)^2\right]. \tag{3.16}$$

On the other hand, if it is assumed that absorption is the rate-limiting step, one can write $k'_{ad} \to \infty$ so that from Eq. (3.8), similarly as in the reasoning above,

$$p_{H_2}(1-\theta)^2 - \frac{\theta^2}{K_{ad}} \to 0. \tag{3.17}$$

Eq. (3.17) then leads to the following solution for the pseudo steady-state surface coverage θ:

$$\theta = \frac{\sqrt{p_{H_2}K_{ad}}}{1+\sqrt{p_{H_2}K_{ad}}}. \tag{3.18}$$

Inserting Eq. (3.18) into Eq. (3.11) finally gives:

$$r_{ab} = k'_{ab}\left[\frac{K_{ab}(1-n)\sqrt{p_{H_2}K_{ad}} - n}{K_{ab}\left(1+\sqrt{p_{H_2}K_{ad}}\right)}\right]. \tag{3.19}$$

Note that equations 3.16 and 3.19, predicting the p_{H_2}-dependences of the adsorption and absorption velocities, have been derived while explicitly assuming $n_{eq} \ll 1$, as is indeed the case for the range of p_{H_2}-values considered in the present kinetic analysis for room temperature hydriding in the alpha phase region ($n_{max}(\alpha) = 0.008$ in bulk Pd [57]).

3.4.2 Kinetic analysis

Recognising the existence of 2 reaction steps, described by respectively, reactions (3.5) and (3.6), one can reasonably assume, as a starting point for a rigorous kinetic analysis, that the two constant slopes that are systematically observed in the beginning of the hydriding cycles (cfr. Fig. 3.2) would correspond to a different kinetic regime, with either ad- or absorption being the rate-limiting step. Since at the beginning of the experiment (when $\theta = 0$ and $n = 0$) the adsorption velocity has already a finite value (cfr. Eq. (3.8)) while the absorption velocity is still 0 (cfr. Eq. (3.11)), and since adsorption can

be considered as relatively unconstrained on a freshly exposed surface, one could reasonably imagine that the first linear kinetic regime corresponds to an absorption-limited step. The second slope would then be indicative for adsorption to become rate-controlling further on in the hydriding cycle. In order to confirm this assumption, a systematic study of the p_{H_2}-dependence of the measured constant slopes was first carried out.

According to Eq. (3.3), these slopes can be taken proportional to $(dn/dt)_{ab}$ and $(dn/dt)_{ad}$ in each of the 2 "linear" kinetic regimes, respectively. Constitutive equations for these quantities therefore still need to be derived first. As to $(dn/dt)_{ab} \equiv r_{ab}$ (cfr. Eq. (3.13)), Eq. (3.19) can be further simplified with the additional assumption that $p_{H_2} K_{ad} \gg 1$. At this stage, the latter can be justified from Eq. (3.7), since, from the state-of-the-art discussion in Section 3.4.1, the equilibrium surface coverage can be considered to be close to one. We will be able to explicitly verify this assumption later in this kinetic analysis, based on derived values for K_{ad}. Combining Eq. (3.19) with Eqs. (3.10) and (3.13) then gives

$$\left(\frac{dn}{dt}\right)_{ab} = k'_{ab}\left[(1-n) - \frac{K_s n}{\sqrt{p_{H_2}}}\right]. \tag{3.20}$$

An absorption-limited hydriding mechanism can therefore be expected to exhibit a hydriding velocity proportional to $(p_{H_2})^{-1/2}$.

The slope $(dn/dt)_{ad}$ of the second linear regime can be derived by linking the differentials of the surface coverage θ and bulk H/Pd atomic ratio n thanks to Eq. (3.15), resulting in

$$d\theta = \frac{K_{ab}}{(K_{ab}+n)^2} dn. \tag{3.21}$$

Combining Eq. (3.21) with Eqs. (3.16), (3.10), (3.12) and (3.13) then provides

$$\left(\frac{dn}{dt}\right)_{ad} = \frac{2k'_{ad}K_{ab}^2}{(K_{ab}+n)^2 + K_{ab}}\left[p_{H_2} - (K_s n)^2\right], \tag{3.22}$$

indicating that an adsorption-limited hydriding mechanism exhibits a hydriding velocity which can be expected to increase linearly with p_{H_2}.

In Figure 3.7, the slopes of the first linear kinetic regime have been plotted as a function of $1/(p_{H_2})^{1/2}$, following constitutive Eq. (3.20) for an absorption-limited hydriding velocity. Similarly, Figure 3.8 shows the slopes of the second

linear regime, which exhibit a linear relationship with p_{H_2}, in agreement with Eq. (3.22). Both figures therefore provide additional, although still qualitative, experimental evidence that the first kinetic hydriding regime is indeed likely to be limited by absorption and the second one by adsorption. Although the p_{H_2} dependencies shown in Figs. 3.7 and 3.8 are consistent with our kinetic interpretation, the same graphs would still look more or less linear with other reaction orders[6], such as proportional with p_{H_2} for Fig. 3.7 or proportional to $1/(p_{H_2})^{1/2}$ for Fig. 3.8. Therefore, if one defines, respectively, S_{ab} and S_{ad} as the slopes and I_{ab} and I_{ad} as the intercepts of the linear fits in Fig. 3.7 and 3.8, these parameters should as such also result in quantitatively relevant kinetic and thermodynamic hydriding parameters. This can be verified based on the following expressions:

$$\frac{S_{ad}}{Q} = \frac{2k'_{ad}K_{ab}^2}{(K_{ab}+n)^2 + K_{ab}}, \tag{3.23}$$

$$\frac{I_{ad}}{Q} = \frac{-2k'_{ad}K_{ab}^2}{(K_{ab}+n)^2 + K_{ab}} (K_s n)^2, \tag{3.24}$$

$$\frac{S_{ab}}{Q} = -k'_{ab}K_s n, \tag{3.25}$$

$$\frac{I_{ab}}{Q} = k'_{ab}(1-n). \tag{3.26}$$

Note that the proportionality constant Q has already been introduced before with Eq. (3.3) in order to convert the measured velocities $(dn/dt)_{ad/ab}$ (expressed in s^{-1}) to the units of the data points in Figs. 3.7 and 3.8 (expressed in MPa/s).

[6]This assumption has also been quantitatively addressed with the reviewer mentioned above. Concerning the slope of the first lineaar kinetic regime (Fig. 3.7), the correlation factors R of the linear fits are, respectively, 0.901 with $(p_{H_2})^2$, 0.929 with p_{H_2}, 0.935 with $(p_{H_2})^{1/2}$ and 0.919 with $1/(p_{H_2})^{1/2}$, while the relative error on the slope of those fits is, respectively 18.19% with $(p_{H_2})^2$, 15.05% with p_{H_2}, 14.32% with $(p_{H_2})^{1/2}$ and 16.23% with $1/(p_{H_2})^{1/2}$. Hence, both the correlation factors as well as the relative slope errors are all reasonable, and definitely not the most confirmative for the expected $1/(p_{H_2})^{1/2}$ dependence. Concerning the second slope (Fig. 3.8), the correlation factors R of the linear fits are, respectively, 0.977 with $(p_{H_2})^2$, 0.984 with p_{H_2}, 0.977 with $(p_{H_2})^{1/2}$ and 0.933 with $1/(p_{H_2})^{1/2}$, while the relative errors on the slopes of those fits is, respectively, 8.3% with $(p_{H_2})^2$, 6.8% with p_{H_2}, 8.18% with $(p_{H_2})^{1/2}$ and 14.62% with $1/(p_{H_2})^{1/2}$. So in this case, although all correlation factors as well as the relative slope errors are again all reasonable, the expected linear p_{H_2} dependence has this time the highest statistical confirmation of linearity. In any case, just checking the p_{H_2}-dependencies expected from the rate expressions is not proof as such for the claimed reaction order. The validation of the model only comes from the quantitative kinetic analysis that is performed in this section.

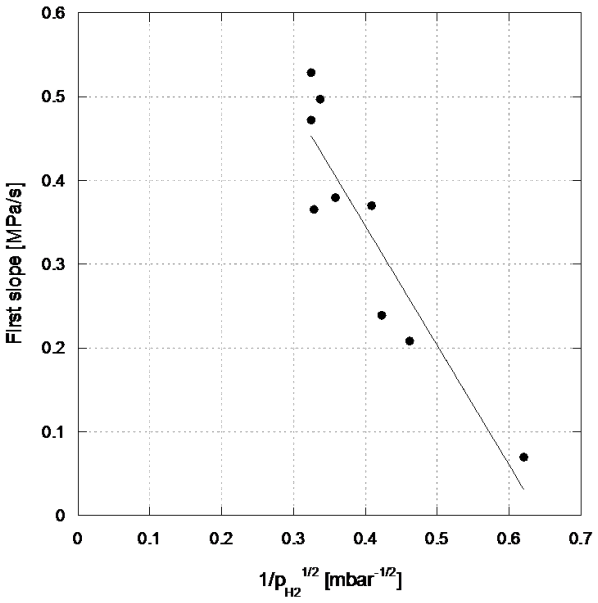

Figure 3.7: Slope of the first linear kinetic regime as a function of $1/(p_{H_2})^{1/2}$.

From Eqs. (3.23) to (3.26), it is clear that S_{ad} and I_{ab} should be positive, while S_{ab} and I_{ad} should be negative. This is indeed observed in the experimental fits obtained in Figs. 3.7 and 3.8. Before trying to solve the 4-equation system involving Eqs. (3.23) to (3.26), one can first define a time t_{tr} to indicate the transition between the first and second kinetic regime. As indicated in the inset of Figure 3.9, this time should respect the following geometrical relationship:

$$\left[\left(\frac{dn}{dt}\right)_{ad}\Big|_{t=t_{tr}}\right]t_{tr} - \frac{I_\sigma}{Q} = \left[\left(\frac{dn}{dt}\right)_{ab}\Big|_{t=t_{tr}}\right]t_{tr}, \tag{3.27}$$

where I_σ is the intercept of the linear fit through the second kinetic regime relative to the initial, as-deposited growth stress value (cfr. inset of Fig. 3.9). The latter parameter has been determined experimentally for all hydriding experiments, resulting in an average value of 446 ± 27 MPa, independent of p_{H_2} in the range 2-10 mbar considered here. By combining Eqs. (3.23) to (3.26) with Eq. (3.27), we obtain:

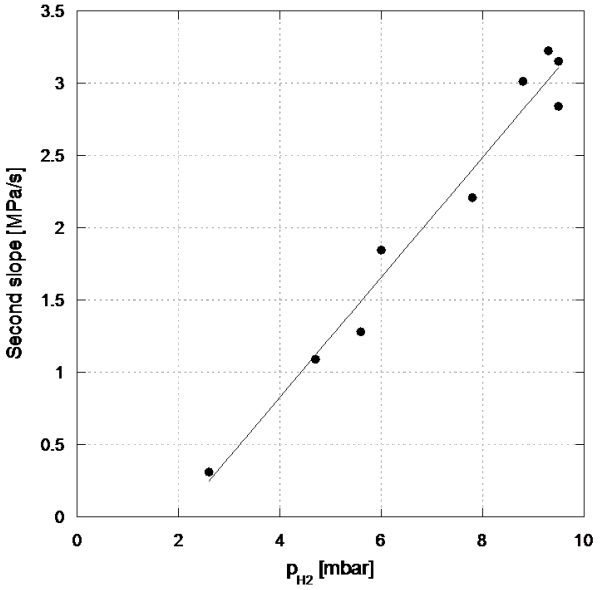

Figure 3.8: Slope of the second linear kinetic regime as a function of p_{H_2}.

$$t_{tr} = \frac{I_\sigma}{\left(S_{ad} p_{H_2} - S_{ab} \frac{1}{\sqrt{p_{H_2}}} + I_{ad} - I_{ab}\right)}. \tag{3.28}$$

Figure 3.9 shows the experimental transition times, determined from the intersection of the linear fits in the first and second kinetic regime, as well as their p_{H_2}-dependence predicted by Eq. (3.28). For the latter, the S_i and I_i values were taken from the linear fits of Figs. 3.7 and 3.8. The excellent correlation obtained between the predicted and experimental t_{tr} values confirms that the kinetic model is qualitatively and quantitatively justified. The parameters of Eq. (3.28) used in Fig. 3.9 are listed in Table 3.4.2.

The 4-equation system involving Eqs. (3.23) to (3.26) then provides a first access to some relevant kinetic and thermodynamic parameters, simply by dividing the slope and intercept values corresponding to the ad- and absorption limited regime:

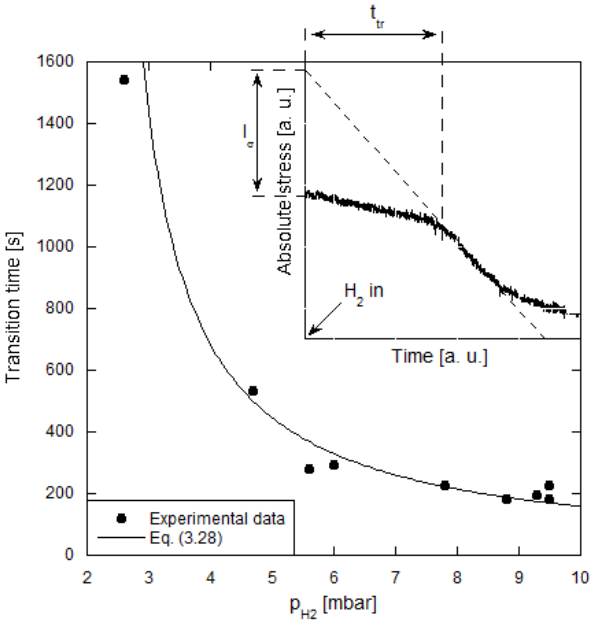

Figure 3.9: Transition time between the first and second kinetic regimes as a function of p_{H_2}. A schematic construction indicating the definition of t_{tr} and I_σ in Eq. (3.27) is included as well.

$$\frac{S_{ad}}{I_{ad}} = -\frac{1}{(K_s n)^2}, \tag{3.29}$$

$$\frac{S_{ab}}{I_{ab}} = -K_s \frac{n}{1-n}. \tag{3.30}$$

Since we already determined the value of Sieverts' constant K_s (cfr. Fig. 3.4), Eq. (3.29) gives a calculated average value for n of (1.3 ± 0.3)·10^{-2} for the second, adsorption-limited kinetic regime, while Eq. (3.30) results in a calculated average n-value of (1.4 ± 0.4)·10^{-2} for the first, absorption-limited regime. These average values can indeed be considered to be sufficiently small in order for Eqs. (3.20) and (3.22) to result in the seemingly constant slopes observed in the first and second kinetic regimes. Moreover, its implication that n at $t = t_{tr}$ is independent of p_{H_2} is not surprising if one considers the constant compressive stress level of our specimens at $t = t_{tr}$, which was found to be - 94 ± 6 MPa relative to the initial, as-deposited growth stress value, independent

Table 3.2: Parameters of Eq. (3.28) used in Fig. 3.9.

Parameter	Value	Unit
S_{ad}	0.41 ± 0.03	[MPa·mbar^{-1}·s^{-1}]
I_{ad}	-0.83 ± 0.21	[MPa·s^{-1}]
S_{ab}	-1.43 ± 0.23	[MPa·mbar$^{1/2}$·s^{-1}]
I_{ab}	0.92 ± 0.09	[MPa·s^{-1}]
I_{σ}	446 ± 27	[MPa]

of p_{H_2}[7]. One can indeed conclude from Fig. 3.10 that the latter does not show a clear trend.

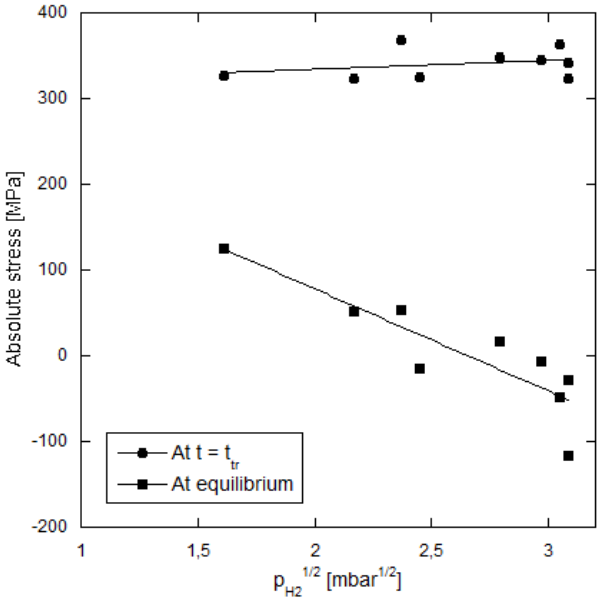

Figure 3.10: Absolute stress at $t = t_{tr}$ as a function of $1/(p_{H_2})^{1/2}$. The equilibrium absolute stress values from Fig. 3.4 are included as well.

As we now explicitly confirmed that $n \ll 1$ in this work, Eq. (3.26) immediately results in $k'_{ab} = (7.4 \pm 0.8) \cdot 10^{-5}$ s^{-1} for the first regime. When taking $k''_{ab} = 1 \cdot 10^{9}$ s^{-1}, calculated at 298.15 K from Ref. [230], and knowing that $K_{ab} \equiv k'_{ab}/k''_{ab}$, we obtain a value of $K_{ab} = (7.4 \pm 0.8) \cdot 10^{-14}$, and therefore $K_{ad} =$

[7] A linear fit of this stress level is performed in Fig. 3.10, showing a positive slope. But the value of this slope is below its experimental error.

$(1.6 \pm 0.8) \cdot 10^{22}$ mbar^{-1} from Eq. (3.10). The latter therefore also validates our earlier hypothesis of $p_{H_2} \cdot K_{ad} \gg 1$, needed for arriving at Eq. (3.20). Moreover, inserting the calculated K_{ab} value and the previously obtained value of n into Eq. (3.23) gives $k'_{ad} = (5 \pm 3) \cdot 10^{17}$ mbar^{-1}s^{-1}. As a value of K_{ad} has already been derived, and since $K_{ad} \equiv k'_{ad}/k''_{ad}$, one also arrives at $k''_{ad} = (3 \pm 2) \cdot 10^{-5}$ s^{-1}, in good agreement with the value of $k''_{ad} = 6.9\dot{1}0^{-5}$ s^{-1} calculated at 298.15 K from Ref. [230].

Besides the presence of the two linear kinetic regimes analysed above, a third non-linear regime is exhibited in Fig. 3.2 before the final hydriding equilibrium. Fig. 3.11 shows, for different p_{H_2}-values, the evolution of the bulk hydrogen concentration in this third kinetic regime, as calculated from the internal stress data using Eq. (3.3). The time scale has been normalised to represent for each experiment the first 500 s of this regime. If we assume that absorption is the rate-limiting step in this regime, the temporal evolution of n can be deduced from Eq. (3.20) by solving what is known as a basic Cauchy problem [235]:

$$\begin{cases} \dfrac{dn(t)}{dt} = n(t)C_1 + C_2, \\ n(t_0) = n_0, \end{cases} \tag{3.31}$$

where t_0 refers to the transition time between the second and third kinetic regime, and

$$\begin{cases} C_1 = -k'_{ab}\left(1 + \dfrac{K_s}{\sqrt{p_{H_2}}}\right), \\ C_2 = k'_{ab}. \end{cases} \tag{3.32}$$

The general solution of this problem is as follows [235]:

$$n(t) = \frac{-C_2}{C_1} + \left(n_0 + \frac{C_2}{C_1}\right) \exp\left(C_1(t - t_0)\right). \tag{3.33}$$

The coarse solid lines in Fig. 3.11 correspond to the fits obtained with the absorption-related Eq. (3.33). Intuitively, it can be understood that the third kinetic regime must indeed be limited by absorption because at the end of the second regime, the surface coverage has already reached its equilibrium value. In this case, the constant C_2 in Eq. (3.32) then directly provides an estimate for k'_{ab}.

The average value of C_2 calculated for all experiments from fitting Eq. (3.33) to the third kinetic regime, results in an average value of $k'_{ab} = (4.1 \pm$

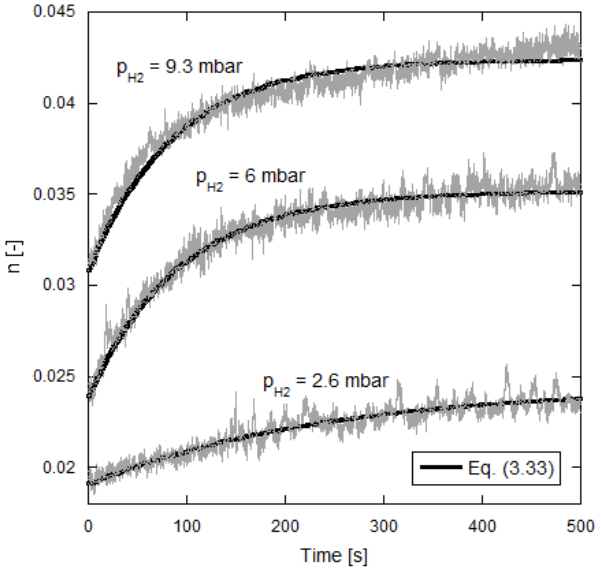

Figure 3.11: Evolution of the bulk atomic concentration n in the third, nonlinear kinetic regime for different values of p_{H_2}. The time scale has been shifted so that $t = 0$ s corresponds to the transition between the second and third kinetic regimes. The coarse solid lines correspond to a fit using Eq. (3.33).

$0.9) \cdot 10^{-4}$ s^{-1} for the third kinetic regime. Moreover, when repeating this procedure for the first kinetic regime, one gets $k'_{ab} = (3.3 \pm 0.8) \cdot 10^{-5}$ s^{-1}, consistent with the value of $k'_{ab} = (7.4 \pm 0.8) \cdot 10^{-5}$ s^{-1} previously obtained with the approximate Eq. (3.26). The value of k'_{ab} for the first kinetic regime is however about one order of magnitude lower than the one characteristic for the third kinetic regime. Therefore, the major outcome of our kinetic study is that the absorption-controlled regimes I and III are characterised by very different values for k'_{ab}. In our opinion, this is related to the fact that the end of region I is being determined by a rather abrupt increase in the positive direction of the heat of adsorption. This is in line with Ref. [101], where such an increase was reported to occur somewhere in the range $0.75 < \theta < 1$. In that case, k'_{ab} must increase as well since the potential energy surface for hydrogen adsorption/absorption indicates that the activation energy for hydrogen absorption should decrease if the heat of adsorption becomes less negative [230]. In this respect, we can also point out that the factor of 10 difference observed between k'_{ab} in regions I and III implies a coverage dependent change in activation energy on the order of $RT \cdot \ln(10)$, corresponding to 6 kJ/molK at 298 K. This number can indeed be considered to be a realistic change for a coverage dependant heat of adsorption,

and is within the range of coverage dependence published for Pd surfaces [101].

As a summary, Figure 3.12 schematically represents the evolution of the adsorption and absorption velocities as a function of surface coverage, as can be anticipated from the current kinetic study. The velocities are superimposed on the experimentally measured hydriding cycle already shown in Fig. 3.2. The latter has also been simulated/fitted according to Eqs. (3.33) and (3.22). According to Eq. (3.8), the θ-dependency of the adsorption velocity is a decreasing parabola, while, according to Eq. (3.11), the absorption velocity increases linearly with θ. In the beginning of the experiment, the initial adsorption and absorption velocities are, respectively, $r_{ad} = 2k'_{ad} \cdot p_{H_2}$ and $r_{ab} = 0$. In the first linear kinetic regime, r_{ad} then rapidly decreases as θ reaches a value close to θ_{eq}. In this zone, Eq. (3.11) predicts the rate-limiting absorption velocity dn/dt to increase linearly with θ and to decrease linearly with n, which is probably the reason why a constant average velocity is observed experimentally. When a critical value of the surface coverage is reached at the end of the first kinetic regime (denoted θ_c in Fig. 3.12), the heat of adsorption is believed to suddenly change in the positive direction. As a result, adsorption then becomes the new rate-limiting step, and the second kinetic regime starts. In this second zone, a plausible explanation for the observation of a constant average velocity is the fact that an increase in θ implies an increase in dn/dt. The increase of surface coverage is thus counterbalanced by the increasing absorption velocity, so that the apparent rate-limiting velocity appears as constant until adsorption equilibrium is reached. When the latter occurs at the end of the second stage ($\theta = \theta_{eq}$), the absorption velocity becomes rate-limiting again in the third kinetic regime. In this regime, dn/dt decreases with n and the kinetics are not linear anymore (cfr. Eq. (3.33)). An equilibrium stress plateau finally appears when absorption equilibrium is reached ($n = n_{eq}$).

Finally, Table 3.4.2 shows all the relevant kinetic and thermodynamic parameters calculated in this work, as well as the kinetic regimes to which they apply. Some literature values are also included, like the constant k''_{ab} that we used in this study for some of the related calculations. Other reference values from the literature show the overall consistency of the obtained results.

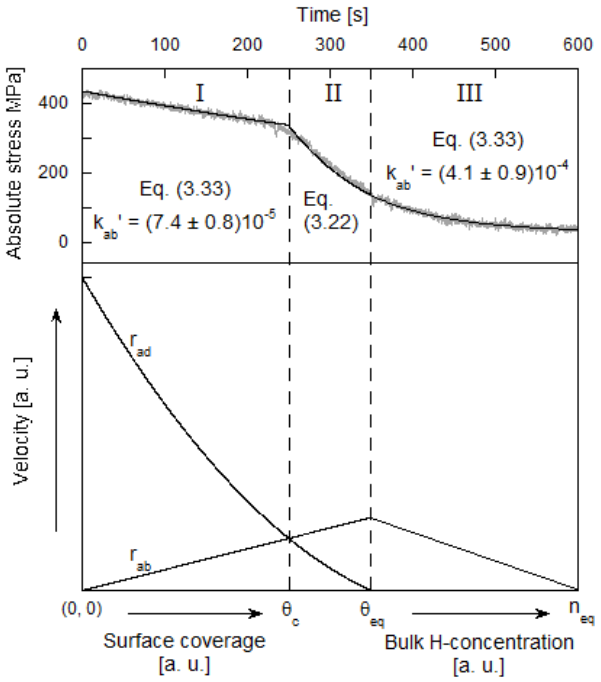

Figure 3.12: Schematic representation of the θ-dependencies of the adsorption (r_{ad}) and absorption (r_{ab}) velocities, superimposed on the experimentally measured hydriding cycle at $p_{H_2} = 6$ mbar. Fits to the experimental data have been included as well, using constitutive Eq. (3.33) for the absorption-controlled first and third regimes, and Eq. (3.22) for the second, adsorption-limited regime. The values mentioned for k'_{ab} in regimes I and III represent average values derived from the fitting parameter C_2 (cfr. Eq. (3.32)) when including all experiments.

Table 3.3: Overview of the kinetic and thermodynamic hydriding parameters calculated in this work for Pd hydriding in the α phase region at 298 K, with the kinetic regimes which they apply to. Some values taken from the literature are displayed for comparison.

Parameter	Origin	1^{st} regime	2^{nd} regime	3^{rd} regime	Overall
k'_{ad} [mbar^{-1}s^{-1}]	This work		$(5 \pm 3) \cdot 10^{17}$		
k''_{ad} [s^{-1}]	This work		$(3 \pm 2) \cdot 10^{-5}$		
	Ref. [230]				$6.9 \cdot 10^{-5}$
K_{ad} [mbar^{-1}]	This work				$(1.6 \pm 0.8) \cdot 10^{22}$
k'_{ab} [s^{-1}]	This work	$(7.4 \pm 0.8) \cdot 10^{-5}$	$(4.1 \pm 0.9) \cdot 10^{-4}$	$(4.1 \pm 0.9) \cdot 10^{-4}$	
k''_{ab} [s^{-1}]	Ref. [230]				$1 \cdot 10^{9}$
K_{ab} [-]	This work				$(7.4 \pm 0.8) \cdot 10^{-14}$
K_s [atm$^{1/2}$]	This work				3.3 ± 0.7
	Ref. [62]				2

3.5 Batch-to-batch reproducibility

The issue of the batch-to-batch reproducibility has been raised from the beginning of the thesis, as huge differences in the hydriding kinetic behaviour were observed between specimens deposited under the same conditions. The aim of this section is to show how this issue has been understood and circumvented.

Firstly, it has to be noted here that the kinetic analysis performed in previous section relies on specimens from Batch 1 (see Table 3.1). Batch 2 has originally been produced because Batch 1 did not contain enough specimens to clearly identify the α to β phase transition of the Pd thin films. Fig. 3.3 therefore contains results from both batches. One one hand, it is thereby obvious that the hydriding thermodynamic behaviour of these two batches is the same. But on the other hand, their kinetic behaviours are markedly different. In this respect, Figs. 3.13 and 3.14 show the slopes of the first and second linear kinetic regimes as a function of $1/(p_{H_2})^{1/2}$ and p_{H_2}, respectively (the data from Batch 1 have already been shown and discussed in the previous section, see Figs. 3.7 and 3.8).

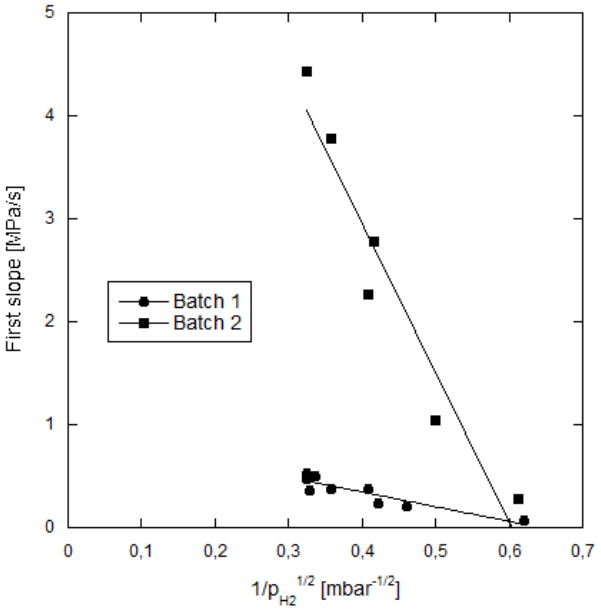

Figure 3.13: Slope of the first linear kinetic regime as a function of $1/(p_{H_2})^{1/2}$ for the two batches presented in Fig. 3.1.

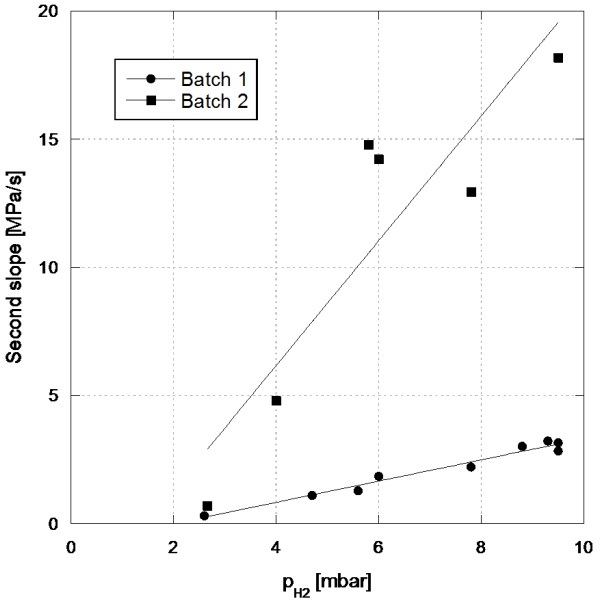

Figure 3.14: Slope of the second linear kinetic regime as a function of p_{H_2} for the two batches presented in Fig. 3.1.

These figures show that the hydriding kinetics of the specimens with the smallest dry air exposure time between deposition and hydrogen cycling is much faster than the hydriding kinetics of the older specimens. This effect is attributed to long-term chemical reactions between the Pd surface and oxygen in air, which is believed to affect the initial Pd surface coverage. These chemical reactions may include [57]:

$$\begin{cases} \text{H-s} + \text{O}_{\text{ad}} = \text{OH}_{\text{ad}}, \\ 2\,\text{OH}_{\text{ad}} = \text{O}_{\text{ad}} + \text{H}_2\text{O}, \\ \text{OH}_{\text{ad}} + \text{H-s} = \text{H}_2\text{O}, \end{cases} \tag{3.34}$$

where O_{ad} and OH_{ad} are, respectively, oxygen and hydroxide adsorbed on the Pd surface. A factor 5 is observed between the values of the slopes and intercepts of the second, adsorption-limited linear kinetic regime, while a factor 10 is observed between the slopes and intercepts of the first, absorption-limited linear kinetic regime. The absorption velocity in first kinetic regime can indeed be expected to be more affected by these undesired reactions, as the oxygen concentration at the palladium surface is higher at the beginning of the experiment than in the second kinetic regime, because part of the surface oxygen

has been eliminated in the form of water. This raise of the slopes and of the intercepts of the two linear kinetic regimes reflects the increase of the rate constants for hydrogen absorption and adsorption when less surface hydrogen is lost in Reactions 3.34. Nevertheless, this has no substantial consequence on the calculations of the averages values of n through Eqs. (3.29) and (3.30). Indeed, the absolute internal stress level at $t = t_{tr}$ is unaffected as well by the dry air exposure time. Consequently, the value of t_{tr} at fixed p_{H_2} is smaller for low dry air exposure times, as confirmed in Fig. 3.15.

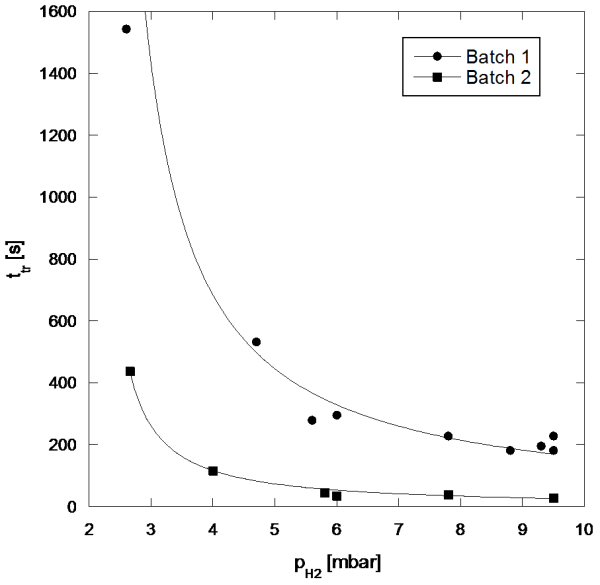

Figure 3.15: Transition times between the first and second kinetic regimes as a function of P_{H_2} for the two batches presented in Fig. 3.1. The experimental data have been fitted with Eq. (3.28), as in previous section.

Very similar mechanisms can also be imagined with hydrocarbons polluting the Pd surface instead of monoatomic oxygen [57]. But in the context of this thesis, a long-term hydrocarbon contamination of the specimens in the dessicator is unlikely to occur. RBS spectra recorded on old specimens indeed revealed small oxygen gradients in our Pd thin films.

The complete interpretation of this dry air exposure effect is out of the scope of the present thesis. However, this short kinetic analysis enabled the identification of this effect and provided the impetus for an experimental procedure in order to avoid it. The classic dessicators have indeed been replaced by dessicators connected to a rotary vacuum pump, allowing for primary vacuum

storage conditions.

Generally speaking, the effect of dry air exposure should always be anticipated if using metallic specimens dedicated to hydriding experiments. Storing the specimens under vacuum is obviously not the only way to prevent modifications of the specimen surface state. This solution has been chosen here because the specimens required for this thesis work were as-deposited, pure Pd thin films. If choosing a more application-oriented approach, one can use more effective solutions like using a protective layer on top of the films or alloying the films with another element which, even in small concentrations, would inhibit interactions between air and the specimen surface. Regular mechanical or chemical cleaning of the film surface could also be used, as long as it does not itself modify the surface (i.e. by introducing roughness or by polluting the surface).

3.6 Conclusions

In this chapter, the stress-time evolution of the hydriding cycles has been empirically interpreted in terms of kinetics and equilibrium behaviour. Three distinct kinetic regimes have been identified after introduction of hydrogen into the vacuum chamber. The first and second regimes are characterised by a linear evolution of the stress with time, while the hydriding rate decreases with time during the third regime. The equilibrium stress level reached between hydrogen inside and outside the Pd thin film has been identified, as well as the residual stress level observed under vacuum and after venting. The latter has been proven to be the consequence of residual hydrogen remaining in the Pd film under vacuum.

The equilibrium room temperature hydriding behaviour of the Pd films has then been analysed. The α to β transition of the Pd hydride has been identified, further enabling to limit the kinetic analysis to the α phase region. Staying in this region ensures a direct derivation of the hydrogen concentration inside the Pd thin film without the additional complexity of the phase transformation. The calculation of Sieverts' constant, when compared to literature data, showed that the Pd films tested in this work contain a high concentration of structural defects, as expected. The analysis of the reversibility of the hydriding mechanism also revealed that our thin films can undergo several hydriding cycles without degradation of their hydriding properties, and enabled the identification of the hydrogen-induced plasticity effects happening at high hydrogen partial pressures.

The hydriding kinetics of the Pd films has then been analysed in detail. A systematic study of the p_{H_2}-dependency of the two constant slopes observed

in the first and second kinetic regimes, based on newly derived constitutive equations, resulted in the identification of the first linear regime to be limited by absorption and the second one by adsorption. After adsorption equilibrium is reached at the end of the second stage, the third, non-linear kinetic regime, was found to be limited by absorption. The quantitative analysis of these different regimes resulted in the calculation of a number of relevant kinetic and thermodynamic hydriding parameters. One of the major outcomes in this respect is that the rate constant for hydrogen absorption k'_{ab} in the first and third kinetic regimes differ by almost one order of magnitude. This has been attributed to the fact that the end of the first regime is being determined by a rather abrupt increase in the positive direction of the heat of adsorption. As a result, this kinetic study was able to provide a self-consistent quantitative interpretation of the entire room temperature Pd hydriding cycle in the α-phase domain.

The study of the batch-to-batch reproducibility of the hydriding cycles in terms of dry air exposure time finally revealed the importance of taking this parameter into account. No effect has been identified on the equilibrium behaviour of our specimens, but the hydriding kinetics is very much affected. The importance of storing the Pd films under vacuum (more generally, with no contact with air or hydrocarbons) in order to preserve the virgin hydriding properties is an important issue regarding hydrogen storage or hydrogen detection applications.

Chapter 4

Effect of internal stress on hydriding properties[1]

In this chapter, the high-resolution in-situ curvature measurement setup has been used for two purposes. The first one is to monitor the in-situ evolution of the growth-induced internal stress in Pd thin films during magnetron sputtering deposition. The high accuracy of the in-situ approach - combined with a fine control of the argon plasma pressure - enables accurate adjustment of the internal stress in the deposit, in the compressive or tensile directions. Simultaneously, the deposition parameters can be set in order to keep the same type of microstructure even when varying the growth-induced stress. As a result, one can isolate the effect of internal stress on the film hydriding properties from the effect of the microstructure itself.

The in-situ approach has also been used to study the hydriding kinetics of these Pd thin films, in order to unravel each kinetic regime in quantitative detail. Firstly, the rate-limiting steps of these regimes have been identified through the systematic study of the p_{H_2}-dependencies of the hydriding velocity, using the same approach as described in previous chapter. This kinetic analysis has been repeated for several batches presenting different levels of growth-induced stress. Next, the effect of a growth-induced internal stress on both the ad- and absorption rate constants has been identified as well. As relevant kinetic and thermodynamic parameters can be derived owing to the kinetic model discussed in the previous chapter, a quantitative analysis the effect of internal stress on the Pd films hydriding properties has been carried out.

[1] Most of the elements presented in this chapter have been submitted to an international journal [236].

4.1 Experimental details

The cantilevers used in this chapter were cut approximately 3 x 0.5 cm^2 in size from oxidized Si wafers. These 380 μm thick wafers were coated by sputtering with a 170 nm thick Pd thin film, on top of a 5 nm Ti adhesion layer. The high resolution curvature measurement technique has been coupled to the sputtering setup in order to measure the Pd thin film growth stress, as detailed in Chapter 2. The room temperature sputtering of the Pd films strongly limits the surface mobility of the deposited atoms, therefore also strongly limiting the grain boundary migration and recrystallisation mechanisms. The deposits can then be expected to be nanocrystalline, and to exhibit porous columnar grains [205]. The growth-induced stress in the deposit, which will be used as a parameter to study the effect of internal stress on the hydriding kinetics, was controlled by properly adjusting the argon sputtering pressure. The higher the amount of argon atoms on the trajectory of the Pd atoms removed from the target, the higher the number of collisions encountered, and, thereby, the lower the mean free path of the Pd atoms. Their impact energy when arriving at the surface of the substrate is then lowered at high argon sputtering pressures, giving rise to an increased tensile component of the growth stress in the film [207]. This effect can be seen in Figure 4.1, which shows the stress*thickness product as a function of time (before and during Ti layer deposition, as well as after Pd deposition) and Pd thickness (during Pd deposition). An initial baseline curvature measurement was first carried out before the Ti layer deposition at p_{Ar} = 3 mTorr for all specimens. The growth-induced stress in the Pd layer is slightly compressive in the first tens of nanometers, and then reaches a constant value given by the constant slope of the stress*thickness vs. thickness curves. Both the sign and magnitude of the latter strongly depend on the value of p_{Ar} used during Pd deposition. The resulting mean internal stress values of the as-deposited Pd films, further denoted as θ_0, are given in Table 4.1, and vary from -152 MPa to 453 MPa for p_{Ar} ranging from 1.5 to 8 mTorr.

The same table also includes results from elementary microstructural characterizations. Cross-sectional and plane-view SEM observations allowed the measurement of the thickness and grain size of all Pd specimens, leading to average values of, respectively, 170 ± 7 and 27 ± 1 nm. Knowing the Pd thin film thickness, Inductively Coupled Plasma (ICP) measurements have been performed on layers dissolved in an acid mixture in order to obtain their density ρ_f. These data indicate an average density for our Pd films of 10.6 ± 0.3 g/cm^3, significantly lower than the Pd bulk density of 12 g/cm^3 [206]. No trend however is visible in the density data as a function of p_{Ar}. X-ray diffractograms showed that the Pd films are strongly (111) textured, as can be expected for vacuum deposited fcc metallic thin films [218–220]. The texture factor reported in Table 4.1 was calculated as the ratio

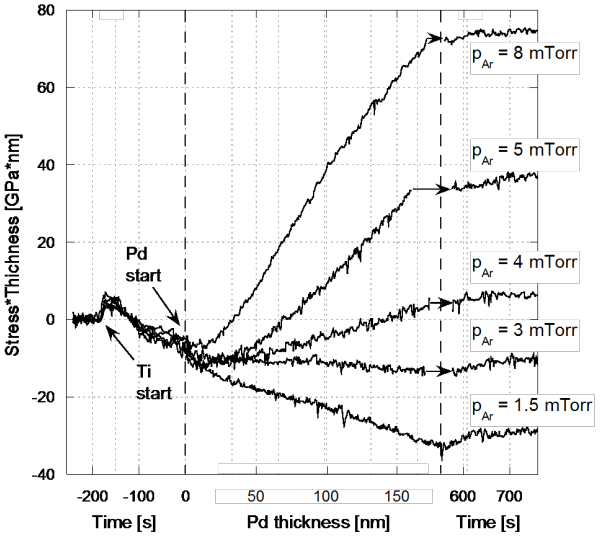

Figure 4.1: Evolution of the stress*thickness product as a function of time (before and during Ti layer deposition, as well as after Pd deposition) and Pd thickness (during Pd deposition) using different argon sputtering pressures.

$$f_{global} = \left(\frac{I_{111}}{I_{200} + I_{311}}\right)_{film} \left(\frac{I_{200} + I_{311}}{I_{111}}\right)_{stand}, \tag{4.1}$$

where the standard intensity ratio is obtained from Ref. [222]. Here again, no trend was visible as a function of p_{Ar}. One can also note that this texture factor is different than the one previously defined in order to analyse the (111) texture of our Pd thin films deposited by evaporation in last chapter (Eq. (3.1)). The reason for this choice is that the diffractograms recorded on the latter did not show any secondary (200) peak, which is not necessarily the case regarding the Pd thin films deposited by sputtering considered in this chapter. As can indeed be seen in Fig. 4.2, the Pd (200) secondary peaks appear on the 3 batches exhibiting tensile growth stresses. The Pd (311) tertiary peaks appear on each batch. The diffractograms have not been recorded between 63° and 78°, i.e. in the region of the Si (100) peak of the underlying substrate, which is so intense that it saturates the detector.

Table 4.1: Argon plasma pressure p_{Ar}, average growth-induced stress σ_0, thickness t_f, density ρ_f, grain size, (111) texture factor and dry air exposure time of the Pd films studied in this work.

Plasma pressure [mTorr]	1.5	3	4	5	8
Growth stress [MPa]	-152	-55	61	272	453
Pd thickness [nm]	180	170	173	160	171
Density [g/cm^3]	10.4	11.0	10.5	11.5	9.8
Grain size [nm]	29	26	29	27	24
(111) texture factor [-]	59	107	93	115	66
Dry air exposure [months]	<2	<2	<2	<2	<2

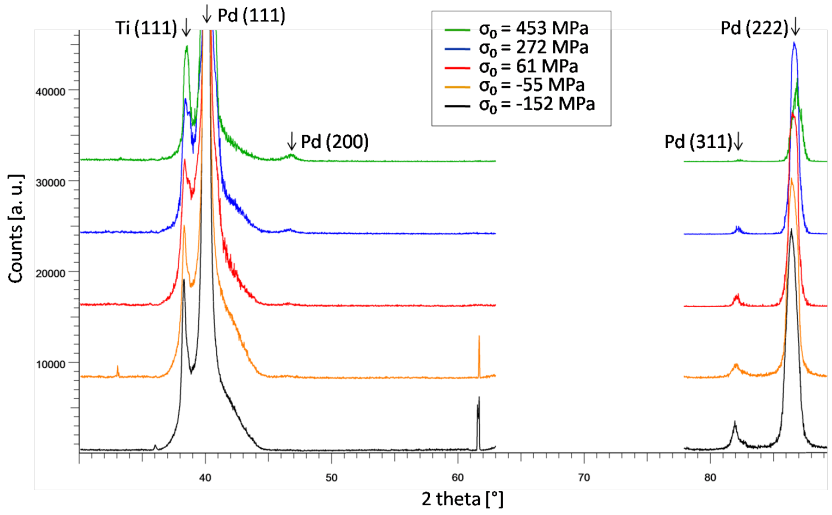

Figure 4.2: Diffractograms recorded on the five batches of Pd thin films considered in this chapter, the latter exhibiting different growth-induced stresses. The upper parts of the intense Pd (111) peaks have been removed for convenience.

The texture of the Pd deposits obtained by evaporation and sputtering is compared through the f_{311} texture factor defined in Eq. (3.1). This is performed in Fig. 4.3, from which it appears that f_{311} increases with increasing tensile growth stress. It is also clear that the relative intensity of the Pd (311) peak is higher for sputtered Pd deposits compared to evaporated Pd deposits, for the same growth stress level. One can also define a f_{200} texture factor in the following way:

$$f_{200} = \left(\frac{I_{111}}{I_{200}}\right)_{film} \left(\frac{I_{200}}{I_{111}}\right)_{stand}. \tag{4.2}$$

The inverse tendencies are observed when using that texture factor: f_{200} decreases with increasing tensile growth stress, and is more important for evaporated Pd deposits than for sputtered Pd deposits, for the same growth stress level (indeed, no (200) secondary peak is observed with evaporated deposits). However, both types of deposits give rise to a strong (111) texture, as expected.

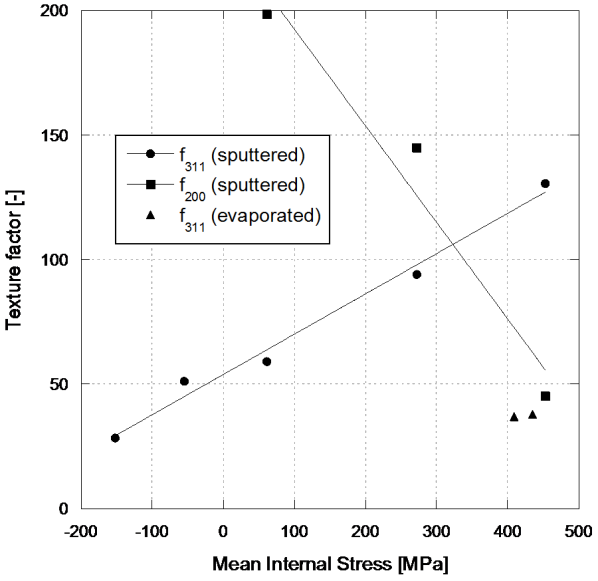

Figure 4.3: f_{311} texture factors of the batches of Pd thin films from Chapters 3 (evaporated) and 4 (sputtered) as a function of the mean internal stress in the Pd deposit. The f_{200} texture factors are also shown for the 3 batches exhibiting tensile growth stresses.

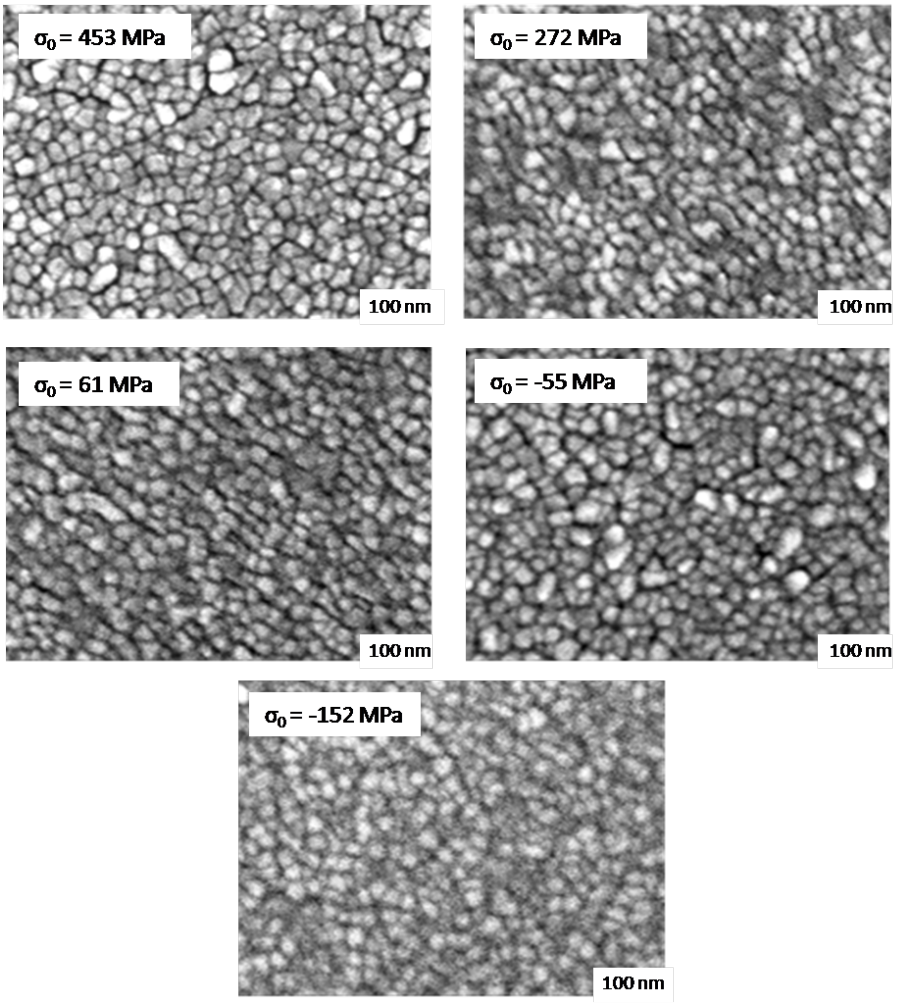

Figure 4.4: Plane-view SEM micrographs of the as-deposited Pd thin films used in this chapter. No variations are observed as a function of the growth-induced stress in the Pd deposit in terms of grain size and shape.

The dry air exposure time of each batch has been kept below two months in order to avoid any effect on the hydriding kinetics (see previous chapter). A potential effect of the microstructure in terms of the grain size has also been avoided, as shown in this section through the microstructural characterisation. Despite some subtle variations in the Pd thin films texture with the growth-induced stress[2], the grain size can be considered as constant from one batch to another. Fig. 4.4 indeed shows that the grains have the same size, but also the same shape in the plane of the deposit.

All the hydriding experiments presented here have been carried out at room temperature. As explained in previous chapter, the kinetic analysis can only be carried out in the α phase of the Pd hydride, because phase transition and plasticity effects would unnecessarily complicate it. Here again, although experiments will be reported for p_{H_2} values up to 100 mbar for the equilibrium analysis, the quantitative stress-affected kinetic analysis - which is the main objective of this chapter - has been limited to the low p_{H_2} range [1 - 10 mbar].

4.2 Hydriding cycle: equilibrium analysis

Figure 4.5 shows hydriding cycles recorded at, respectively, $p_{H_2} = 1.4$ mbar and 1.5 mbar using specimens cut out from Pd films initially exhibiting, respectively, a 61 MPa and 272 MPa tensile internal stress. The initial stages of a hydriding cycle is also provided for a specimen initially at -55 MPa, to already show the dramatic slowing down of the hydriding kinetics that occurs when using Pd films initially in compression. As opposed to the hydriding cycle previously shown in Fig. 3.2, the initial stress before bringing the specimen into contact with hydrogen has arbitrarily been set to zero for the sake of convenience.

In order to proceed with the equilibrium analysis of such hydriding cycles, the explicit assumption underlying Eq. (3.3) of elastic deformation in the Pd film must first be addressed. Besides the hydriding-induced compressive stress change, also the initial, growth-induced stress state of the films needs to be considered. As to the latter, Table 4.1 indicated already that our Pd films show growth-induced stress levels ranging from -152 to 453 MPa. The latter value is above the theoretical tensile yield stress of bulk Pd measured by Sanders et al. [107], but below the yield stress of 550 MPa reported for nanocrystalline Pd specimens. It is also below the value obtained by Colla et al. for Pd

[2]Even if the texture factors in the (200)/(311) directions are multiplied/divided by a factor 4 from the most compressive to the most tensile deposition conditions (see Fig. 4.3), these variations remain subtle because the ratio between the overwhelming (111) and, respectively, the (200) and (311) peaks, is, in the worst case, 28 times and 45 times what it would be in a sample with randomly oriented grains. The texture is then influenced by the deposition conditions, but the grains are still mainly oriented in the (111) direction.

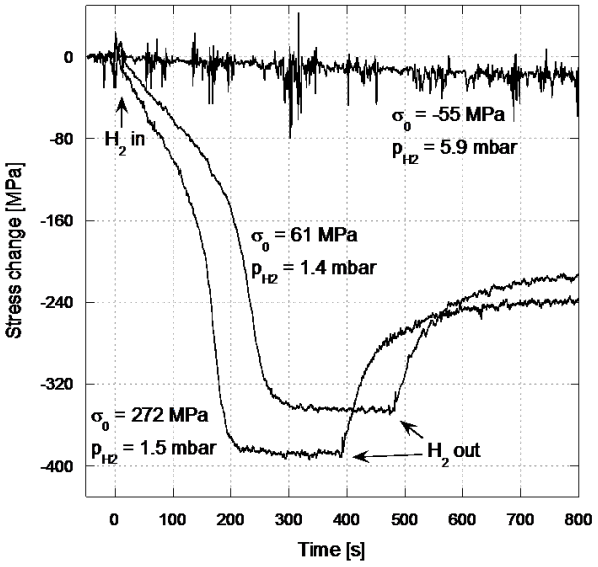

Figure 4.5: Evolution of the compressive stress change as a function of time during three hydriding cycles recorded using specimens exhibiting different growth-induced stresses.

films of similar thickness and grain size [109]. As to the hydriding-induced stresses, Figure 4.6 shows room temperature pressure-stress isotherms, obtained by successively increasing the hydrogen partial pressure p_{H_2} in the chamber and waiting for equilibrium (such an experiment is shown in Fig. 4.7). It is observed that all the specimens end up at about -950 MPa in compression for $p_{H_2} = 100$ mbar, regardless their initial growth-induced stress state. This observation is in agreement with the measurements of Youngdahl et al. [226], who reported that the compressive yield stress of nanocrystalline Pd is on the order of 1 GPa. In other words, when this yield stress level is reached in our Pd thin films, the direct proportionality between internal stress and hydrogen content as given by Eq. (3.3) vanishes, and the films can still absorb hydrogen without giving rise to a curvature or stress change. Moreover, on the same Fig. 4.6, the $\alpha \rightarrow \beta$ phase transition can be identified to start at room temperature between 10 and 20 mbar for the film initially at 435 MPa in tension[3] and between 30 and 40 mbar for the film initially at 272 MPa in tension. The films initially in compression do not exhibit any phase transition between 1 and 100 mbar, while the $\alpha \rightarrow \beta$

[3]This result is in agreement with the identification of the $\alpha \rightarrow \beta$ phase transition performed in previous chapter on Pd thin film specimens deposited by e-gun evaporation, and exhibiting the same level of growth-induced stress.

phase transition for the film initially at 61 MPa is interrupted when the absolute stress reaches -950 MPa. This shift of the $\alpha \rightarrow \beta$ phase transition lower limit towards higher values of p_{H_2} as the initial stress state in the metal increases in the compressive direction has already been observed for Fe-Pd [121] and Mg [122] compounds. In order to avoid such complicating plasticity and phase transition effects, the present kinetic analysis has therefore been limited to the p_{H_2} interval [1 - 10 mbar]. In this range, the equilibrium absolute stress does not exceed -700 MPa for any of our specimens, staying below the compressive yield stress for nanocrystalline Pd thin films [226]. Under these conditions, the proportionality between the hydriding-induced stress change and the bulk hydrogen content n, as given by Eq. (3.3), will remain valid throughout the kinetic analysis performed in the next section.

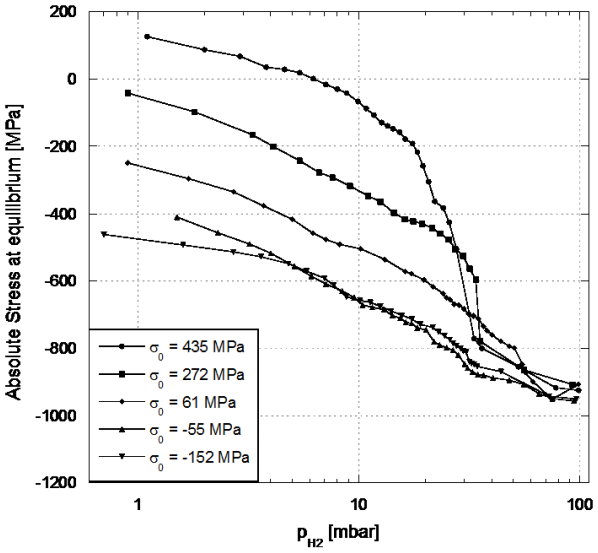

Figure 4.6: Room temperature pressure-absolute stress isotherms of the 5 sets of specimens presented in Table 4.1, obtained by successively introducing small amounts of hydrogen into the chamber and waiting for equilibrium.

Based on the above considerations, it is now possible to calculate Sieverts' constant K_s in the α-PdH region from the data of Fig. 4.6, based on the well-known Sieverts' law (see Eq. (3.4)). The resulting K_s values, obtained with $\Delta v/\Omega_{Pd} = 0.19$ [225], $E_{Pd} = 121$ GPa and $\nu_{Pd} = 0.39$ [106], are listed in Table 4.2. The latter do not show any trend as a function of the initial, growth-induced stress state of the Pd films before hydriding, except for the higher K_s value observed for the specimen with the most compressive growth stress. We

can already point out here that this specimen will not be further considered for the kinetic analysis, as its hydriding behaviour is excessively slow (cfr. Fig. 4.5). Since K_s has been reported to be a function of the concentration of structural defects in the host metal lattice [62], the data in Table 4.2 indicate that, while obtaining different growth-induced stress levels in the Pd films by changing the Ar sputtering pressure, one may still arrive to keep the for hydriding most relevant microstructural parameters constant. The same statement was already inferred from the similar elementary characterisation results reported for the different specimens in Table 4.1.

For all the hydriding cycles presented here, the residual compressive stress change, i.e. the difference between the absolute stress at the beginning and at the end of the hydriding cycle, is on the order of 200 MPa. It has already been shown before to disappear upon venting (see previous chapter), and therefore cannot be attributed to a plasticity effect.

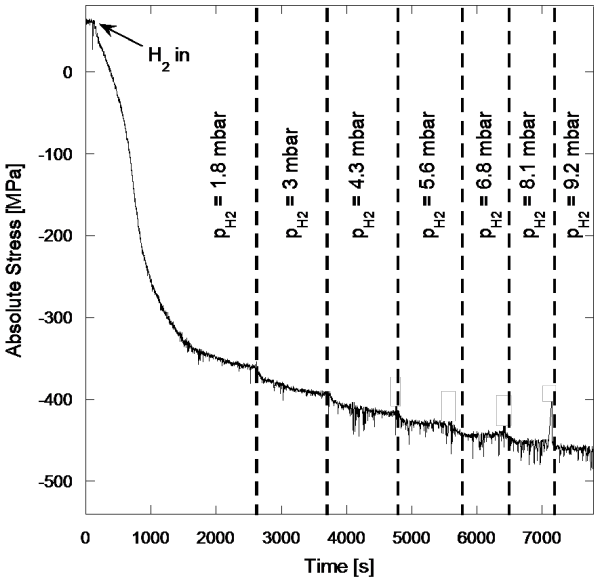

Figure 4.7: Successive introduction of small amounts of hydrogen into the chamber in order to produce a room temperature pressure-absolute stress isotherm. Corresponds to the batch initially exhibiting 61 MPa tensile growth stresses. Stress plateaus are shown here for p_{H_2} values between 1 and 10 mbar.

Table 4.2: Sieverts' constant of the Pd thin films studied in this work, calculated from the data of Fig. 4.6 in the α-PdH region.

σ_0 [MPa]	K_s [atm$^{1/2}$]
-152	4.79 ± 0.18
-55	3.53 ± 0.15
61	3.74 ± 0.22
272	3.19 ± 0.12
453	3.94 ± 0.12

4.3 Hydriding kinetics

In this section, the kinetic rate expressions derived in the previous chapter are applied to analyze in more detail the hydriding cycles produced here. Similarly to the kinetic analysis performed in previous chapter, the rate-limiting steps of the hydriding mechanism are identified and a quantitative data analysis is performed. Our kinetic model is then extended to address the effect of internal stress on the hydriding kinetics, based on the activation volume theory.

4.3.1 Kinetic model: applicability and qualitative analysis

In previous chapter, we already presented a kinetic model able to provide a self-consistent interpretation of the entire room temperature hydriding cycle of Pd thin films in the α-phase domain. Its constitutive equations have been derived starting from the observation that two mechanistic steps are potentially rate-limiting during Pd film hydriding. One of them includes H_2 adsorption and its dissociative chemisorption on the Pd surface (Eq. (3.5)). The second one is the absorption and involves an equilibrium reaction between atomic hydrogen at, respectively, surface and interstitial bulk sites (Eq. (3.6)). No diffusion step is taken into account in this model because of the very small room-temperature diffusion time on the order of milliseconds in the case of Pd films that are only 170 nm thin. The derivation of rate expressions corresponding to the ad- and absorption limited regime has been carried out by assuming a specific rate-controlling step, and by considering the other one to be in a pseudo steady-state. This method is the common way to proceed in chemical kinetics when dealing with complex second order reactions [234]. The time evolution dn/dt of the bulk H/Pd atomic ratio when the rate-limiting step is, respectively, absorption and adsorption have thus been derived in the forms of Eqs. (3.20) and (3.22).

As already observed in the previous chapter with Pd thin films deposited by e-gun evaporation, the hydriding cycles in Fig. 4.5 for the specimens with an initial tensile growth-induced internal stress exhibit three characteristic kinetic regimes. At the beginning, a first linear region is observed in the stress-time curves. This has been shown before to correspond to an absorption-limited kinetic regime, adsorption still being relatively unconstrained on the freshly exposed Pd surface. A transition to a second linear kinetic regime is then observed, which we have already attributed before to a change of the heat of adsorption in the positive direction as the surface coverage reaches a critical value. As a result of the associated decrease in stability of the adsorbed hydrogen atoms, adsorption then becomes the new rate-limiting step in this second kinetic regime. The amount of hydrogen in the specimen continues to increase linearly with time until adsorption equilibrium is reached. This marks the end of the second linear kinetic regime. Absorption then becomes rate-limiting again and a third, nonlinear kinetic regime is observed until absorption equilibrium is reached ($n = n_{eq}$).

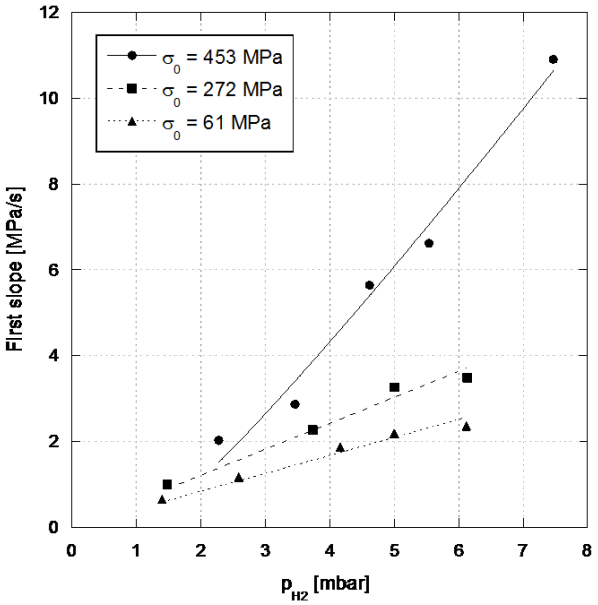

Figure 4.8: Slope of the first linear kinetic regime as a function of p_{H_2}, fitted with Eq. (3.20) and including the p_{H_2}-dependence of k'_{ab} (Eq. (4.4)).

The slopes of the first and second linear kinetic regimes have been plotted as a function of p_{H_2} in, respectively, Figures 4.8 and 4.9. Since the time scale involved in the hydriding of specimens initially under compression was excessively

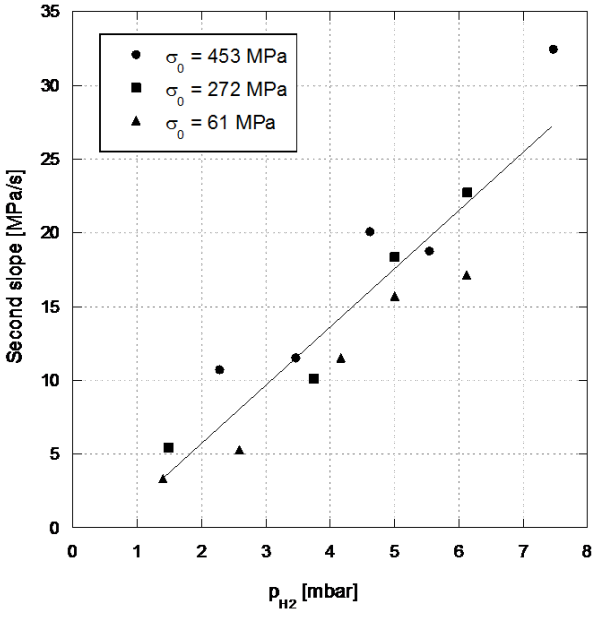

Figure 4.9: Slope of the second linear kinetic regime as a function of p_{H_2}, fitted with Eq. (3.22) with one single fit for the three sets of specimens.

large (cfr. Fig. 4.5), our kinetic analysis has been limited to specimens with a tensile growth-induced stress, as already mentioned before. In Fig. 4.8, the effect of the initial, growth-induced internal stress state of the Pd films is clearly visible. This indicates that at least one of the parameters of the absorption-limited rate equation Eq. (3.20) is affected by internal stress. Since K_s was shown before in Table 4.2 to be stress-independent in the σ_0 range considered here, the stress-affected kinetic parameter in Eq. (3.20) should be k'_{ab}. As was already inferred from Fig. 4.5, increasing the internal stress in the tensile direction leads to a faster rate of hydrogen uptake in the first, absorption-limited kinetic regime. From the results in Figure 4.9, it is seen that this is not the case in the second, adsorption-limited regime. Indeed, no statistical differences could be observed between data points coming from the three batches, leading to one single linear fit (note that the observed linear p_{H_2} dependence observed both in Figure 4.8 and 4.9 will be justified in the next section). As a result, the parameters of the adsorption-limited rate equation 3.22 can be considered to be independent of the internal stress state of the film. The above observations agree with intuition, in that the stress due to hydrogen uptake by the Pd films is compressive, so that one may expect an additional driving force for hydrid-

ing when stretching the host lattice in the tensile direction. At the free surface however, no significant volume expansion occurs during adsorption, making the latter much less sensitive to internal stress effects inside the film.

4.3.2 Quantitative analysis: rate constants and activation volume

We now proceed with a quantitative analysis of the absorption rate constant k'_{ab}. For this purpose, the temporal evolution of n for an absorption-limited kinetic regime has previously been deduced by integrating Eq. (3.20), thereby arriving at Eq. (3.33). The fitting constant C_2 from Eq. (3.32) gives direct access to the parameter of interest k'_{ab}. Figure 4.10 shows the values of k'_{ab} in the first kinetic regime for the experiments already presented in Fig. 4.8. As expected from the data in Fig. 4.8, k'_{ab} increases for a given p_{H_2} when increasing the growth-induced internal stress. Besides being stress-affected, k'_{ab} also turns out to exhibit a linear dependence with p_{H_2}. In their hydrogen membrane permeation model [230], Ward et al. suggested that k'_{ab} may indeed depend on surface coverage at freshly exposed surfaces, which is the case in the first kinetic regime.

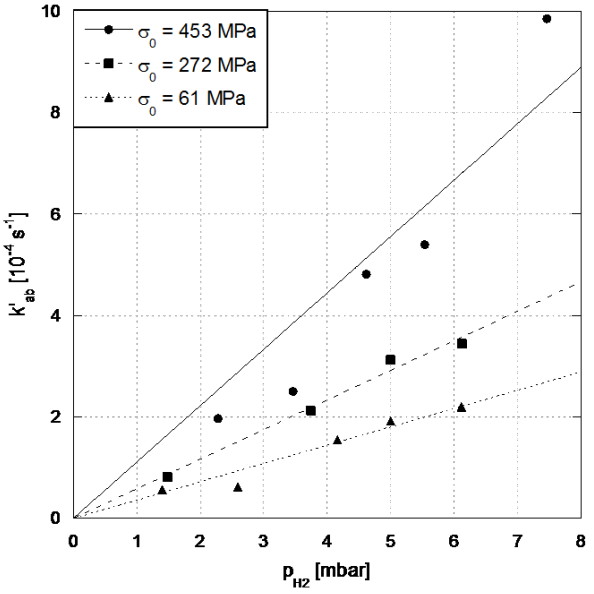

Figure 4.10: Rate constant for hydrogen absorption as a function of p_{H_2}. Linear fits are shown for each set of specimens.

The dependence of k'_{ab} on both internal stress and p_{H_2}, as unraveled in Fig. 4.10, can be quantified as follows. Firstly, based on the general expression for the hydrogen absorption rate constant k'_{ab} [230, 237, 238]:

$$k'_{ab} = A_{ab} \exp\left[\frac{-\Delta H^{0\ddagger}_{ab}}{RT}\right], \tag{4.3}$$

where $\Delta H^{0\ddagger}_{ab}$ represents the standard activation enthalpy change related to hydrogen absorption, its linear p_{H_2}-dependence unraveled in Fig. 4.10 can simply be taken into account by writing the pre-exponential factor for hydrogen absorption A_{ab} rather as a product $A'_{ab}p_{H_2}$

$$k'_{ab} = A'_{ab}p_{H_2} \exp\left[\frac{-\Delta H^{0\ddagger}_{ab}}{RT}\right]. \tag{4.4}$$

We can now also justify the observed linear p_{H_2} dependence of the data in Fig. 4.8. The latter are proportional to the hydrogen absorption rate $(dn/dt)_{ab}$ given by Eq. (3.20), where the parameter k'_{ab} is now known to include itself an additional linear p_{H_2} dependence and the last term can be shown to vanish when $n \ll 1$. This is indeed the case for the initial stages of hydriding in the p_{H_2}-range 1-10 mbar corresponding to the α-PdH phase considered here.

With respect to the stress-dependence, according to the schematic energy diagram for hydrogen ad- and absorption, reproduced from ref. [230] in Figure 4.11, the standard activation enthalpy change $\Delta H^{0\ddagger}_{ab}$ in the absence of an internal stress field is equal to the activation energy E_a needed for a hydrogen surface-to-bulk transition. In order to take into account that the host lattice undergoes a biaxial stress σ, the standard activation enthalpy change of absorption can be written as [239]:

$$\Delta H^{0\ddagger}_{ab} = E_a - \frac{2V\sigma}{3}, \tag{4.5}$$

where V represents the activation volume for hydrogen absorption, and $2\sigma/3$ is the hydrostatic stress felt by the Pd crystalline lattice. Hence, the presence of internal stress will decrease the energy barrier for H-absorption, thereby increasing the rate constant k'_{ab}. The representative activation volume V for hydrogen absorption can be extracted by combining Eqs. (4.4) and (4.5):

$$\frac{\partial \ln\left(k'_{ab}/p_{H_2}\right)}{\partial \sigma} = \frac{2V}{3RT}. \tag{4.6}$$

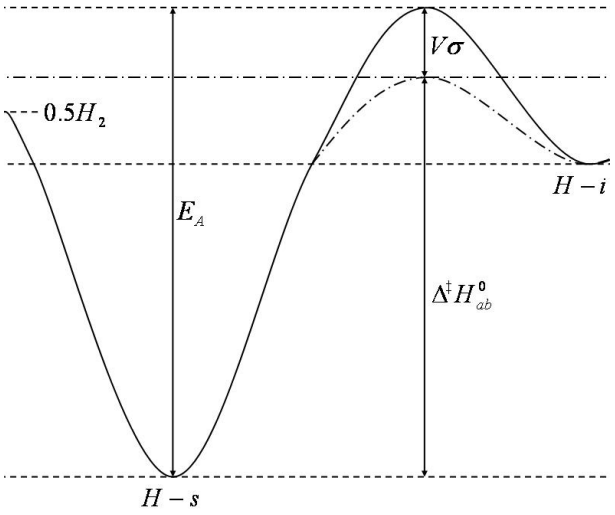

Figure 4.11: Schematic energy level diagram for H adsorption/absorption into palladium, showing the effect of internal stress on the activation enthalpy for hydrogen absorption.

In Fig. 4.12, the slopes of the k'_{ab} curves corresponding to the specimens presented in Fig. 4.10 have been plotted as a function of the growth-induced internal stress in the Pd thin films. The slope of the linear fit in this graph leads to an activation volume $V = 17.6 \pm 2.3$ Å^3 for H-absorption into our Pd thin films. This value, is higher than the 2 ± 0.3 Å^3 obtained by Baranowski and Majorowski for the activation volume for hydrogen diffusion in palladium hydride [240]. This observation seems very meaningful because in the case of diffusion, the hydrogen atoms jump between equivalent bulk interstitials sites. In the case of H-absorption, the hydrogen atoms jump from Pd surface sites, where the lattice is highly distorted as in β-PdH, to bulk interstitial sites, where the hydrogen concentration is much smaller and the lattice is much less distorted [232]. This mechanism may therefore require a much higher activation volume, as observed here. This activation volume for H-absorption, combined with an internal tensile stress on the order of 450 MPa in our nanocrystalline Pd films, leads to a decrease of the activation energy E_a for H-absorption of 3 kJ/mol. This decrease can seem small with respect to typical values for $E_a \cong 66$ kJ/mol [230] reported in the literature. However, its effect is not all negligible, leading to a factor 3.3 increase in the room-temperature absorption rate in the initial stages of hydriding corresponding to the first kinetic regime. Therefore, it may lead to interesting applications, increasing for instance the response time of integrated hydrogen sensors, or allowing to decrease the temperature

of charging/discharging in storage applications.

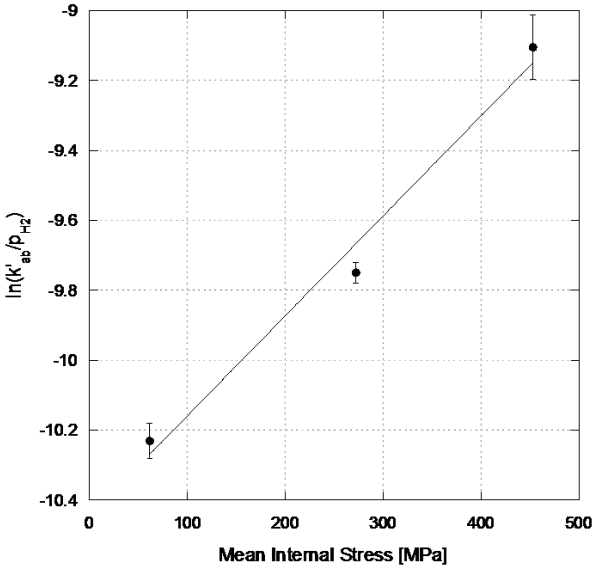

Figure 4.12: Slopes of the linear fits of Fig. 4.10 as a function of σ_0.

With respect to the data of the second, adsorption-limited kinetic regime, the rate constant for hydrogen adsorption k'_{ad} has been calculated as well, based on Eq. (3.22) and using a 4^{th} order Runge-Kutta algorithm to simulate the temporal evolution of n, just like previously preformed in previous chapter (see Fig. 3.12). As expected from the data already presented in Fig. 4.9, the fitted k'_{ad} values do not show any trend as a function of the growth-induced internal stress. Their mean values, averaged over the experimentally-covered p_{H_2} range 1-10 mbar, are, respectively, (1.1 ± 0.1)·10^{21} mbar^{-1}s^{-1} for σ_0 = 61 MPa, (1.0 ± 0.2)·10^{21} mbar^{-1}s^{-1} for σ_0 = 272 MPa and (1.3 ± 0.2)·10^{21} mbar^{-1}s^{-1} for σ_0 = 453 MPa. The absence of any p_{H_2}-dependence for k'_{ad} can be expected from the basic expression of its pre-exponential factor [101,230]. The latter can indeed be written as $1/(2\pi m_{H_2} k_B T)^{1/2}$, where m_{H_2} is the molecular mass of H_2 and k_B is the Boltzmann constant. This also allows to justify the linear fit used in Fig. 4.9, confirming the linear p_{H_2}-dependence of $(dn/dt)_{ad}$ predicted in Eq. (3.22).

Finally, the rate constant for hydrogen absorption k'_{ab} has been calculated as well in the third kinetic regime, using the same algorithm as in the first regime. Figure 4.13 shows the evolution of the bulk hydrogen concentration in this case, as calculated at different p_{H_2}-values from the internal stress data

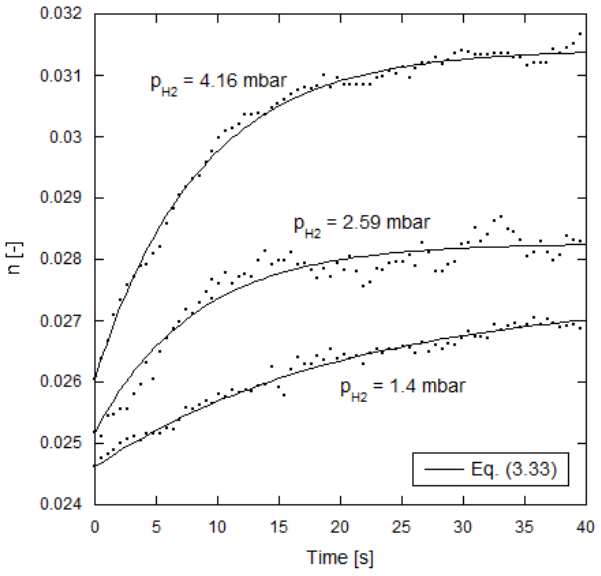

Figure 4.13: Evolution of the hydrogen bulk atomic concentration n in the third, non-linear kinetic regime for different values of p_{H_2} ($\sigma_0 = 61$ MPa). The time scale is normalised to represent for each experiment the first 40 s of the third kinetic regime. The coarse solid lines correspond to a fit using Eq. (3.33).

for the batch of specimens initially at $\sigma_0 = 61$ MPa. The time scale was normalised to represent for each experiment the first 40 s of the third kinetic regime. Excellent agreement is obtained in all cases with the constitutive Eq. (3.33), confirming that the third kinetic regime is indeed limited by absorption. The mean k'_{ab} values for the three batches of specimens, averaged over the experimentally-covered p_{H_2} range 1-10 mbar, are, respectively, (3.6 ± 0.8)·10^{-3} s^{-1} for $\sigma_0 = 61$ MPa, (3.4 ± 0.8)·10^{-3} s^{-1} for $\sigma_0 = 272$ MPa and (3.9 ± 0.9)·10^{-3} s^{-1} for $\sigma_0 = 453$ MPa. Contrary to the k'_{ab} values obtained in the first kinetic regime, no trend is visible in this case, neither as a function of the initial, growth-induced internal stress, nor as a function of p_{H_2}. As to the independence with p_{H_2}, this can be understood as follows : while k'_{ab} may depend on the surface coverage and thus on p_{H_2} at low surface coverage [230], this cannot be the case anymore when the surface coverage is at equilibrium, as is the case in the third kinetic regime. The independence with internal stress might, at first, seem more surprising, in view of the results obtained for the first kinetic regime which was also absorption-limited. However, some important differences exist with respect to the hydriding state of the Pd films in the first and the third regimes. First of all, the absolute stress in the films in the third regime is a

compressive one (cfr. Fig. 4.5). Our results therefore seem to indicate that any stress-affect on the absorption kinetics might only become significant for specimens under tension. Secondly, in the third regime, specimens are close to the equilibrium state of hydrogen uptake (n ≅ n_{eq}). This may suggest that the absorption rate only becomes stress-modulated in a specimen volume that is still relatively free of hydrogen. Finally, the values of k'_{ab} calculated for the third kinetic regime are roughly one order of magnitude higher that those of the first kinetic regime. This is in agreement with our earlier observations (see previous chapter), and was attributed to a change of the heat of adsorption of about 6 kJ/mol when the surface coverage reaches reaches a critical value at the end of the first kinetic regime. This change being twice the stress-affected change in activation energy, the kinetics of hydrogen absorption in the third kinetic regime can therefore be expected to be mainly driven by an increased surface repulsion of dissociatively chemisorbed hydrogen.

The kinetic effect that is proposed here - i.e. the influence of the stress on the energy barrier for hydrogen absorption, as illustrated in Fig. 4.11 - does not intrinsically exclude a thermodynamic effect affecting the energy level of the surface hydrogen. This would indeed also explain the change in the activation enthalpy for H-absorption. But this possibility seems unlikely for two reasons: it would affect the parameters of the adsorption-limited kinetic regime, and it would also slow down the dehydriding kinetics. None of these effects is observed in this study. Nonetheless, it has been shown above that the texture of our Pd thin films slightly changes with the deposition conditions. As Pd is mechanically anisotropic [102], this affects its elastic response upon hydrogen absorption, which may also result in a small effect on the hydriding kinetics. However, this effect cannot explain the specimens kinetic response on its own, as the elastic response of our films is mainly driven by their strong (111) texture. Let us also specify here that there is no change of the films roughness as a function of the deposition conditions (see chapter 2), so that any effect of the roughness on the films hydriding behaviour can be excluded.

4.4 conclusions

In this chapter, our high resolution in-situ curvature measurement set-up has been used to study the effect of pre-existing growth-induced internal stress on the hydriding kinetic and equilibrium behaviour of nanocrystalline Pd thin films. The analysis of the room temperature pressure-absolute stress isotherms produced here showed a shift of the $\alpha \rightarrow \beta$ phase transition lower limit towards higher values of p_{H_2} as the initial stress state in the metal increases in the compressive direction, as expected from the state of the art. The derivation of Sieverts' constant in the α phase region also showed that the microstructure

of our sputtered Pd thin films does not substantially change with the growth-induced stress.

In the kinetic analysis, three kinetic regimes have been resolved, as expected from the kinetic analysis performed in previous chapter. Unsurprisingly, the first kinetic regime has been found to be limited by absorption, the second one by adsorption, and a switch back to absorption-limited kinetics is finally observed before the final equilibrium. The analysis of the effect of internal stress on the absorption kinetics in the first kinetic regime shows that tensile stresses accelerate the hydriding kinetics, while compressive stresses dramatically slow down the hydriding kinetics. No effect of internal stress on the adsorption kinetics has been observed. A quantitative analysis of the p_{H_2} and internal stress dependence of the rate constant of the first kinetic regime enabled to calculate the activation volume for hydrogen absorption into our nanocrystalline Pd thin films. An increase by a factor 3.3 has been determined in the room-temperature absorption rate in the initial stages of hydriding, which is not at all negligible regarding, for instance, hydrogen storage and hydrogen sensing applications.

Chapter 5

Effect of microstructure on hydriding properties

As opposed the to previous chapter, whose objective was to study the effect of internal stress on the hydriding properties of the Pd thin films at constant microstructure, this chapter is dedicated to the study of the effect of microstructure on their hydriding properties at constant internal stress.

The microstructure of the Pd films has been controlled by annealing in order to eliminate part of the defects massively generated by the room temperature magnetron sputtering deposition. As the microstructural changes induced by the annealing process also result in a change of the internal stress state of the film, a specific annealing setup has been designed and installed in the course of this thesis (as explained in Chapter 2) in order to couple the annealing process to the high resolution in-situ curvature measurement system. In this chapter, the internal stress change is controlled in order to be able to compare the hydriding properties of the annealed films with as-deposited specimens exhibiting the same initial internal stress state.

Using the same approach as in the two previous chapters, the hydriding kinetics of the annealed and as-deposited specimens has been studied, firstly resulting in the identification of different kinetic regimes and the determination of the associated rate-limiting steps. A quantitative analysis of the curvature data has then been performed in order to derive relevant kinetic and thermodynamic hydriding parameters, and to compare as-deposited specimens with annealed specimens.

5.1 Experimental details

The cantilevers used in this chapter - cut 3 x 0.5 cm^2 in size from 180 μm thick, oxidized Si wafers - were coated with a 150 nm thick Pd thin film on top of a 10 nm Ti adhesion layer. As detailed in Chapter 2, and already performed in previous chapter, these metallic layers were generated by DC magnetron sputtering with a real-time monitoring of the specimen curvature thanks to the multi-beam optical sensor. Similarly to the approach considered in the previous chapter, the idea was to cover the widest possible range of growth stress states.

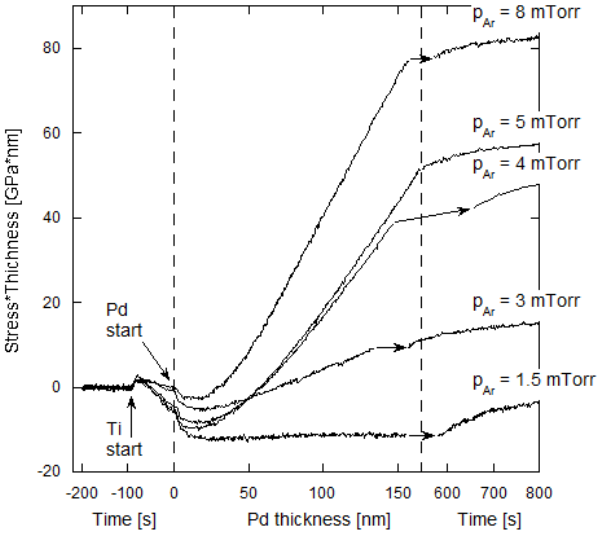

Figure 5.1: Evolution of the stress*thickness product as a function of time (before and during Ti layer deposition, as well as after Pd deposition) and Pd thickness (during Pd deposition) using different argon sputtering pressures.

But as the annealing of nanocrystalline thin metallic films above the deposition temperature leads to a volume shrinkage - due to the recovery of growth defects - and subsequently to the development of tensile stresses [214, 241], the deposition strategy has been slightly modified here. The objective was to deposit a batch of specimens with a zero internal stress level, and a set of batches with different tensile internal stress levels starting from the maximal reachable value (approximately 500 MPa at $p_{Ar} \cong 7$ mTorr). Then, the batch with internal stress close to zero was annealed so that the tensile stress produced are close to the tensile internal stress level of one of the other batches. Fig. 5.1 - showing the stress*thickness product as a function of time (before and during

Ti layer deposition, as well as after Pd deposition) and Pd thickness (during Pd deposition) - illustrates this approach. Five batches in total have been deposited to allow enough trial-and-errors, as the reachable internal stress states after annealing were a priori not known.

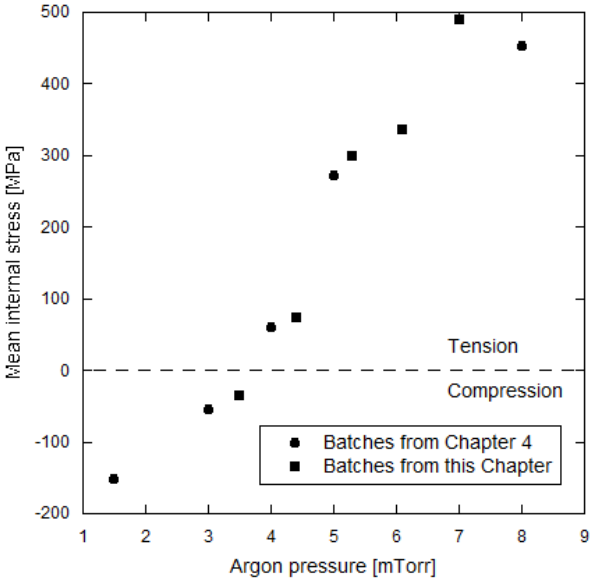

Figure 5.2: Evolution of the mean internal stress in the Pd deposit as a function of the argon sputtering pressure for the batches of Pd thin films from this chapter and from Chapter 4.

The internal stress levels after deposition are listed in Table 5.1. The latter demonstrate the excellent reproducibility of our sputtering process when compared to the data of Table 4.1, as shown in Fig. 5.2. One can indeed notice a good control of the Pd internal stress, which reflects the high stability of the deposition process. Therefore, one can logically expect a high stability of the microstructure. This is confirmed by the plane-view SEM observations performed on the five batches, which reveal a mean grain size of 24 nm, very similar to the films deposited in last chapter. XRD diffractograms did not bring new information when compared to the previous XRD studies performed in Chapters 3 and 4, only confirming the pronounced (111). The dry air exposure time has been kept below two months in order to avoid its undesirable effect on the film hydriding properties.

The experimental parameters of the annealing cycles performed in this chapter have been set the following way: a heating rate of 15°C/min has been

Table 5.1: Argon plasma pressure p_{Ar}, average growth-induced stress σ_0, thickness t_f, grain size and dry air exposure time of the Pd films studied in this work.

Plasma pressure [mTorr]	3.5	4.4	5.3	6.1	7
Growth stress [MPa]	-35	74	299	336	491
Pd thickness [nm]	156	133	146	165	157
Grain size [nm]	23	25	22	23	26
Dry air exposure [months]	<2	<2	<2	<2	<2

imposed to the furnace resistances, resulting in an effective heating rate of about 8°C/min inside the quartz tube - which is known to exhibit a high thermal inertia - from the beginning of the heating phase to the attainment of the temperature plateau, the latter taking place approximately 10 min after the end of the heating phase, as can be seen in Fig. 2.18. The cooling phase taking place after the temperature plateau is not really controlled, as the furnace resistances are simply turned off. The tube is under high vacuum during the entire annealing cycle (on the order of 10^{-6} mbar). The internal stress in the Pd thin film and the temperature inside the tube are both monitored in-situ during annealing. Nevertheless, the internal stress cannot be measured throughout the whole cycle because the laser system has not been designed to work for periods as long as half a day, which is the time necessary for the tube to reach back room temperature from temperature plateaus of several hundreds degrees Celsius. The film internal stress is therefore measured during heating, high temperature maintaining and during the beginning of cooling. When the annealing cycle is over, the stress final value is also measured during 500 sec.

The temperature plateau, as well as the time interval of this plateau, have been selected on the basis of 4-point probe electrical resistivity measurements (see Chapter 2 for more details), performed in the range [20-350°C]. The heating rate was 25°C/min, and the temperature was maintained 5 min at 350°C before the cooling phase. Cooling was performed by turning off the heating element and by making cooling water circulate in the structure of the heating stage. Voltage and temperature were measured in-situ throughout the whole temperature cycle.

The hydriding experiments presented here have been carried out at room temperature. The cantilevers from the batch initially exhibiting a growth stress of -35 MPa have been previously annealed as explained above, and the specimens from the batch initially exhibiting a growth stress of 491 MPa have directly been subjected to hydrogen cycling. As in the two previous chapters, the low p_{H_2} range [1 - 10 mbar] has been considered for the kinetic analysis performed here.

5.2 In-situ study of annealing

In this section, the annealing cycles undergone by the Pd films have firstly been optimised through 4-point probe electrical resistivity measurements, to identify the onset of defect recovery mechanisms responsible for the generation of tensile stress in the Pd film. These results, combined with practical experimental requirements, enabled to define suitable annealing conditions. The annealing cycle itself is then presented and interpreted.

5.2.1 Optimising the annealing conditions

The effect of annealing on the microstructure of as-deposited thin films can include thermally activated restoration processes like recovery of growth defects, recrystallisation and grain growth, like in classic bulk materials. But as thin films are attached to a substrate, recovery and grain growth can lead to undesirable effects like hillock formation [242,243], which are known to degrade the thin film properties. In this study, the aim was to thermally activate defect recovery - in order to change the film microstructure, and subsequently the film stress, as explained above - but without inducing grain boundary motion. It is indeed possible to induce defect recovery while keeping a negligible grain boundary motion kinetics [214, 244], since these restoration processes do not have the same activation energies. Many authors identified direct relationships between the stress evolution during annealing and the concentration of point defects [245–248] and dislocations [214, 241, 246]. The twin concentration can also be expected to be affected by annealing [249, 250], but should not give rise to volume changes, and hence to stress changes (although it is expected to affect the hydriding behaviour). Let us also specify that the annealing of Pd thin films can be expected to result in the production of a strong (111) texture [251]. However, in this study, the Pd films are strongly (111) textured in their as-deposited state, which is the reason why no evolution of the texture has been observed after annealing.

In the context of the 4-point probe electrical resistivity measurements, the temperature coefficient of resistance of the Pd films was directly deduced from the in-situ voltage and temperature measurements by the following reasoning: as the electrical measurement is performed in constant-current mode, the ratio $\Delta U/U_0$ between the voltage U at a given temperature and the voltage U_0 at room temperature is equal to $\Delta R/R_0$, where R is the specimen electrical resistance. This ratio is itself linked to the temperature coefficient of resistivity (TCR) by the following relationship [252]:

$$\frac{R}{R_0} = 1 + \alpha\,(T - T_0)\,, \tag{5.1}$$

where α is the Pd film TCR, expressed in K^{-1}. At temperatures close to the ambience, this coefficient can be expected to be constant [253], meaning that the electrical resistivity of the material evolves linearly with temperature. This is the classic behaviour of the resistivity of metals at such temperatures, driven by electron-phonon scattering. But according to Matthiessen's rule, two other sources of electron scattering exist, i.e. defects and impurities. Although our Pd thin films have already been proven to be highly pure, one also knows that the latter contain a lot of crystalline defects. Their contribution to the resistivity of the material is independent of temperature as long as their concentration is not affected by recovery, recrystallisation or grain growth mechanisms. If the temperature is high enough for such mechanisms to occur, defect-free channels are created into the lattice, thereby decreasing the TCR.

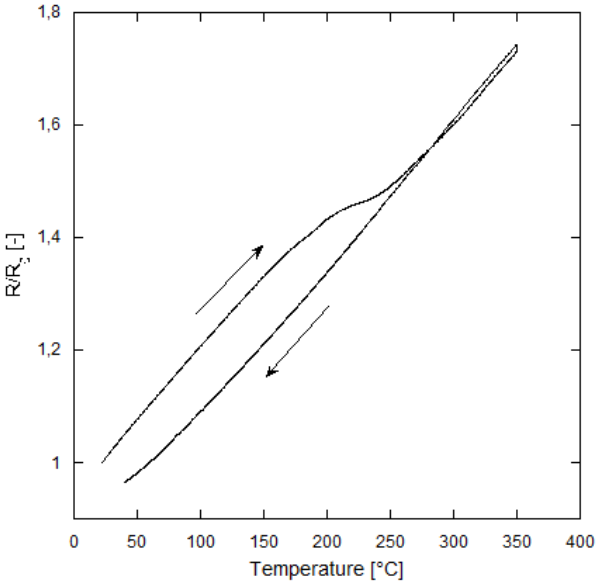

Figure 5.3: Evolution evolution of the ratio $\Delta R/R_0$ as a function of temperature during a whole heating cycle, performed in the range [20-350°C] with a heating rate of 25°C/min and a 5 min high temperature maintaining.

Fig. 5.3 shows the evolution of the ratio $\Delta R/R_0$ as a function of temperature during a heating cycle performed on a cantilever covered with a Pd film specimen. The specimen has the same dimensions as the specimen used

for hydriding experiments because after annealing, the same specimen is used in the same experimental setup (see Chapter 2) for a hydriding experiment in order to keep the same experimental conditions, and, among others, the same clamping.

The behaviour of the ratio $\Delta R/R_0$ during heating up to 200°C shows that the Pd thin film is responding normally to the electron flow travelling through it, without any apparent change of the concentration of defects in the film. The slope of the curve, i.e. the TCR of the Pd film, starts to decrease between 200 and 210°C, indicating the onset of recovery phenomenons affecting part of the crystalline defects present in the film. The temperature plateau at which the Pd films will be maintained during the annealing experiments must thereby be chosen above 200°C. Annealing tests with in-situ curvature measurements have then been run in order to choose the appropriate temperature plateau, taken into account that the stress level reached at the end of the annealing cycle must be close to the growth stress level of one of the other batches, and that the annealing time should not be too long in order to be able to measure the specimen curvature in-situ during the whole region of the temperature plateau. As will be detailed below, a temperature plateau of 300°C, combined with an annealing time of 20 minutes, and performed on a cantilever from the batch initially exhibiting a growth stress of -35 MPa, gave rise to a final internal stress of 490 MPa, very close to the specimen exhibiting an as-deposited internal stress of 491 MPa. These experimental conditions have therefore been chosen for the kinetic analysis performed in this chapter, as well as the batches deposited at p_{Ar} = 3.5 and 7 mTorr.

The rest of the heating cycle shown in 5.3 shows that the specimen resistance is slightly increasing during the temperature plateau, probably because the specimen temperature still slightly increases in this time interval. The cooling phase only reflects the temperature dependence of the thermal resistivity of the Pd film, thereby exhibiting the same TCR as in the interval [20-200°C] of the heating phase (before defect recovery starts), as expected.

The TCR of the films has been estimated in the interval [20-200°C] from test specimens with different Pd film thicknesses in order to compare it to available literature data. The results - shown in Fig. 5.4 - indicate that the TCR of our nanocrystalline Pd thin films is smaller than what is usually measured on bulk Pd specimens (typically $3.7 \cdot 10^{-4}$ K^{-1}), as expected [254]. One can also clearly see that the TCR increases with increasing film thickness, as previously reported in similar studies [252, 255]. According to Wedler and Alshorachi, the TCR of a thin film can be expressed as a function of its thickness as follows [252]:

$$\alpha = \alpha_0 \left(\frac{1}{1 + K' l_0 / t_f} \right), \tag{5.2}$$

where α_0 is the TCR of the bulk material having the same density of imperfections as the film. This value is then smaller than the value of $3.77 \cdot 10^{-3}$ K^{-1} for classic bulk specimens, shown in Fig. 5.4 and taken from Ref. [252]. l_0 is the mean free path of the electrons and K' is a proportionality factor. A reliable value of l_0 is impossible to obtain, as the electrons in Pd do not behave as a free electron gas. These two last factors thereby cannot be estimated separately. A fit of the Pd films TCR with Eq. (5.2) is performed in Fig. 5.4, with α_0 and $K'l_0$ as free parameters. Our data appear to be in excellent agreement with these of Wedler and Alshorachi, confirming the trend previously expected by them. More quantitatively, the fit results in $\alpha_0 = 3.1 \pm 0.2 \cdot 10^{-3}$ K^{-1}, smaller than the bulk Pd value, as expected. As already concluded from the previous derivations of Sieverts' constant in Chapters 3 and 4, the thin Pd films contain a high concentration of crystalline defects.

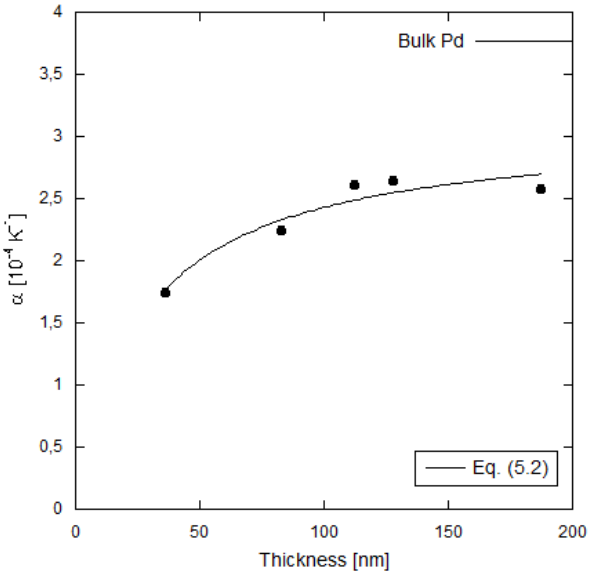

Figure 5.4: Temperature coefficient of resistance of Pd thin films with different thicknesses, fitted with Eq. (5.2). The value for bulk Pd is also shown (taken from Ref. [252]).

During the preliminary tests of the heating procedure, partly aiming at the adjustment of the temperature plateau, several annealed specimens have been produced, exhibiting different levels of internal stress and different microstructures. These specimens have been subjected to plane-view SEM observation in order to qualitatively determine which type of defect elimination process took place on the temperature plateau of 300°C considered here, as well as above and

below this plateau. As shown in Fig. 5.5, the grain size is not affected by the annealing conditions chosen for the present study, therefore excluding recrystallisation and grain growth mechanisms. Increasing the annealing time above 1h and the temperature above 350°C gives rise to a very different microstructure. The grain size distribution is now very wide, from grain sizes on the order of 100 nm to grain sizes on the order of 10 nm, partly even smaller than the original, as-deposited grains. The larger grains tend to form hillocks, as commonly observed on thin films undergoing important thermal stress [242, 243]. These features are undesirable as regards applications requiring a stable structure of the films, especially when the film has to be electrically active [256, 257]. Further increasing the annealing temperature only shows that the mean grain size increases, and consequently the number of hillocks, as expected. Note also that the final internal stress levels reached by the Pd thin films annealed at 370°C and 484°C are on the order of 1 GPa, indeed much too large to be reachable by as-deposited specimens.

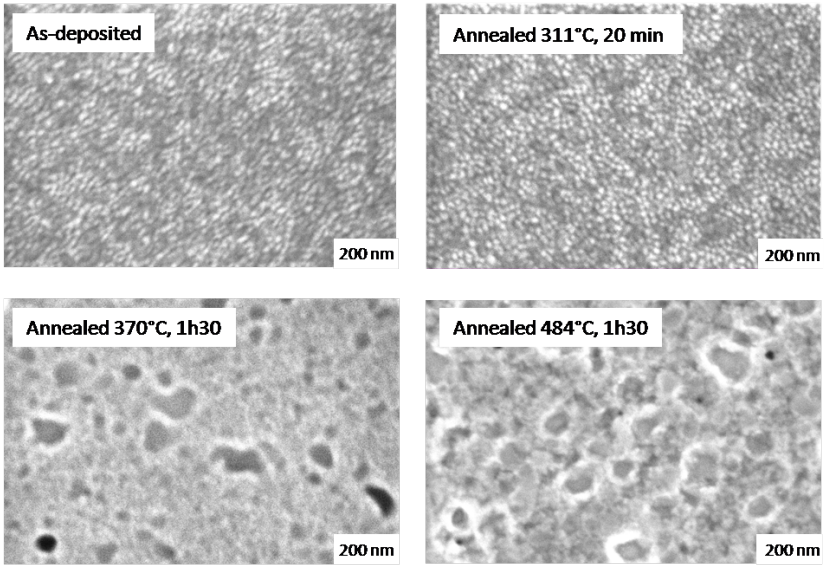

Figure 5.5: Plane-view SEM micrographs of Pd thin films, as deposited and with different annealing conditions.

To conclude, one can state that suitable annealing conditions have been found in order to obtain thin Pd films with presumably the same internal stress and different microstructures. These annealing conditions result in the recovery of growth defects such as dislocations and twins present in the Pd lattice, but not to recrystallisation and grain growth mechanisms. This statement is

confirmed by the 4-point probe resistivity measurements, as well as by the in-plane SEM observations.

5.2.2 Annealing cycle

Now that the optimal annealing conditions have been found out, one can apply them on a set of specimens from the batch initially exhibiting a growth stress of -35 MPa (see previous section), while measuring in-situ the Pd thin film internal stress and the temperature inside the quartz tube. Fig. 5.6 shows such an annealing cycle performed under high vacuum conditions.

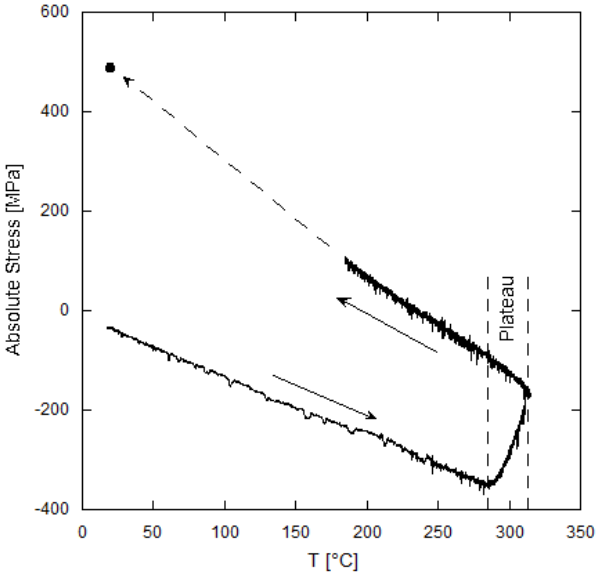

Figure 5.6: Evolution of the internal stress as a function of the temperature inside the quartz tube. The Pd thin film internal stress has been measured during the first 5000 seconds of the annealing cycle, which includes the heating phase, the temperature plateau and part of the cooling phase. The last point is the mean of a 500 sec ex-situ stress measurement performed at room temperature.

During the annealing cycle presented in Fig. 5.6, the biaxial stress σ undergone by the Pd thin film can be divided into the following structure-dependent components [214]:

$$\sigma = \sigma_0 + \sigma_i + \sigma_{th} + \sigma_e, \tag{5.3}$$

where σ_i is the intrinsic stress, consisting, in the case of thin film annealing, in the contribution from a structure evolution mechanism, i.e. volume changes (shrinkage) due to the elimination of growth defects such as grain boundaries, dislocations and point defects [246]. This contribution is tensile, as opposed to hydriding-induced stress. The thermal stress component σ_{th} depends on both thermal expansion coefficients of the film (α_f) and of its substrate (α_s), according to the following law [214, 258]:

$$\sigma_{th} = \frac{E_f}{1-\nu_f}\left(\alpha_s - \alpha_f\right)\left(T - T_d\right), \tag{5.4}$$

where T is the temperature at which σ_{th} is measured and T_d in the film deposition temperature. In this work, T_d is room temperature, and consequently $(T - T_d)$ is positive during the entire annealing cycle. Therefore, the sign of the thermal stress depends on the difference between the thermal expansion coefficients of the thin film and the substrate. Here, this stress contribution is expected to be compressive, as $\alpha_s = 0.56 \cdot 10^{-6}$ K^{-1} [259] and $\alpha_f = 11.8 \cdot 10^{-6}$ K^{-1} [218]. The extrinsic stress σ_e - attributed to structural misfit, phase transformation, precipitation, plastic or creep deformation, chemical reactions, etc. [241] - can be neglected here, taken in to account the yield stress of nanocrystalline Pd in tension and in compression [107, 226].

During the heating phase in Fig. 5.6, the total absolute stress change ($\sigma - \sigma_0$ in Eq. (5.3)) is equal to -311 MPa. Knowing that $E_f = 121$ GPa and $\nu_f = 0.39$ [106], and using Eq. (5.4), one obtains σ_{th} = -602 MPa. This results in $\sigma_i = -311 + 602 = 291$ MPa. This contribution is tensile, as expected. Its substantial amount shows us that an important concentration of growth defects is recovered in the heating phase, which is logical because the temperature is above the Pd deposition temperature right from the beginning of the experiment. The temperature of the quartz tube then slightly increases when the temperature of the furnace resistances is kept constant during the temperature plateau, as already explained in Chapter 2. During this temperature plateau, the stress goes in the tensile direction, as expected because the additional thermal stress is very small. The total absolute stress change is equal to 182 MPa, and the thermal stress calculated from Eq. (5.4) is equal to -45 MPa. At 300°C, the amount of defects recovered is important, thus giving rise to an intrinsic stress of 227 MPa. Finally, the total absolute stress change during the cooling phase is equal to 654 MPa, very close to the 647 MPa predicted by Eq. (5.4). This indicates that the defects recovery process that has been activated through this thermal cycle is almost complete, and that the amount of tensile intrinsic

stress produced during the cooling phase is very small (7 MPa in Fig. 5.6). This annealing cycle then results in the generation of an intrinsic stress of 291 + 227 + 7 = 525 MPa due to the recovery of growth defects. This results of a final tensile internal stress of 490 MPa, taken into account the -35 MPa growth stress of the Pd film.

This thermal cycle has thus been applied to 5 cantilevers before exposure to hydrogen. The in-situ curvature measurements performed on these specimens showed a good reproducibility of the thermal cycle, as the mean value of the internal stress obtained after annealing in the same conditions is 518 ± 15 MPa, close enough to the 491 MPa obtained with the Pd thin film deposited at p_{Ar} = 7 mTorr. Therefore, two sets of Pd film specimens are available with very close internal stresses and different defect densities, as a good basis for a quantitative kinetic analysis. Moreover, as the grain size does not change with the annealing conditions selected here, the effect of microstructure will be studied independently from the contribution of the grain boundaries.

5.3 Hydriding cycle

Fig. 5.7 shows two hydriding cycles recorded at very similar hydrogen partial pressures. One of the Pd films used in these experiments has been directly cut out of the wafer exhibiting 491 MPa internal stress, while the second one comes from the most compressive Pd deposit (-35 MPa) and has undergone an annealing cycle into the quartz tube before being subjected to hydrogen cycling. These films have very close internal stress levels before hydrogen introduction, as can be seen in Fig 5.7.

From Fig. 5.7, it appears that the as-deposited thin film specimen has a much faster hydriding kinetics than the annealed specimen. The time needed for chemical equilibrium to be reached between gaseous hydrogen in the quartz tube and atomic hydrogen inside the Pd thin film differs of one order of magnitude, the latter raising from 100 sec for the as-deposited specimen to 1000 sec for the annealed specimen. This is the expected behaviour for a film containing less growth defects. More specifically, some of these growth defects - namely, dislocations [144], twins [155] and vacancies [151, 152] - have recently been shown to act as pathways for hydrogen transport, thereby potentially accelerating the kinetics of mechanisms such as hydrogen dissociation on the surface, surface-to-bulk transition or diffusion. This issue will be quantitatively considered below, through the application of the kinetic model developed in Chapter 3.

Let us secondly address the assumption of elastic deformation in the Pd films, which is mandatory in order to properly derive the hydrogen content in

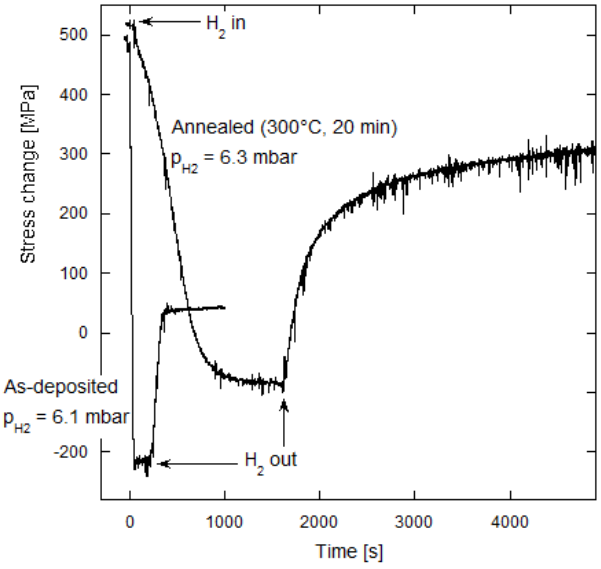

Figure 5.7: Evolution of the compressive stress change as a function of time during two hydriding cycles recorded, respectively, using an as-deposited Pd thin film and a film annealed 20 min at 300°C.

the film with Eq. (3.3). Firstly, the tensile as-deposited growth stress of the Pd film specimens is, in the worst case, on the order of 500 MPa, as well as the internal stress reached after annealing. This value is below the nanocrystalline Pd tensile yield stress [107]. Furthermore, as the present kinetic analysis has been limited to the low p_{H_2} range [1 - 10 mbar], and as we already showed in the two previous chapters that this range ensures to remain in the α phase of the palladium hydride, one can expect the absolute internal stress levels at equilibrium to be low enough to avoid plasticity effects accompanying the α to β phase transition. As can be seen in Fig. 5.7, the absolute internal stress at equilibrium is far below the 1 GPa compressive yield strength of nanocrystalline palladium measured by Youngdahl et al. [226]. Even at $p_{H_2} = 10$ mbar, the absolute stress indeed does not exceed -350 MPa.

Still regarding the equilibrium absolute stress, a compressive stress difference of 129 MPa is observed in Fig. 5.7 between the as-deposited specimen and the annealed specimen. This difference is small, but it may be significant if it becomes systematic for all the p_{H_2} values considered here. Indeed, while acting as pathways for hydrogen transport, growth defects can also act as trap sites for monoatomic hydrogen, thereby also affecting the thermodynamics of hydriding. The amount of hydrogen present in the Pd lattice at equilibrium

- and therefore the internal compressive stress in the film - can thus be more important with Pd thin films containing more growth defects. This trapping effect has already been the object of extensive studies [71], especially in the case of dislocations [130][1] and vacancies [131, 263]. Let us note here that grain boundaries also act as hydrogen traps [129, 264], but this effect is not an issue here as the fraction of grain boundaries is the same in the as-deposited and in the annealed specimens. Precipitates can act as traps as well (typically in steel embrittlement applications [132]), which cannot be the case here.

Once the equilibrium stress plateaus have been reached in Fig. 5.7, the gas mixture has been pumped out of the chamber. On the one hand, one can see that the desorption kinetics is affected as well, also more rapid here for the most defected specimen. But, one the other hand, the residual compressive stress change is equal to 423 MPa with the most defected specimen, while it is only 215 MPa with the annealed specimen. In Chapter 3, the origin of this compressive stress level has already been addressed, leading to the conclusion that it comes from highly stable, residual hydrogen remaining in the Pd film, and that it cannot be the result of plasticity effects. Consequently, this would mean that more hydrogen remains in the most defected film after pumping the gas out of the chamber. This observation makes sense, and will also be quantitatively discussed the in next section.

5.4 Hydriding thermodynamics

In this study, 5 cantilevers from the batch initially exhibiting 491 MPa growth stress have been subjected to hydrogen cycling in the low p_{H_2} range [1 - 10 mbar], as well as 5 specimens from the batch exhibiting 518 MPa internal stress after annealing 20 min at 300°C. In Fig. 5.8, the equilibrium absolute stress change has been plotted as a function of $p_{H_2}^{1/2}$ for these 10 experiments. As already explained in Chapter 3, this enables computing the well known Sieverts' constant with Eq. (3.4).

The calculation of Sieverts' constant for the two batches considered in Fig. 5.8 results in $K_s = 2.4 \pm 0.5$ atm$^{1/2}$ for the as-deposited batch and $K_s = 2.2 \pm 0.3$ atm$^{1/2}$ for the annealed batch. As expected, these values indicate that the Pd films contain a high concentration of structural defects [62]. But, a shift of 180 MPa of the fit performed in Fig. 5.8 towards more

[1] In the particular case of dislocations, studies have shown that edge dislocations exhibit a strong interaction with hydrogen [142,260], while screw dislocations interact weakly [261,262]. This is due to the dilatational strain field of the edge dislocation, which interacts much stronger with the hydrostatic stress component of the hydrogen atom than the dominant shear strain component of the screw dislocation [71].

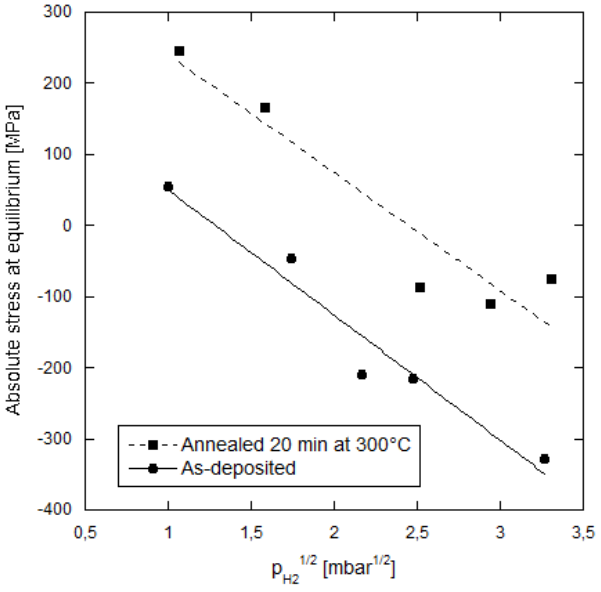

Figure 5.8: Equilibrium absolute stress as a function of $p_{H_2}^{1/2}$ in the α phase region. Two batches with very similar internal stress are compared, one being subjected to hydrogen cycling as-deposited and the other one after annealing 20 min at 300°C.

compressive values is observed for the annealed specimen, independent of the hydrogen partial pressure. This would mean that, even if the most defected specimens contain more hydrogen, they involve a sensitivity to the hydrogen partial pressure in the chamber similar to the annealed specimen. Consequently, part of the hydrogen is absorbed by the Pd films must be located in saturable trapping sites, which are readily fully filled over the whole p_{H_2}-range considered in this study. Hydrogen trapping sites in metals and metallic alloys are indeed commonly divided into unsaturable and saturable sites [227, 265], part of the latter being irreversible [266, 267], i.e. potential wells being too deep to allow the hydrogen atoms to escape without external energy source. Frappart et al. recently found out that the irreversibly trapped hydrogen concentration is constant in the elastic regime [268], which is consistent with our results. This is not the case for the interstitial hydrogen and the reversibly trapped hydrogen, which are both sensitive to the hydrogen partial pressure. The potential wells corresponding to the reversible traps are deeper than these of the octahedral interstitial sites of the Pd lattice, but the reversibly trapped hydrogen is still in equilibrium with the interstitial hydrogen. The Sieverts' constant of a material

thereby reflects the presence of interstitial hydrogen and reversibly trapped hydrogen. Consequently, our results indicate that the reversible traps are not significantly modified by annealing, while irreversible traps - like dislocation cores [268] - seem to be affected.

If the as-deposited specimens contain more irreversible traps than the annealed specimens, this would also mean that the residual compressive stress change observed at the end of the hydriding cycles - reflecting the presence of irreversibly trapped hydrogen, as already inferred in Chapter 3 - must be higher when submitting an as-deposited Pd thin film to hydrogen cycling. As already observed in the experiments from Chapters 3 and 4, the residual compressive stress changes can be considered as constant for the two batches considered here. Their values are, respectively, 403 ± 31 MPa for the as-deposited Pd thin films and 192 ± 14 MPa for the annealed Pd thin films. A compressive stress difference of 211 MPa is then observed, confirming the statement that a higher concentration of irreversible trap sites are present in the as-deposited specimens. Moreover, this value fits well with the 180 MPa observed at equilibrium.

5.5 Hydriding kinetics

In this section, we use the same approach as in the two previous chapters in order to qualitatively and quantitatively analyse the hydriding kinetics of the Pd thin films. The applicability of the kinetic model is firstly discussed, and the rate-limiting steps of the hydriding mechanism are identified. A quantitative kinetic analysis is then performed in order to access relevant kinetic/thermodynamic hydriding parameters. The energetics of hydrogen trapping in Pd crystalline defects is finally addressed by studying the calculated rate constants for hydrogen absorption and adsorption.

5.5.1 Kinetic model: applicability and qualitative analysis

As in the kinetic analyses performed in the two previous chapters, the present kinetic analysis has been limited to the low p_{H_2} range [1 - 10 mbar], and the kinetic model - able to provide a self-consistent interpretation of the room temperature hydriding cycle in this range - is an appropriate tool in the context of this study. Here again, one will start from the observation that two mechanistic steps are potentially rate-limiting, i.e. H_2 adsorption and its dissociative chemisorption on the Pd surface (Eq. (3.5)) and surface-to-bulk transition (Eq. (3.6)). As the present hydriding experiments have been performed at room temperature, the diffusion time of the hydrogen atoms in the Pd films - on the order

of the millisecond - is too small to be considered as potentially rate-limiting in this kinetic model. As to the latter, its constitutive equations have been derived by assuming one of the two mechanistic steps to be rate-limiting, and the other one to be in a pseudo steady-state, as commonly performed in chemical kinetics when dealing with complex second order reactions [234]. The time evolution dn/dt of the bulk H/Pd atomic ratio when the rate-limiting step is, respectively, absorption and adsorption, have thus been derived in the forms of Eqs. (3.20) and (3.22).

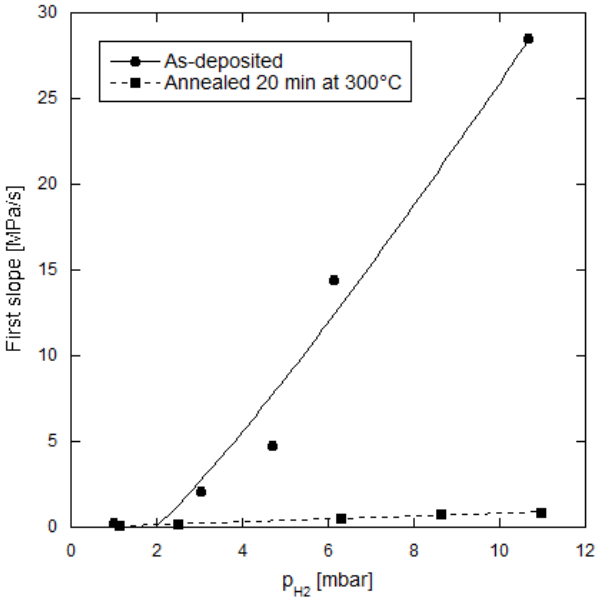

Figure 5.9: Slope of the first linear kinetic regime as a function of p_{H_2}, fitted with Eq. (3.20) and including the p_{H_2}-dependence of k'_{ab} (Eq. (4.4)).

Unsurprisingly - when taking into account the hydriding profile of the stress-time curves produced by the hydriding setup on both e-gun evaporated and magnetron sputtered specimens throughout this thesis work - the hydriding cycles performed on the Pd thin films studied here show three characteristic kinetic regimes (see Fig 5.7). A linear kinetic regime is firstly observed, and has been shown to be limited by absorption. A transition to a second linear kinetic regime - limited by adsorption - is then systematically observed, as a result of a change of the heat of adsorption in the positive direction as the surface coverage reaches a critical value. Later on in the hydriding cycle, the adsorption equilibrium becomes reached, but hydrogen atoms are still absorbed into the bulk. This marks the beginning of a third, nonlinear kinetic regime,

limited by absorption. This last regime ends when the absorption equilibrium is finally reached (see Chapter 3 for more details).

The slopes of the first and second kinetic regime have been plotted as a function of p_{H_2} in, respectively, Figures 5.9 and 5.10. Fig. 5.9 firstly shows that the microstructure of the Pd films has an important effect on their absorption velocity, the annealed specimens being critically slowed down in the first kinetic regime. At least one of the parameters of Eq. (3.20) must then be affected by microstructure. As K_s has already been shown to be very similar for the two batches, this microstructure-sensitive parameter should be k'_{ab}.

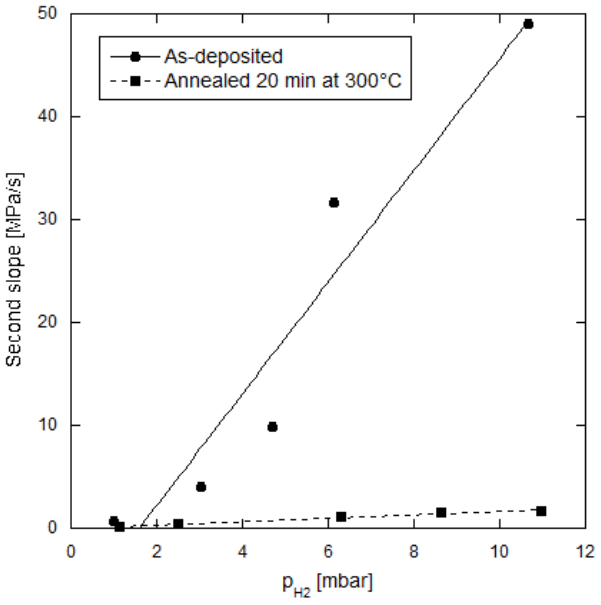

Figure 5.10: Slope of the second linear kinetic regime as a function of p_{H_2}, fitted with Eq. (3.22).

Fig. 5.10 shows the same trend, i.e. an important decrease of the absorption velocity of the annealed Pd thin films in the second, adsorption-limited kinetic regime. As opposed to the effect of internal stress, which has been shown in last chapter to have no effect on the adsorption-related parameters of Eq. (3.22), the effect of microstructure affects both absorption and adsorption-related parameters. As regards the parameters Eq. (3.22), K_{ab} should indeed stay the same if the concentration of reversible traps present on the surface and in the bulk is not significantly modified, as discussed in previous section. One may thereby expect k'_{ad} to be affected by microstructure as well. Intuitively,

one may indeed expect growth defects from both the Pd thin film surface and bulk to be affected by annealing. Such a modification of the microstructure of the host material results in a decrease of the concentration of the deepest potential wells generated by part of the growth defects, which accelerate the hydriding kinetics when they are present.

5.5.2 Quantitative analysis: rate constants and energetics of hydrogen trapping

Let us firstly address the case of the rate constant for hydrogen absorption k'_{ab} in the first kinetic regime. Eq. (3.20) - representing the evolution of n for an absorption-limited kinetic regime - can be directly integrated, resulting in Eq. (3.33). The fitting constant C_2 is highly relevant, as it provides a direct access to k'_{ab} (see Eq. (3.32)). Fig. 5.11 shows the obtained values of k'_{ab} in the first kinetic regime for the experiments performed on the two batches considered in this study, already shown in Fig. 5.9.

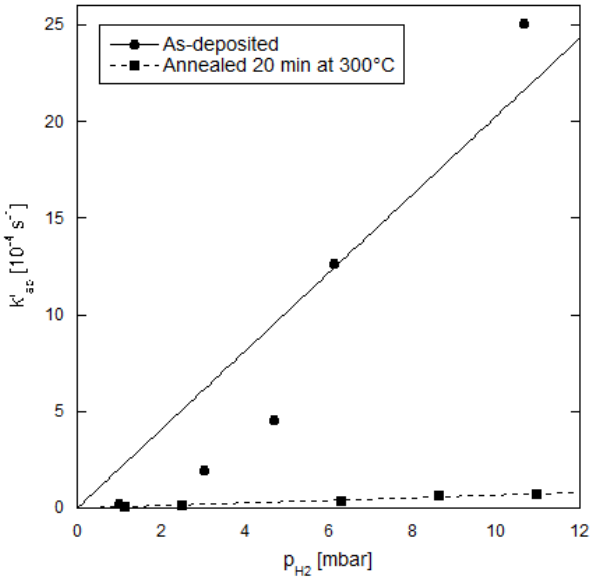

Figure 5.11: Rate constant for hydrogen absorption as a function of p_{H_2}. Linear fits are shown for each set of specimens.

A factor 30 is observed between the k'_{ab} values of the annealed specimen and the as-deposited specimen. This was expected from the internal stress be-

haviour shown in Fig. 5.9. As already observed in the kinetic study performed in last chapter, the rate constant for hydrogen absorption exhibits a linear dependence with p_{H_2}. This dependence has been taken into account here by integrating it in the pre-exponential factor of k'_{ab}, according to Eq. (4.4). The slopes of the linear fits shown in Fig. 5.11 can then be expressed as:

$$\begin{cases} \dfrac{k'_{ab,dep}}{p_{H_2}} = A'_{ab,dep} \exp\left[\dfrac{-\Delta H^{0\ddagger}_{ab,dep}}{RT}\right], \\ \dfrac{k'_{ab,an}}{p_{H_2}} = A'_{ab,an} \exp\left[\dfrac{-\Delta H^{0\ddagger}_{ab,an}}{RT}\right], \end{cases} \tag{5.5}$$

where the subscripts *dep* and *an* are indicative for the as-deposited batch and the annealed batch, respectively. The results from Fig. 5.11 result in $k'_{ab,dep}/k'_{ab,an} = 30.2 \pm 4.3$. Two possibilities can be considered here to explain the differences between $k'_{ab,dep}$ and $k'_{ab,an}$, i.e. an effect of microstructure on the pre-exponential factor A'_{ab} and an effect of microstructure on the activation enthalpy change for hydrogen absorption $\Delta H^{0\ddagger}_{ab}$. One will discuss here the implications of these hypotheses.

Let us firstly assume that $\Delta H^{0\ddagger}_{ab,dep} = \Delta H^{0\ddagger}_{ab,an}$, and that the thin film microstructure only affects the pre-exponential factor for hydrogen absorption. This would immediately result in $A'_{ab,dep}/A'_{ab,an} \cong 30$. In their hydrogen membrane permeation model, Ward et al. stated that the jump attempt frequency for bulk-to-surface transition can be considered as very similar to that for diffusion in bulk Pd because the H atom is jumping from a bulk interstitial site in both cases [230]. Consequently, the pre-exponential factor for hydrogen bulk-to-surface transition is proportional to the jump attempt frequency for hydrogen diffusion. In the same study, these authors showed that the pre-exponential factor for hydrogen surface-to-bulk transition (A'_{ab} here) is consequently directly proportional to the jump attempt frequency for hydrogen diffusion as well[2]. Recent extensive studies of the effect of hydrogen trapping on the diffusion mechanism already showed that the jump attempt frequency for hydrogen diffusion is lowered by the trapping phenomenon because part of the hydrogen atoms are located in potential wells that are deeper than the regular lattice sites [265, 267, 269]. This undoubtedly rules out the hypothesis that $\Delta H^{0\ddagger}_{ab,dep} = \Delta H^{0\ddagger}_{ab,an}$ in this study.

Secondly, on can assume that $A'_{ab,dep} = A'_{ab,an}$ and examine the effect of microstructure on k'_{ab}. If E_a is the activation energy needed for a hydrogen surface-to-bulk transition in the as-deposited film and E_d is the energy change due to the recovery of growth defects, one would have:

[2]This is a direct consequence from the proportionality between k'_{ab} and k''_{ab} (Eq. (3.9)).

$$\begin{cases} \Delta H^{0\ddagger}_{ab,dep} = E_a, \\ \Delta H^{0\ddagger}_{ab,an} = E_a + E_d. \end{cases} \tag{5.6}$$

In our case, one obtains $E_d = \ln 30 \cdot RT \cong 8.5$ kJ/mol by combining Eqs. (5.5) and (5.6). This means that part of the surface defects are eliminated by annealing as well, resulting in an increase of the activation energy for surface-to-bulk transition, thereby slowing down the absorption kinetics (this situation is schematically illustrated in Fig. 5.12). This conclusion is realistic, as the energy of structural defects in palladium does not exceed 60 kJ/mol [270], while the energy of regular surface sites is higher, on the order of 100 kJ/mol [87, 101]. Moreover, as discussed above, one may expect $A'_{ab,dep} < A'_{ab,an}$. Consequently, we have shown here that reduction of the activation energy for surface-to-bulk transition in nanocrystalline Pd by defect introduction can be on the order of 10%. This result may lead to interesting engineering applications like hydrogen storage materials, hydrogen separation membranes of hydrogen detection.

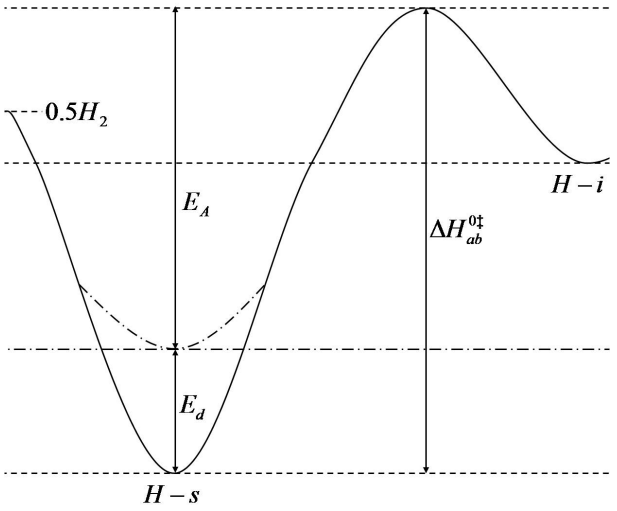

Figure 5.12: Schematic energy level diagram for H adsorption/absorption into palladium, showing the effect of microstructure on the activation enthalpy for hydrogen absorption.

As already explained before in Chapters 3 and 4, Eq. (3.22) can be solved by using a 4^{th} order Runge-Kutta algorithm to simulate the temporal evolution of n in the second, adsorption-limited kinetic regime. k'_{ad} has been extracted from this simulation for the two batches considered here. As expected from the trends showed in Fig. 5.10, k'_{ad} is higher for the as-deposited batch ((2.6 ±

0.5)·10^{18} mbar^{-1}s^{-1}) than for the annealed batch ((7 ± 2)·10^{16} mbar^{-1}s^{-1}). The jump attempt frequency for hydrogen adsorption seems to be increased by the presence of additional surface sites generated by the surface defects induced by thin film growth. As also inferred in Chapter 4, no trend as a function of p_{H_2} is visible in the k'_{ad} data.

Finally, the rate constant for hydrogen absorption has been calculated in the third kinetic regime, also with Eq. (3.33). One can state from Fig. 5.13 - showing the temporal evolution of n calculated at different p_{H_2}-values for the annealed batch - that the third kinetic regime is indeed limited by absorption. As expected from the calculations performed in the two last chapters in that kinetic regime, no trend is again visible as a function of p_{H_2} in the k'_{ab} data. The as-deposited batch provides k'_{ab} = (4.2 ± 1.7)·10^{-3} s^{-1} and the annealed batches provides k'_{ab} = (2.5 ± 0.7)·10^{-4} s^{-1}. This confirms the trend discussed above, in that the kinetics of hydrogen absorption is accelerated for the as-deposited batch because the activation enthalpy change decreases when more surface defects are present.

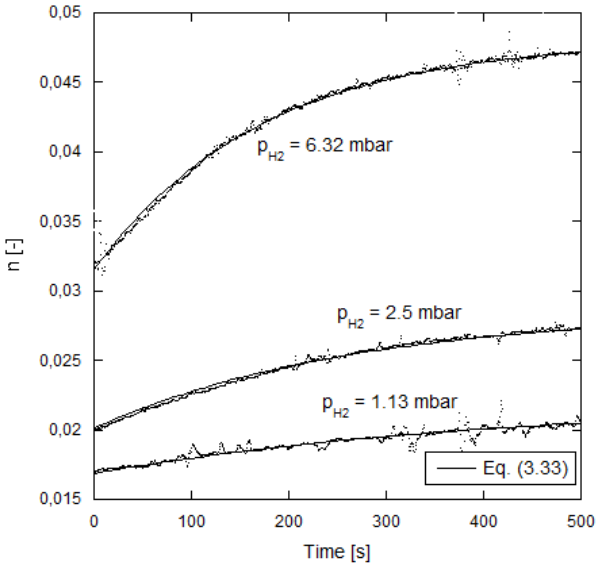

Figure 5.13: Evolution of the hydrogen bulk atomic concentration n in the third, non-linear kinetic regime for different values of p_{H_2} (batch annealed 20 min at 300°C). The time scale is normalised to represent for each experiment the first 500 s of the third kinetic regime. The coarse solid lines correspond to a fit using Eq. (3.33).

The kinetic effect that has been addressed here is clearly due to the microstructural changes in the Pd thin films upon hydrogen absorption, but more characterisation work is needed in order to deeply understand which defects have been recovered, and in which concentration. High resolution TEM analyses have been planned in this respect. Even if the grain size has not been significantly affected by the films annealing conditions, changes in the surface morphology cannot be excluded at this stage. This should also be included in our future characterisation work, namely in the form of AFM measurements.

5.6 Conclusions

In this chapter, an original annealing setup - combined with the high resolution in-situ experimental setup - has been successfully designed and tested. It has firstly been shown how the Pd thin films annealing conditions have been adjusted in order to obtain a given internal stress change and microstructure change. In particular, the internal stress has been successfully adjusted in order to obtain specimens with very similar internal stress and different microstructures. Once the appropriate annealing conditions have been chosen, the corresponding stress-temperature cycles have been discussed in details. Tensile internal stress are produced upon thermal cycling through the elimination of part of the growth defects.

The study of hydriding equilibrium at room temperature for the as-deposited and annealed specimens enabled to calculate the well-known Sieverts' constant for the two batches. A deep analysis of the internal stress level at equilibrium and after pumping down brought the following conclusions: the concentration of reversible traps in the palladium lattice is not significantly affected by annealing, while the concentration of saturable, irreversible traps seems to be decreased. A high resolution TEM analysis has been planned in order to verify these conclusions.

The use of the kinetic model allowed again to identify the rate-limiting steps involved in the hydriding mechanism of the Pd thin films. An important effect of microstructure on both the adsorption and absorption kinetics has been observed. The quantitative kinetic analysis confirmed these tendencies, by showing an important effect on both rate constants for dissociative adsorption and surface-to-bulk transition. In particular, it has been shown that the absorption kinetics of the as-deposited specimens is accelerated as a result of a destabilisation of the thin film surface which is on the order of 10% of the energy of the regular surface sites.

Conclusions and perspectives

In this thesis work, the effects of internal stress and microstructure have been independently investigated in Pd thin films submitted to hydrogen cycling. The high resolution analysis of their hydriding kinetics enabled for a self-consistent interpretation of the hydriding mechanism, involving the determination of multiple kinetic regimes and rate limiting steps. Our kinetic model then enabled to quantitatively address the issues of the influence of internal stress and microstructure.

The presentation of our experimental setup and methods in Chapter 2 firstly enabled to verify the validity and accuracy of the stress derivation through the use of Stoney's equation in the context of this thesis work. The validity and limitations of the high resolution curvature measurement have then been studied, showing a high accuracy and stability of the measurements in vacuum and gases. The application of the multi-beam optical sensor to the deposition and hydriding experiments has been successfully performed. The development of an original setup able to perform accurate curvature measurements in both annealing and hydriding experiments has also been achieved. As to the latter, critical convection issues linked to the high temperature conditions have been controlled in order to enable a stable curvature measurement without loosing too much resolution. An original quartz clamping system able to undergo high temperature conditions has also been designed.

In Chapter 3, the thermodynamic analysis of the Pd thin films revealed a behaviour typical of a highly defected material, as expected. The α-β phase transition of the palladium hydride has been identified as well, and avoided for the kinetic analysis. Plasticity phenomenons related to the α-β phase transition have been identified on the hydriding cycle profiles. Multiple cycling experiments revealed a constant hydrogen concentration remaining in the specimens under vacuum, confirming the idea that the specimens are highly defected. As

the high resolution in-situ approach developed in Chapter 2 also enabled to reveal the kinetic details of hydriding of the Pd thin film specimens, a complete interpretation of the mechanistic steps involved in the hydriding mechanism was possible. A self-consistent kinetic model has been derived from the bases of solid-gas interactions, and its application resulted in the identification of the rate-limiting steps involved in Pd thin film hydriding. In particular, a kinetic profile has been unravelled with a first kinetic regime limited by hydrogen absorption, a second kinetic regime limited by hydrogen adsorption and a switch back to an absorption-limited kinetics. This behaviour has been attributed to an abrupt change in the heat of adsorption that occurs when the surface reaches a critical value. A quantitative analysis of the hydriding kinetics also enabled to calculate relevant kinetic and thermodynamic parameters such as rate and equilibrium constants. The study of the batch-to-batch reproducibility revealed the importance of storing the specimens in a dry place and under vacuum in order to properly compare their kinetics.

The study of the effect of internal stress on the hydriding properties of the Pd thin films performed in Chapter 4 firstly showed that the α-β phase transition is shifted towards lower p_{H_2} values for the most tensile batches, as expected from the available literature results. The values of Sievert's constant, as well as the specimens microstructural parameters, do not significantly change from one deposition condition to another. The kinetic analysis showed an accelerating effect of tensile stress and a slowing down effect of compressive stress. Moreover, only the first, absorption-limited kinetic regime is affected by internal stress. The quantitative analysis confirmed these trends in term of rate constants, and enabled to derive, for the first time, the value of 17.6 ± 2.3 $Å^3$ for the activation volume of H surface-to-bulk transition in palladium. This value is encouraging, and suggests that non-negligible destabilisation of metal hydrides is possible by controlling internal stress.

Chapter 5 has finally been dedicated to the effect of microstructure on the hydriding properties of the Pd thin films. Proper annealing conditions have been found out in order to obtain two batches with the same internal stress level and different microstructures. Defect recovery has been confirmed during annealing at 300°C, while the fraction of grain boundaries does not change. The defects recovered during annealing are believed to be mainly saturable, irreversible trap sites, as Sievert's constant does not significantly change after annealing and an additional compressive stress is observed in the as-deposited batch. The kinetic analysis revealed a strong slowing down effect induced by defect recovery, with an associated increase of the activation energy for surface-to-bulk transition on the order of 10%. Consequently, the microstructural parameters cannot be ignored at both kinetic and thermodynamic levels. Our results indicate that growth defects have probably been recovered during annealing, but this has to be quantitatively confirmed by high resolution TEM.

Internal stress and microstructure are two fundamental material parameters which, besides the fact that they are linked to each other, independently influence the hydriding kinetics in applications such as hydrogen sensors, hydrogen permeation or hydrogen storage. In the case of thin films, it is possible to separately adjust these two parameters, as the growth stress is influenced by the plasma pressure and the microstructure is mainly driven by the deposition/annealing temperature (even if small textural changes are reported here). Let us note that reaching the highest possible tensile internal stress in a thin film is not systematically a good approach, as the material must be able to mechanically withstand this amount of stress. Similarly, controlling the material microstructure in order to optimise its kinetic/thermodynamic hydriding behaviour must be carried out in a smart way, i.e. by keeping in mind that each type of defect interacts differently with hydrogen. Coming back to the application of the kinetic model developed in this thesis, it is important to realise that the surface state of thin films - which depends on the deposition, storage and working conditions of the required application - critically determines their kinetic behaviour. Tuning the internal stress and monitoring the defect concentration won't produce the desired kinetics if the film surface state is not carefully taken into account.

Taking the present conclusions a basis for future investigations, a first, insightful type of work that could be carried out would be the study of more advanced thin film hydrides. If the in-situ approach enabled to unravel new kinetic details for the Pd model system, then many kinetic issues intrinsic to complex alloys could be solved as well.

Secondly, if new hydrides are studied using the experimental approach, then one may need to record p-c isotherms at high temperatures if the hydriding/dehydriding reaction turns out to be impossible at room temperature. In this respect, the new annealing/hydriding setup developed in the course of this thesis work could be used to perform such experiments.

The study of the effect of internal stress with the Pd model system is promising, and may also be used with more complex hydride materials. The reachable internal growth stress state depends on the material that is deposited, and may lead to stronger effects in specific metals or alloys.

The study of the effect of microstructure needs more characterisation at the nanometer scale in order to separate the contributions from each defect type. Specific materials and/or deposition/annealing conditions may lead to the isolation of the contribution of only one type of defect.

Appendix: remarks on the hydrogen society

Since 2007, the worldwide total primary energy consumption has overtaken the huge number of 12 Gtoe [271], i.e. the amount of energy released by burning 12 Gton of crude oil (about 140 TWh). About 80% of this energy is transformed into heat, electricity and movement through the use of fossil fuel combustion processes, generating CO_2 emissions into the earth atmosphere roughly equivalent to 7 Gton of carbon every year [272]. In a no-change scenario - on basis of the International Energy Agency - this number could double by the year 2050 [272]. The existence of an impact of such enormous amounts of CO_2 in the atmosphere is no longer a matter of debate. The only real debate considered nowadays by the international community is the quantitative effect of this level of CO_2 and other greenhouse gases, which varies from one model to another [273]. This environmental need is so crucial that is currently turning into a political obligation, with early consequences such as the Kyoto protocol and other international agreements.

However, fossil fuels are not sustainable. Linear extrapolations of the growth rate of oil consumption and the rate of increase of known oil reserves predicted the end of petroleum supply to take place around 2050 [273]. Similar calculations performed on natural gas showed that the latter can only be considered in the medium term, its total consumption will indeed take place in maximum one century. Coal is predicted to last two centuries, considering its increasing rate of consumption.

Unfortunately, mid-term environmental or supply issues are not enough to induce a rapid change of mentalities. But additionally, since 2005, a crucial turning point has been reached in oil economy, forcing governments to reduce fossil fuel use in the short term. In a recent study, Murray and King [274] showed that this transition is real, on basis of two distinct observations. Firstly, Fig. A1 shows us that up to 2005, the oil production could follow the rising

price, resulting in a classic, elastic relationship between supply end demand. Since 2005, the oil production has hit a ceiling, despite continued price increases. More precisely, production in existing oil fields around the world is declining at rates of about 4.5% to 6.7% every year. The world oil production is only kept constant through the opening of new wells [274]. Consequently, supply cannot currently match demand, leading to important price swings. This economic transition, similar to a phase transition in physics, is shown in Fig. A2. Murray and King argue that the price of oil is now one of the most important head winds against economic recovery in Europe and the USA. More specifically, the recent euro crisis in southern Europe could have been limited by a faster political reaction regarding the fact that 'oil's tipping point has passed' [274].

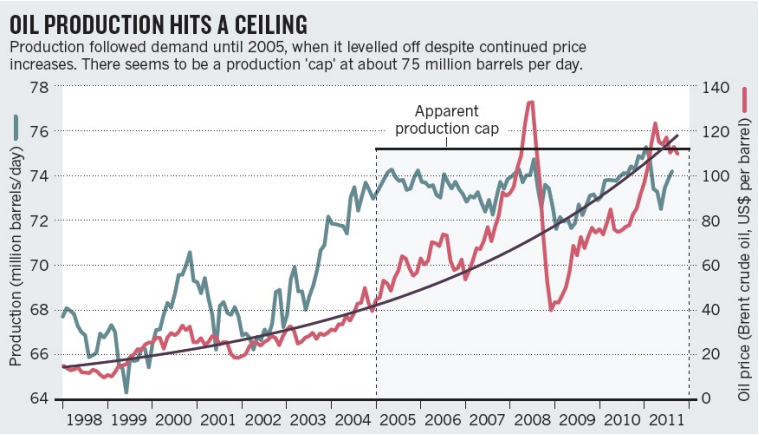

Figure A1: World crude oil production and price evolution from 1998 to 2011. Reproduced from Ref. [274].

This economic transition may seem surprising, as oil is still available for several decades. Reality is that we don't suffer from a lack of oil, but from a lack of oil that can be produced at acceptable cost [274]. Whether the oil is too deep in the ground in the old production sites, or simply too difficult to access in the new production sites. The biggest of these new, non-conventional oil production sites - Canada's tar sands - is sometimes called the 'oil junkie's last fix' [274]. Murray and King also show that the same kind of economic transition will soon take place with the reserves of coal and natural gas, mainly because the easily accessible amounts of these resources is overestimated.

If the environmental and supply issues were not strong enough to immediately push the governments in action, this new economical issue will definitely end up the age of fossil fuels. It is time for the junkies to start rehab. And

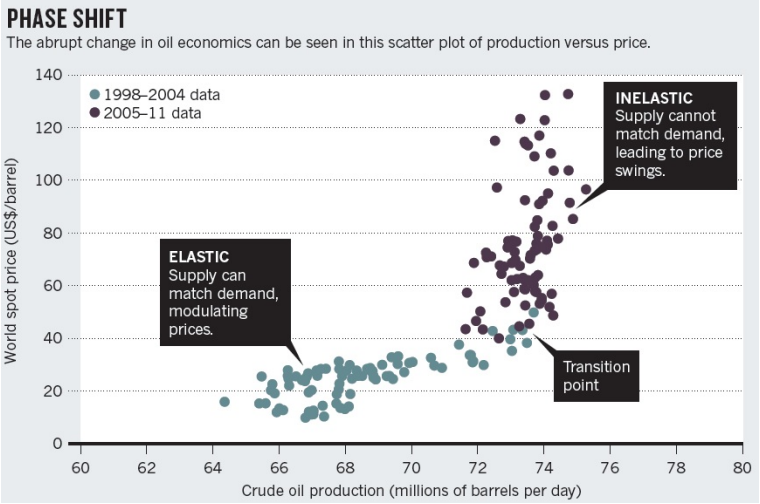

Figure A2: World crude oil price as a function of its production, showing a phase shift in oil economics. Reproduced from Ref. [274].

rehab is not a too strong word, as the transition from the current world energy infrastructure - based almost entirely on fossil fuel use - to a cleaner one must obviously be 'revolutionary rather than evolutionary' [94]. This appendix explains how hydrogen will participate to the construction of this new infrastructure by clarifying four fundamental statements which are too often forgotten when talking about the hydrogen society.

Hydrogen is the best available energy carrier

This is the most important source of public misunderstanding regarding hydrogen energy. Despite being the most abundant element in the universe [275], hydrogen in its molecular H_2 form readily forms covalent compounds with most elements. On earth, one can find it mostly in water and in organic compounds. Consequently, hydrogen is not a primary energy source.

But a positive consequence of its relative instability is that hydrogen releases a lot of energy when it recombines into water, a much more stable form than dihydrogen. The low heating value of hydrogen (LHV) is equal to 120 MJ/kg [21], i.e. 4 times greater than that of coal, 2.8 times higher than that of gasoline and 2.2 times higher than that of methane [272]. Moreover, water is naturally abundant on earth and is thereby totally acceptable as a hydrogen carrier and as a by-product. The hydrogen-water cycle, shown in Fig. A3, is

closed and sustainable if the energy used to split water comes itself from renewable sources. Consequently, hydrogen is not only a sustainable energy vector, but also the most powerful available energy vector.

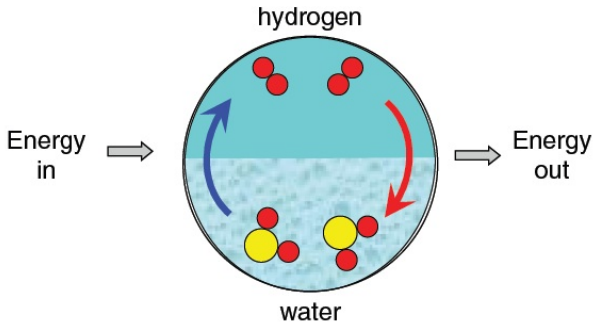

Figure A3: The hydrogen-water cycle. Reproduced from Ref. [276].

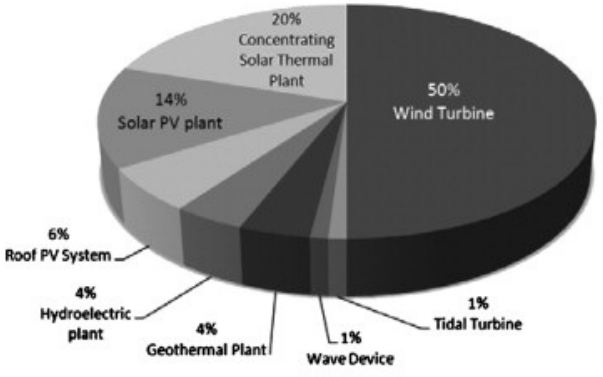

Figure A4: Mix of renewable energy sources able to meet the world energy demand in 2030. Reproduced from Ref. [277].

Let us temporarily go back to the need for sustainable primary energy sources. Many sustainable solutions exist, such as wind turbines [278], solar thermal [279] and photovoltaic [280] devices, hydro power [281], geothermal energy [282], tidal [283] and wave [284] turbines. If a smart concomitant exploitation of these natural forces is organised, the energy needs of the whole world can theoretically be satisfied, according to Jacobson and Delucchi [277, 285]. Fig. A4 shows a recently imagined mix of renewable energy sources able to meet the world energy demand in 2030. But the distribution logistics of such intermittent energy sources cannot become a reality without an efficient en-

ergy storage technology [286, 287]. Hydrogen energy can be the answer to that problem, as discussed above.

Hydrogen is closely connected to electricity

The three facts discussed above - hydrogen is not a primary energy source, hydrogen is sustainable and highly powerful, and hydrogen is a good energy vector - which are known for a long time, were firstly put together in 1970, and published in 1975 as follows [288]:

"The phrase 'A Hydrogen Economy' arose for the first time in a discussion between Bockris and Triner of the General-Motors Technical Center, 3 February 1970. They had been discussing (along with others in a Group) the various fuels which could replace polluting gasoline in transportation and had come to the conclusion that hydrogen would be the eventual fuel for all types of transports. The discussion went to other applications of hydrogen in providing energy to households and industry, and it was suggested that we might live finally in what could be called 'A Hydrogen Society'. The phrase 'A Hydrogen Economy' was then used later in the same conversation".

This early vision was based on the exclusive production of hydrogen by electrolysis of fresh and sea water. The energy needed for this large-scale electrolysis was seen to be provided by solar power and/or nuclear fission. The hydrogen produced was seen to be transmitted to population centres by pipelines all over the world. Since then, a lot of extensive works have been carried out in order to re-envision the role of hydrogen in a future sustainable society [277, 289–291]. Let us briefly present their main recommendations. The massive production of hydrogen as an energy vector is not a good reason to keep on relying on nuclear fission extensively. Using electrolysis alone - performed only with renewable energies - currently implies too important technological obstacles. But hydrogen is not only present in water in its natural state. The additional, concurrent use of steam reforming of natural gas and biomass gasification can provide hydrogen at lower energetic costs. The use of fossil fuel power stations with carbon capture and storage is also considered, but this is currently not a really sustainable option. Photo-electrochemical and photobiological processes may also be used in a more distant future [94]. However, whatever the chosen combination of energy sources to produce hydrogen, part of the total energy generated will be inevitably lost through the production process. But even when taking into account this amount of lost energy, the renewable energy sources available on earth are enough to satisfy the world primary energy needs, according to Jacobson and Delucchi [277, 285].

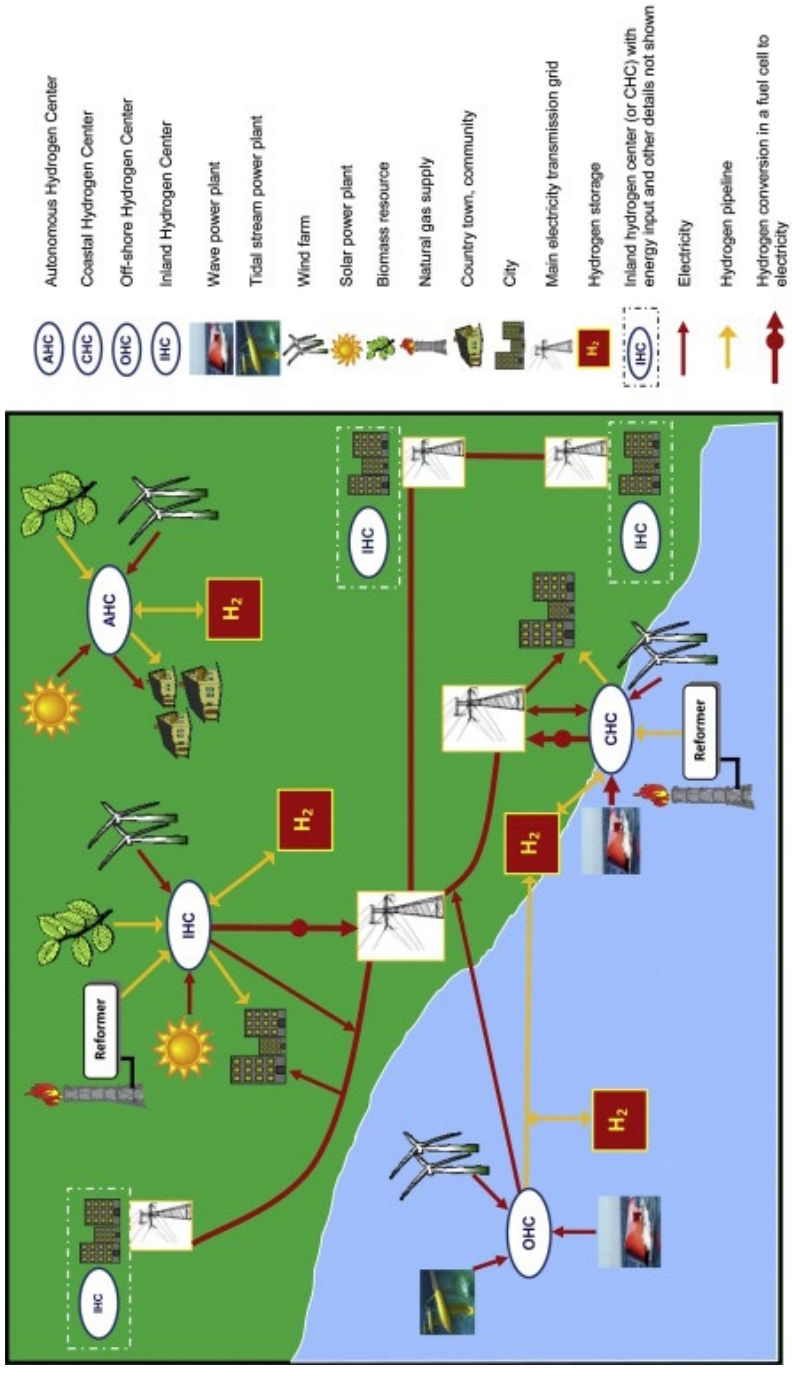

Figure A5: Schematic illustration of the proposed hierarchy of sustainable hydrogen centers showing the principal renewable energy inputs to each type of centre, the local hydrogen distribution system, and the interconnection of higher-order centers via the main electricity grid. Reproduced from Ref. [292].

Once the hydrogen is produced and transported to the location of its end use, it can be converted to electricity in a fuel cell. The electricity can be directly used, or converted into motion, light or heat. A 60% efficiency of the energy conversion can be achieved [276, 293]. This is much better than the average 34% efficiency achieved with electricity generation by fossil fuels [276, 294].

Therefore, the integration of hydrogen into the global electricity grid is feasible. Andrews and Shabani propose to do this via the integration of inland, coastal, offshore and autonomous hydrogen centers [292], as shown in Fig. A5.

Hydrogen is adaptable to stationary and mobile applications

As explained above, hydrogen for stationary applications is a very concrete field of technology. The European HYPER project (Installation Permitting Guidance for Hydrogen and Fuel Cells Stationary Applications) is a good example of this concreteness [295]. The existing stationary fuel cells are indeed at a sufficiently advanced development stage to be considered for integration in the electricity grid. The issues related to the safety of hydrogen storage and distribution for stationary applications are manageable as well. Moreover, such stationary applications are not necessarily large-scale, but can also be designed for household applications, thereby being able to directly convert the excess renewable energy from residential zones into hydrogen, which can in turn be converted into electricity when needed [296].

Hydrogen is also seen a an excellent candidate for sustainable mobile applications. On-board fuel cells have an energy efficiency up to 60%, just as stationary fuel cells. The energy efficiency of the electric motor is more than 90%, well above the 25% achieved by gasoline motors [276]. But even if the motor and the fuel are more efficient than their gasoline counterparts, this is currently not enough to counterbalance the extreme volatility of hydrogen. Even the most resistant 4^{th} generation carbon fiber tanks only allow for a 400 km car autonomy, and are thus still not gasoline competitive. This problem is less critical regarding bigger vehicles such as buses, trains, planes or boats. Nevertheless, important efforts are still needed in the field of hydrogen storage. The best performances will be achieved through the use of advanced storage technologies such as metallic hydrides, complex hydrides, adsorption technologies or organic liquid carriers [7]. Many European, American and Japanese car companies are working on research models. Honda was the first company to propose commercial models in 2002. Its latest model of fuel cell vehicle, the Honda FCX Clarity (see Fig. A6), has an autonomy of 450 km and a top speed of 160 km/h [297].

Figure A6: Photograph of the Honda FCX Clarity fuel cell vehicle. Reproduced from Ref. [297].

Two other types of green fuels must also be considered for sustainable transportation. The first one is electricity. Considered on its own, the electric car cannot be competitive with the hydrogen car in terms of autonomy, but its inherent energy efficiency is above these of the hydrogen car [292]. But as shown above, hydrogen is closely connected to electricity. As a result, a coupling of these two technologies will allow to reach the best performances. Biofuels are sustainable in principle, as the CO_2 released in the atmosphere has been previously assimilated by the plants during their lifetime. But there will never be enough surface on earth to satisfy the world needs without encroaching on the agro-alimentary sector [292].

Hydrogen won't solve all energetic issues if humanity keeps on wasting energy

In his attempt of re-envisioning the role of hydrogen in a sustainable energy economy [292], John Andrews propose the six following principles as a basis for a near future hydrogen society:

- A hierarchy of sustainable hydrogen production, storage and distribution centers relying on local renewable energy sources producing hydrogen as required.
- Complementary use of hydrogen and electricity as energy vectors to minimize the extent of new hydrogen pipeline distribution networks.
- Production of hydrogen from a range of renewable energy sources and feedstocks, without dependence on nuclear fission power or carbon capture and storage, but with the application of energy efficiency measures to the economic limit across all sectors of the economy.

- Recognition of the complementary roles of hydrogen and battery storage across a range of transport vehicles and transport services.
- Use of hydrogen for longer-duration energy storage on centralized grids relying extensively on renewable energy inputs.
- Employment of bulk hydrogen storage as the strategic energy reserve to guarantee national and global energy security in a world relying increasingly on renewable energies.

This vision is definitely not an utopia. But it may become one if we don't carefully reconsider our energy consumption. Indeed, Hetland and Mulder sowed that a large-scale transition to hydrogen may considerably increase the primary energy demand and greenhouse gas emissions [298]. This phenomenon could become worse and worse if the whole humanity starts to waste as much energy as the occidentals. The most sceptic people against the hydrogen society concept warn us that the vision of abundant energy for everyone with no negative consequences is indeed an utopia [299], and they are probably right.

Acknowledgements

Bringing a Ph. D. thesis up to its end is obviously an important personal challenge. But it cannot be properly carried out without the scientific, technical and human contribution of numerous people, who I wish to warmly acknowledge here.

The most important contribution comes from my thesis advisor, Prof. Joris Proost. He was there from the very beginning of this thesis, and even before when he proposed me to work with him for my master's thesis. Thank you Joris, for offering me this stimulating research project, for helping me to raise the necessary funds, for learning me to produce quality research, for these uncountable hours of intense scientific discussions and for supporting me in the darkest moments of the elaboration of this thesis.

The international conferences which I attended throughout these last four years enabled me to meet experts in the field who gave me precious advice that efficiently oriented my research. I would like to thank Profs. Andreas Borgschulte, Ronald Griessen, Markus Wilde, Andreas Züttel, Richard Chahine and Jacques Huot for introducing me to the most relevant challenges relative to the hydrogen community.

I would also like to cordially thank the people from UCL who supported me at the scientific level, i.e. Prof. Thomas Pardoen and his Ph. D. student Marie-Stéphane Colla for their help on the mechanical behaviour of palladium thin films, Prof. Juray de Wilde and his Ph. D. student Philippe Eliaers for their help on the numerical modelling aspects of complex gas-solid interactions, and Prof. Yaroslav Filinchuck for his precious knowledge of the hydrides chemistry.

I also kindly thank the mysterious "reviewer #1" for the huge help provided to improve our kinetic model, which is nothing else than the core of this thesis.

Many thanks to Prof. Nick Schryvers and to Hosni Idrissi for their (ongoing) parallel TEM investigations which bring light to the nano-scale arrangement of our thin films.

Finally, I would like to thank Profs. Laurent Francis and Grégoire Winckelmans for carefully correcting my manuscript.

Et comme la science n'est rien sans la technique, je voudrais remercier chaleureusement les personnes du labo IMAP sans qui rien n'eût été possible: Quentin Van Overmeere et Jean-François Vanhumbeeck pour m'avoir initié au périlleux maniement du MOS, Marc Sinnaeve pour ses innombrables contributions allant du montage de dispositifs expérimentaux à l'assistance informatique, Sébastien Michotte pour les dépôts par sputtering, Ronny Santoro pour les analyses chimiques, Frédéric Van Wonterghem pour les analyses XRD, Cécile D'Haese et Barbara De Maeyer pour les mesures AFM, Laurence Ryelandt pour l'assistance lors des mesures SEM, Liza Lecarme pour l'assistance Latex, ainsi qu'Emile Clembos, Jonathan Lorfevre et Luc Wautier pour l'assistance technique. Merci aussi au Prof. Stéphane Lucas (FUNDP Namur) pour les analyses RBS, ainsi qu'à Christian Renaux, Nicolas André et Aurore Segreef de l'équipe WINFAB pour leur assistance en chambres propres.

Merci aux personnes avec qui j'ai partagé mon bureau: Charles Brugger, Liza Lecarme et Quentin Van Overmeere pour leur bonne humeur et leur entrain au quotidien.

Merci aussi à Albert Hellebrandt, Viviane Abeels et Catherine Bauwens pour leur indispensable support administratif.

Merci à toute l'équipe IMAP pour l'ambiance unique qui règne dans ce laboratoire, tant au niveau de l'organisation du travail que de la convivialité.

Finalement, je remercie ma famille, mes potes et mon équipe de volley, qui m'ont rappelé à chaque instant que la vie ne se résume pas à la science, et qui de ce fait m'ont empéché de sombrer dans la folie. En particulier, je remercie Marc Février (alias "Dartman") pour son établissement si bien tenu, Quentin Duvivier pour nos débats mouvementés sur la subjectivité de la production du savoir, Billy Lardinoit pour ses concertos subtils et Lionel Galand pour nos pauses midi littéraires si apaisantes. Et enfin, last but not least, merci à ma compagne Hélène Gérain pour son soutien inconditionnel (mais pas aveugle!) et pour sa patience dans les moments difficiles.

The *Fonds de la Recherche Scientifique - FNRS* is acknowledged for funding this work through a FRIA doctoral fellowship.

Bibliography

[1] Burger, H. & van Milaan, J. Measurement of the reflective power of metallic mirrors. *Physica* **6**, 435–438 (1939).

[2] Yamamoto, Y. Technological innovation of thin-film transistors: Technology development, history, and future. *Japanese Journal of Applied Physics* **51**, 060001 (2012).

[3] Metroke, T. L., Kachurina, O. & Knobbe, E. T. Spectroscopic and corrosion resistance characterization of amine and super acid-cured hybrid organic-inorganic thin films on 2024-T3 aluminum alloy. *Progress in Organic Coatings* **44**, 185–199 (2002).

[4] Hermann, A. M. Polycrystalline thin-film solar cells - A review. *Solar Energy Materials and Solar Cells* **55**, 75–81 (1998).

[5] Sberveglieri, G. Recent developments in semiconducting thin-film gas sensors. *Sensors and Actuators B: Chemical* **23**, 103–109 (1995).

[6] Craig, P. J. Book review: Chemistry of the elements, 2nd edn. *Applied Organometallic Chemistry* **12**, 880–880 (1998).

[7] Stolten, D. *Hydrogen and Fuel Cells: Fundamentals, Technologies and Applications* (John Wiley & Sons, 2010).

[8] Villatoro, J., Luna-Moreno, D. & Monzón-Hernández, D. Optical fiber hydrogen sensor for concentrations below the lower explosive limit. *Sensors and Actuators B: Chemical* **110**, 23–27 (2005).

[9] Schmidtchen, U. FUELS - SAFETY - Hydrogen: Overview. In Garche, J. (ed.) *Encyclopedia of Electrochemical Power Sources*, 519–527 (Elsevier, Amsterdam, 2009).

[10] Grimes, C. A. *et al.* A sentinel sensor network for hydrogen sensing. *Sensors* **3**, 69–82 (2003).

[11] Lampe, U., Gerblinger, J. & Meixner, H. Carbon-monoxide sensors based on thin films of $BaSnO_3$. *Sensors and Actuators B: Chemical* **25**, 657–660 (1995).

[12] Patel, N., Makhija, K. & Panchal, C. Fabrication of carbon dioxide gas sensor and its alarm system using indium tin oxide (ITO) thin films. *Sensors and Actuators B: Chemical* **21**, 193–197 (1994).

[13] Tamaki, J., Hayashi, A., Yamamoto, Y. & Matsuoka, M. Detection of dilute nitrogen dioxide and thickness effect of tungsten oxide thin film sensors. *Sensors and Actuators B: Chemical* **95**, 111–115 (2003).

[14] Torsi, L., Dodabalapur, A., Cioffi, N., Sabbatini, L. & Zambonin, P. NTCDA organic thin-film-transistor as humidity sensor: weaknesses and strengths. *Sensors and Actuators B: Chemical* **77**, 7–11 (2001).

[15] Tan, G.-L., Wu, X.-J., Wang, L.-R. & Chen, Y.-Q. Investigation for oxygen sensor of LaF_3 thin film. *Sensors and Actuators B: Chemical* **34**, 417–421 (1996).

[16] Xie, G., Sun, P., Yan, X., Du, X. & Jiang, Y. Fabrication of methane gas sensor by layer-by-layer self-assembly of polyaniline/PdO ultra thin films on quartz crystal microbalance. *Sensors and Actuators B: Chemical* **145**, 373–377 (2010).

[17] Patel, N., Patel, P. & Vaishnav, V. Indium tin oxide (ITO) thin film gas sensor for detection of methanol at room temperature. *Sensors and Actuators B: Chemical* **96**, 180–189 (2003).

[18] Brousse, T. & Schleich, D. Sprayed and thermally evaporated SnO_2 thin films for ethanol sensors. *Sensors and Actuators B: Chemical* **31**, 77–79 (1996).

[19] Karunagaran, B., Uthirakumar, P., Chung, S., Velumani, S. & Suh, E.-K. TiO_2 thin film gas sensor for monitoring ammonia. *Materials Characterization* **58**, 680–684 (2007).

[20] Hübert, T., Boon-Brett, L., Black, G. & Banach, U. Hydrogen sensors - A review. *Sensors and Actuators B: Chemical* **157**, 329–352 (2011).

[21] Shin, B., Cho, Y., Han, D., Song, S. & Chun, K. M. Hydrogen effects on NO_x emissions and brake thermal efficiency in a diesel engine under low-temperature and heavy-EGR conditions. *International Journal of Hydrogen Energy* **36**, 6281–6291 (2011).

[22] Lee, E.-B. *et al.* Micromachined catalytic combustible hydrogen gas sensor. *Sensors and Actuators B: Chemical* **153**, 392–397 (2011).

[23] Qiu, F. *et al.* Miniaturization of thermoelectric hydrogen sensor prepared on glass substrate with low-temperature crystallized SiGe film. *Sensors and Actuators B: Chemical* **103**, 252–259 (2004).

[24] Pollak-Diener, G. & Obermeier, E. Heat-conduction microsensor based on silicon technology for the analysis of two- and three-component gas mixtures. *Sensors and Actuators B: Chemical* **13**, 345–347 (1993).

[25] Lu, X., Wu, S., Wang, L. & Su, Z. Solid-state amperometric hydrogen sensor based on polymer electrolyte membrane fuel cell. *Sensors and Actuators B: Chemical* **107**, 812–817 (2005).

[26] Kosacki, I. & Anderson, H. U. Nanostructured oxide thin films for gas sensors. *Sensors and Actuators B: Chemical* **48**, 263–269 (1998).

[27] Aroutiounian, V. Metal oxide hydrogen, oxygen, and carbon monoxide sensors for hydrogen setups and cells. *International Journal of Hydrogen Energy* **32**, 1145–1158 (2007).

[28] Xu, T. *et al.* Self-assembled monolayer-enhanced hydrogen sensing with ultrathin palladium films. *Applied Physics Letters* **86**, 203104 (2005).

[29] Potje-Kamloth, K. Semiconductor junction gas sensors. *Chemical Reviews* **108**, 367–399 (2008).

[30] Scharnagl, K. *et al.* Low temperature hydrogen detection at high concentrations: comparison of platinum and iridium. *Sensors and Actuators B: Chemical* **80**, 163–168 (2001).

[31] Eriksson, M., Salomonsson, A., Lundstrom, I., Briand, D. & Abom, A. E. The influence of the insulator surface properties on the hydrogen response of field-effect gas sensors. *Journal of Applied Physics* **98**, 034903 (2005).

[32] Chou, Y.-I., Chiang, H.-C. & Wang, C.-C. Study on Pd functionalization of microcantilever for hydrogen detection promotion. *Sensors and Actuators B: Chemical* **129**, 72–78 (2008).

[33] Kiefer, T., Salette, A., Villanueva, L. G. & Brugger, J. Large arrays of chemo-mechanical nanoswitches for ultralow-power hydrogen sensing. *Journal of Micromechanics and Microengineering* **20**, 105019 (2010).

[34] Bévenot, X., Trouillet, A., Veillas, C., Gagnaire, H. & Clément, M. Hydrogen leak detection using an optical fibre sensor for aerospace applications. *Sensors and Actuators B: Chemical* **67**, 57–67 (2000).

[35] Bearzotti, A., Caliendo, C., Verona, E. & D'Amico, A. Integrated optic sensor for the detection of H_2 concentrations. *Sensors and Actuators B: Chemical* **7**, 685–688 (1992).

[36] Chadwick, B. & Gal, M. Enhanced optical detection of hydrogen using the excitation of surface plasmons in palladium. *Applied Surface Science* **68**, 135–138 (1993).

[37] Tabib-Azar, M., Sutapun, B., Petrick, R. & Kazemi, A. Highly sensitive hydrogen sensors using palladium coated fiber optics with exposed cores and evanescent field interactions. *Sensors and Actuators B: Chemical* **56**, 158–163 (1999).

[38] Sutapun, B., Tabib-Azar, M. & Kazemi, A. Pd-coated elastooptic fiber optic bragg grating sensors for multiplexed hydrogen sensing. *Sensors and Actuators B: Chemical* **60**, 27–34 (1999).

[39] Sumida, S. *et al.* Distributed hydrogen determination with fiber-optic sensor. *Sensors and Actuators B: Chemical* **108**, 508–514 (2005).

[40] Miura, N., Minamoto, H., Sakai, G. & Yamazoe, N. New-type calorimetric gas sensor using temperature characteristics of piezoelectric quartz crystal fitted with noble metal catalyst film. *Sensors and Actuators B: Chemical* **5**, 21– 217 (1991).

[41] Jakubik, W. P., Urbańczyk, M. W., Kochowski, S. & Bodzenta, J. Palladium and phthalocyanine bilayer films for hydrogen detection in a surface acoustic wave sensor system. *Sensors and Actuators B: Chemical* **96**, 321–328 (2003).

[42] Lomperski, S., Anselmi, M. & Huhtiniemi, I. Ultrasonic and resistive hydrogen sensors for inert gas-water vapour atmospheres. *Measurement Science and Technology* **11**, 518 (2000).

[43] Song, T., Wu, J., Shen, L. & Xiao, J. Experimental investigation on hydrogen production from biomass gasification in interconnected fluidized beds. *Biomass and Bioenergy* **36**, 258–267 (2012).

[44] Lu, G. *et al.* Inorganic membranes for hydrogen production and purification: A critical review and perspective. *Journal of Colloid and Interface Science* **314**, 589–603 (2007).

[45] Uemiya, S. *et al.* Separation of hydrogen through palladium thin film supported on a porous glass tube. *Journal of Membrane Science* **56**, 303–313 (1991).

[46] Xomeritakis, G. & Lin, Y. Fabrication of a thin palladium membrane supported in a porous ceramic substrate by chemical vapor deposition. *Journal of Membrane Science* **120**, 261–272 (1996).

[47] McCool, B., Xomeritakis, G. & Lin, Y. Composition control and hydrogen permeation characteristics of sputter deposited palladium-silver membranes. *Journal of Membrane Science* **161**, 67–76 (1999).

[48] Armor, J. Applications of catalytic inorganic membrane reactors to refinery products. *Journal of Membrane Science* **147**, 217–233 (1998).

[49] Tsuru, T., ichi Wada, S., Izumi, S. & Asaeda, M. Silica-zirconia membranes for nanofiltration. *Journal of Membrane Science* **149**, 127–135 (1998).

[50] Tsai, C.-Y., Tam, S.-Y., Lu, Y. & Brinker, C. Dual-layer asymmetric microporous silica membranes. *Journal of Membrane Science* **169**, 255–268 (2000).

[51] de Souza, S., Visco, S. J. & Jonghe, L. C. D. Thin-film solid oxide fuel cell with high performance at low-temperature. *Solid State Ionics* **98**, 57–61 (1997).

[52] Chun, Y.-G., Kim, C.-S., Peck, D.-H. & Shin, D.-R. Performance of a polymer electrolyte membrane fuel cell with thin film catalyst electrodes. *Journal of Power Sources* **71**, 174–178 (1998).

[53] Leng, Y., Chan, S., Khor, K. & Jiang, S. Performance evaluation of anode-supported solid oxide fuel cells with thin film YSZ electrolyte. *International Journal of Hydrogen Energy* **29**, 1025–1033 (2004).

[54] Ko, C., Kerman, K. & Ramanathan, S. Ultra-thin film solid oxide fuel cells utilizing un-doped nanostructured zirconia electrolytes. *Journal of Power Sources* **213**, 343–349 (2012).

[55] Beckel, D. *et al.* Thin films for micro solid oxide fuel cells. *Journal of Power Sources* **173**, 325–345 (2007).

[56] Sieverts, A. The absorption of gases by metals. *Zeitschrift für Metallkunde* **21**, 37–46 (1929).

[57] Wicke, E. & Brodowsky, H. Hydrogen in palladium and palladium alloys. In Alefeld, G. & Voelkl, J. (eds.) *Hydrogen in Metals*, vol. 2, 73–155 (Springer, Berlin, 1978).

[58] Kirchheim, R. Solid solutions of hydrogen in complex materials. In Ehrenreich, H. & Spaepen, F. (eds.) *Solid State Physics*, vol. 59, 203–291 (Academic Press, 2004).

[59] Smirnov, L. & Pronchenko, D. Chemical potential and phase diagrams of hydrogen in palladium. *International Journal of Hydrogen Energy* **27**, 825 – 828 (2002).

[60] Tsirlina, G. A., Levi, M. D., Petrii, O. A. & Aurbach, D. Comparison of equilibrium electrochemical behavior of PdH_x and $Li_xMn_2O_4$ intercalation electrodes in terms of sorption isotherms. *Electrochimica Acta* **46**, 4141–4149 (2001).

[61] Tsirlina, G., Nagaev, E. & Rusanova, M. Isotope effect in perfect and imperfect hydrogenized palladium. *Physics Letters A* **267**, 71–80 (2000).

[62] Bucur, R. V. Effect of trapping on the solubility and diffusivity of hydrogen in palladium (α-phase). *Journal of Materials Science* **22**, 3402–3406 (1987).

[63] Kapischke, J. & Hapke, J. Measurement of the pressure-composition isotherms of high-temperature and low-temperature metal hydrides. *Experimental Thermal and Fluid Science* **18**, 70–81 (1998).

[64] Lexcellent, C. & Gondor, G. Analysis of hydride formation for hydrogen storage: Pressure-composition isotherm curves modeling. *Intermetallics* **15**, 934–944 (2007).

[65] Schwarz, R. & Khachaturyan, A. Thermodynamics of open two-phase systems with coherent interfaces: Application to metal-hydrogen systems. *Acta Materialia* **54**, 313–323 (2006).

[66] Gremaud, R. *et al.* Hydrogenography of $Mg_yNi_{1-y}H_x$ gradient thin films: Interplay between the thermodynamics and kinetics of hydrogenation. *Acta Materialia* **58**, 658–668 (2010).

[67] Zeng, K., Klassen, T., Oelerich, W. & Bormann, R. Critical assessment and thermodynamic modeling of the Mg-H system. *International Journal of Hydrogen Energy* **24**, 989–1004 (1999).

[68] Gremaud, R. *et al.* Hydrogenography of PdH_x thin films: Influence of H-induced stress relaxation processes. *Acta Materialia* **57**, 1209–1219 (2009).

[69] Baldi, A. *et al.* Nanoscale composition modulations in $Mg_yTi_{1-y}H_x$ thin film alloys for hydrogen storage. *International Journal of Hydrogen Energy* **34**, 1450–1457 (2009).

[70] Griessen, R. *et al.* Yttrium and lanthanum hydride films with switchable optical properties. *Journal of Alloys and Compounds* **253-254**, 44–50 (1997).

[71] Pundt, A. & Kirchheim, R. Hydrogen in metals: Microstructural aspects. *Annual Review of Materials Research* **36**, 555–608 (2006).

[72] Salomons, E., Feenstra, R., de Groot, D., Rector, J. & Griessen, R. Pressure-composition isotherms of thin PdH_c films. *Journal of the Less Common Metals* **130**, 415–420 (1987).

[73] Sakamoto, Y., Ishimaru, N. & Mukai, Y. Thermodynamics of solution of hydrogen in Pd-Cu and Pd-Cu-Au solid solution alloys. *Berichte der Bunsengesellschaft für physikalische Chemie* **95**, 680–688 (1991).

[74] Westerwaal, R. *et al.* High throughput screening of Pd-alloys for H_2 separation membranes studied by hydrogenography and CVM. *International Journal of Hydrogen Energy* **36**, 1074–1082 (2011).

[75] Pivak, Y., Schreuders, H., Slaman, M., Griessen, R. & Dam, B. Thermodynamics, stress release and hysteresis behavior in highly adhesive Pd-H films. *International Journal of Hydrogen Energy* **36**, 4056–4067 (2011).

[76] Zhao, Z., Sevryugina, Y., Carpenter, M. A., Welch, D. & Xia, H. All-optical hydrogen-sensing materials based on tailored palladium alloy thin films. *Analytical Chemistry* **76**, 6321–6326 (2004).

[77] Puszkiel, J., Larochette, P. A. & Gennari, F. Hydrogen storage properties of Mg_xFe (x: 2, 3 and 15) compounds produced by reactive ball milling. *Journal of Power Sources* **186**, 185–193 (2009).

[78] Bououdina, M., Sun, D.-L., Enoki, H. & Akiba, E. Improved kinetics by the multiphase alloys prepared from laves phases and $LaNi_5$. *Journal of Alloys and Compounds* **288**, 229–237 (1999).

[79] Chu, H. *et al.* Structure, morphology and hydrogen storage properties of composites prepared by ball milling with La-Mg-based alloy. *International Journal of Hydrogen Energy* **32**, 3363–3369 (2007).

[80] Rongeat, C. *et al.* Effect of additives on the synthesis and reversibility of $Ca(BH_4)_2$. *Journal of Alloys and Compounds* **493**, 281–287 (2010).

[81] Barkhordarian, G., Klassen, T. & Bormann, R. Kinetic investigation of the effect of milling time on the hydrogen sorption reaction of magnesium catalyzed with different Nb_2O_5 contents. *Journal of Alloys and Compounds* **407**, 249–255 (2006).

[82] Avrami, M. Kinetics of phase change. I general theory. *The Journal of Chemical Physics* **7**, 1103–1112 (1939).

[83] Heller, E., Vredenberg, A. & Boerma, D. Hydrogen uptake kinetics of Pd coated FeTi films. *Applied Surface Science* **253**, 771–777 (2006).

[84] Shalaan, E. & Schmitt, H. Mg nanoparticle switchable mirror films with improved absorption-desorption kinetics. *Surface Science* **600**, 3650–3653 (2006).

[85] Tan, Z., Chiu, C., Heilweil, E. J. & Bendersky, L. A. Thermodynamics, kinetics and microstructural evolution during hydrogenation of iron-doped magnesium thin films. *International Journal of Hydrogen Energy* **36**, 9702–9713 (2011).

[86] Hu, Z., Thundat, T. & Warmack, R. J. Investigation of adsorption and absorption-induced stresses using microcantilever sensors. *Journal of Applied Physics* **90**, 427–431 (2001).

[87] Jewell, L. L. & Davis, B. H. Review of absorption and adsorption in the hydrogen-palladium system. *Applied Catalysis A: General* **310**, 1–15 (2006).

[88] Matelon, R. *et al.* Substrate effect on the optical response of thin palladium films exposed to hydrogen gas. *Thin Solid Films* **516**, 7797–7801 (2008).

[89] Pedersen, T. L. *et al.* Hydrogen-induced changes of mechanical stress and optical transmission in thin Pd films. *Thin Solid Films* **458**, 299–303 (2004).

[90] Lemier, C. & Weissm J. Grain boundary segregation, stress and stretch: Effects on hydrogen absorption in nanocrystalline palladium. *Acta Materialia* **55**, 1241–1254 (2007).

[91] Pasturel, M. *et al.* Hydrogen absorption kinetics and optical properties of Pd-doped Mg thin films. *Journal of Applied Physics* **100**, 023515 (2006).

[92] Borgschulte, A. *et al.* Complex hydrides (opening lecture). *18^{th} World Hydrogen Energy Conference, Essen* 186–187 (2010).

[93] Lewis, F. *The palladium hydrogen system* (Academic Press, 1967).

[94] Jones, R. & Thomas, G. An overview of materials for the hydrogen economy. *JOM Journal of the Minerals, Metals and Materials Society* **59**, 50–55 (2007).

[95] Schlapbach, L. Hydrogen as a fuel and its storage for mobility and transport **27**, 675–679 (2002).

[96] Chen, P. & Zhu, M. Recent progress in hydrogen storage. *Materials Today* **11**, 36–43 (2008).

[97] Kulprathipanja, A., Alptekin, G. O., Falconer, J. L. & Way, J. D. Pd and Pd-Cu membranes: Inhibition of H_2 permeation by H_2S. *Journal of Membrane Science* **254**, 49–62 (2005).

[98] Züchner, H. Ewald wicke and his work on metal-hydrogen systems. *Journal of Alloys and Compounds* **330-332**, 2–7 (2002).

[99] Levine, P. L. & Weale, K. E. The palladium + hydrogen equilibrium at high pressures and temperatures. *Trans. Faraday Soc.* **56**, 357–362 (1960).

[100] Ferrin, P., Kandoi, S., Nilekar, A. U. & Mavrikakis, M. Hydrogen adsorption, absorption and diffusion on and in transition metal surfaces: A DFT study. *Surface Science* **606**, 679–689 (2012).

[101] Johansson, M. *et al.* Hydrogen adsorption on palladium and palladium hydride at 1 bar. *Surface Science* **604**, 718–729 (2010).

[102] Rayne, J. A. Elastic constants of palladium from 4.2-300°k. *Phys. Rev.* **118**, 1545–1549 (1960).

[103] Baral, D., Hilliard, J., Ketterson, J. & Miyano, K. Determination of the primary elastic constants from thin foils having a strong texture. *Journal of Applied Physics* **53**, 3552–3559 (1982).

[104] Schwarz, R., Bach, H., Harms, U. & Tuggle, D. Elastic properties of Pd?hydrogen, Pd?deuterium, and Pd?tritium single crystals. *Acta Materialia* **53**, 569–580 (2005).

[105] Safarik, D. *et al.* Composition dependence of the elastic constants of β-phase and (α+β)-phase pdh_x. *Ultrasonics* **50**, 155–160 (2010).

[106] Tsai, H. Elastic properties, damping capacity and shape memory alloys. In Gale, W. & Totemeier, T. (eds.) *Smithells Metals Reference Book (Eighth Edition)*, 1–45 (Butterworth-Heinemann, Oxford, 2004).

[107] Sanders, P., Eastman, J. & Weertman, J. Elastic and tensile behavior of nanocrystalline copper and palladium. *Acta Materialia* **45**, 4019–4025 (1997).

[108] Jen, S. & Wu, T. Young's modulus and hardness of Pd thin films. *Thin Solid Films* **492**, 166–172 (2005).

[109] Colla, M.-S. *et al.* High strength-ductility of thin nanocrystalline palladium films with nanoscale twins: On-chip testing and grain aggregate model. *Acta Materialia* **60**, 1795–1806 (2012).

[110] Idrissi, H. *et al.* Ultrahigh strain hardening in thin palladium films with nanoscale twins. *Advanced Materials* **23**, 2119–2122 (2011).

[111] Fabre, A., Finot, E., Demoment, J. & Contreras, S. In situ measurement of elastic properties of pdh_x, pdd_x, and pdt_x. *Journal of Alloys and Compounds* **356?357**, 372–376 (2003).

[112] Smith, R. & Otterson, D. The effect of hydrogen on the tensile properties of palladium. *Journal of the Less Common Metals* **24**, 419–426 (1971).

[113] Jahromi, S. J. & Najmi, M. Embrittlement evaluation and lifetime assessment of hydrocracking pressure vessel made of 3Cr-1Mo low-alloy steel. *Engineering Failure Analysis* **14**, 164–169 (2007).

[114] Hardie, D., Charles, E. & Lopez, A. Hydrogen embrittlement of high strength pipeline steels. *Corrosion Science* **48**, 4378–4385 (2006).

[115] Birnbaum, H. & Sofronis, P. Hydrogen-enhanced localized plasticity-a mechanism for hydrogen-related fracture. *Materials Science and Engineering: A* **176**, 191–202 (1994).

[116] von Pezold, J., Lymperakis, L. & Neugebeauer, J. Hydrogen-enhanced local plasticity at dilute bulk H concentrations: The role of H-H interactions and the formation of local hydrides. *Acta Materialia* **59**, 2969–2980 (2011).

[117] Oriani, R. & Josephic, P. Equilibrium aspects of hydrogen-induced cracking of steels. *Acta Metallurgica* **22**, 1065–1074 (1974).

[118] Song, J. & Curtin, W. A nanoscale mechanism of hydrogen embrittlement in metals. *Acta Materialia* **59**, 1557–1569 (2011).

[119] Flanagan, T. B., Mason, N. & Birnbaum, H. The effect of stress on hydride precipitation. *Scripta Metallurgica* **15**, 109–112 (1981).

[120] Wagner, S. & Pundt, A. Combined impact of microstructure and mechanical stress on the electrical resistivity of PdH_c thin films. *Acta Materialia* **59**, 1862–1870 (2011).

[121] Wagner, S. & Pundt, A. Mechanical stress impact on thin $Pd_{1-x}Fe_x$ film thermodynamic properties. *Applied Physics Letters* **92**, 051914 (2008).

[122] Baldi, A., Gonzalez-Silveira, M., Palmisano, V., Dam, B. & Griessen, R. Destabilization of the Mg-H system through elastic constraints. *Phys. Rev. Lett.* **102**, 226102 (2009).

[123] Yamamoto, K., Orimo, S., Fujii, H. & Kitano, Y. Hydriding properties of the heat-treated MgNi alloys with nanostructural designed multiphase. *Journal of Alloys and Compounds* **293-295**, 546–551 (1999).

[124] Bobet, J.-L., Chevalier, B. & Darriet, B. Effect of reactive mechanical grinding on chemical and hydrogen sorption properties of the Mg + 10 wt.% Co mixture. *Journal of Alloys and Compounds* **330-332**, 738–742 (2002).

[125] Bobet, J.-L., Chevalier, B., Song, M., Darriet, B. & Etourneau, J. Hydrogen sorption of Mg-based mixtures elaborated by reactive mechanical grinding. *Journal of Alloys and Compounds* **336**, 292 – 296 (2002).

[126] Laudahn, U. *et al.* Hydrogen-induced stress in Nb single layers. *Journal of Alloys and Compounds* **293-295**, 490–494 (1999).

[127] Ludwig, A., Cao, J., Savan, A. & Ehmann, M. High-throughput characterization of hydrogen storage materials using thin films on micromachined Si substrates. *Journal of Alloys and Compounds* **446-447**, 516–521 (2007).

[128] Pundt, A., Nikitin, E., Pekarski, P. & Kirchheim, R. Adhesion energy between metal films and polymers obtained by studying buckling induced by hydrogen. *Acta Materialia* **52**, 1579–1587 (2004).

[129] Weissmüller, J. & Lemier, C. Lattice constants of solid solution microstructures: The case of nanocrystalline Pd-H. *Phys. Rev. Lett.* **82**, 213–216 (1999).

[130] Myers, S. M. *et al.* Hydrogen interactions with defects in crystalline solids. *Rev. Mod. Phys.* **64**, 559–617 (1992).

[131] Fukai, Y. Formation of superabundant vacancies in M-H alloys and some of its consequences: a review. *Journal of Alloys and Compounds* **356-357**, 263–269 (2003).

[132] Mine, Y., Tachibana, K. & Horita, Z. Grain-boundary diffusion and precipitate trapping of hydrogen in ultrafine-grained austenitic stainless steels processed by high-pressure torsion. *Materials Science and Engineering: A* **528**, 8100–8105 (2011).

[133] Mütschele, T. & Kirchheim, R. Segregation and diffusion of hydrogen in grain boundaries of palladium. *Scripta Metallurgica* **21**, 135–140 (1987).

[134] Mütschele, T. & Kirchheim, R. Hydrogen as a probe for the average thickness of a grain boundary. *Scripta Metallurgica* **21**, 1101–1104 (1987).

[135] Johnson, W. Crystal-to-glass transformation in metallic materials. *Materials Science and Engineering* **97**, 1–13 (1988).

[136] Yong-Gyoo, K., Sung-Man, L. & Jai-Young, L. Hydrogen-induced amorphization of the Laves compound $CeNi_2$ and the structural and thermal characteristics of the amorphous phase. *Journal of the Less Common Metals* **169**, 245–256 (1991).

[137] Kirchheim, R. *Hydrogen Solubility and Diffusivity in Defective and Amorphous Metals*. Progress in materials science (Pergamon Press, 1988).

[138] Yao, J. & Cahoon, J. Experimental studies of grain boundary diffusion of hydrogen in metals. *Acta Metallurgica et Materialia* **39**, 119–126 (1991).

[139] Janßen, S. *et al.* Hydrogen diffusion in nanocrystalline Pd by means of quasielastic neutron scattering. *Nanostructured Materials* **9**, 579–582 (1997).

[140] Maxelon, M., Pundt, A., Pyckhout-Hintzen, W., Barker, J. & Kirchheim, R. Interaction of hydrogen and deuterium with dislocations in palladium as observed by small angle neutron scattering. *Acta Materialia* **49**, 2625–2634 (2001).

[141] Maxelon, M., Pundt, A., Pyckhout-Hintzen, W. & Kirchheim, R. Small angle neutron scattering of hydrogen segregation at dislocations in palladium. *Scripta Materialia* **44**, 817–822 (2001).

[142] Kirchheim, R. Interaction of hydrogen with dislocations in palladium - I. Activity and diffusivity and their phenomenological interpretation. *Acta Metallurgica* **29**, 835–843 (1981).

[143] Tien, J., Thompson, A., Bernstein, I. & Richards, R. Hydrogen transport by dislocations. *Metallurgical and Materials Transactions A* **7**, 821–829 (1976). 10.1007/BF02644079.

[144] Mommer, N., Hirscher, M., Cuevas, F. & Kronmüller, H. Influence of the microstructure on the desorption kinetics of single- and multiphase LaNiFe alloys. *Journal of Alloys and Compounds* **266**, 255–259 (1998).

[145] Isaeva, L. *et al.* Dynamic stability of palladium hydride: An ab initio study. *International Journal of Hydrogen Energy* **36**, 1254–1258 (2011).

[146] Formation of superabundant vacancies in pd hydride under high hydrogen pressures. *Physical Review Letters* **73**, 1640.

[147] Masanao, I. & Yuh, F. Superabundant vacancy formation in iron under high hydrogen pressures: Thermal desorption spectroscopy. *Materials Transactions, JIM* **40**, 606–611 (1999).

[148] Čížek, J. *et al.* Hydrogen-induced defects in bulk niobium. *Phys. Rev. B* **69**, 224106 (2004).

[149] He, J. *et al.* Stability of a hydrogen molecule in a vacancy of palladium hydrides. *International Journal of Hydrogen Energy* **37**, 12351–12357 (2012).

[150] Carr, N. Z. & McLellan, R. B. The thermodynamic and kinetic behavior of metal-vacancy-hydrogen systems. *Acta Materialia* **52**, 3273–3293 (2004).

[151] Singh, S. & Eijt, S. W. H. Hydrogen vacancies facilitate hydrogen transport kinetics in sodium hydride nanocrystallites. *Phys. Rev. B* **78**, 224110 (2008).

[152] Borgschulte, A. *et al.* Hydrogen dissociation on oxide covered MgH_2 by catalytically active vacancies. *Applied Surface Science* **254**, 2377–2384 (2008).

[153] Koyama, M., Akiyama, E., Sawaguchi, T., Raabe, D. & Tsuzaki, K. Hydrogen-induced cracking at grain and twin boundaries in an Fe-Mn-C austenitic steel. *Scripta Materialia* **66**, 459–462 (2012).

[154] So, K. H. *et al.* Hydrogen delayed fracture properties and internal hydrogen behavior of a Fe-18Mn-1.5Al-0.6C TWIP steel. *ISIJ International* **49**, 1952–1959 (2009).

[155] Danaie, M., Tao, S., Kalisvaart, P. & Mitlin, D. Analysis of deformation twins and the partially dehydrogenated microstructure in nanocrystalline magnesium hydride (MgH_2) powder. *Acta Materialia* **58**, 3162–3172 (2010).

[156] Delmelle, R., Bamba, G. & Proost, J. In-situ monitoring of hydride formation in Pd thin film systems. *International Journal of Hydrogen Energy* **35**, 9888–9892 (2010).

[157] Vanhumbeeck, J.-F. *In situ monitoring of the internal stress evolution during titanium thin film anodising.* Ph. D. thesis, Université catholique de Louvain (2009).

[158] Van Overmeere, Q. *The role of internal stress on the growth and breakdown of barrier and porous anodic oxide films.* Ph. D. thesis, Université catholique de Louvain (2011).

[159] Michotte, S. & Proost, J. In situ measurement of the internal stress evolution during sputter deposition of ZnO:Al. *Solar Energy Materials and Solar Cells* **98**, 253–259 (2012).

[160] Stoney, G. G. The tension of metallic films deposited by electrolysis. *Proceedings of the Royal Society of London* **82**, 172–175 (1909).

[161] Janssen, G., Abdalla, M., van Keulen, F., Pujada, B. & van Venrooy, B. Celebrating the 100th anniversary of the stoney equation for film stress: Developments from polycrystalline steel strips to single crystal silicon wafers. *Thin Solid Films* **517**, 1858–1867 (2009).

[162] Pureza, J., Lacerda, M., Oliveira, A. D., Fragalli, J. & Zanon, R. Enhancing accuracy to Stoney equation. *Applied Surface Science* **255**, 6426–6428 (2009).

[163] Zhang, X. C., Xu, B. S., Wang, H. D. & Wu, Y. X. Error analyses on some typically approximate solutions of residual stress within a thin film on a substrate. *Journal of Applied Physics* **98**, 053516–053520 (2005).

[164] Huang, Y. & Rosakis, A. Extension of Stoney's formula to non-uniform temperature distributions in thin film/substrate systems. the case of radial symmetry. *Journal of the Mechanics and Physics of Solids* **53**, 2483–2500 (2005).

[165] Blech, I. A., Blech, I. & Finot, M. Determination of thin-film stresses on round substrates. *Journal of Applied Physics* **97**, 113525–113532 (2005).

[166] Chou, T.-L., Yang, S.-Y. & Chiang, K.-N. Overview and applicability of residual stress estimation of film-substrate structure. *Thin Solid Films* **519**, 7883–7894 (2011).

[167] Zhang, X., Xu, B., Wang, H., Wu, Y. & Jiang, Y. Underlying mechanisms of the stress generation in surface coatings. *Surface and Coatings Technology* **201**, 6715–6718 (2007).

[168] Ngo, D., Feng, X., Huang, Y., Rosakis, A. & Brown, M. Thin film/substrate systems featuring arbitrary film thickness and misfit strain distributions. Part I: Analysis for obtaining film stress from non-local curvature information. *International Journal of Solids and Structures* **44**, 1745–1754 (2007).

[169] Nix, W. D. Mechanical properties of thin films. *Metallurgical and Materials Transactions A* **20**, 2217–2245 (1989).

[170] Kovacs, G. *Micromachined Transducers Sourcebook*. McGraw-Hill series in electrical and computer engineering (WCB/McGraw-Hill, 1998).

[171] Mézin, A. Coating internal stress measurement through the curvature method: A geometry-based criterion delimiting the relevance of Stoney's formula. *Surface and Coatings Technology* **200**, 5259–5267 (2006).

[172] Doerner, M. F. & Nix, W. D. Stresses and deformation processes in thin films on substrates. *Critical Reviews in Solid State and Materials Sciences* **14**, 225–268 (1988).

[173] Zhang, Y. Extended Stoney's formula for a film-substrate bilayer with the effect of interfacial slip. *Journal of Applied Mechanics* **75**, 011008 (2008).

[174] Sader, J. E. Surface stress induced deflections of cantilever plates with applications to the atomic force microscope: V-shaped plates. *Journal of Applied Physics* **91**, 9354–9361 (2002).

[175] Janssen, G. Stress and strain in polycrystalline thin films. *Thin Solid Films* **515**, 6654–6664 (2007).

[176] Choi, H. M., Choi, S. K., Anderson, O. & Bange, K. Influence of film density on residual stress and resistivity for Cu thin films deposited by bias sputtering. *Thin Solid Films* **358**, 202–205 (2000).

[177] McKenzie, D. R. & Bilek, M. M. M. Electron diffraction from polycrystalline materials showing stress induced preferred orientation. *Journal of Applied Physics* **86**, 230–236 (1999).

[178] Sohi, A. N., Nieva, P. & Khajepour, A. A new bimaterial microcantilever with tunable thermomechanical response. *Microelectronic Engineering* **96**, 18–23 (2012).

[179] Ma, H.-Y., Huang, Q.-A., Qin, M. & Lu, T. A micromachined silicon capacitive temperature sensor for wide temperature range applications. *Journal of Micromechanics and Microengineering* **20**, 055036 (2010).

[180] Fragiacomo, G., Ansbæk, T., Pedersen, T., Hansen, O. & Thomsen, E. V. Analysis of small deflection touch mode behavior in capacitive pressure sensors. *Sensors and Actuators A: Physical* **161**, 114–119 (2010).

[181] ming Sun, C., Wang, C. & Fang, W. On the sensitivity improvement of CMOS capacitive accelerometer. *Sensors and Actuators A: Physical* **141**, 347–352 (2008).

[182] Saeidpourazar, R. & Jalili, N. Microcantilever-based force tracking with applications to high-resolution imaging and nanomanipulation. *Industrial Electronics, IEEE Transactions on* **55**, 3935–3943 (2008).

[183] Waggoner, P. S. & Craighead, H. G. Micro- and nanomechanical sensors for environmental, chemical, and biological detection. *Lab Chip* **7**, 1238–1255 (2007).

[184] Rosakis, A., Singh, R., Tsuji, Y., Kolawa, E. & Jr., N. M. Full field measurements of curvature using coherent gradient sensing: Application to thin film characterization. *Thin Solid Films* **325**, 42–54 (1998).

[185] Park, T.-S., Suresh, S., Rosakis, A. & Ryu, J. Measurement of full-field curvature and geometrical instability of thin film-substrate systems through CGS interferometry. *Journal of the Mechanics and Physics of Solids* **51**, 2191–2211 (2003).

[186] Pyun, S.-I., Go, J.-Y. & Jang, T.-S. An investigation of intercalation-induced stresses generated during lithium transport through Li1 - δCoO_2 film electrode using a laser beam deflection method. *Electrochimica Acta* **49**, 4477–4486 (2004).

[187] Meyer, G. & Amer, N. M. Novel optical approach to atomic force microscopy. *Applied Physics Letters* **53**, 1045–1047 (1988).

[188] Dini, D., Passerini, S., Scrosati, B. & Decker, F. Stress changes in electrochromic thin film electrodes: Laser beam deflection method (LBDM) as a tool for the analysis of intercalation processes. *Solar Energy Materials and Solar Cells* **56**, 213–221 (1999).

[189] Beaulieu, L., Godin, M., Laroche, O., Tabard-Cossa, V. & Grütter, P. A complete analysis of the laser beam deflection systems used in cantilever-based systems. *Ultramicroscopy* **107**, 422–430 (2007).

[190] Kobeda, E. & Irene, E. A. A measurement of intrinsic SiO_2 film stress resulting from low temperature thermal oxidation of Si. *Journal of Vacuum Science & Technology B: Microelectronics and Nanometer Structures* **4**, 720–722 (1986).

[191] Kobeda, E. & Irene, E. A. In situ stress measurements during thermal oxidation of silicon. *Journal of Vacuum Science & Technology B: Microelectronics and Nanometer Structures* **7**, 163–166 (1989).

[192] Floro, J. A., Chason, E. & Lee, S. R. Real time measurement of epilayer strain using a simplified wafer curvature technique. *MRS Proceedings* **405**, 381–386 (1996).

[193] Raghavan, S., Weng, X., Dickey, E. & Redwing, J. M. Correlation of growth stress and structural evolution during metalorganic chemical vapor deposition of GaN on (111) Si. *Applied Physics Letters* **88**, 041904 (2006).

[194] MacArthur, K., Shi, B., Conley, R. & Macrander, A. T. Periodic variation of stress in sputter deposited Si/WSi_2 multilayers. *Applied Physics Letters* **99**, 081905 (2011).

[195] Shi, B., Meng, W. J., Rehn, L. E. & Baldo, P. M. Intrinsic stress development in Ti-C:H ceramic nanocomposite coatings. *Applied Physics Letters* **81**, 352–354 (2002).

[196] Amano, H. *et al.* Stress and defect control in GaN using low temperature interlayers. *Japanese Journal of Applied Physics* **37**, L1540–L1542 (1998).

[197] Sethuraman, V. A., Chon, M. J., Shimshak, M., Srinivasan, V. & Guduru, P. R. In situ measurements of stress evolution in silicon thin films during electrochemical lithiation and delithiation. *Journal of Power Sources* **195**, 5062–5066 (2010).

[198] Vanhumbeeck, J.-F. & Proost, J. In-situ monitoring of the dielectric and electrostrictive properties of anodised thin films for biochip applications. *Colloids and Surfaces B: Biointerfaces* **56**, 163–169 (2007).

[199] Smetanin, M. *et al.* Surface stress-charge response of a (111)-textured gold electrode under conditions of weak ion adsorption. *Langmuir* **24**, 8561–8567 (2008).

[200] Jiang, J. & Kee, B. On astigmatism of multi-beam optical stress sensor mounted at large incident angle. *Optik - International Journal for Light and Electron Optics* **114**, 427–432 (2003).

[201] Van Overmeere, Q., Vanhumbeeck, J.-F. & Proost, J. On the use of a multiple beam optical sensor for in situ curvature monitoring in liquids. *Review of Scientific Instruments* **81**, 045106 (2010).

[202] Weber, M. *Handbook of Optical Materials.* The CRC Press Laser and Optical Science and Technology Series (CRC Press, 2003).

[203] Ciddor, P. E. Refractive index of air: New equations for the visible and near infrared. *Appl. Opt.* **35**, 1566–1573 (1996).

[204] Owens, J. C. Optical refractive index of air: Dependence on pressure, temperature and composition. *Appl. Opt.* **6**, 51–59 (1967).

[205] Thornton, J. A. Influence of apparatus geometry and deposition conditions on the structure and topography of thick sputtered coatings. *Journal Of Vacuum Science And Technology* **11**, 666–670 (1974).

[206] Taarea, D. & Bakhtiyarov, S. General physical properties. In Gale, W. & Totemeier, T. (eds.) *Smithells Metals Reference Book (Eighth Edition)*, 1–45 (Butterworth-Heinemann, Oxford, 2004).

[207] Thornton, J. A., Tabock, J. & Hoffman, D. Internal stresses in metallic films deposited by cylindrical magnetron sputtering. *Thin Solid Films* **64**, 111–119 (1979).

[208] Floro, J. A. *et al.* The dynamic competition between stress generation and relaxation mechanisms during coalescence of Volmer-Weber thin films. *Journal of Applied Physics* **89**, 4886–4897 (2001).

[209] He, L., Lim, C. & Wu, B. A continuum model for size-dependent deformation of elastic films of nano-scale thickness. *International Journal of Solids and Structures* **41**, 847–857 (2004).

[210] Bicker, M., Von Hülsen, U., Laudahn, U., Pundt, A. & Geyer, U. Optical deflection setup for stress measurements in thin films. *Review of Scientific Instruments* **69**, 460–462 (1998).

[211] Dornheim, M. *et al.* Stress development in thin yttrium films on hard substrates during hydrogen loading. *Journal of Applied Physics* **93**, 8958–8965 (2003).

[212] Ludwig, A., Cao, J., Dam, B. & Gremaud, R. Opto-mechanical characterization of hydrogen storage properties of Mg-Ni thin film composition spreads. *Applied Surface Science* **254**, 682–686 (2007).

[213] El-Kareh, B. *Fundamentals of Semiconductor Processing Technology* (Kluwer Academic Publishers, 1995).

[214] Daniel, R., Holec, D., Bartosik, M., Keckes, J. & Mitterer, C. Size effect of thermal expansion and thermal/intrinsic stresses in nanostructured thin films: Experiment and model. *Acta Materialia* **59**, 6631–6645 (2011).

[215] Ichinohe, T., Masaki, S., Uchida, K., Nozaki, S. & Morisaki, H. Fabrication of nanostructured palladium-doped SiO_2 films with variable temperature coefficient of resistivity. *Thin Solid Films* **466**, 27–33 (2004).

[216] Chang-zhi, S., Xiao-wei, L. & Rong-yan, C. Current-induced recrystallization of polycrystalline silicon nano thin films deposited at different temperatures and its influences on piezoresistive sensitivity and temperature coefficients. *Sensors and Actuators A: Physical* **162**, 284–290 (2010).

[217] Smits, F. M. Measurement of sheet resistivities with the four-point probe. *Bell System Technical Journal* **37**, 711–718 (1958).

[218] Kuru, Y., Wohlschlögel, M., Welzel, U. & Mittemeijer, E. Coefficients of thermal expansion of thin metal films investigated by non-ambient X-ray diffraction stress analysis. *Surface and Coatings Technology* **202**, 2306–2309 (2008).

[219] Joshi, N., Aswal, D., Debnath, A., Gupta, S. & Yakhmi, J. Growth of nanocrystalline Pd films on Si (111). *Applied Surface Science* **228**, 302–305 (2004).

[220] Singh, U., Jha, N., Singh, T. P., Kapoor, A. & Perrone, A. Investigation of transmittance property of palladium thin films fabricated by pulsed laser deposition with polarization using single layer model. *Optics and Laser Technology* **42**, 1128–1133 (2010).

[221] Delmelle, R. & Proost, J. An in situ study of the hydriding kinetics of Pd thin films. *Physical Chemistry Chemical Physics* **13**, 11412–11421 (2011).

[222] Kern, A. & Eysel, W. *Mineralogisch-Petrograph. Inst.* Univ. Heidelberg, Germany, ICDD Grant-in-Aid (1993).

[223] Wang, B. *et al.* Texture-dependent twin formation in nanocrystalline thin Pd films. *Scripta Materialia* **66**, 866–871 (2012).

[224] EL Gowini, M. M. & Moussa, W. A. A finite element model of a MEMS-based surface acoustic wave hydrogen sensor. *Sensors* **10**, 1232–1250 (2010).

[225] Peisl, H. Lattice strains due to hydrogen in metals. In Alefeld, G. & Voelkl, J. (eds.) *Hydrogen in Metals*, vol. 1, 57–73 (Springer, Berlin, 1978).

[226] Youngdahl, C. J., Sanders, P. G., Eastman, J. A. & Weertman, J. R. Compressive yield strengths of nanocrystalline Cu and Pd. *Scripta Materialia* **37**, 809–813 (1997).

[227] Krom, A. & Bakker, A. Hydrogen trapping models in steel. *Metallurgical and Materials Transactions B* **31**, 1475–1482 (2000).

[228] Rajagopalan, J., Han, J. H. & Saif, M. T. A. Bauschinger effect in unpassivated freestanding nanoscale metal films. *Scripta Materialia* **59**, 734–737 (2008).

[229] Rajagopalan, J., Han, J. H. & Saif, M. T. A. On plastic strain recovery in freestanding nanocrystalline metal thin films. *Scripta Materialia* **59**, 921–926 (2008).

[230] Ward, T. L. & Dao, T. Model of hydrogen permeation behavior in palladium membranes. *Journal of Membrane Science* **153**, 211–231 (1999).

[231] Bucur, R. V. Adsorption and absorption of hydrogen by thin palladium layers. *Surface Science* **62**, 519–535 (1977).

[232] Hong, S. & Rahman, T. S. Adsorption and diffusion of hydrogen on Pd(211) and Pd(111): Results from first-principles electronic structure calculations. *Phys. Rev. B* **75**, 155405 (2007).

[233] Rawlings, J. & Ekerdt, J. *Chemical reactor analysis and design fundamentals* (Nob Hill Pub., 2002).

[234] Froment, G., Bischoff, K. & De Wilde, J. *Chemical reactor analysis and design (Third Edition)* (Wiley, 2010).

[235] Polyanin, A. & Zaitsev, V. *Handbook of Exact Solutions for Ordinary Differential Equations*. Mathematics, Physics, Mechanics, Control, Engineering Sciences (Chapman & Hall/CRC, 2003).

[236] Delmelle, R., Michotte, S., Sinnaeve, M. & Proost, J. Effect of internal stress on the hydriding kinetics of nanocrystalline Pd thin films. *Acta Materialia* submitted (2012).

[237] Mejdell, A., Chen, D., Peters, T., Bredesen, R. & Venvik, H. The effect of heat treatment in air on co inhibition of a ~3 μm Pd-Ag (23 wt.%) membrane. *Journal of Membrane Science* **350**, 371–377 (2010).

[238] Wang, H.-C. & Baltruschat, H. Determination of the activation volume for CO oxidation on platinum by pressure modulation. *ChemPhysChem* **11**, 2798–2801 (2010).

[239] White, J. On internal stress and activation volume in polymers. *Journal of Materials Science* **16**, 3249–3262 (1981).

[240] Baranowski, B. & Majorowski, S. Activation volume for hydrogen diffusion in palladium hydride. *Journal of the Less Common Metals* **98**, 27–29 (1984).

[241] Daniel, R., Martinschitz, K., Keckes, J. & Mitterer, C. The origin of stresses in magnetron-sputtered thin films with zone T structures. *Acta Materialia* **58**, 2621–2633 (2010).

[242] Nazarpour, S., Jambois, O., Zamani, C., Afshar, F. & Cirera, A. Stress distribution and hillock formation in Au/Pd thin films as a function of aging treatment in capacitor applications. *Applied Surface Science* **255**, 8995–8999 (2009).

[243] kee Kim, D. *et al.* Microstructure of thermal hillocks on blanket Al thin films. *Thin Solid Films* **371**, 278–282 (2000).

[244] Kumar, D. & Gupta, A. Evolution of structural and magnetic properties of sputtered nanocrystalline Co thin films with thermal annealing. *Journal of Magnetism and Magnetic Materials* **308**, 318–324 (2007).

[245] K H. Annealing of intrinsic stresses in sputtered TiN films: The role of thickness-dependent gradients of point defect density. *Surface and Coatings Technology* **201**, 4777–4780 (2007).

[246] Karlsson, L., Hörling, A., Johansson, M., Hultman, L. & Ramanath, G. The influence of thermal annealing on residual stresses and mechanical properties of arc-evaporated TiC_xN_{1-x} (x=0, 0.15 and 0.45) thin films. *Acta Materialia* **50**, 5103 – 5114 (2002).

[247] Bull, S., Evans, P. & Saleh, A. Positron annihilation studies of defects in PVD TiN coatings. *Surface and Coatings Technology* **78**, 42–49 (1996).

[248] Valvoda, V. *et al.* X-ray analysis of heat-treated titanium nitride films. *Thin Solid Films* **170**, 201–210 (1989).

[249] Xu, H., Heinrich, H. & Wiezorek, J. M. Microstructural changes during annealing of fepd-based thin films. *Intermetallics* **11**, 963–969 (2003).

[250] Miller, D. C. *et al.* Intrinsic stress development and microstructure evolution of Au/Cr/Si multilayer thin films subject to annealing. *Scripta Materialia* **52**, 873–879 (2005).

[251] Mizsei, J., Voutilainen, J., Saukko, S. & Lantto, V. Structural transformations of ultra-thin sputtered Pd activator layers on glass and SnO_2 surfaces. *Thin Solid Films* **391**, 209–215 (2001).

[252] Wedler, G. & Alshorachi, G. The influence of thickness on the resistivity, the temperature coefficient of resistivity and the thermoelectric power of evaporated palladium films at 77 K and 273 K. *Thin Solid Films* **74**, 1–16 (1980).

[253] Vries, J. D. Temperature and thickness dependence of the resistivity of thin polycrystalline aluminium, cobalt, nickel, palladium, silver and gold films. *Thin Solid Films* **167**, 25–32 (1988).

[254] Tripodi, P. *et al.* The effect of hydrogenation/dehydrogenation cycles on palladium physical properties. *Physics Letters A* **373**, 3101–3108 (2009).

[255] Shivaprasad, S. M. & Angadi, M. A. Temperature coefficient of resistance of thin palladium films. *Journal of Physics D: Applied Physics* **13**, L171 (1980).

[256] Koseva, R. *et al.* Evolution of hillocks in Bi thin films and their removal upon nanoscale mechanical polishing. *Thin Solid Films* **520**, 5589–5592 (2012).

[257] Berla, L. A., Joo, Y.-C. & Nix, W. D. A model for power law creep controlled hillock growth. *Materials Science and Engineering: A* **488**, 594–600 (2008).

[258] Hanabusa, T., Kusaka, K. & Sakata, O. Residual stress and thermal stress observation in thin copper films. *Thin Solid Films* **459**, 245–248 (2004).

[259] Tada, H. *et al.* Thermal expansion coefficient of polycrystalline silicon and silicon dioxide thin films at high temperatures. *Journal of Applied Physics* **87**, 4189–4193 (2000).

[260] Rodrigues, J. & Kirchheim, R. More evidence for the formation of a dense cottrell cloud of hydrogen (hydride) at dislocations in niobium and palladium. *Scripta Metallurgica* **17**, 159–164 (1983).

[261] Heuser, B. J. & King, J. S. SANS measurements of deuterium-dislocation trapping in deformed single crystal Pd. *Journal of Alloys and Compounds* **261**, 225–230 (1997).

[262] Ross, D., Stefanopoulos, K. & Kemali, M. The use of small angle neutron scattering in the study of hydrogen trapping at defects in metals. *Journal of Alloys and Compounds* **293-295**, 346–350 (1999).

[263] Besenbacher, F., Myers, S. & Nørskov, J. Interaction of hydrogen with defects in metals. *Nuclear Instruments and Methods in Physics Research Section B: Beam Interactions with Materials and Atoms* **7-8**, 55–66 (1985).

[264] Natter, H., Wettmann, B., Heisel, B. & Hempelmann, R. Hydrogen in nanocrystalline palladium. *Journal of Alloys and Compounds* **253-254**, 84–86 (1997).

[265] Jr, G. Y. & Scully, J. The diffusion and trapping of hydrogen in high purity aluminum. *Acta Materialia* **46**, 6337–6349 (1998).

[266] Frappart, S. *et al.* Study of the hydrogen diffusion and segregation into Fe-C-Mo martensitic HSLA steel using electrochemical permeation test. *Journal of Physics and Chemistry of Solids* **71**, 1467–1479 (2010).

[267] Cao, Y., Li, H., Szpunar, J. & Shmayda, W. Modeling of hydrogen trapping in the deformed Pd and $Pd_{77}Ag_{23}$ alloy. *Materials Science and Engineering: A* **379**, 173–180 (2004).

[268] Frappart, S. *et al.* Hydrogen solubility, diffusivity and trapping in a tempered Fe-C-Cr martensitic steel under various mechanical stress states. *Materials Science and Engineering: A* **534**, 384–393 (2012).

[269] Legrand, E., Bouhattate, J., Feaugas, X. & Garmestani, H. Computational analysis of geometrical factors affecting experimental data extracted from hydrogen permeation tests: II - Consequences of trapping and an oxide layer. *International Journal of Hydrogen Energy* In press, corrected proof (2012).

[270] Gesari, S., Pronsato, M. & Juan, A. Simulation of hydrogen trapping at defects in Pd. *International Journal of Hydrogen Energy* **34**, 3511–3518 (2009).

[271] Goldemberg, J. & Prado, L. T. S. The decline of the world's energy intensity. *Energy Policy* **39**, 1802–1805 (2011).

[272] Pacala, S. & Socolow, R. Stabilization wedges: Solving the climate problem for the next 50 years with current technologies. *Science* **305**, 968–972 (2004).

[273] Marbán, G. & Valdés-Solís, T. Towards the hydrogen economy? *International Journal of Hydrogen Energy* **32**, 1625–1637 (2007).

[274] Murray, J. & King, D. Climate policy: Oil's tipping point has passed. *Nature* **481**, 433–435 (2012).

[275] Puy, D. & Signore, M. From nuclei to atoms and molecules: the chemical history of the early universe. *New Astronomy Reviews* **46**, 709–723 (2002).

[276] Crabtree, G. & Dresselhaus, M. The hydrogen fuel alternative. *MRS Bulletin* **33**, 421–428 (2008).

[277] Jacobson, M. Z. & Delucchi, M. A. Providing all global energy with wind, water, and solar power, part I: Technologies, energy resources, quantities and areas of infrastructure, and materials. *Energy Policy* **39**, 1154–1169 (2011).

[278] Hansen, M., Sørensen, J., Voutsinas, S., Sørensen, N. & Madsen, H. State of the art in wind turbine aerodynamics and aeroelasticity. *Progress in Aerospace Sciences* **42**, 285–330 (2006).

[279] Thirugnanasambandam, M., Iniyan, S. & Goic, R. A review of solar thermal technologies. *Renewable and Sustainable Energy Reviews* **14**, 312–322 (2010).

[280] Parida, B., Iniyan, S. & Goic, R. A review of solar photovoltaic technologies. *Renewable and Sustainable Energy Reviews* **15**, 1625–1636 (2011).

[281] Paish, O. Small hydro power: technology and current status. *Renewable and Sustainable Energy Reviews* **6**, 537–556 (2002).

[282] Lund, J. W., Freeston, D. H. & Boyd, T. L. Direct utilization of geothermal energy 2010 worldwide review. *Geothermics* **40**, 159–180 (2011).

[283] Kim, K.-P., Ahmed, M. R. & Lee, Y.-H. Efficiency improvement of a tidal current turbine utilizing a larger area of channel. *Renewable Energy* **48**, 557–564 (2012).

[284] Setoguchi, T., Santhakumar, S., Maeda, H., Takao, M. & Kaneko, K. A review of impulse turbines for wave energy conversion. *Renewable Energy* **23**, 261–292 (2001).

[285] Delucchi, M. A. & Jacobson, M. Z. Providing all global energy with wind, water, and solar power, part II: Reliability, system and transmission costs, and policies. *Energy Policy* **39**, 1170–1190 (2011).

[286] Lindley, D. Smart grids: The energy storage problem. *Nature* **463**, 18–20 (2010).

[287] Taljan, G. & Gubina, A. F. Energy-based system well-being analysis for small systems with intermittent renewable energy sources. *Renewable Energy* **34**, 2651–2661 (2009).

[288] Bockris, J. *Energy : the solar-hydrogen alternative* (Australia and New Zealand Book Co., Sydney, 1975).

[289] Hunt, J. C. *Hydrogen Energy: Challenges and Prospects*. RSC Energy Series (The Royal Society of Chemistry, 2008).

[290] Agency, I. E. *Prospects for Hydrogen and Fuel Cells*. Energy technology analysis (International Energy Agency, 2005).

[291] Rifkin, J. *The Hydrogen Economy: The Creation of the Worldwide Energy Web and the Redistribution of Power on Earth* (J.P. Tarcher/Penguin, 2003).

[292] Andrews, J. & Shabani, B. Re-envisioning the role of hydrogen in a sustainable energy economy. *International Journal of Hydrogen Energy* **37**, 1184–1203 (2012).

[293] Thorstensen, B. A parametric study of fuel cell system efficiency under full and part load operation. *Journal of Power Sources* **92**, 9–16 (2001).

[294] Lanzi, E., Verdolini, E. & Haščič, I. Efficiency-improving fossil fuel technologies for electricity generation: Data selection and trends. *Energy Policy* **39**, 7000–7014 (2011).

[295] Brennan, S. *et al.* Hydrogen and fuel cell stationary applications: Key findings of modelling and experimental work in the hyper project. *International Journal of Hydrogen Energy* **36**, 2711–2720 (2011).

[296] Corbo, P., Migliardini, F. & Veneri, O. Experimental analysis and management issues of a hydrogen fuel cell system for stationary and mobile application. *Energy Conversion and Management* **48**, 2365–2374 (2007).

[297] Matsunaga, M., Fukushima, T. & Ojima, K. Powertain system of Honda FCX Clarity fuel cell vehicle. *World Electric Vehicle Journal* **3**, 1–10 (2009).

[298] Hetland, J. & Mulder, G. In search of a sustainable hydrogen economy: How a large-scale transition to hydrogen may affect the primary energy demand and greenhouse gas emissions. *International Journal of Hydrogen Energy* **32**, 736–747 (2007).

[299] Hultman, M. Back to the future: The dream of a perpetuum mobile in the atomic society and the hydrogen economy. *Futures* **41**, 226–233 (2009).

List of Figures

List of Tables